THE UNIVERSITY *of* EDINBURGH

Frequency Selective Surfaces for Terahertz Applications

Juan Jose Sanz Fernandez

A thesis submitted for the degree of Doctor of Philosophy.
The University of Edinburgh.
December 1, 2011

Abstract

This thesis presents both theoretical and experimental investigations of the performance and capabilities of frequency selective surfaces (FSS) applied at THz frequencies. The aim is to explore and extend the use of FSS, traditionally limited to microwave frequencies, towards the THz regime of the spectrum, where interesting applications such as imaging, sensing and communications exist. The contribution of this work lies in three main areas within the scope of THz FSS, namely, performance, prototyping and applications.

Unlike microwave FSS where extensive research has been performed to evaluate the performance of different FSS designs, particular problems arise at THz frequencies, significantly, the ohmic losses. While a few notable studies can be found on the issue of ohmic losses, part of this thesis investigates, for the first time, the power dissipation due to the presence of both ohmic and dielectric losses, in relation to the power stored in the vicinity of the FSS, the currents induced in the elements of the array and the array's terminal impedance. By doing so, a better understanding of the performance of THz FSS has been given in terms of their quality factor, allowing for design guidelines previously unavailable.

In order to demonstrate multiband operation experimentally, a novel fabrication process has been designed and developed to manufacture capacitive or dipole-based THz FSS on a dielectric layer. Dry deep-reactive ion etching has been employed in order to avoid the use of wet etching to provide better control of etch characteristics. Various FSS operating around 15THz have been demonstrated experimentally.

In addition, THz FSS have been investigated theoretically in the realm of three different applications, namely, multiband operation, sensing capability and reconfigurability. Multiband characteristics using single-screen FSS have been achieved by perturbed dipole FSS exhibiting up to four resonances due to the excitation of even and odd current modes. After studying the near-fields in perturbed FSS, it has been found that this type of FSS represent a very attractive candidate for sensing applications due to the revealed near-field enhancement phenomena related to the excitation of the odd mode, where currents flow in opposite directions. Finally, a novel tunability approach

to reach frequency reconfigurability by varying the near-field coupling between two closely spaced layers in a dual-layer configuration has been proposed. A MEMS movable four-arm membrane has been suggested to vary the distance between the two layers mechanically, leading to the frequency tuning effect. This approach has been shown to be particularly suitable for THz frequencies, and has been applied to demonstrate theoretically tunable FSS and other periodic structures, such as artificial magnetic conductors and dielectric gratings.

Declaration of Originality

I hereby declare that the research recorded in this thesis and the thesis itself was composed and originated entirely by myself in the School of Engineering at the University of Edinburgh.

Juan Jose Sanz Fernandez

Acknowledgements

It is a pleasure for me to thank those who have made this thesis possible. First and foremost, I owe my deepest gratitude to my supervisor Prof. Rebecca Cheung for her constant and thorough supervision. She has contributed with great ideas, invaluable advice and expertise. I could not have written this thesis without her support and encouragement.

Likewise, I am really grateful to Dr. George Goussetis, previously at Heriot-Watt University and now at Queen's Belfast University, who has played a key role in my understanding of the theory of periodic structures, and whose collaboration has made this thesis possible.

It is an honor for me also to thank Wolfson Microelectronics for the financial support, that has allowed me to undertake the research needed for the development of this thesis.

I must thank also Dr. Jose Luis Gsmez Tornero, at Technical University of Cartagena, Spain, for encouraging me to apply for the PhD position back in 2007.

I would like to thank Dr. Carolina Mateo-Segura, recently appointed Lecturer at Heriot-Watt University, with whom I have had the opportunity to collaborate during these years. I am indebted to many of my colleagues at the SMC, namely Dr. Enrico Mastropaolo, Dr. Damien Thuau, Graham Woods, Isaac Gual, and Dr. Andreas Tsiamis, for accompanying me during my PhD. They have been not only supportive colleagues, but also great friends.

I am also grateful to the technicians at the SMC Andy Bunting, Bill Parks, Camelia Dunare, Richard Blair, Ewan MacDonald, Hugh Frizell, Kevin Tierney, and Alec Ruthven for their advice and help regarding the microfabrication theory and techniques. I want to show my gratitude to Prof. Antonio Sanz Martnnez de Galinsoga, at the University of Murcia, Spain, and to Dr. Robert MacPheat at the Molecular Spectroscopy Facility, Rutherford Appleton Laboratory, Oxford, U.K., for their advice and support during FTIR measurements.

I would like to show my most sincere gratitude to my girlfriend Yi-Hsin Liu, also PhD

candidate at the University of Edinburgh, with whom I have shared the sweet and bitter moments in our way towards obtaining the PhD degree. To her and to my father Antonio, mother Dolores, sister Lola and brother Nono, I really need to thank them for understanding, supporting and loving me throughout these years.

Contents

Contents . . . vii
List of figures . . . x
List of tables . . . xix

1 Introduction **1**
1.1 Overview . . . 1
1.2 Motivation and Objectives . . . 2
1.3 Chapters outline . . . 4

2 FSS Background **6**
2.1 Introduction . . . 6
2.2 General description of FSS performance . . . 6
2.2.1 Historical perspective of periodic structures . . . 6
2.2.2 FSS Definition . . . 8
2.2.3 FSS Characteristics . . . 8
2.2.4 Configurations: fixed and tunable FSS performance . . . 15
2.2.5 Applications . . . 17
2.3 Analysis techniques . . . 21
2.3.1 Method of Moments (MoM) . . . 23
2.3.2 Finite Element Method (FEM) . . . 25
2.3.3 Commercial softwares . . . 27
2.4 Microfabrication techniques . . . 27
2.4.1 Deposition . . . 28
2.4.2 Patterning . . . 31
2.4.3 Etching . . . 34
2.5 Measurement methods . . . 37
2.5.1 Microwave regime . . . 38
2.5.2 Submillimeter waves . . . 38
2.5.3 Infrared spectroscopy . . . 40
2.6 Conclusions . . . 44

3 Methodology for the analysis, fabrication and measurements of FSS at THz frequencies **45**
3.1 Introduction . . . 45
3.2 Analysis of FSS with no ohmic losses . . . 46
3.2.1 Wave equation in homogeneous medium . . . 46
3.2.2 Modal analysis of lossless FSS and solution using MoM . . . 51
3.3 Analysis of FSS with ohmic losses . . . 76
3.3.1 Interaction of THz radiation with matter: material models . . . 76
3.3.2 Analysis of lossy FSS using commercial softwares . . . 89
3.4 Fabrication Process . . . 94
3.4.1 General considerations . . . 94

3.4.2 SiO_2-Si-SiO_2 substrate . . . 97
3.4.3 Patterning process . . . 98
3.4.4 Deep-etching step . . . 100
3.5 Measurement Scheme: FTIR equipment and set-up . . . 103
3.6 Conclusions . . . 107

4 Energy storage, dissipation and quality factors of FSS at THz frequencies 109
4.1 Introduction . . . 109
4.2 Material considerations . . . 110
4.2.1 Metal and dielectric dissipation . . . 111
4.2.2 Metal thickness . . . 113
4.2.3 Surface roughness and native oxide . . . 116
4.3 Resonant Characteristics of FSS . . . 118
4.3.1 Circuital model of FSS . . . 118
4.3.2 Definitions of the quality factors in FSS . . . 122
4.4 Q-factors and powers assessment in free-standing FSS . . . 129
4.4.1 Power stored in FSS (no ohmic losses) . . . 129
4.4.2 Power dissipated (ohmic losses) . . . 134
4.4.3 External, Loaded and Unloaded Quality Factors . . . 138
4.4.4 Influence of varying length and width of the dipoles . . . 140
4.5 Conclusions . . . 142

5 Substrate effects in FSS at THz frequencies 145
5.1 Introduction . . . 145
5.2 FSS operation in the presence of dielectrics . . . 146
5.2.1 Circuital model of FSS with a dielectric loading . . . 146
5.2.2 Substrate effects on the resonance shape and location . . . 149
5.3 Currents and Near-Field excited in FSS supported by a dielectric substrate 153
5.3.1 Induced currents . . . 153
5.3.2 Floquet modes excitation . . . 155
5.4 Dielectric behavior at THz frequencies . . . 155
5.5 Power dissipated in the presence of a substrate . . . 157
5.5.1 Ohmic losses only . . . 157
5.5.2 Dielectric losses only . . . 160
5.5.3 Dielectric and ohmic losses . . . 163
5.6 Conclusions . . . 164

6 Single-screen FSS for filters and sensing components at THz frequencies 167
6.1 Introduction . . . 167
6.2 Conventional-elements FSS for single-band applications . . . 168
6.3 Perturbed FSS for multiband and sensing applications . . . 175
6.3.1 Perturbed FSS operation . . . 175
6.3.2 Multiband perturbed FSS . . . 179
6.3.3 Sensing using perturbed FSS . . . 183
6.4 Experimental validation of perturbed FSS . . . 190
6.5 Conclusions . . . 193

7 Multilayered and Tunable FSS at THz frequencies **196**
7.1 Introduction . . . 196
7.2 Closely Coupled FSS . . . 198
7.2.1 Equal-tuning and aligned dipoles . . . 198
7.2.2 Equal-tuning and misaligned dipoles . . . 200
7.2.3 Staggered-tuning and aligned dipoles . . . 203
7.2.4 Staggered-tuning and misaligned dipoles . . . 205
7.3 Tunable FSS . . . 207
7.3.1 Tunability approach . . . 209
7.3.2 MEMS analysis and design . . . 212
7.3.3 Applicability in tunable FSS . . . 213
7.3.4 Other tunable applications: AMC and all-dielectric FSS . . . 214
7.4 Conclusion . . . 216

8 Conclusions and Future Work **219**

A Publications **225**
A.1 Journal Papers . . . 225
A.2 Conference Papers . . . 225

References **227**

List of Figures

1.1 Summary of the different areas investigated in this thesis and outline of the chapters. 4

2.1 Principle of Operation of FSS under electric field a) parallel and b) perpendicular to the elements length. 9
2.2 Complementary FSS, a) patch-based FSS, b) aperture-based FSS and c) typical reflection and transmission characteristic as a function of frequency. 9
2.3 Representation of the propagating and evanescent waves in periodic arrays under plane-wave incidence 10
2.4 a) Traditional elements of FSS, and b) harmonic (even and odd) modes in dipole elements. 12
2.5 a) FSS on ferrite substrate magnetically actuated, b) LC layer sandwiched by two FSS acting as electrodes (sealing of the liquid omitted for clarity), c) PIN, varactor or MEMS switches interconnecting collinear dipoles, and d) array of tilting dipoles based on magnetic MEMS. 17
2.6 a) NASA DSS 13 beam-waveguide antenna, and b) NASA Cassegrain subreflector (adapted from [64]) 18
2.7 FSS radomes integrated in a) airplanes, and b) ground antenna systems 18
2.8 a) Absorbers consisting of Salisbury, Jaunmann and FSS screens, and b) linear and meanderline polarizers 19
2.9 FSS applications in a) frequency-scanned antennas, b) frequency-dependent wall in waveguides and horn antennas, c) waveguide filters, d) EM isolation in buildings, and e) FSS/planar antennas. 20
2.10 a) One of the first type of FSS studied at infrared (e.g. in [123]), b) FSS in TPV conversion system, and c) d) FSS for sensing materials. 21
2.11 Description of sub-regions in FEM. a) Triangular elements for 1, 2 and 3 dimensions, b) example of dividing EM into subregions, c) potential in the nodes of the element, and d) adjacent elements 25
2.12 Manual spinners available at the Scottish Microelectronics Centre and used for spin-coating in wafers (a) and single chips (b) 29
2.13 Schemes of a) LPCVD furnace, b) sputtering PVD. 30
2.14 Main steps in the patterning process using photolithography 31
2.15 Photolithography equipments and its parts available at the SMC, a) Karl Suss MA8, (3, 4, 6 and 8") and b) Cobilt 2020 soft contact (3"). The inset figures in a) show a 5" chrome mask and a 4" silicon wafer. 33
2.16 Diagrams of the etching techniques based on a) RIE and b) ICP. 35
2.17 a) STS Multiplex load locked Al and $Poly - Si$ RIE etcher using $SiCl_4$, and Cl_2 chemistry, and b) Plasmatherm PK244O RIE system using Fluorine chemistry to anisotropically etch SiO_2 and Si_3N_4. 36

2.18 STS Multiplex ICP - Load locked inductively coupled plasma etch system configured for deep Si etching. a) ICP view 1 (inset shows glow discharge), b) ICP view 2. 37
2.19 Measuring FSS at microwave frequencies using a) network analyzers [picture of model Agilent 8714ES from macro-test.com] in b) antenna configuration in anechoic chamber or c) waveguide configuration. 39
2.20 Diagram of THz-TDS spectroscopy 39
2.21 Diagram of the principle of operation of FTIR spectrometers 41
2.22 Mylar efficiency (adapted from [187]). 43

3.1 1D periodic structure 52
3.2 Periodic array of (a) rectangular waveguides and (b) dipoles 53
3.3 Propagating and evanescent waves in FSS of arbitrary elements. 56
3.4 Definition of parameters in rectangular (a), and skewed unit cell (b). . . 58
3.5 Field regions of an FSS supported by a dielectric layer 64
3.6 a) Dipole FSS, b) cosine and c) sine entire-domain basis functions 73
3.7 Example of 1D rooftop subdomain basis functions. S_1, S_2, and S_3 represent three elements of the mesh 74
3.8 "Field-cell transmission lines" equivalence of space and schematic representation of an infinitesimally short segment of one field cell consisting of parallel conducting strips (adapted from [190]). 82
3.9 Linearly y-polarized plane wave normally incident to a conducting medium and penetrating according to the skin depth effect, and equivalent transmission line problem 84
3.10 Skin depth comparison between the two formulations 85
3.11 Power reflectance (green dash-dot line and right y-axis) and surface resistance for Al (left y-axis) using the experimental model (3.253) in black dotted line and classical models (3.250)-(3.251) in red dashed and blue solid lines, respectively. The inset zooms in the far-IR band and shows just the Rs 88
3.12 a) Infinitely long wires, b) lossless, and c) lossy dipoles of finite length. Adapted from [1] 89
3.13 a) Planar 2.5D model of a four-legged FSS, b) 3D view of the FSS on a substrate, c) mesh of the element, and d) zoom in the mesh, where the currents normal to the edges of triangular elements are calculated and the current inside the element is obtained as superposition of the normal currents 91
3.14 HFSS FSS analysis steps, FSS drawing, incident wave, radiation boundaries, and master/slave boundaries 93
3.15 Example of mesh of an FSS in HFSS 93
3.16 FSS on a thin substrate(a), supported by a hollowed thicker substrate (b) 96
3.17 Fabrication process develop in this thesis for the fabrication of THz FSS . 97
3.18 Bird view of FSS 97
3.19 Chrome mask containing the membrane patterns and patterned oxide . . 99
3.20 a) Cr mask of FSS patterns, b) patterned wafer and c) zoom in patterned FSS before (left) and after (right) etching 100
3.21 Patterned FSS on rough PI-SiO_2 membrane after DRIE etching 101

3.22 Flat membrane 102
3.23 Study on the oxide etch-rate for ammonium fluoride and acetic acid . . . 102
3.24 a) Set-up for measuring FSS with the Perkin Elmer FTIR (University of Murcia, Spain), and b) measuring scheme 104
3.25 Schematic of Bruker 120HR (STFC, Oxford) 104
3.26 Measurement frequency range using a) MCT detector and KBr-Ge beam-splitter, b) DGTS detector and Mylar beam-splitter 105
3.27 General view of Bruker 120HR (STFC, Oxford) 105
3.28 Close look at sample, detectors and beam-splitter compartments of Bruker 120HR (STFC, Oxford) 106
3.29 a) Interferogram, b) energy at the detector without and with FSS, c)-e) transmission (energy with/energy without) of the FSS for 100, 50, and 10scans, respectively 107

4.1 Absorption of FSS at resonance for various frequency regions. The green and red lines show the absorption due to dielectric-only and ohmic-only losses, respectively. The solid blue line represents both ohmic and dielectric losses present simultaneously. The dotted blue line shows the addition of ohmic and dielectric losses obtained separately. 112
4.2 Surface resistance (3.238) versus frequency of Al films with varying thickness. The skin depth at each frequency is also shown for reference. At 100THz two values of skin depth are shown δ_1 and δ_2 corresponding to (3.231) and (3.237), respectively. 114
4.3 Reflection parameter for variable thickness of the elements (thin metal). 115
4.4 Absorption for variable thickness of the elements (thin metal). 115
4.5 Reflection parameter for variable thickness of the elements (thick FSS). . 116
4.6 Representation of a) thin FSS, and b) thick FSS 116
4.7 Conductivity of Al films ($\sigma_{bulk} = 3.8 \cdot 10^7 S/m$) versus frequency for variable surface roughness. The inset zooms in the FIR frequency regime. 117
4.8 Equivalent circuits of capacitive FSS with arbitrary shape (a), in the lossless (b) and the lossy case (c) 118
4.9 Equivalent circuit and far-field response of FSS a-c) in the absence of losses and d-f) in the presence of losses. 120
4.10 Terminal reactance calculated with MoM formulation (blue straight line) and Taylor approximation (red dashed line) for FSS resonant at 18.5THz. 125
4.11 Currents flowing in the equivalent circuit at resonance in a) lossless FSSs and b) lossy FSSs 127
4.12 Capacitive FSS based on parallel strip of length L, width w and thickness t. The strips are periodically arranged at a distance d_x and d_y from each other. J_s, P_{dis} and P_{st} represent the surface current density induced in the dipoles, the dissipated power and the stored power (either in the electric or magnetic field), respectively. 129
4.13 Reflection coefficient of the lossless FSS depicted in Figure 4.12 with dimensions $L = 9\mu m$, $w = 1\mu m$, $d_y = 11\mu m$ and varying d_x as calculated by MoM and EC. 130

4.14 Average current induced in the dipoles in the lossless FSS of Figure 4.13 calculated by MoM and EC various d_x. The inset shows the peak value of the average current induced in the dipoles versus the periodicity. . . . 131
4.15 Surface-current densities for lossless FSS with variable width (1,0.5, and $0.1\mu m$) and dimensions $L = 9\mu m$, $dx = 8\mu m$,$dy = 11\mu m$. a-c) Bird's view, d-f) view along the width, and g-i) top view. 132
4.16 Terminal resistance (left y-axis) and reactance slope parameter (right y-axis) for the FSS of Figure 4.13 and different values of periodicity d_x. . 133
4.17 a) Bird's and b) side view of the dimensions of the integral volume for calculating the power stored 135
4.18 Power radiated from the FSS of Figure 4.13 to free space at resonance using (4.44)-(4.45) and power stored at the same FSS at resonance using (4.46)-(4.47) for varying periodicities d_x. 135
4.19 Reflection coefficient of the FSS of Figure 4.13 where the metallic elements are fabricated using aluminum calculated by MoM and EC for different periodicities d_x. 136
4.20 Ohmic resistance R_{ohmic} (left y-axis) and ratio $\kappa = R_{ohmic}/R_a$ (right y-axis) of the FSS of Figure 4.19 for different periodicities d_x. 137
4.21 Surface currents for variable conductivities 137
4.22 Surface currents (maximum amplitude and phase) vs frequency for variable conductivities 138
4.23 Absorption coefficient of the FSS of Figure 19 as calculated by MoM and EC for different periodicities d_x. 138
4.24 Power dissipated at resonance for the FSS of Figure 19 for varying periodicity d_x. 139
4.25 External quality factor in the lossless FSS of Figure 13 calculated by the definition, EC, and the inverse of the $3dB$ fractional bandwidth for different periodicities d_x. 139
4.26 a) Loaded quality factor for the FSS of Figure 4.13 (lossless) and Figure 4.19 (lossy) for varying periodicity d_x. b) Unloaded quality factor for the FSS of Figure 4.19 for varying periodicities d_x. 140
4.27 a) Reflection coefficient, b) averaged induced currents, c) loaded and external q-factors, and d) unloaded q-factor of FSS with varying length L 141
4.28 a) Reflection coefficient, b) averaged induced currents, c) loaded and external q-factors, and d) unloaded q-factor of FSS with varying width w 142

5.1 Free-standing capacitive FSS consisting of dipoles (a), and its equivalent circuit based on the terminal impedance $Z_{a0} = R_{a0} + jX_{a0}$ in the presence (b) and absence (c) of ohmic losses. Capacitive FSS on a dielectric substrate (d), and its equivalent circuit based on the terminal impedances Z_{a0} (free-standing FSS) and Z_{a1} (FSS immersed in an infinite dielectric) in the presence (e) and absence (f) of ohmic and dielectric losses. 147
5.2 a) Transmission-line model for FSS loaded with a dielectric substrate. Equivalent impedance of a capacitive (b), and inductive (c) FSS. 148

5.3 Influence of the dielectric on capacitive FSS reflection obtained by full-wave MoM (solid lines) and EC (dotted lines). a) Free-standing lossless FSS ($L = 9\mu m$, $w = 1\mu m$, $d_x = 10\mu m$, $d_y = 11\mu m$) (blue line) and FSS immersed in an infinite dielectric of permittivity equal to 2 (red line); b) free-standing lossy FSS ($s = 3.810^6 S/m$); c) lossless FSS on lossless substrate ($t_{die} = 1.7\mu m$); and d) lossy FSS on lossy substrate ($tan\delta = 0.008$). The inset shows the circuital models employed in each subfigure. R_{a0}, R_{a1}, and R_{ohmic} employed are 36.82, 26.03 and 1.52Ω, respectively. The reactance slope parameter corresponding to X_{a0} and X_{a1} are 92.13 and 70.42Ω, respectively. 150
5.4 Contour plot of the reflection coefficient of an FSS with dimensions $L = 9\mu m$, $w = 1\mu m$, $d_x = 10\mu m$, $d_y = 11\mu m$. The horizontal and vertical axis represent the thickness $t = t_{die}$ and the frequency, respectively. The black solid-line corresponds to the resonant frequency and the grey dashed-lines represent secondary resonances due to the presence of the dielectric. 151
5.5 a) Zoom in the contour plot of Figure 5.4. The frequency range is reduced to cover between 7.25 and $13.5THz$, and the contour lines of the reflection are focused on the range from 0.2 to $-4dB$. b) Reflection coefficient for the FSS of Figure 5.4 versus frequency at three particular thicknesses, namely 20, 22.5 and $25\mu m$. The effect of secondary dielectric resonances is evident. 152
5.6 Averaged currents induced in the FSS for varying thickness and dielectric permittivity $\epsilon_r = 2$ 154
5.7 Averaged currents induced in the FSS for varying dielectric permittivity and thickness $t_{die} = 1\mu m$ 154
5.8 Amplitude of the slowest decaying Floquet mode TE_{01} for various thickness (fixed $\epsilon_r = 2$) (a) and permittivity (fixed thickness $t_{die} = 1\mu m$) (b) 155
5.9 Dispersion study of the reflection coefficient of a lossless FSS supported by a dielectric substrate with no dispersion 156
5.10 Dispersion study of the reflection coefficient of a lossless FSS supported by a dielectric substrate with a) linear and b) sinusoidal dispersion . . . 156
5.11 Reflection coefficient versus frequency for low values of thickness of the substrate ($0.25\mu m$ to $5\mu m$). On the right-hand side, the reflection and absorption near the resonance is zoomed in. FSS with same dimensions as in Figure 5.4 and only ohmic losses. 158
5.12 Reflection coefficient versus frequency for thick substrates ($7.5\mu m$ to $17.5\mu m$). On the right-hand side, the reflection and absorption near the resonance is zoomed in. FSS with same dimensions as in Figure 5.4 and only ohmic losses. 158
5.13 Absorption coefficient versus thickness of the supporting dielectric layer t_{die}. FSS with same dimensions as in Figure 5.4 and only ohmic losses. . 159
5.14 Contour plot of the absorption coefficient versus thickness of the supporting dielectric layer t_{die} and frequency. FSS with same dimensions as in Figure 5.4 and only ohmic losses. 160

5.15 Reflection coefficient versus frequency for low values of thickness of the substrate ($0.25\mu m$ to $5\mu m$). On the right-hand side, the reflection and absorption near the resonance is zoomed in. FSS with same dimensions as in Figure 5.4 and only dielectric losses. 161
5.16 Reflection coefficient versus frequency for thick substrates (7.5um to 17.5um). On the right-hand side, the reflection and absorption near the resonance is zoomed in. FSS with same dimensions as in Figure 5.4 and only dielectric losses. 161
5.17 Absorption coefficient versus thickness of the supporting dielectric layer t_{die}. FSS with same dimensions as in Figure 5.4 and only dielectric losses. 162
5.18 Contour plot of the absorption coefficient versus thickness of the supporting dielectric layer t_{die} and frequency. FSS with same dimensions as in Figure 5.4 and only dielectric losses. 162
5.19 Contour plot of the absorption coefficient versus thickness of the supporting dielectric layer t_{die} and frequency. FSS with same dimensions as in Figure 5.4 and both dielectric and ohmic losses. 163
5.20 Absorption coefficient versus thickness of the supporting dielectric layer t_{die}. FSS with same dimensions as in Figure 5.4 and both dielectric and ohmic losses. 163
5.21 Summary of absorption contributions from ohmic and dielectric losses. . 164

6.1 Derivation of different types of elements from the array of infinitely-long dipoles. a) finite-length dipoles, b) crossed-dipoles and Jerusalem crosses, c) plate and loop-type elements, and d) four-legged loaded elements. 169
6.2 Reflection and absorption characteristic (left) and amplitude of induced current (right) of polarizer with dimensions $w = 1.5\mu m$, $d_x = 3\mu m$. . . . 170
6.3 Reflection and absorption characteristic (left) and amplitude of induced current (right) of dipole FSS with dimensions $L = 14\mu m$, $w = 2\mu m$, $d_x = 10\mu m$, $d_y = 20\mu m$. 170
6.4 Reflection and absorption characteristic (left) and amplitude of induced current (right) of cross-dipole FSS with dimensions $L = 10\mu m$, $w = 2\mu m$, $d_x = 16\mu m$, $d_y = 16\mu m$. 171
6.5 Reflection and absorption characteristic (left) and amplitude of induced current (right) of Jerusalem-cross FSS with dimensions $L = 8\mu m$, $w = 2\mu m$, $d_x = 16\mu m$, $d_y = 16\mu m$, $L_{load} = 4\mu m$. 171
6.6 Reflection and absorption characteristic (left) and amplitude of induced current (right) of tripole FSS with dimensions $L_{leg} = 5.15\mu m$, $w = 4\mu m$, $d_x = 16\mu m$, $d_y = 16\mu m$. 172
6.7 Reflection and absorption characteristic (left) and amplitude of induced current (right) of square-loop FSS with dimensions $L_{max} = 12\mu m$, $L_{min} = 8\mu m$, $d_x = 20\mu m$, $d_y = 20\mu m$, $w = 2\mu m$. 173
6.8 Reflection and absorption characteristic (left) and amplitude of induced current (right) of ring FSS with dimensions $r_{max} = 5\mu m$, $r_{min} = 3\mu m$, $d_x = 12\mu m$, $d_y = 20\mu m$, $w = 2\mu m$. 173

6.9 Reflection and absorption characteristic (left) and amplitude of induced current (right) of four-legged FSS with dimensions $L_{max} = 14\mu m$, $L_{min} = 3\mu m$, $d_x = 28\mu m$, $d_y = 28\mu m$, $w = 2\mu m$. 175
6.10 a) Unperturbed FSS ($L_1 = 9\mu m$, $w = 1\mu m$, $d_x = 8\mu m$, and $d_y = 11\mu m$), and b) simply perturbed FSS ($L_2 = 9\mu m$, $L_2 = 7um$, $w = 1\mu m$, $d_x = 8\mu m$, and $d_y = 11\mu m$). 176
6.11 Far-field reflection coefficient of perturbed FSS vs frequency for length of the dipoles of subarray 1 fixed at $9\mu m$ and subarray 2 ranging from $L_2 = 9$ to $3\mu m$. The numbers in the figure indicates the various resonances of each case. 1 indicates the even mode in unperturbed FSS. 2, 3, and 4 indicate the odd mode, even mode and interaction null in perturbed FSS, respectively. 180
6.12 Simulated reflection coefficient versus frequency by full-wave MoM of a) unperturbed FSS ($L_1 = 9\mu m$, $w = 1\mu m$, $d_x = 8\mu m$, and $d_y = 11\mu m$), and b) simply perturbed FSS ($L_2 = 9\mu m$, $L_2 = 7\mu m$, $w = 1\mu m$, $d_x = 8\mu m$, and $d_y = 11\mu m$). The magnitude and direction of the currents at the even and/or odd modes are also shown. 181
6.13 Simulated reflection coefficient versus frequency by full-wave MoM of a) doubly perturbed FSS ($L_1 = 9\mu m$, $L_2 = 7\mu m$, $L_3 = 5\mu m$, $w = 1\mu m$, $d_x = 12\mu m$, and $d_y = 11\mu m$), and c) triply perturbed FSS ($L_1 = 10\mu m$, $L_2 = 8.5\mu m$, $L_3 = 7\mu m$, $L_4 = 5.5\mu m$, $w = 1\mu m$, $d_x = 16\mu m$, and $d_y = 11\mu m$). The magnitude and direction of the currents at the even and/or odd modes are also shown. 182
6.14 Reflection coefficient of a dipole-ring FSS ($L = 9\mu m$, $w = 1\mu m$, $d_x = 8\mu m$, $d_y = 16\mu m$, and $r = 4\mu m$). 183
6.15 Reflection coefficient S_{11} versus frequency for the perturbed FSS of Figure 6.10, with L_1 = 8.2μm, L_2 = 7.5μm, w = 0.5μm, d_y = 10.6μm, and d_x = 7.7μm. For comparison the S_{11} for an unperturbed FSS with the same dimensions and L = 8.2μm is added. 185
6.16 a-b) Magnitude of current induced on the long and short dipole, respectively. c-d) Phase of current induced on the long and short dipole, respectively. The dimensions of the FSS are those employed in Figure 6.15.186
6.17 a-b) z-component of magnetic near-field for the even and odd modes, respectively. The dimensions of the FSS are those employed in Figure 6.15.186
6.18 Loaded Q-factor Q_L as a function of L_2 for the perturbed FSS of Figure 6.10, with L_1 = 8.2μm, w = 0.5μm, d_y = 10.6μm, and d_x = 7.7μm. For comparison the Q_L for an unperturbed FSS with the same dimensions and L = 8.2μm is added. 187
6.19 a) Magnitude of electric field in the unit cell of a perturbed FSS (L_1 = 9μm, L_2 = 7μm, w = 1μm, d_y = 8μm, d_x = 10μm) supported by a dielectric layer (t_{die} = 1.7μm, ϵ_r = 3.5, $tan\delta$ = 0.008). b) Scheme of the sensing mechanism, showing the expected measured resonant shift after the sensed material is deposited on the FSS. 188
6.20 Frequency shift for a) 300nm of a material with variable permittivity ϵ_r, and b) various thicknesses t_{mat} of a material of ϵ_r = 3. The shift is shown for both the odd (left) and even (right) modes 189
6.21 Transmission FTIR measurements of $1.7\mu m$ thick PI membrane. 191

6.22 Transmission FTIR measurements of an a) unperturbed FSS ($L = 7\mu m$, $w = 1\mu m$, $d_x = 8\mu m$, and $d_y = 11\mu m$) and a b) perturbed FSS ($L_1 = 9\mu m$, $L_2 = 5\mu m$, $w_1 = w_2 = 1\mu m$, $d_x = 8\mu m$, and $d_y = 11\mu m$) on a $1.7\mu m$ thick PI membrane. Measured responses are normalized by the PI transmission of Figure 6.21, and compared to simulated responses under vertically and elliptically polarized plane-waves. 192
6.23 Transmission FTIR measurements of an dual-band dual-polarized FSS based on rings and dipoles, $L = 9\mu m$, $D = 8\mu m$, $w = 1\mu m$, $d_x = 12\mu m$, and $d_y = 11\mu m$. Measured response normalized by the PI transmission of Figure 6.21. 193

7.1 S_{11} (blue solid line) and Abs (red dashed line) versus frequency for varying gap between the layers $g = 0, 0.25, 0.65, 1, 2.5, 5\mu m$. 199
7.2 Currents induced for $1\mu m$ gap in the FSS of Figure 7.1. 199
7.3 S_{11} (blue solid line) and Abs (red dashed line) versus frequency for varying gap between the layers $g = 0, 0.25, 0.65, 1, 2.5, 5\mu m$. 201
7.4 S_{11} (blue solid line) and Abs (red dashed line) versus frequency for varying gap between the layers $g = 0, 0.25, 0.65, 1, 2.5, 5\mu m$. 202
7.5 Currents induced for $1\mu m$ gapin the FSS of Figure 7.4. 203
7.6 S_{11} (blue solid line) and Abs (red dashed line) versus frequency for varying gap between the layers $g = 0, 0.25, 0.65, 1, 2.5, 5\mu m$, ($L_1 = 6\mu m$, $L_2 = 9\mu m$). Solid blue and red dashed lines represent $L_{upper} = L_2$, and $L_{lower} = L_1$. Dotted blue and red lines represent $L_{upper} = L_1$, and $L_{lower} = L_2$. 204
7.7 Currents induced for $1\mu m$ gap in the FSS of Figure 7.6, and $L_{upper} = L_1$, and $L_{lower} = L_2$. 204
7.8 S_{11} (blue solid line) and Abs (red dashed line) versus frequency for varying gap between the layers $g = 0, 0.25, 0.65, 1, 2.5, 5\mu m$, ($L_1 = 6\mu m$, $L_2 = 9\mu m$). Solid blue and red dashed lines represent $L_{upper} = L_2$, and $L_{lower} = L_1$. Dotted blue and red lines represent $L_{upper} = L_1$, and $L_{lower} = L_2$. 205
7.9 Currents induced for $1\mu m$ gap in the FSS of Figure 7.8, and $L_{upper} = L_1$, and $L_{lower} = L_2$. 206
7.10 S_{11} (blue solid line) and Abs (red dashed line) versus frequency for varying gap between the layers $g = 0, 0.25, 0.65, 1, 2.5, 5\mu m$, ($L_1 = 6\mu m$, $L_2 = 9\mu m$). Solid blue and red dashed lines represent $L_{upper} = L_2$, and $L_{lower} = L_1$. Dotted blue and red lines represent $L_{upper} = L_1$, and $L_{lower} = L_2$. 207
7.11 Tunability approach by varying the coupling between two layers (near-field interaction). 208
7.12 Tunability principle based on movable membranes. The actuation takes place in the arms of the membrane, that in turns pull down the membrane itself. a) Bird's view, b) cross-sectional view, and c) description by layer. 209
7.13 Various possible configurations using MEMS-based dual-layer FSS. . . . 210
7.14 Electro-static and electro-thermal actuation methods for actuating the movable membrane. 210

7.15 Independent FSS and MEMS design in the proposed method. As shown, the actuation only takes place in the arms, so that the membrane area is not covered and it is free for transmission and reflection of EM waves . . 211
7.16 Comparison between tunability configurations for periodic structures. . . 212
7.17 Electro-statically actuated MEMS movable metallic membrane. 213
7.18 Electro-thermally actuated MEMS movable dielectric membrane. 213
7.19 Transmission parameter of a tunable FSS based on complementary arrays, with and without losses, for variable separation D. The curves which exhibit lower S_{21} amplitude are those in which losses are included. 214
7.20 Transmission (left) and absorption (right) parameter of a tunable all-dielectric FSS based on a dielectric grating with two different materials separated a distance D from a dielectric layer. 215
7.21 Reflection phase of a tunable AMC consisting of an FSS separated a distance D from a ground plane 216

List of Tables

2.1 Common processes used in CVD. 30
2.2 Dry and wet etching comparison (adapted from [174]). 34

3.1 Propagation constant dependence in homogeneous medium and lossless FSS 46
3.2 Units of parameters in the EFIE (*dls = dimensionless). 71
3.3 Summary of the steps for the analysis of lossless FSS 75
3.4 Propagation dependence of lossy homogeneous medium and lossy FSS . 76
3.5 Effects of the introduction of losses in the FSS 90
3.6 Recipes for thermal and PECVD oxide employed for the fabrication of the SiO_2-Si-SiO_2 substrate 98
3.7 Recipes for RIE oxide etching using Plasmatherm and JLS 99
3.8 Recipes for RIE etching of Al 100
3.9 Etching and passivation steps in DRIE Bosch process 101
3.10 Perkin Elmer FTIR characteristics 103

4.1 Summary of the performance of capacitive FSS 122
4.2 Summary of the quality factors of FSS in the presence and absence of losses 128

Abbreviations

AMC - Artificial Magnetic Conductor
APCVD - Atmospheric Pressure CVD
BC - Boundary Conditions
CFSS - Complementary FSS
CCFSS - Closely Coupled FSS
DFSS - Dielectric FSS
DRIE - Deep Reactive Ion Etching
DTGS - Deuterated Triglycine Sulfate
DUT - Device Under Test
EBG - Electromagnetic Band-Gap
EFIE - Electric Field Integral Equation
EM - Electromagnetic
HIS - High Impedance Surface
HMDS - Hexamethyldisilazane
FIR - Far Infrared
FEM - Finite Element Method
FDTD - Finite Difference Time Domain
FDFD - Finite Difference Frequency Domain
FOM - Figure Of Merit
FSH - Floquet Space Harmonic
FSS - Frequency Selective Surface
FTIR - Fourier Transform Infra Red
GA - Genetic Algorithm
HFSS - High Frequency Structure Simulator
HIS - High Impedance Surface
ICP - Inductively Coupled Plasma
IE - Integral Equation
IR - Infrared
LC - Liquid Crystals
LPCVD - Low-pressure CVD
MCT - Mercury Cadmium Telluride
MEMS - Microelectromechanical Systems
MIR - Mid Infrared
MFIE - Magnetic Field Integral Equation
MoM - Method of Moments
NIM - Negative Index Material
NIR - Near Infrared
RCS - Radar Cross Section
RF - Radio Frequency
RIE - Reactive Ion Etching
SIWC - Substrate Integrated Waveguide Cavities
PBG - Photonic Band-Gap
PCB - Printing Circuit Board
PEC - Perfect Electric Conductor
PECVD - Plasma enhanced CVD
PI - Polyimide
PML - Perfectly Matched Layer
PVD - Physical vapor deposition
RIU - Refractive Index Univet
RLC - Resistance, Inductance, Capacitance
SMC - Scottish Microelectronics Centre
TE - Transverse Electric
THz-TDS - THz Time Domain

Spectroscopy

TM - Transverse Magnetic

TPV - Thermophotovoltaic

UV - Ultraviolet

WRM - Weighted Residual Method

1D, 2D, 3D - One, two, three dimensional

Mathematical Symbols

λ - Free-space wavelength

f - Frequency

ω - Angular frequency

ϵ - Dielectric permittivity

σ - Electric conductivity

μ - Magnetic permeability

n - Index of refraction

k_{ext} - Extinction coefficient

δ_{skin} - Skin depth

S_{11} - Reflection coefficient

S_{21} - Transmission coefficient

Abs - Absorption coefficient

R_s - Surface resistance

Z_0 - Intrinsic impedance

Z_a - Terminal impedance

x - Reactance slope parameter

t - Thickness of metal elements

t_{die} - Thickness of dielectric

R_{ohmic} - Ohmic resistance

κ - Ratio R_{ohmic}/R_a

β_{pq} - Propagation constant of Floquet mode (p, q)

$J(r)$ - Surface current

I_{av} - Averaged surface current

P_{rad} - Power radiated

P_{st} - Power stored

E - Electric field intensity

H - Magnetic field intensity

D - Electric flux density

B - Magnetic flux density

Ξ_{pq} - Modal field solution of Floquet mode (p, q)

Ψ_{pq} - Transverse component of the field of Floquet mode (p, q)

R^{-}_{mpq} - Reflection coefficient of Floquet mode (q, p) at the array

T^{1}_{mpq} - Transmission coefficient of Floquet mode (q, p) at the array

R^{1}_{mpq} - Reflection coefficient of Floquet mode (q, p) at the dielectric-air interface

T^{+}_{mpq} - Transmission coefficient of Floquet mode (q, p) at the dielectric-air interface

$\underline{\tilde{J}}_{pq}$ - Floquet transformation of surface current of Floquet mode (p, q)

η - Free-space modal admittance

η_{1pq} - TM modal admittance of Floquet mode (p, q)

η_{2pq} - TE modal admittance of Floquet mode (p, q)

$\underline{h}_n(\underline{r})_n$) - Basis functions

$\underline{h}_i(\underline{r}_i)$ - Test functions

c_n - Current coefficients of basis functions

Chapter 1
Introduction

1.1 Overview

Frequency selective surfaces (FSS) are resonant periodic arrays which exhibit selectivity in frequency, polarization and angle of incidence. Under plane-wave excitation, the incident wave induces electric currents flowing through the elements of the array, and leading to re-radiated energy from the array towards both sides of the array. These re-radiated fields add constructively or destructively with the incident wave giving rise to ideally total reflection or transmission depending on the type of the elements. In the absence of losses, metallic elements represent capacitive screens and give rise to total reflection, while apertures in a metallic sheet represent inductive screens and give rise to total transmission. In addition, the shape and dimensions of the elements determine the resonant frequency, that is the frequency of maximum coupling of the incident wave to the array. The filtering characteristics of FSS have been investigated in great detail in the past, mostly for applications in the microwave, but also at higher frequencies. FSS have been used widely in antenna systems for satellite communications and radomes for reducing the radar cross section. For instance, a very common application results from using an FSS to share a parabolic reflector with a single focal point by two different feeds working in different frequency bands (e.g. C- and X-band). The FSS is designed to reflect the X-band and transmit the C-band. The feeds (C- and X-bands) of the reflector are then placed at either side of the FSS resulting in a reflected X-band and transmitted C-band well focused towards the reflector (in transmitting mode). In the absence of an FSS, it would be physically impossible to have both feeds at the focal point. The application of FSS in waveguide filters, polarizers and absorber have been also exploited [1–5].

1.2 Motivation and Objectives

The motivation for the realization of this thesis lies in the need for deeper analysis of FSS operating at THz frequencies (mm-waves and infrared) and for the search of potential applications and higher-capabilities at these frequencies. From there, particular investigations have been carried out in various directions.

Performance studies with physical insight on the behavior of several type of FSS are readily available in the literature at microwave frequencies, where the metallic elements of the array may be considered perfect electric conductors (PEC). At these frequencies, thermal losses arising from the propagation of wave inside lossy dielectrics (dielectric losses) dominates the contribution of heat dissipation in the structure. At higher frequencies, however, ohmic losses arising from the finite conductivity of the metallic elements increase significantly and their contribution to the overall heat dissipation must be considered. Investigations on the absorption in FSS at THz frequencies have been carried out recently, in the noteworthy thesis by J. Pryor [6] and other published papers [7, 8]. However, thermal losses are mostly studied separately from other important parameters, such as the power stored in the near-field of the array and the Q-factors. The importance of studying the effects of thermal losses in relation to the power stored lies in the resonant nature of the FSS. Due to their resonant characteristics, for instance, FSS consisting of metallic elements have been shown to exhibit stronger absorption than a metallic sheet, even though FSS have less metalization per unit area [8]. Although this behavior have been observed in the past, it was simply addressed as a consequence of the resonant nature of the FSS, but no further investigations were carried out. Thus, a detailed assessment of FSS performance at THz frequencies in terms of thermal absorption in relation to the power stored, which defines the resonant characteristics of the array, is presented in the first part of this thesis.

The use of FSS at THz frequencies opens a window for new and interesting applications. Some of the applications recently suggested at these frequencies are in filter components and sensing systems [9–12]. In the past, the efforts were focused on the analysis and design of passive single-band FSS exhibiting one resonance, and therefore, a single band. The extension of FSS technology for multiband and tunable capabilities is of great interest. Multiband characteristics at THz frequencies

have been only achieved so far using fractal FSS by using a genetic algorithm for its optimization [13]. Although they exhibit good performance, they lack any direct relation between the performance and its geometry, and therefore, rely decisively on time-consuming computational trials. An interesting alternative followed in this thesis is the use of perturbed FSS, which have been demonstrated to exhibit dual-band performance at microwave frequencies. Perturbed FSS consist on arrays of dipoles, where the length of every second dipole is reduced [14]. By doing so, two resonances appear and a dual-band characteristic is relatively simple to achieve. In this thesis, experimental demonstration of multiband performance at THz has been pursued. In addition, during the study of the induced currents and near-fields in perturbed FSS, it was realized that strong currents and near-fields were obtained as a consequence of a small perturbation in the length of every second dipole. Further analysis was carried out to analyze perturbed FSS in sensing components, where materials can be characterize or differentiate from other materials observing the shift produced in the resonance when sensed in the vicinity of an array.

Finally, tunable mechanisms were investigated to reach electronic tunability of the FSS characteristics. Many different ways have been analyzed to achieve tunable configurations in the past, using varactor diodes, magnetic, semiconductor or liquid crystals substrates, or MEMS switches [15–19]. However, FSS working at THz frequencies have dimensions in the micro-scale, and therefore, opens the possibility to integrate FSS and MEMS technology in a relatively simple manner. Electromagnetically coupled FSS arrays and mechanically movable membranes have been integrated to achieve tunability in the THz regime.

Figure 1.1 summarizes the research undertaken in this thesis.

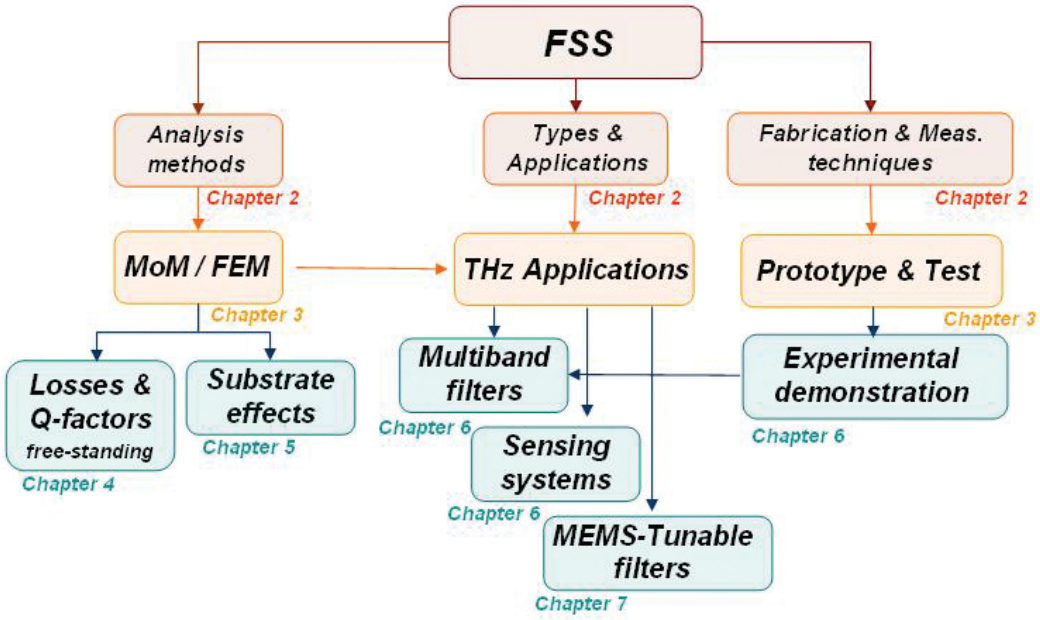

Figure 1.1: *Summary of the different areas investigated in this thesis and outline of the chapters.*

1.3 Chapters outline

The contents of each chapter are briefly introduced below:

- *Chapter 2 'FSS Background'* serves as an introduction of the FSS technology. Analysis methods, fabrication approaches and measurement techniques are revised, particularly for those techniques more suitable for FSS at THz frequencies.

- *Chapter 3 'Methodology for the analysis, fabrication and measurements of FSS at THz frequencies'* provides a detailed description of the actual methods and techniques used in the rest of the thesis for the analysis, fabrication and test of THz FSS. In-house mathematical model, based on the method of moments, and commercial softwares used for the simulation of lossless and lossy THz FSS are explained. In addition, a fabrication process and a measurement set-up is developed in this chapter.

- *Chapter 4 'Energy storage, dissipation and quality factors of FSS at THz frequencies'* concentrates upon the assessment of the power dissipation and storage in THz FSS. Both circuital models and full-wave analysis are employed to obtain the unloaded,

loaded and external quality factors in THz FSS. Far-field and near-field properties (e.g. S-parameters, induced currents, evanescent Floquet modes, power dissipated, power stored, terminal impedance) of THz FSS are evaluated and design-guidelines are given.

- *Chapter 5 'Substrate effects in FSS at THz frequencies'* extends the analysis to the influence of dielectric surroundings on the FSS performance. The circuital model for free-standing FSS is modified to account for substrate loading, and the effects on the resonance shape and frequency is addressed. Absorption due to dielectric and ohmic losses, both independently and simultaneously, are obtained and explained through the induced currents and the resonances due to the only presence of dielectrics.

- *Chapter 6 'Single-screen FSS for filters and sensing components at THz frequencies'* studies THz FSS in the realm of two different applications, namely, multiband filters and sensing components. First, traditional single-screen FSS are revised with particular interest in the induced currents and power dissipated at these frequencies. Subsequently, perturbed FSS are exploited for multiband and sensing applications. The presence of even and odd modes separated by interaction nulls have been shown attractive to reach multiple resonances and near-field enhancement. Experimental demonstration of perturbed FSS are also presented using the fabrication and measurement techniques developed in chapter 3.

- *Chapter 7 'Multilayered and tunable FSS at THz frequencies'* moves on to investigate FSS with more than one layer. First, dual-layer FSS with identical elements of similar or different dimensions are studied in terms of the reflection and absorption coefficients as well as induced currents. The efforts are then concentrated on closely-coupled dual-layer FSS, which are shown to exhibit attractive tunability capability by means of varying the distance in between. Several configurations are investigated and MEMS movable membranes are suggested to carry out the necessary mechanical displacement. Tunability is obtained in three different periodic structures, namely, FSS, dielectric gratings and artificial magnetic conductors.

Chapter 2
FSS Background

2.1 Introduction

This chapter aims to survey the existing literature on frequency selective surfaces (FSS) concerning its operation and applications, theoretical analysis approaches and design configurations, fabrication procedures and measurements techniques. The chapter is divided into four sections, each of which deals with one of the aforementioned areas. Section 2.1 provides a general introduction to FSS focusing on its principle of operation, circuital models, thermal losses, types, configurations and applications. Section 2.2 introduces various approaches for the analysis of electromagnetic (EM) structures, particularly for periodic arrays. The general idea of variational methods such as the method of moments (MoM) and the finite element method (FEM) is explained. In section 2.3, the micro-fabrication procedures and equipments for prototyping FSS operating at THz frequencies is revised. Finally, the measurement techniques for testing manufactured FSS are reviewed for microwave and THz frequencies. Indications relating the existing literature to the research undertaking in the rest of the thesis is appropriately given.

2.2 General description of FSS performance

2.2.1 Historical perspective of periodic structures

Periodic structures, either occurring naturally or man-made, have been examined throughout time. The first mathematical analysis of periodic structures was done on a one-dimensional periodic lattice by Newton in 1686 in order to derive a formula for the velocity of sound [20]. In this work, Newton assumed sound to propagate as an elastic wave along a lattice of point masses, separated by a constant distance and attracted to each other through an elastic force. In 1830, Cauchy tried to analyze the

dispersion of optical waves using Newton's model, assuming that light was a elastic wave of very high frequency. After Cauchy, Baden-Powell further discussed lattices with identical particles, Kelvin proposed a theory of dispersion for 2-particle lattice and Vicent built a mechanical model [21]. At the beginning of the twentieth century, periodic networks were utilized to build electric filters (low-pass by Pupin in 1900 and high-pass in 1906 by Campbell) [21]. In 1912 Born applied Kelvin's theory for the propagation of waves in crystals, and by 1928 Bloch generalized Floquet's results on partial differential equations with periodic coefficients (solutions of which are now known as Bloch waves) and laid the foundations of the theory of solids [20, 21].

In parallel with the developments of the current theory of solids, other periodic structures were investigated. Light diffraction first observations by F. Grimaldi date back to 1665 and the first man-made diffraction grating was studied by D. Rittenhouse in 1785 [22]. Another key step in the use of periodic grating was the invention of the spectroscope by J. Fraunhofer in 1813. A theoretical understanding of light was shaping up during the 17th, 18th and 19th centuries, from the particle theory of Gassendi (1660) and Newton (1675), through the wave theory of Hooke (1660), Huygens (1698) and Fresnel (1817) to the electromagnetic theory of Faraday (1845) and Maxwell (1873). Maxwell's equations led to investigations on other regions of the spectrum apart from optical light. From 1950 great attention was given at the microwave frequencies in the field of wave guiding, antennas and phased arrays [23], and the scattering of periodic arrays of conducting plates and aperture in conducting sheets was also investigated [2, 24, 25].

Frequency selective surfaces (FSS) have been suggested to appear first in the patent of Marconi and Franklin in 1919 describing a 'Reflector for Use in Wireless Telegraphy and Telephony', but they have been exploited thoroughly from the second half of the twentieth century [1]. More recently, other periodic structures have been investigated. Photonic band gaps (PBG) were introduced in 1987 [26–28], artificial magnetic conductors (AMC) in 1999 by Sievenpiper [29, 30], and negative refraction index (NIM) in 2000 by Smith [31, 32]. Periodic structures exhibiting special characteristics have been recently classified under the broad terminology of 'Electromagnetic Band-gaps (EBG)' [33]. Under this term we can identify any 1D, 2D or 3D metallo-dielectric or dielectric periodic structure which prevents propagation in

a particular band of frequencies ideally for all angles of incidence and polarizations.

2.2.2 FSS Definition

Frequency Selective Surfaces (FSS) are defined from a structural perspective as periodically arranged metallic patches or apertures within a metallic sheet with arbitrarily shape, generally supported by or embedded in a dielectric substrate. From an electromagnetic point of view, FSS are essentially resonant periodic arrays which exhibit selectivity in frequency, polarization and angle of incidence. In contrast to electrical filters, FSS are spatial filters because their performance depends not only on frequency, but also on angle and polarization of the incident wave. Generally, they are employed as plane-wave filters at radio frequency, microwave and THz frequencies.

2.2.3 FSS Characteristics

2.2.3.1 Principle of operation

The underlying physical mechanism which determines the behavior of the FSS is depicted in Figure 2.1. When a plane-wave impinges an FSS based on parallel metallic dipoles (with perfectly conducting electrons) we can identify two different scenarios. When the electric field is oriented along the length of the dipoles, this electric field exerts a force on the electrons causing them to oscillate according to the sinusoidal nature of the electric field orientation. A portion of the incident-wave energy is therefore converted into kinetic energy and used to sustain the electrons oscillating (i.e. induced current). Oscillating electrons (currents) give rise to radiated energy in the way that an electric dipole does. This re-radiated wave on the right side of the FSS interfere destructively with the incident wave avoiding any transmitted wave. The energy re-radiated towards the left represents the reflected wave. When the electric field is oriented perpendicular to the dipoles, however, the electrons cannot oscillate up and down, and do not re-radiate. In this case, the FSS is invisible to the incident wave and total transmission is produced [34]. The reflection and transmission characteristics depend on the absorption and re-radiation efficiency of the metallic elements and the frequency, angle and polarization of the incident wave. In general, FSS are resonant structures, so that the maximum absorption and re-radiation efficiency is given at the

resonant frequency, which depends on the shape of the elements and its spacings.

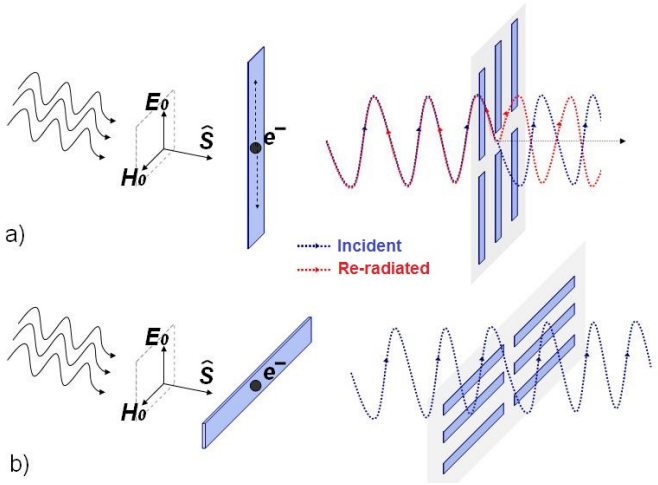

Figure 2.1: *Principle of Operation of FSS under electric field a) parallel and b) perpendicular to the elements length.*

In the absence of losses arising from the finite conductivity of the metallic elements and in a free-standing configuration (i.e. no dielectric surrounding the FSS), an infinitely thin FSS consisting of metallic patches exhibits complementary characteristic to that consisting of apertures of equal dimensions in a metallic sheet. This is known as the Babinet's principle [1, 35] and is depicted in Figure 2.2. Patch-based FSS exhibit total reflection when illuminated with an incident wave of electric field parallel to the dipoles, while aperture-based FSS show total transmission when illuminated with an incident wave of electric field parallel to the slots. Therefore, band-stop and band-pass filters are obtained by means of FSS based on patch and aperture elements, respectively.

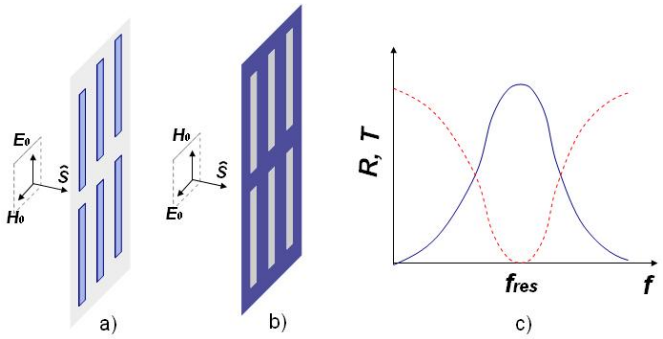

Figure 2.2: *Complementary FSS, a) patch-based FSS, b) aperture-based FSS and c) typical reflection and transmission characteristic as a function of frequency.*

Because of the periodic nature of the FSS, the behavior of the currents induced in the elements and the transmitted and reflected waves can be represented by an infinite set of spatial harmonics [3]. Although this will be developed fully in Chapter 3, it is worthy to introduce a few basic concepts here. The spectrum of FSS, shown in Figure 2.3, consists of a main always-propagating harmonic (i.e. incident, reflected and transmitted waves) and higher-order harmonics which may be evanescent or propagating towards different angles (in this case, they are called grating lobes). Because of satisfying the Floquet theorem of periodic functions, these harmonics are called Floquet harmonics or modes. The onset of propagating grating lobes depends on the periodicity of the FSS and the frequency and angle of the incident wave. This is an important issue because the onset of grating lobes may reduce energy in the main transmitted and reflected harmonics. Therefore, the spacing or periodicity of the FSS elements must be designed so that grating lobes do not appear at the frequency band of interest, with the exception of specific applications that take advantage of propagating grating lobes (e.g. frequency-scanned antennas).

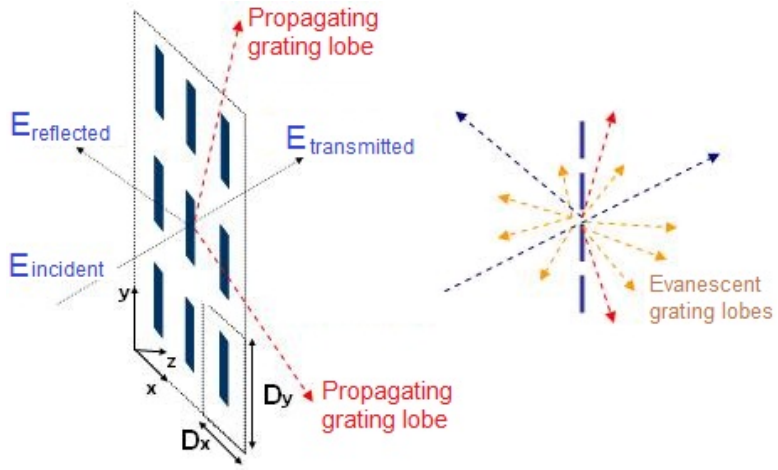

Figure 2.3: *Representation of the propagating and evanescent waves in periodic arrays under plane-wave incidence*

The operation of FSS, owing to its resonant nature, can be represented by an RLC circuit over a transmission line, where the losses (metallic and/or dielectric) are represented by a resistance R, while the reactive behavior appears as a result of the combination of capacitance C and inductance L components [1, 4]. For perfect electric conductors (PEC) such circuital equivalence turns into a lossless LC circuit. Simple lumped-element

equivalent circuits based on the empirical values given by Marcuvitz [36] for obtaining the equivalent capacitance and inductance of infinite strips have been used successfully to model lossless FSS consisting of single and double square-loops [37, 38], and Jerusalem crosses [39] in the microwave regime of the spectrum. Superdensed dipole FSS have also been modeled in a similar way with a more complicated combination of capacitances and inductances [40]. Circuital models based on Marcuvitz's empirical expressions, however, are single-mode formulations (only fundamental transmitted and reflected waves) and not accurate at high frequencies (e.g. propagating grating lobes). In addition, these methods are mostly suitable for a few particular simple free-standing FSS types, in the absence of losses, and for normal incidence, although some effort has been done to extend their validity to oblique incidence [41]. An accurate single-mode equivalent circuit based on the terminal impedance of the array calculated by full-wave method of moments was presented in [1]. A different approach was taken in [42], where the circuital model of a dipole FSS is extracted based on its performance instead of the physical dimensions of its geometry. The values of the boundary admittances at the FSS were extracted numerically. Multimode networks of the FSS under plane-wave excitation with arbitrary angle of incidence have been derived for a more accurate formulation of the FSS problem, including grating lobes [43–47].

2.2.3.2 Element types

The transmission and reflection characteristics of FSS are mainly dependent on the size and shape of the elements. The electrical dimension of the elements is the main factor which determines the resonant frequency, and the element shape and spacing strongly determine the bandwidth and shape of the resonance. Dielectric surroundings, thickness of the metallic elements or thermal losses further modify both resonant frequency and bandwidth. Traditional FSS geometries can be categorized into four classes, namely, (1) center-connected, (2) loop types, (3) solid types, and (4) combinations [1]. In Figure 2.4a, examples of the first three categories are shown. The resonant frequency is located roughly at a frequency in which the electrical length of center-connected elements is $\lambda/2$, the average circumference of the loop types is around λ, and the distance across the solid types is $\lambda/2$. The resonant frequency of the combination is somehow more complicated and depends on the particular shape of the elements.

So far, we have revised incidence normal to the array. In this case, only a fundamental resonance or even mode is present [1, 48]. However, oblique angles of the incident wave may give rise to odd modes at higher frequency (the odd modes vanish at normal incidence [48]). These odd modes represent current distributions in the FSS elements different from that of the fundamental mode and they usually appear at a harmonic frequency ($2f_{res}$, $3f_{res}$...). Odd modes vanish at normal incidence because their bandwidth becomes narrower and narrower as the incidence angle gets closer to zero [48]. In Figure 2.4b, the distribution of the currents induced in simple dipole elements are shown in conjunction to the far-field response associated. The first odd mode appears when the length of the dipole is λ, that is twice the even mode. The so-called interaction null appears between the fundamental and odd modes. This interaction null can be readily understood following Foster's reactance theorem [1], which states that between two poles there always exists a null. Other resonances due to different current distributions in the elements may also be excited at oblique angles for more complicated elements, such as the crooked or bent mode in the Jerusalem cross [1].

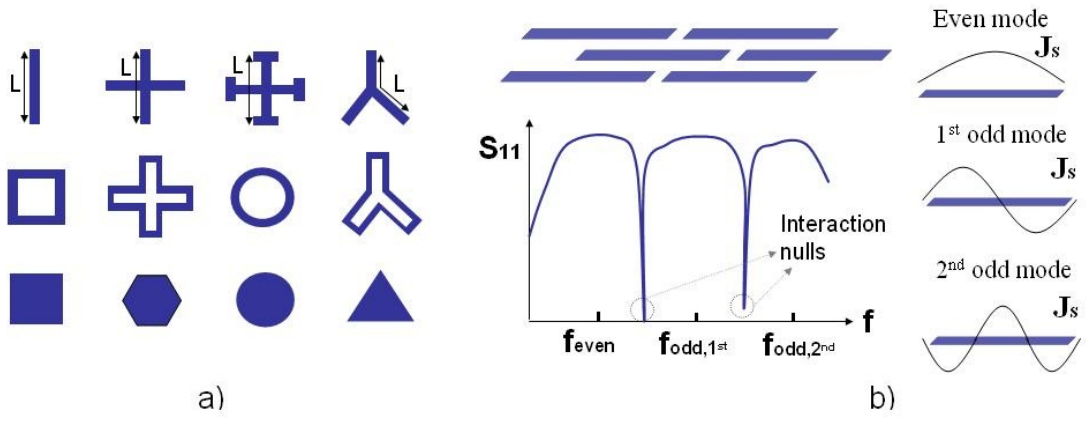

Figure 2.4: *a) Traditional elements of FSS, and b) harmonic (even and odd) modes in dipole elements.*

The bandwidth of the FSS depends strongly on the spacing between elements. The shorter spacings in either direction of the array (i.e. elements closely packed), the larger bandwidth obtained. The variation in bandwidth produced by bringing the elements closer or separating them further apart is accompanied by a change in the resonant

frequency. This frequency shift might be minimum (in some loop-type elements) or significant (in elements with capacitive end loadings, such as the Jerusalem cross) [1]. Thus, shape, dimensions and spacing of the elements must be designed altogether to reach the desired resonant frequency and bandwidth, and to avoid grating lobes.

In addition to the traditional elements explained before, new types of FSS have been investigated in the past. Fractal (e.g. Hilbert types or arbitrarily shaped generated by genetic algorithms), perturbed, convoluted and miniaturized elements represent good examples [14, 49–51]. Apart from metallo-dielectric FSS, which may exhibit unacceptable losses for certain THz applications, superconducting FSS has been shown as a candidate for high frequency applications in order to minimize the ohmic losses [52]. Other alternatives to metalic FSS are dielectric periodic structures such as thin film optical filters [53], wave-guide grating filters [54–58] and all-dielectric FSS [59–62].

2.2.3.3 Dielectric loading

The presence of dielectric layers around the FSS may not only be required for the physical integrity of certain FSS (e.g. patch FSS), but may also add further capability in tailoring the frequency response of FSS. Dielectric layers modify the resonant frequency and bandwidth of free-standing FSS [1, 3, 63, 64]. In addition, FSS embedded in a dielectric layer have been shown to exhibit stable reflection and transmission characteristics with the angle of the incident wave [1].

The major effect of dielectric layers is to alter the frequency of the fundamental resonance. The resonant frequency depends on both the dielectric permittivity and thickness. The FSS resonance is shifted towards lower frequencies following the expression [1, 63, 64]:

$$f^{dielectric} = \frac{f^{free-standing}}{\sqrt{\epsilon_{averaged}}} \tag{2.1}$$

where $\epsilon_{averaged}$ is the averaged permittivity at both sides of the FSS (ϵ_r^{left} and ϵ_r^{right}) and is equal to:

$$\epsilon_{averaged} = \frac{\epsilon_r^{left} + \epsilon_r^{right}}{2} \tag{2.2}$$

The value of the resonant frequency in (2.1) is achieved for thick enough substrates,

where the amplitude of evanescent Floquet modes have decayed to near zero at the air-dielectric interfaces. The resonant frequency is gradually pulled downwards as a function of the thickness of the dielectric, from the value of a free-standing FSS to the limiting value of (2.1), which corresponds to an infinite medium of permittivity $\epsilon_{average}$ [1, 63, 64]. The resonant frequency becomes independent of the thickness for thick substrates in patch-type FSS. For aperture-type FSS, however, the resonant frequency exhibit an oscillatory behavior around the limiting value of (2.1), due to the presence of substrate-generated pass-bands sweeping through the passband of the FSS consisting of slot elements [63]. The existence of the dielectric-only resonances does also make the bandwidth of the FSS wider or narrower as a function of the substrate thickness [63]. The effects of dielectric supporting layers, not only on resonant frequency and bandwidth, but also on induced currents and dissipated power, will be the main target for the research undertaken in Chapter 5.

2.2.3.4 Thermal losses

Another important issue, particularly at THz frequencies, is the thermal absorption arising as a consequence of heat dissipation due to the currents flowing through metals of finite conductivity and electromagnetic fields propagating inside lossy dielectric (conductivity higher than zero). In patch FSS, the introduction of losses leads to non-total reflection and non-zero transmission due to energy dissipated in the form of heat. Similarly, in aperture FSS, the introduction of losses leads to non-total transmission and non-zero reflection. Thus, any absorption reduces the efficiency of the FSS performance (except for absorber applications). Absorption is usually determined from the transmission and reflection coefficients as follows:

$$Abs = 1 - S_{11}^2 - S_{21}^2 \tag{2.3}$$

It has not been until recent years that the issue of absorption due to non-perfect metals have received increasing attention because in traditional applications at microwaves, dielectric losses are the main source of absorption [6, 8, 65, 66]. With the advent of potential applications at higher frequencies (such as thermophotovoltaic (TPV) [67] and optical-metamaterials applications [68]), the issue of ohmic losses has been increasingly important. In [6] a detailed investigation of the absorption

and current distributions in several type of FSS elements, such as wire-grids, dipoles, crossed-dipoles, square- and hexagon-loops, was provided. Wire-grid FSS exhibited the least absorption ($< 5\%$), dipole and loop-type FSS gave rise to losses between 9 and 14%, and crossed-dipoles were the most dissipative giving rise to near 20% absorption. Two interesting results were also derived in [6]. Firstly, lossy FSS were shown to exhibit more losses than a lossy infinite ground plane. This is certainly due to the resonant behavior of FSS. The strong currents induced in the elements are the main cause determining the losses, apart from the physical properties of the material. It was warned correctly that less quantity of metal do not imply less ohmic losses [8]. Secondly, there seemed to be a close relation between the bandwidth and the absorption. FSS types with wider bandwidth exhibit less absorption. This is also due to the distribution and amplitude of the currents induced in the different FSS elements. The understanding of ohmic losses is, thus, paramount at higher frequencies. In this thesis, the issue of losses (ohmic and/or dielectric) is studied for free-standing and dielectric-supported FSS. Chapter 4 is devoted enterily to the study of ohmic losses in free-standing FSS in relation to the induced currents, and the near-fields and stored power in the vicinity of the array. In Chapter 5, ohmic as well as dielectric losses are investigated for FSS supported by a dielectric layer.

2.2.4 Configurations: fixed and tunable FSS performance

Generally, single-screen FSS based on traditional elements give rise to single stop- or pass-bands. However, communication systems working at various frequencies may require multiband filters to reject or transmit more than one band simultaneously. Multiband FSS can be obtained by stacking various layers, but also by modifying traditional single-screen FSS. Since cascading different FSS can bring out unacceptable losses at THz frequencies, multiband single-screen FSS seem to be more appropriate in this region of the spectrum. Various single-screen configurations have been analyzed in the microwave to reach multiband response, including ring and square-loop elements [51, 69–71], simple element or spacing perturbation of the FSS [14], perturbed FSS based on substrate integrated waveguide cavities (SIWC) technology [72] and fractal FSS [50, 73]. Only fractal FSS has been also employed at THz to achieve multiband characteristics [13]. In Chapter 6, multiband dipole FSS elements with length perturbation are investigated, designed to operate at THz, and

experimentally demonstrated for the first time. Its application for sensing systems is also investigated.

In more complex devices, their characteristics are required to be adjustable or controlled externally. Many approaches have been followed in order to achieve tunable FSS, where the transmission characteristics are reconfigurable and controlled electrically: (1) PIN diodes have been used to change dynamically the electrical features of the unit cell [15, 74–76] and switch between two possible transmission characteristics for the diodes states ON and OFF. (2) Varactors have been also employed in tunable FSS by applying a bias voltage [16, 77, 78] in order to shift the transmission or reflection band. (3) FSS printed on ferrite substrates which are biased by a DC magnetic field have been presented in [79, 80] with the aim of controlling the properties of the substrate dynamically. (4) In [81, 82], plasma is suggested as a substitute of metal in the FSS, which is tuned by varying the plasma density of the elements. (5) Optically controlled FSS have been proposed in [17], where semiconductors are used as a substrate and its conductive and dielectric properties are changed by optical illumination, altering in turn the transmission characteristics of the FSS. (6) Liquid crystals (LC) have received great attention for its use in tunable devices such as displays, phase shifters [83–85], phase agile reflectarrays [86], wavelength selectors [87], capacitors [88], metamaterials [89, 90] and frequency selective surfaces [18, 90, 91]. (6) Finally, tunable FSS based on Microelectromechanical Systems (MEMS) have been proposed by tilting the elements (dipoles) using MEMS magnetic actuation technology [19], although with very poor transmission characteristics. Switchable FSS by MEMS bridges have been also presented as good candidates for switchable filters [92, 93]. Figure 2.5 depicts some of these tunable configurations. In Chapter 7 of this thesis, we theoretically propose a novel tunable mechanism to reach tunable FSS based on MEMS. The same mechanism is applied to other tunable periodic structures.

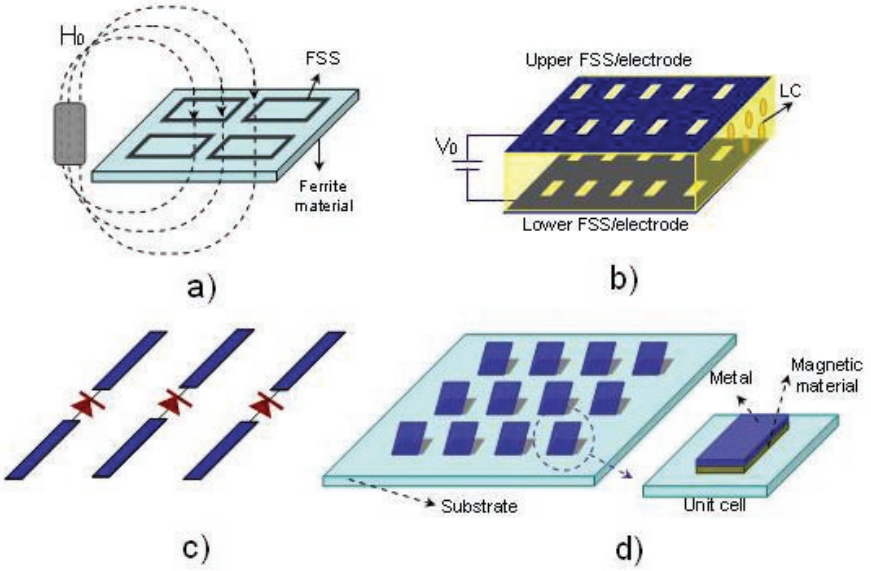

Figure 2.5: *a) FSS on ferrite substrate magnetically actuated, b) LC layer sandwiched by two FSS acting as electrodes (sealing of the liquid omitted for clarity), c) PIN, varactor or MEMS switches interconnecting collinear dipoles, and d) array of tilting dipoles based on magnetic MEMS.*

2.2.5 Applications

Traditionally, FSS have found applications mainly in the microwave regime, particularly in antenna systems and radomes. However, the use of FSS at infrared frequencies was also investigated in the past for filter components and, more recently, in sensing or TPV systems. In general, the design of the FSS strongly depends on the requirements of specific applications in terms of bandwidth, dissipative loss, polarization, angular stability, environmental effects, power handling, out-of-band performance, multimode use, or manufacturability [64]. Here we review traditional and more recent applications of FSS throughout the EM spectrum.

By incorporating FSS into microwave antenna systems, the use of a single reflector antenna across multiple bands is possible, and may be used instead or in conjunction with multifrequency feedhorn antennas to increase the channel capacity in communication systems [1, 3, 64]. Planar or curved FSS are employed to combine or filter frequency bands, as shown in Figure 2.6. In the NASA DSS 13 beam-waveguide antenna the FSS reflects the S-band (2-2.3GHz) and transmits

the X-band (7.1-8.5GHz), while the Cassegrain subreflector in the NASA Cassini spacecraft contains a three-layer FSS transmitting the S-band and reflecting the X, Ku (10.95-14.5GHz), and Ka (26.5-40GHz) bands.

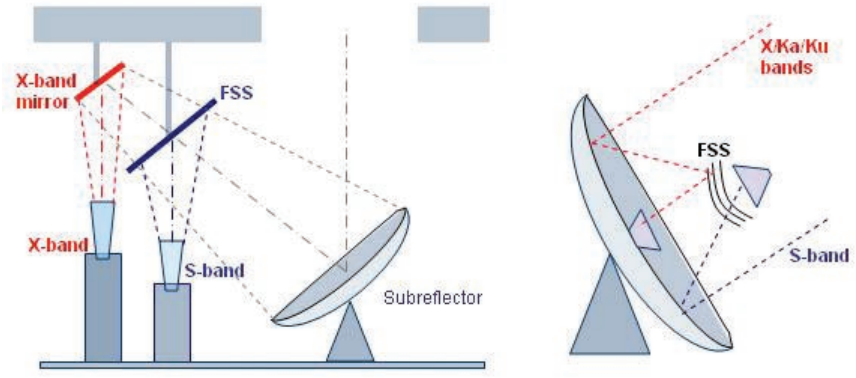

Figure 2.6: *a) NASA DSS 13 beam-waveguide antenna, and b) NASA Cassegrain subreflector (adapted from [64])*

Another common application of FSS is in radomes that protect antenna systems from the environment or reduce its radar cross section (RCS) [1, 3, 64, 94]. The FSS can be designed to be pass- or stop-band, as shown in Figure 2.7. A pass-band FSS may be employed, for instance, covering the radar antenna at the front of an airplane in order to reduced its RCS. Out-of-band frequencies will be scattered away in different directions (minimizing backscattering to the enemy radar), while the FSS appear transparent for in-band frequencies. A stop-band FSS can be used within high strength materials to protect an antenna system, and to avoid higher-order resonances that could affect useful microwave bands at higher frequencies.

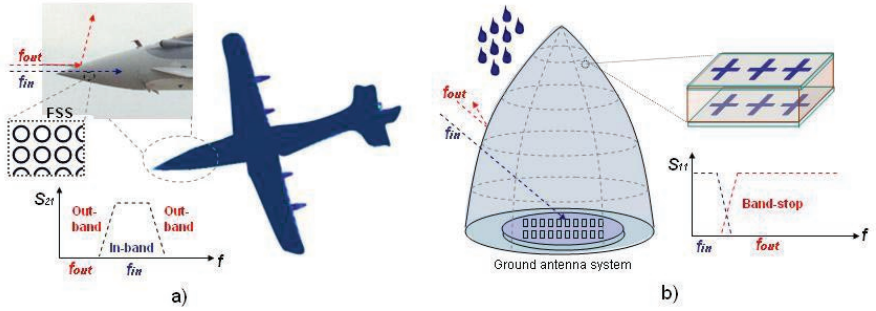

Figure 2.7: *FSS radomes integrated in a) airplanes, and b) ground antenna systems*

Another method to reduce the RCS signature of a vehicle uses FSS screens absorbing the radiation instead of reflecting it. A useful example of absorbers are the well-known arrays of pyramidal elements made of carbon-loaded foam in anechoic chambers for microwave measurements [64]. Absorbing screens with wide bandwidths can be designed similar to Salisbury or Jaunmann screens, but substituting the resistive sheets for FSS consisting of crossed elements made of lossy material [1], as shown in Figure 2.8a.

FSS have also been widely utilized as polarizers, as shown in Figure 2.8b. Linear polarizers which selects between the vertical or horizontal polarization are readily achieved using FSS consisting of infinitely long dipoles or slots [1]. If the infinitely long dipole is meandering instead of straight, we can achieve 'meanderline' polarizers, which transform linear into circular polarization [1,3,64]. A meanderline polarizer acts as a shunt inductance to the vertical component, and as a capacitance to the horizontal component. Under a 45 degrees linearly polarized wave, the vertical and horizontal components are delayed (+45 degrees) and advanced (-45 degrees), respectively, giving rise to a 90 degrees difference, and are recombined into a circularly polarized wave [1].

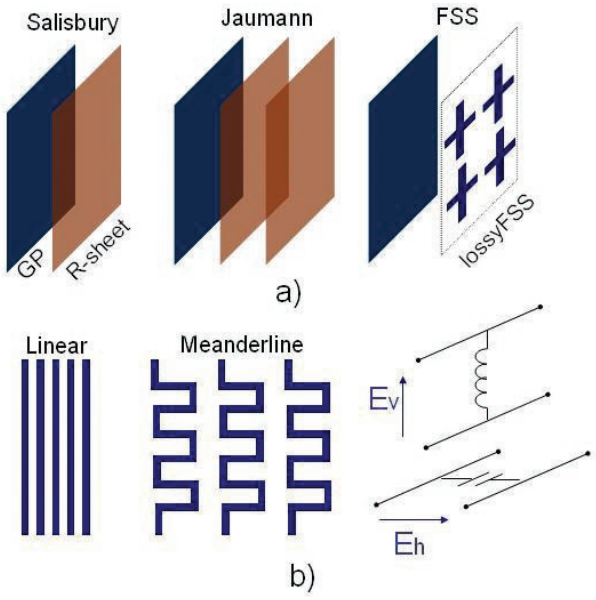

Figure 2.8: *a) Absorbers consisting of Salisbury, Jaunmann and FSS screens, and b) linear and meanderline polarizers*

Reflectarrays where EM radiation is reflected towards a single focal point consist of an FSS with variable element size or spacing along the periodicity directions and backed by a ground plane [95]. A frequency-scanned antenna can be designed using an FSS/reflectarray with appropriate dimensions, so that when a feedhorn shines on the surface at certain frequency, a different harmonic will be propagating at a different angle [64]. Other applications in the microwave include waveguide filters [96–100], frequency-dependent walls for waveguides and horn antennas [101–103], FSS in microstrip [104], planar [105, 106], and leaky-wave [101, 107–109] antennas, negative or low/zero index of refraction metamaterials [110], high impedance surfaces such as artificial magnetic conductors [29, 30], microwave lens [111], automotive electromagnetics (where FSS are laid in the highway to allow autonomous driving) [112], and frequency selective walls for EM isolation in buildings for wireless applications [113–116]. Some of these applications are depicted in Figure 2.9.

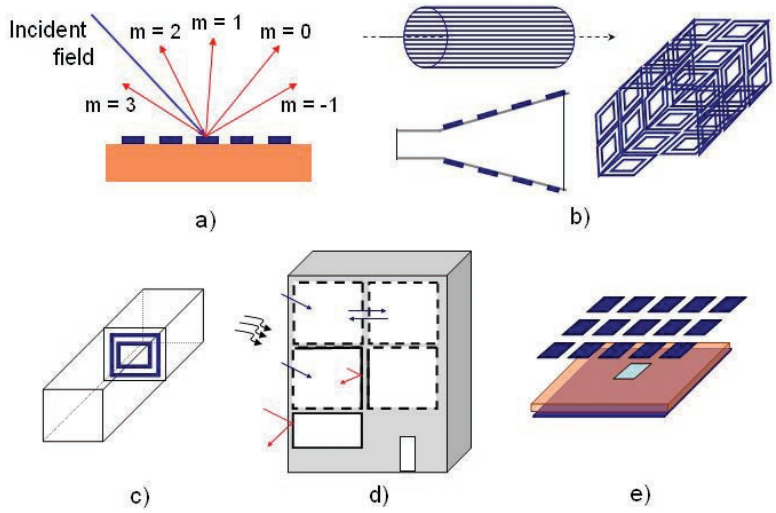

Figure 2.9: *FSS applications in a) frequency-scanned antennas, b) frequency-dependent wall in waveguides and horn antennas, c) waveguide filters, d) EM isolation in buildings, and e) FSS/planar antennas.*

Metallo-dielectric FSS have also been studied at higher frequencies, including (sub)mm-waves, infrared and optics. FSS are employed as (sub)mm-waves filters [117, 118], frequency multiplier [119], efficient beam-splitters and filters in (sub)mm-waves radiometers for meteorological and remote sensing applications [120–125], mm-waves waveguide beamsplitters [126] and on-chip

mm-waves antennas [127].

FSS have been investigated for several decades in the far-, mid- and near-infrared as low-, high-, band-pass, band-stop and dichroic filters [9, 10, 128–156]. Other applications studied in the past for FSS include infrared Fabry-Perot interference filters [157], laser-cavity output couplers [158, 159], where an FSS totally reflects at the wavelength of the energy used to pump the laser cavity and partially transmits at the lasing wavelength, and mirrors for solar power applications [160]. More recently, FSS have attracted great interest as filter components for increasing the energy-conversion efficiency in thermophotovoltaic (TPV) systems [67, 141, 161–164], infrared emitters with tailored spectral features [165–167], devices capable of manipulating light on the nanoscale by exciting surface plasmon-polaritons (SPP) [168], and pollutant [169] and sensing [11, 170, 171] systems. FSS for infrared filters, energy conversion and sensing systems are schemed in Figure 2.10.

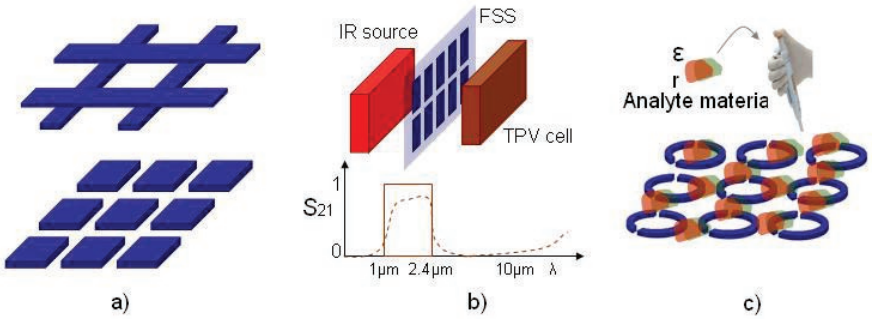

Figure 2.10: *a) One of the first type of FSS studied at infrared (e.g. in [123]), b) FSS in TPV conversion system, and c) d) FSS for sensing materials.*

2.3 Analysis techniques

From a general point of view, electromagnetic (EM) problems may be analyzed experimentally, analytically and/or numerically. Experimental analysis of EM problems entails prototyping and measuring the structure of interest, and it is an expensive, time-consuming and inflexible method. Due to the existence of a well-established and accurate EM theory based on Maxwell's equations, however, analytical and/or numerical methods are employed commonly for the analysis and design of FSS. Throughout this thesis, FSS are analyzed mainly using numerical methods and,

therefore, a brief and concise description of the most common numerical methods is mandatory and it is provided in this section 2.3. Fabrication and testing of FSS is also investigated in this thesis, so that the available processes for prototyping and the techniques for measuring THz FSS are also explained in the following sections 2.4 and 2.5.

Most of EM problems can be described by means of a differential or integral operator L and an excitation g [172]:

$$L\Phi = g \tag{2.4}$$

Analytical methods provide exact solutions (exact Φ) and, therefore, are preferably employed in EM problems of relative simplicity, such as waveguides of simple shape (rectangular, circular), strip transmission lines, scattering of EM waves by simple structures (e.g. dielectric sphere), simple antennas, etc. Several analytical methods have been used to solved EM problems, being the most common one the separation of variables. Series expansion, conformal mapping, integral solutions (e.g. Fourier or Laplace transforms) or perturbation methods represents other analytical techniques [172].

However, complex EM problems can not be solved analytically and numerical solutions are needed. In addition, the advent of modern computational capabilities has facilitated the numerical analysis of increasingly complex EM problems. Although numerical techniques do not provide exact solutions of the EM problem, they give approximate solutions of sufficient accuracy ($\Phi = \tilde{\Phi}$). The most common numerical techniques are the finite difference method (either time domain, FDTD, or frequency domain, FDFD), variational methods, which form the base of two other methods such as method of moments (MoM) and finite element method (FEM), transmission-line modeling, Monte Carlo method and method of lines [172]. These methods provide different ways of solving integral or differential equations such as that in (2.4). In this section we provide a brief and general description of the numerical methods available for the simulation of EM problems, and particularly for periodic structures. In the next Chapter 4, the Method of Moments is described thoroughly for the analysis of Frequency Selective Surfaces (FSS) because it represents the main numerical technique used in this thesis.

2.3.1 Method of Moments (MoM)

The method of moments (MoM) is a technique for solving inhomogeneous differential or integral equations, such as the one discussed for EM problems (2.4). For in-depth information of the origin, characteristics and mathematical development of the method we refer to detailed publication on the topic [172].

The method of moments is basically the weighted residual method (WRM) [172, 173] and aims to reduce the integral equation (IE) into a linear system of equations. The solution of (2.4) can be approximated using expansion functions, u_n, as follows:

$$\Phi \approx \hat{\Phi} = \sum_{n=1}^{N} a_n u_n \tag{2.5}$$

where a_n are the expansion coefficients. Since $\hat{\Phi}$ is an approximation:

$$L\hat{\Phi} \approx g \tag{2.6}$$

there is a residual error R given by:

$$R = L\hat{\Phi} - g = L\sum_{n=1}^{N} a_n u_n - g \neq 0 \tag{2.7}$$

In the MWR or MoM methods, we seek to obtain a system of linear equations that we can solve readily in matrix form and, once solved we obtain the unknown coefficients a_n, which provide an acceptable accuracy for the function Φ. For doing so, we need to calculate the coefficients a_n which produce a residual error equal to zero over the domain of interest. We may integrate the residual error over the domain and force it to be zero:

$$\int_v R dv = 0 \tag{2.8}$$

Evaluating with Eq. (2.7)

$$\int_v \left(\sum_{n=1}^{N} a_n L\hat{\Phi} - g \right) \, dv = 0 \tag{2.9}$$

By doing so, however, we end up with one equation and N unknown variables (the N expansion coefficients a_n). To obtain N equations, we force the residual error to zero

in some average sense over the domain, using weighting functions w_m, hence:

$$\int_v w_m R \, dv = 0, \quad m = 1, 2, ..., N \quad or \ \langle w_m, R \rangle = 0 \tag{2.10}$$

where the number of the weighting functions w_m is equal to the number of unknown constants a_n in $\hat{\Phi}$. Using (2.7) we obtain:

$$\int_v w_m R \, dv = \int_v w_m \left(L\hat{\Phi} - g \right) \, dv = \int_v w_m L\hat{\Phi} \, dv - \int_v w_m g \, dv =$$

$$= \int_v w_m L \sum_{n=1}^{N} a_n u_n \, dv - \int_v w_m g \, dv = \sum_{n=1}^{N} a_n \int_v w_m L u_n \, dv - \int_v w_m g \, dv = 0 \tag{2.11}$$

and therefore:

$$\sum_{n=1}^{N} a_n \langle w_m, L u_n \rangle = \langle w_m, g \rangle \tag{2.12}$$

By doing so, we obtain a system of N linear equations with N unknown constants. In matrix form:

$$[A][X] = B \tag{2.13}$$

where:

- $A_{mn} = \langle w_m, L u_n \rangle$ is a matrix of dimension $N \times N$ with the known weighting functions w_m, source g and integral operator L.

- $B_m = \langle w_m, g \rangle$ is a vector of dimension N with the known weighting functions w_m and source g.

- $X_n = a_n$ is a vector of dimension N with the unknown expansion coefficients a_n.

Different weighting functions can be chosen [172]. A common weighting function used in the analysis of periodic structures corresponds to the derivative of the approximated function respect to the expansion coefficients, which is equal to the expansion functions. This method is known as Garlekin Method, where the weighting and the expansion functions are the same.

$$w_i = \frac{\partial \hat{\Phi}}{\partial a_i} = u_n \tag{2.14}$$

As we will discuss thoroughly in the next Chapter 3, MoM is employed to solve numerically the IE obtained from the analysis of the FSS structure. The unknown

coefficients a_n will be related to the unknown currents induced in the FSS elements, and the source g will be, in our case, a $1V/m$ incident plane-wave.

2.3.2 Finite Element Method (FEM)

Similar to the MoM, the Finite Element Method (FEM) is a variational method which intends to solve (2.4) by minimizing the functional (2.7). FEM reduces the EM problem into a finite number of subregions, which are easier to treat. This approach makes FEM extremely versatile and suitable for analyzing complex EM problems and develop general-purpose computer programs. As described in [172], FEM is based on four basic steps. The first step consists of discretizing the solution region into subregions or elements. For doing this, several types of elements may be utilized depending on the characteristics and dimensions of the EM problem (Figure 2.11a-b). The most common elements are based on triangular or quadrilateral shape. Secondly, governing equations for a typical element must be derived. The potential Φ and source g at any point within the element (e.g. triangular in Figure 2.11c) can be expressed in terms of shape functions α_i:

$$\Phi_e(x,y) = \sum_{i=1}^{3} \alpha_i \Phi_{ei}; \quad g_e(x,y) = \sum_{i=1}^{3} \alpha_i g_{ei} \tag{2.15}$$

where Φ_{ei} and g_{ei} represent the potential and source values at the vertices, respectively.

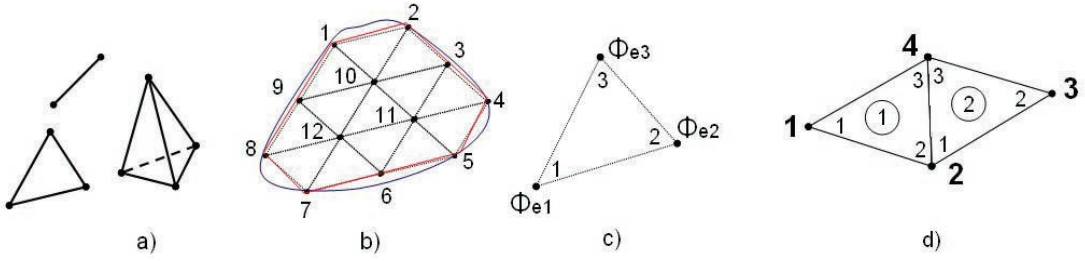

Figure 2.11: *Description of sub-regions in FEM. a) Triangular elements for 1, 2 and 3 dimensions, b) example of dividing EM into subregions, c) potential in the nodes of the element, and d) adjacent elements*

If we are solving the inhomogeneous wave equation, $\nabla^2\Phi + k^2\Phi = g$, the functional can be demonstrated to be [172]:

$$I(\Phi_e) = \frac{1}{2}[\Phi_e]^t[C^{(e)}][\Phi_e] - \frac{k^2}{2}[\Phi_e]^t[T^{(e)}][\Phi_e] + [\Phi_e]^t[T^{(e)}][G_e] \tag{2.16}$$

where $[\Phi_e] = [\Phi_{e1}, \Phi_{e2}, \Phi_{e3}]$, $[G_e] = [g_{e1}, g_{e2}, g_{e3}]$, while $[C^{(e)}] = \int \nabla\alpha_i \cdot \nabla\alpha_j dS$ and $[T^{(e)}] = \int \alpha_i \cdot \alpha_j dS$ represent the element coefficient matrices.

Thirdly, after the potential of each element are obtained, all the elements within the solution region must be assembled. The process of assembling aims to obtain global coefficient matrices $[C]$ and $[T]$. This is done by adding all the element coefficients C_{ij} or T_{ij} in each global node of the total solution. This is well explained in Figure 2.11d and the following relations for two adjacent elements:

$$\begin{gathered} C_{11} = C_{11}^{(1)}; C_{22} = C_{22}^{(1)} + C_{11}^{(2)} \\ C_{14} = C_{41} = C_{13}^{(1)}; C_{12} = C_{21} = C_{12}^{(1)}; C_{23}^{(1)} + C_{13}^{(2)} \qquad (coupling\ \ between\ \ nodes) \\ C_{13} = C_{31} = 0 \qquad\qquad (no\ \ coupling,\ \ no\ \ direct\ \ link) \end{gathered}$$

Fourthly and last, the equation derived for a single element is generalized for the solution region $I(\Phi) = \sum_{e=1}^{N} I(\Phi_e)$ and solved.

An issue in applying the FEM in scattering or radiating EM problems is that these are usually unbounded or open problems and, therefore, the space domain is infinite. Hence, we need to truncate the solution domain to a finite domain by applying certain artificial boundary conditions which will limit the solution domain without affecting the accuracy of the solution. Absorbing boundary conditions (ABC) which exhibit nearly-free reflection at the truncation of the space domain must be employed. The most commonly used ABC are the radiation boundary condition and the perfectly matched layers (PML). A further space domain truncation must be employed when analyzing infinite or finite periodic structures. Periodic boundary conditions (PBC) which model the repetition of a unit cell must be employed. All PBC are based on Floquet theory (which will be further explained in Chapter 3), which relates the field in consecutive unit cells by a simple phase delay, and hence transforms the problem of the analysis of infinite periodic structures into the analysis of its unit cell. FEM is used throughout the thesis to simulate the behavior of lossy FSS.

2.3.3 Commercial softwares

Several commercial EM solvers are available using one of the method described before or a hybrid method. Among those more commonly employed and used in this thesis for the analysis of periodic structures are Ansoft HFSS (High Frequency Structure Simulator) based on the FEM and Ansoft Designer based on the MoM. In-house code of MoM is employed in this thesis for the analysis of lossless FSS, particularly for the study of the currents induced in the FSS elements, the near-fields and the power stored in the vicinity of the array. HFSS and Ansoft Designer, on the other hand, are employed for the study of lossy FSS and the dissipation of power. Detailed descriptions of both in-house code and commercial softwares are given in Chapter 3.

2.4 Microfabrication techniques

This section concentrates upon the techniques for the fabrication of periodic arrays with dimensions ranging from few millimeters to few nanometers, that is operating at frequencies ranging from (sub)mm-waves to visible light. The techniques for the manufacturing of 2D arrays range from simple shaping methods for arrays operating at RF or microwave frequencies to sophisticated and expensive micro/nanofabrication techniques for arrays operating at higher mm-waves or THz frequencies [32]. For the fabrication of 3D arrays, three different approaches are traditionally employed, namely machining from solid, staking layer-by-layer, or growth [32].

For the fabrication of FSS with micron-scale dimensions, standard microfabrication techniques employed in the integrated circuit (IC) industry must be employed. These techniques can be categorized generally regarding its functionality under four groups, namely (1) deposition, (2) patterning, (3) pattern-transfer or etching, and (4) surface treatment. Within each category we can identify several processes using different technologies. In this section, we provide a brief description of the most common microfabrication techniques, focusing on those which are more useful for the fabrication of THz periodic structures (three first categories) and are employed in this thesis for prototyping micron-scale FSS.

2.4.1 Deposition

Most devices manufactured with micro/nanofabrication techniques start from a wafer of silicon (Si), glass or another material of various size (e.g. 3", 4", or 8"). Deposition methods refer to the techniques for adding materials onto the wafer. Depending on the nature of the material (metal, semiconductor, polymer) there are different deposition approaches. Here, we discuss the deposition of polymers by spin-coating, silicon-related materials, such as SiO_2, Si_3N_4 or $Poly-Si$, by chemical vapor deposition (CVD) either low-pressure (LPCVD) or plasma-enhanced (PECVD), and metals by physical vapor deposition (PVD), either evaporation or sputtering.

I. Spin-coating

Spin-coating refers to the deposition technique in which the material in viscous liquid state is deposited onto the wafer, which is spun rapidly so that the material spreads homogeneously throughout the wafer. The centrifugal force of the spinning process causes the liquid to flow from the center of the wafer, where the material was dispensed, to the edges. The thickness of the deposited layer depends on the spinning rate ω, the solution concentration C and viscosity η, as shown in the following empirical expression for photoresists [174]:

$$T = K\frac{C^{\beta}\eta^{\gamma}}{\omega^{\alpha}} \tag{2.18}$$

where K is a calibration constant, and the exponential factors α, β and γ must be obtained experimentally. Figure 2.12, shows two manual spinners in the Scottish Microelectronics Centre (SMC), suitable for spin-coating on wafers and single smaller chips.

II. Chemical Vapor Deposition (CVD)

In the CVD process, the wafer is exposed in a reaction chamber to a gas flow consisting of inert carrier gas and different precursors (reactants) which react with the surface giving rise to a deposited material on the wafer and volatile by-products which are removed from the reaction chamber. In order for reactions to take place, energy must be provided somehow (e.g. thermal, photons, electrons) [174]. Thermal energy is the most common type of energy used in CVD processes. Low-pressure chemical vapor deposition (LPCVD) works at below 10Pa and very high temperatures, increasing

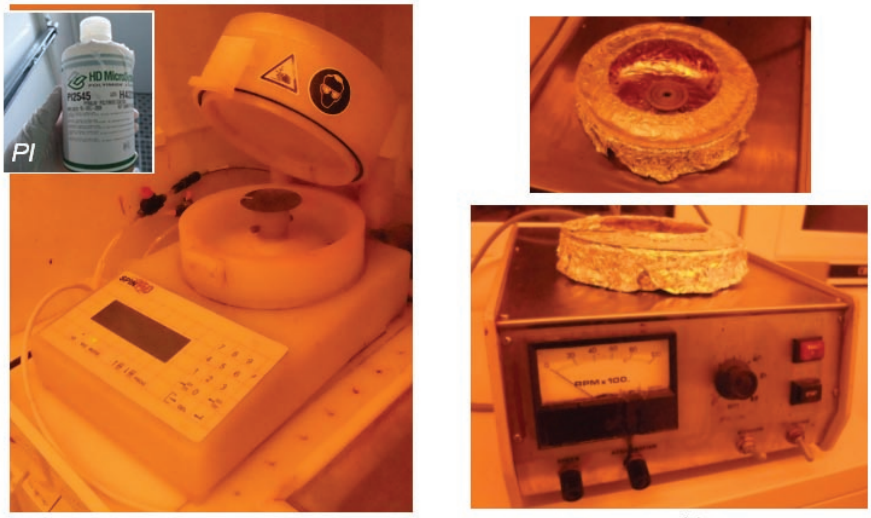

Figure 2.12: *Manual spinners available at the Scottish Microelectronics Centre and used for spin-coating in wafers (a) and single chips (b)*

the uniformity (including on steps) and reducing particle contamination compared to atmospheric-pressure chemical vapor deposition (APCVD) [174]. LPCVD equipment usually consists of furnaces with hot wall reactors, such as that shown in Figure 2.13a.

The deposition temperatures in either APCVD or LPCVD may be prohibiting when the wafers already has other deposited materials which may be damaged or melted. In order to decrease the temperature in the reaction chamber, i.e. lower deposition temperatures, plasma-enhanced chemical vapor deposition (PECVD) is employed. Chemically reactive plasma is a partially-ionized gas consisting of positive and negative charges together with unionized neutral molecules. This plasma is usually obtained when a gas is under the effect of a DC or radio-frequency (RF) potential and low pressure conditions. The plasma contains active species which can readily react with the substrate material. Thus, the plasma provides the radicals that result in the deposited material, and ion bombardment transfers energy into the reactant gases which lead to lower temperature deposition [174]. PECVD processes are very similar to reactive ion etching (RIE) which is explained later in the etching section.

The most common processes employed in CVD equipment are listed in Table 2.1, where the material to be deposited, main reactants and temperature are shown:

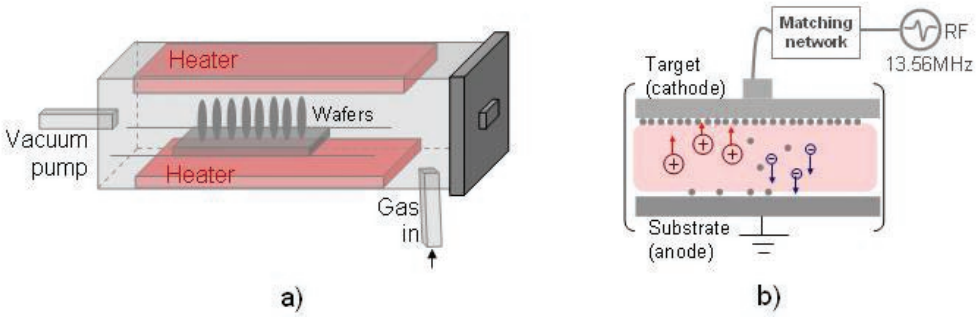

Figure 2.13: *Schemes of a) LPCVD furnace, b) sputtering PVD.*

III. Physical Vapor Deposition (PVD)

PVD is not carried out through the reaction of the substrate with a gas containing the necessary reactants as done in CVD processes. In PVD, the deposition of material onto the substrate is a "line-of-sight impingement type" [174]. Two of the most widely used PVD techniques are thermal evaporation and sputtering. Evaporation deposits a melted material (by heating) onto the substrate in a vacuum chamber. The source of heating to evaporate the material (e.g. metal) may be resistive (tungsten filament), electron-beam, RF or laser induced. During sputtering, however, the material to be deposited (called target) is biased at high negative potential and bombarded with positive argon ions (inert gas) which appears within a plasma [174]. The target material is then sputtered away by momentum transfer and deposited onto the substrate (in the anode), as shown in Figure 2.13b. The advantages of sputtering over evaporation are the wider choice of materials (including alloy compositions control), the greater adhesion, uniformity of the deposited thin film and control of its thickness. Sputtering, however, represent also a more expensive equipment, with lower deposition rates and more sensitive to introduction of impurities [174].

Material	Reaction	T^a
LPCVD $Poly\text{-}Si$	$SiH_4 \rightarrow Si + 2H_2$	$> 600°$
LPCVD SiO_2	$SiH_4 + O_2 \rightarrow SiO_2 + 2H_2$	$> 900°$
LPCVD Si_3N_4	$3SiH_2Cl_2 + 4NH_3 \rightarrow Si_3N_4 + 6HCl + 6H_2$	$> 700°$
PECVD SiO_2	$3SiH_4 + 6N_2O \rightarrow 3SiO_2 + 4NH_3 + 4N_2$	$< 300°$
PECVD Si_3N_4	$3SiH_4 + 4NH_3 \rightarrow Si_3N_4 + 24H_2$	$< 300°$

Table 2.1: *Common processes used in CVD.*

2.4.2 Patterning

The concept of patterning describes the process of transferring copies from a master pattern onto the surface of a solid material such as silicon wafers. The master pattern can, therefore, be reused innumerable times in the fabrication of the designed micro-system. There are several techniques for patterning using various technologies. However, the most commonly used patterning process is the *photolithography*. Photolithography or optical lithography uses light of a certain wavelength to impinge in a light-sensitive resin (photoresist) on the substrate after passing through the master pattern or mask. By doing this, the photoresist exposed to the light undergoes a chemical reaction, altering the solubility of the photoresist in a solvent, known as developer. The photolithography process, including resist spin-coating, exposure and developing is depicted in Figure 2.14.

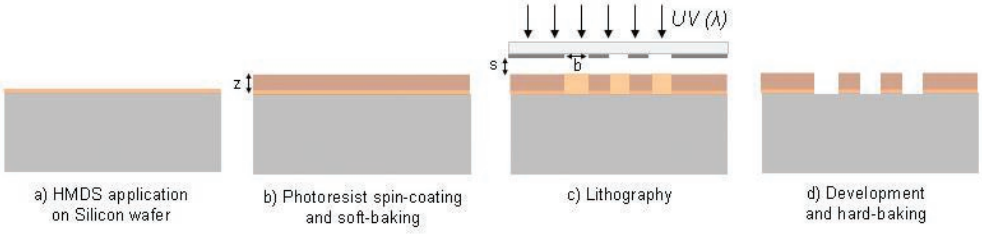

Figure 2.14: *Main steps in the patterning process using photolithography*

As we can see in the figure above, the first step (a) of the photolithography process (after cleaning and annealing the wafer surface) consists of applying a liquid or *gaseous adhesion promoter* to enhance the adhesion of the photoresist to the wafer surface. A common adhesion promoter to improve adhesion of photoresists onto oxides is hexamethyldisilazane (HMDS). This includes silicon as well, since a very thin native oxide layer (less than 5nm) is always present on silicon surfaces. A strong bond is created between the oxide and the HMDS through its reactive $Si - NH - Si$ functional groups. The methyls are responsible for the adhesion of the photoresist to the HMDS [174, 175].

The photoresist, a viscous and liquid solution, is then deposited onto the wafer by *spin coating* (b). The main components in common photoresists are a polymer (resin), a sensitizer, and a solvent. The polymer changes its structure and, therefore its solubility, under the exposure of radiation of a certain wavelength (for instance PMMA,

that is poly(methylmethacrylate), is sensitive at $220nm$ wavelength) and intensity (in terms of mJ/cm^2). Exposed positive photoresist increases its solubility due to the rupture of the polymer chains. On the other hand, negative photoresist strengthens its polymer chains when exposed by radiation. The sensitizer controls the reactions (weakening or strengthening) of the polymer under radiation exposure, and hence, can increase the sensitivity of the photoresist to certain wavelength, decreasing the required radiation intensity or exposure time. The sensitizer may be responsible for rendering the exposed photoresist transparent to the incoming light in order for light to reach through the thickness of the photoresist (specially for thick photoresist). The solvent simply allows the photoresist to be spin coated in thin-film form onto silicon wafers. After spin-coating, the photoresist on the wafer must be soft or pre-baked, normally between 75 and $100°C$, in order to remove rests of the solvent [174, 175].

The photoresist layer is then ready for the exposure step (c). The main parameters to be adjusted during the exposure steps are the wavelength and intensity of light. These are determined by the source of light used. The simplest optical lithography source of light consists of a ultraviolet (UV) lamp which illuminates directly the resist-coated wafer through the mask. The wavelength of the light source ranges from near-UV (g-line at 435nm and i-line at 365nm in mercury lamps) to extreme ultraviolet EUV (10 to 14nm) [174]. In general, shorter wavelengths exhibit lower brightness as compared to longer wavelengths. Thus, higher sensitivity photoresist is needed when using shorter wavelengths (e.g. EUV). The importance of using short wavelengths relies on the maximum resolution achieved, that is the minimum feature size that can be patterned. The resolution of a simple lithography system, as that shown in (2.23), (assuming perfect wafer flatness, wafer-mask alignment,...) depends on the wavelength of the light source λ, the gap between the mask and the photoresist s, and the photoresist thickness z [174]:

$$Resolution = \frac{3}{2}\sqrt{\lambda\left(s + \frac{z}{2}\right)} \tag{2.19}$$

Normally, the wavelength of the light source is fixed for a particular lithography equipment. Hence, in order to obtain maximum resolution, the thickness of the spin-coated photoresist and the gap between mask and photoresist must be minimized. Contact lithography represents the particular case in which the gap s is reduced to 0, and therefore the mask is in contact with the photoresist layer. Although this

may increase the resolution, it can give rise to problems related to mask damage and contamination. When the mask and photoresist layer are separate a distance s (proximity lithography), the contamination problem is solved at the expense of reducing the resolution due to diffraction. Alternatives to traditional optical lithography are being explored and used for the patterning of micro/nano-scale arrays (e.g. THz FSS), such as bilayer nanoimprint lithography [176], electron beam lithography (EBL) [10, 176, 177], masked ion beam lithography (MIBL) [141], optical lithography and phase-shift masks [149], microlens projection photolithography [150] and stencil mask method [178]. The different parts in photolithography equipments available at the SMC are shown in Figure 2.15.

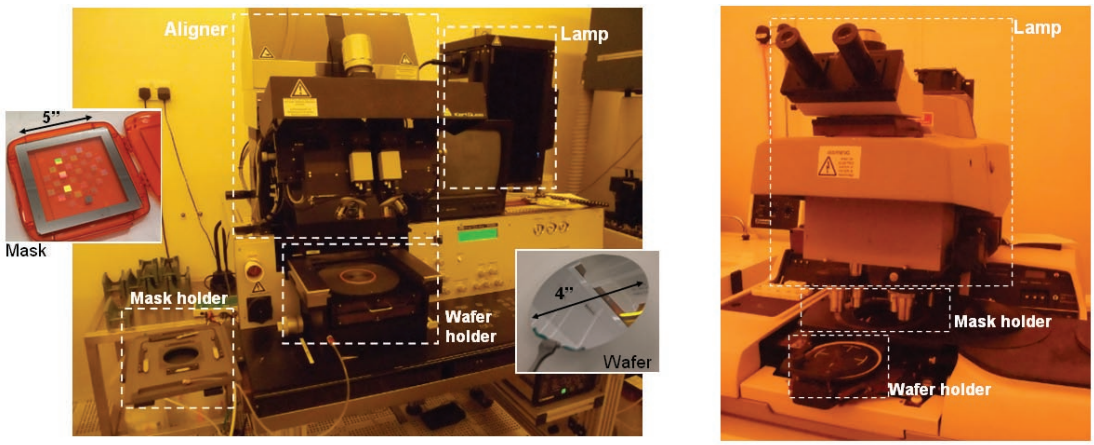

Figure 2.15: *Photolithography equipments and its parts available at the SMC, a) Karl Suss MA8, (3, 4, 6 and 8") and b) Cobilt 2020 soft contact (3"). The inset figures in a) show a 5" chrome mask and a 4" silicon wafer.*

Post-exposure treatment might be required after lithography (e.g. flood exposure when using negative photoresist) and before the development step (d). Developing the patterned photoresist layer can be carried out by means of dry or wet processes. In wet development, a selective solvent is applied (either by immersion or spray) and it removes the exposed photoresist which, as commented before, had suffered changes in the polymer chains. Dry development, on the other hand, uses oxygen-reactive ion etching (O_2-RIE) to etch the photoresist, taking advantaged of the fact that exposed and non-exposed photoresist exhibit different etch rate. After development, hard-baking of

the wafer is required to remove residual solvents and to strengthen the adhesion of the remaining non-exposed photoresist onto the substrate for future processing (e.g. etching) [174, 175].

2.4.3 Etching

Etching can be defined generally as the process by which the pattern of a certain masking material (e.g. the photoresist after lithography and development) is transferred onto another layer of material (e.g. silicon, oxides, metals,...). This pattern transfer is realized by means of physical and/or chemical removal of the material to be etched. Dry etching uses etchants in gas or vapor state, whereas wet etching employes liquid chemicals to carry out the etching process. Dry and wet etching processes are complementary and one of them will be preferable depending on the material to be etched, critical dimensions and final application. A good comparison between dry and wet etching can be found in [174], and is described partially in Table 2.2. Dry etching is usually significantly more expensive and complex than wet etching, but it is preferable for better critical dimension control and submicron etching.

Parameter	Dry etching	Wet etching
Directionality	High	Only high for single crystals
Masking film adherence	Not critical	Very critical
Materials that can be etched	Only few	All
Critical dimensions control	Very good ($< 0.1\mu$)	Poor
Equipment cost	Expensive	Inexpensive
Chemical cost	Inexpensive	Expensive
Submicron features	Applicable	Not applicable
Etch rate (control)	Slow (good)	High (difficult)
Complexity (operation parameters)	Very complex	Simpler

Table 2.2: *Dry and wet etching comparison (adapted from [174]).*

I. Dry etching

Dry etching methods remove the material by physical ion-bombardment, chemical reaction with reactive species or combining both mechanisms. One of the most common etching method employed is the Reactive Ion Etching (RIE), which uses a chemically reactive plasma to remove the substrate material. As commented before

in the section dedicated to the deposition techniques, chemically reactive plasma is a partially-ionized gas consisting of positive and negative charges together with unionized neutral molecules. This plasma is obtained usually when a gas is under the effect of a DC or radio-frequency (RF) potential and low pressure conditions. The plasma contains active species which can readily react with the substrate material, removing it. The volatile products of the reaction between the substrate and the etchant species are removed by a vacuum pump. A glow discharge produced in the chamber is due to excited species in the plasma emitting ultraviolet and visible light [174]. Figure 2.16a depicts a diagram of a typical RIE equipment such as those in the SMC shown in Figure 2.17.

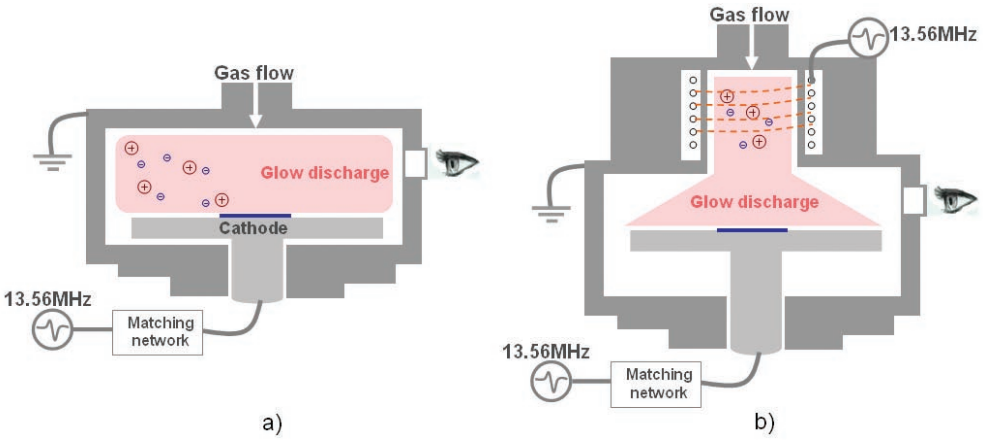

Figure 2.16: *Diagrams of the etching techniques based on a) RIE and b) ICP.*

In order to obtain higher plasma densities, so that higher etch rate can be achieved, Inductively Coupled Plasma (ICP) RIE can be employed [174]. The difference with the previous RIE scheme lies in the use of an additional RF powered magnetic field to generate the plasma. In the ICP configuration, the DC bias in the cathode, where the wafer is placed, is responsible solely for the attraction of positive ions (e.g. Ar^{+}) to impact the wafer and allow etching in the presence of reactant radicals (e.g. Cl^{*}). The density of the plasma is independently set by a secondary RF magnetic field. By doing so, higher density plasma is achievable while maintaining a low DC bias and, therefore avoiding damaging the wafer. In the RIE configuration, the increase in plasma density was linked to the DC bias of the cathode, so that the basic idea of the ICP is to avoid this dependence by introducing a secondary RF field generator. ICP uses helium gas flow under the wafer for efficient heat transfer from the wafer chuck cooled down to

cryogenic temperatures. This result in condensation of the reactants protecting the sidewalls and, therefore, obtaining more anisotropic etching [174]. This is particularly useful for deep silicon etching with straight vertical sidewalls. Figure 2.16b shows the schematic of an ICP equipment such as that in the SMC pictured in Figure 2.18. ICP equipment is very useful for the fabrication of thin free-standing membranes on silicon substrates, due to its high etching rates. Vertical walls (i.e. high aspect ratios) are also possible using the Bosch process, which alternate etching and passivation steps to avoid etching on the walls, as we shall see in the next Chapter when describing the process developed in this thesis for the fabrication of THz FSS.

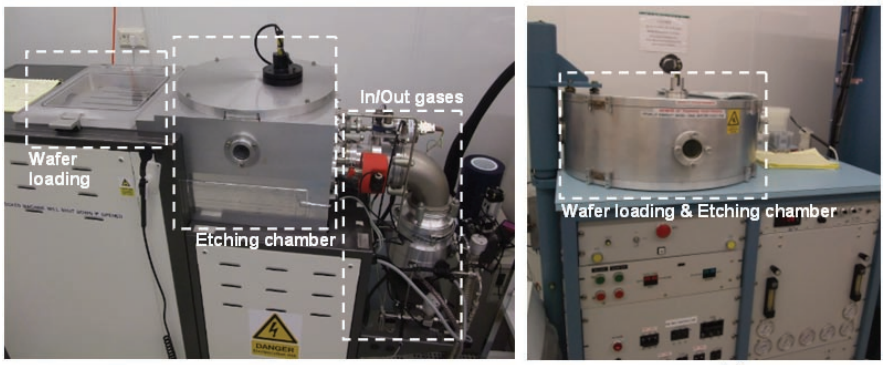

Figure 2.17: *a) STS Multiplex load locked Al and $Poly - Si$ RIE etcher using $SiCl_4$, and Cl_2 chemistry, and b) Plasmatherm PK244O RIE system using Fluorine chemistry to anisotropically etch SiO_2 and Si_3N_4.*

II. Wet etching

Wet etching employs reactants in liquid state instead of gases or plasma. The wafer is immersed in a glass or plastic bucket where the different reactant liquids are present. The temperature can be increased to speed up the etching process.

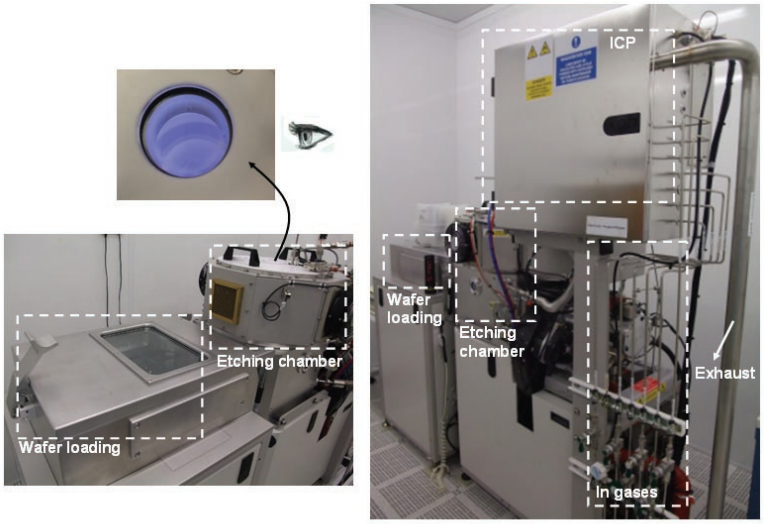

Figure 2.18: *STS Multiplex ICP - Load locked inductively coupled plasma etch system configured for deep Si etching. a) ICP view 1 (inset shows glow discharge), b) ICP view 2.*

2.5 Measurement methods

There exist different technologies for the characterization of periodic arrays working at different frequencies. Reflection and transmission measurements are commonly the main target for characterizing periodic arrays. In this section we describe the techniques available for measuring periodic arrays in three different regions of the spectrum. First, microwave measurements based on vector-network analyzers are briefly described in combination with either horn antennas in anechoic chambers or waveguides. Subsequently, THz Time-Domain Spectroscopy (THz-TDS) is explained for the characterization of arrays working at a hundreds of GHz or few THz, in the so-called THz gap. Finally, at higher frequencies (i.e. tens or hundreds of THz), Fourier Transform Infrared (FTIR) spectroscopy is described. The measurement technique employed in this thesis consist of FTIR equipment and, therefore, a more in-depth description of the FTIR operation and components is provided.

2.5.1 Microwave regime

Network analyzers represent a key component for testing EM devices in the microwave. The general block diagram describing its operation is shown in Figure 2.19a. The incident signal is generated by a variable frequency source such as voltage-controlled oscillators. In the signal-separation blocks, splitters or directional couplers are used to measure a portion of the incident wave for reference, and to separate the incident and reflected signals at the input port of the device under test (DUT) block. The transmitted signal from the DUT is finally detected and used in conjunction with the incident and reflected signals to calculate the scattering S-parameters [179].

For measuring the transmission and reflection of FSS, network analyzers must be employed in an antenna or a waveguide configuration, as shown in Figure 2.19b. In the antenna configuration, two horn antennas (transmitting and receiving) are connected to the input and output ports of the network analyzer in order to obtained a radiated wave suitable for FSS measurements. The FSS array is then placed between the transmitting and receiving antennas. This can be carried out in an anechoic chamber in order to avoid undesired reflections from the room where the measurements are performed. In order to avoid degradation of measurements owing to diffraction from the edges of the array (real finite array), microwave absorbers may be employed around the FSS as well as tapering the illumination of the antennas [19]. In the waveguide configuration, instead of measuring the entire array, a single unit cell is inserted within a waveguide connected to the input and output ports. This measurement technique resembles the analysis methods explained before with only the unit cell using Floquet theorem [180].

2.5.2 Submillimeter waves

A way of characterizing the response of an array from high microwave frequencies up to a few THz is by using very short pulses with THz frequency components. THz spectral components can be generated by ultrashort pulsed lasers, with femtoseconds pulse width. By detecting the pulse after passing through the sample, the frequency response of the sample can be measured in the time-domain. The Fourier Transform can be employed to extract the frequency spectrum from the time-domain data. This characterization method is known as THz Time-Domain Spectroscopy (THz-TDS) [181]

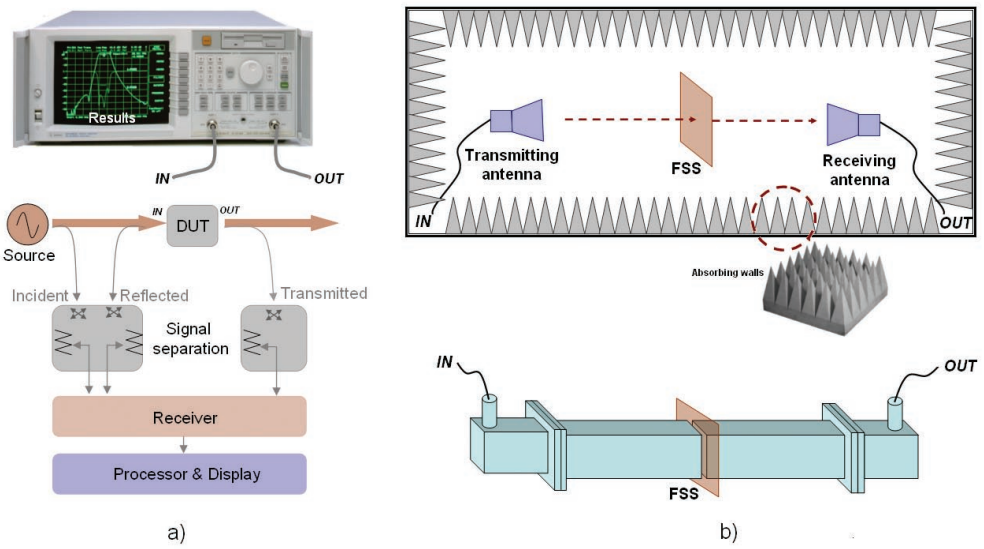

Figure 2.19: *Measuring FSS at microwave frequencies using a) network analyzers [picture of model Agilent 8714ES from macro-test.com] in b) antenna configuration in anechoic chamber or c) waveguide configuration.*

and the basic components are illustrated in Figure 2.20. THz radiation can be generated

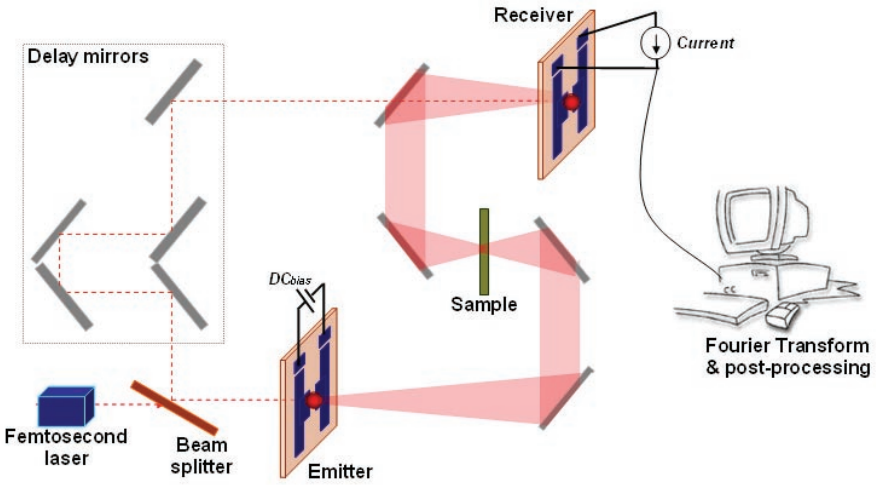

Figure 2.20: *Diagram of THz-TDS spectroscopy*

and collected by photoconductive dipole antennas [182, 183]. The emitter antenna is excited by a pump laser beam, creating electron-hole pairs in the photoconductor. A DC bias accelerates the free carriers giving rise to a transient photocurrent which is responsible for the radiation of EM waves with THz frequency components. After passing through the sample, the THz radiation impinges the receiving antenna and provides a transient bias across the photoconductive gap. The same laser used for

exciting the emitter is now applied to the receiving photoconductor resulting in a current pulse with amplitude to the transient bias, that is to the THz radiation. The electric field in the time domain is obtained integrating the detected field for different delays of the laser beam. The field in the frequency domain is simply extracted from performing the Fourier Transform to the time-domain data.

2.5.3 Infrared spectroscopy

The FSS studied in this thesis consist of arrays of elements in the micro-scale (effective length between $5\mu m$ and $10\mu m$), so that free-standing configurations resonate at infrared wavelengths between $10\mu m$ and $20\mu m$, wavenumbers between $500cm^{-1}$ and $1000cm^{-1}$, or frequencies between $15THz$ and $30THz$. With the addition of supporting dielectric layers, the resonant frequency shifts downwards (e.g. for effective permittivity around the FSS equal to 3, the frequency pulls down a factor 1.73). Infrared spectroscopy is the technique employed for testing prototyped FSS in this thesis, so that a more detailed description is given.

2.5.3.1 General description

The most intuitive way of measuring the spectral signature (reflection, transmission or absorption) at infrared frequencies is by the so-called dispersive spectroscopy. This technique consists of shining monochromatic light at the sample to obtain the transmission at a single frequency. The process is repeated for the frequency range of interest by sweeping from the lower to the upper frequency. The most important drawback of this approach is its slowness. Instead, Fourier Transform Infrared (FTIR) spectroscopy shines at the sample a broadband beam containing several frequencies simultaneously. Several scans are performed changing the wave interference of the beam after passing through a certain configuration of mirrors. The raw measured data (interferograms in the time-domain) from different positions of the mirrors are then processed using the Fourier Transform in order to obtained the spectrum of the sample. FTIR is then a time-domain or space-domain (mirror position) technique. Since the information from all wavelengths is collected at once, the signal-to-noise (S/N) ratio for a given scan-time or resolution is higher than dispersive spectroscopy [184, 185].

The principle of operation of an FTIR spectrometer can be well understood from Figure 2.21. Light from an infrared source is collimated (parallel light rays) and directed to a beam-splitter, which ideally reflects and transmit 50% of the incoming light. The reflected light impignes a fixed mirror located at a distance d_{fixed}, while the transmitted light is directed to a moving mirror located at a variable distance d_{moving}. The light beams from both mirrors is then directed back to the beam-splitter which transmit both beams interferance (interferogram) to the sample. After passing through the sample, the detector collects the interference of the beams. The same process is repeated for a different distance d_{moving} of the moving mirror. The number of scans determines the resolution of the measurement.

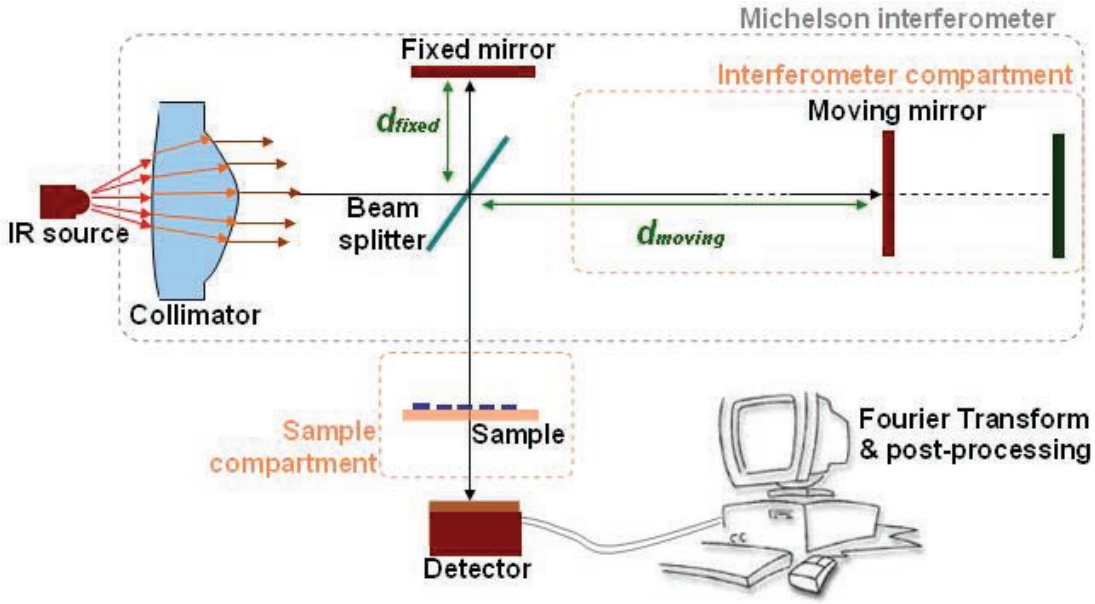

Figure 2.21: *Diagram of the principle of operation of FTIR spectrometers*

The Fourier transform algorithm employed to obtain the final spectrum of the sample is as follows [184]. The detector measures the intensity of the light from the sample for various positions of the moving mirror. Thus, the intensity as a function of the path length difference $p = d_{moving} - d_{fixed}$ and the wavenumber $k = 2\pi/\lambda$ is obtained.

$$I(p,k) = I(k)[1 + cos(2\pi kp)] \tag{2.20}$$

where $I(k)$ is the spectrum to be determined. The total intensity at a given position p

is:

$$I(p) = \int_0^\infty I(p,k)dk = \int_0^\infty I(k)cos(2\pi kp)dk \tag{2.21}$$

which is Fourier cosine transform, and its inverse result in the intensity as a function of the wavenumber:

$$I(k) = 4\int_0^\infty [I(p) - \frac{1}{2}I(p=0)]cos(2\pi kp)dp \tag{2.22}$$

The resolution depends on the maximum path length difference p (also called retardation). The spectral resolution is given by the inverse of the retardation. Then, 0.25cm, 1cm, 10cm, and 100cm retardation provides a $4cm^{-1}$, $1cm^{-1}$, $0.1cm^{-1}$, and $0.01cm^{-1}$ spectral resolution, respectively.

2.5.3.2 Components

I. Infrared sources

The first component that is needed for infrared measurements is the infrared source. Infrared radiation can be produced by different techniques, namely 1) thermal radiation (Resistor heated by current flow or ceramic heating), 2) cold radiation (gas discharge, such as xenon, mercury or cesium), and 3) Stimulated emission (lasers) [186]. However, the most critical components in an FTIR spectrometer are the beam-splitter and the detector.

II. Infrared beam-splitters

The beam-splitter is responsible for splitting or dividing the light towards the fixed mirror (reflection) and the moving mirror (transmission), ideally 50% of the intesnsity at each direction (i.e. zero absorption) and for both polarization. There are various types of beam-splitters [187], namely 1) thick substrate-coated, 2) wire-grid polarizing, 3) single layer, free-standing dielectric filsm. The first type consists of a transparent, flat, and coated substrate with low enough index of refraction to avoid reflection loss. This type is highly efficient, but can generally be employed only above 500cm^{-1} due to the lack of transparent materials at lower wavenumber. Potassium Bromide with germanium coating (KBr/Ge) represents a good example of this type [188]. The second type consists of wire-grid polarizing elements, which performance depends

on the wire spacing. These beam-splitters are more efficient at wavenumbers below $150cm^{-1}$. The third type employs free-standing single-layer dielectric films, normally some kind of polymers. The reflectance/transmission depends on consecutive reflections at both surfaces of the dielectric according to the well-known interefeces equations for a single-layer dielectric film. For this type of beam-splitter, the efficiency and its range of frequencies depends on the thickness of the dielectric. One of the most common dielectric employed as beam-splitters is the Biaxially-oriented polyethylene terephthalate (BoPET), commonly known as Mylar (one of the manufacturer). Figure 2.22 shows the variation of efficiency versus frequency for various thickness of a Mylar film [187].

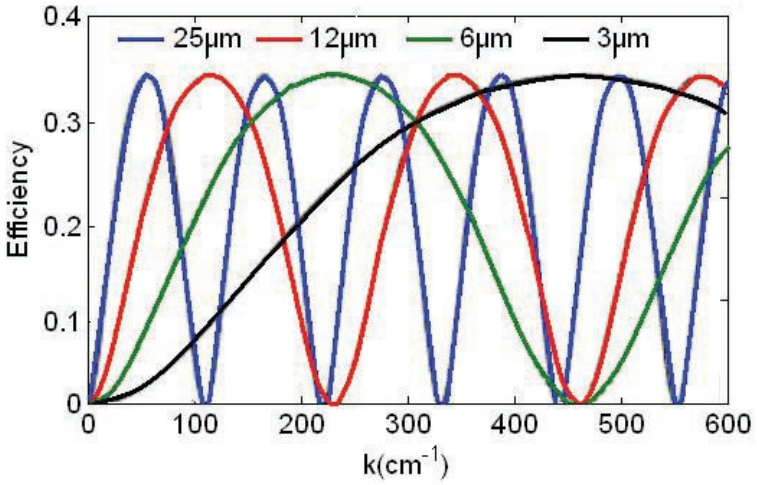

Figure 2.22: *Mylar efficiency (adapted from [187]).*

III. Infrared detectors

Detectors of infrared radiation employed in FTIR spectrometers are commonly either photoconductive or pyroelectric. Photoconductive detectors have an voltage-biased absorbing region which captures lights with energy exceeding the the energy gap of the absorbing material (semiconductor). Mercury cadmium telluride (HgCdTe), known as MCT, represent the most common alloy used for infrared detection and exhibits a wavelength cutoff proportional to the alloy composition. Pyroelectric detectors, on the other hand, are based on the pyroelectric effect, that is the generation of a charge (polarisability change) with a temperature change. Pyroelectric detectors consist of thermally isolated chips coated with a black absorbing coating. The black

coating converts the infrared radiation into heat, and the change of temperature in the chip (with a pyroelectric material) produces a charge which is detected by two electrodes [189]. Deuterated triglycine sulfate (DTGS) is the most common material employed in pyroelectric detectors for FTIR spectroscopy. In general, MCT detector is faster and more sensitive than the DTGS detector, however, DTGS detectors operate at room temperature, whereas MCT detectors must be maintained at liquid nitrogen temperature 77K to be effective.

2.6 Conclusions

This chapter has presented a detailed literature review of the main properties, types and applications of FSS, the different numerical methods for analyzing FSS performance, the fabrication tools to manufacture FSS at THz frequencies, and the methods for measuring their scattering characteristics. Explanations of the relevance of the reviewed topics in each section for the research undertaken throughout this thesis has been appropriately given.

In the first sections, attention has been paid to the general performance of FSS. A brief introduction to ohmic losses, dielectric effects, multiband operation or tunable configurations was considered necessary for the understanding of the following chapters. Likewise, an introduction to the numerical techniques and boundary conditions for the analysis of periodic structures used in this thesis has been provided. Special attention has been given to the MoM and the radiation and periodic boundary conditions, which will be further explained in Chapter 3.

In the second part of the chapter, the operation of the microfabrication equipment available at the Scottish Microelectronics Centre (SMC) has been described in great detail. The review has mainly focused on the tools used in this thesis for the fabrication of THz FSS, such as spin-coating, PECVD and sputtering deposition, RIE and ICP etching, and optical lithography.

In the last section, measurement techniques for the testing of prototyped FSS have been revised for the microwave, millimeter-wave and THz regimes of the EM spectrum. More details has been presented for the operation of FTIR spectroscopy and its components, since this technology is the one employed to measure the FSS fabricated in this thesis.

Chapter 3
Methodology for the analysis, fabrication and measurements of FSS at THz frequencies

3.1 Introduction

In the previous chapter we have given a brief description of the analysis methods that can be employed for simulating the FSS behavior; the fabrication techniques and their operation principles needed for the prototyping of FSS of μm dimensions; and the measurement equipment and strategies for testing real FSS devices throughout the EM spectrum. In this chapter, we provide a detailed and thorough description of the "Theoretical and Experimental Methods" employed throughout the research undertaken for the development of this thesis. We can divide this chapter in three well-defined parts, namely, theoretical and simulation framework, fabrication processes and measurements set-up. In the first part, we describe a rigorous mathematical model for analyzing lossless FSS based on an in-house code of the MoM, and link this mathematical description to the underlying physics of the FSS operation (e.g. Floquet modes). We also describe the design and simulation of lossy FSS using commercial simulators (HFSS and Ansoft Designer). Secondly, we develop a fabrication scheme for the prototyping of micron-scale FSS using common microfabrication techniques available at the Scottish Microelectronics Centre (SMC). In doing so, we need to consider materials selection and compatibilities with chemical processes. Finally, a description of the measurement equipment, Fourier Transform Infra Red (FT-IR) spectrometer, employed to obtain the far-field response of fabricated FSS is given.

3.2 Analysis of FSS with no ohmic losses

In this section, a modal analysis of lossless FSS is described in great detail. The analysis of lossless FSS is solely related to the FSS geometry (length, width and periodicity of the elements, and thickness of surrounding substrates) and no properties of the material are considered, except for the dielectric permittivity ϵ_r of the dielectric layers surrounding the FSS. The conductivity of the metallic elements is set to be infinite (perfect electric conductor, PEC).

Two main parts can be distinguished in this section, as shown in Table 3.1. First, the wave equation and propagation constant in an homogeneous medium (e.g. free space) with no FSS is derived from Maxwell's equations. Subsequently, the wave equation is solved for a lossless FSS using the Floquet theorem, a modal analysis is carried out to obtain an integral equation (IE) relating the incident plane-wave to the currents induced in the FSS elements, and the MoM is applied to solved such integral equation.

Analyzed structure	Propagation constant dependence
Homogeneous medium	Constant (no material properties or geometry dependency)
Lossless FSS	Geometry dependency (only dielectric properties, ϵ_r and $tan\delta$)

Table 3.1: *Propagation constant dependence in homogeneous medium and lossless FSS*

3.2.1 Wave equation in homogeneous medium

Maxwell equations contain the foundations for analyzing any electromagnetic problem. They consist of a set of four equations as follows [190]:

$$\nabla \times H = J + \frac{\partial D}{\partial t} \tag{3.1}$$

$$\nabla \times E = -\frac{\partial B}{\partial t} \tag{3.2}$$

$$\nabla B = 0 \tag{3.3}$$

$$\nabla D = \rho \tag{3.4}$$

Where E is the electric field intensity (V/m), D the electric flux density (C/m^2), H the magnetic field intensity (A/m), B the magnetic flux density ($T = W_b/m^2$), J the

current density (A/m^2), and ρ the electric charge density (C/m^3).

In addition to these equations, we need the so-called constitutive relations which relates D with E through the electric permittivity ϵ, and B with H through the magnetic permeability μ, and Ohm's law which relates J and E, through the electric conductivity σ:

$$D = \epsilon E \tag{3.5}$$

$$B = \mu H \tag{3.6}$$

$$J = \sigma E \tag{3.7}$$

In the problem under consideration, there is no electric charge density ($\rho = 0$), so then $\nabla D = 0$.

From vector field theory, we know that any given vector field A can be expressed as the sum of the gradient of an scalar potential ϕ and the curl of a vector potential Ψ:

$$A = \nabla\phi + \nabla \times \Psi \tag{3.8}$$

In addition, the following relations are also known from vector field theory:

$$\nabla \times \nabla\phi = 0 \tag{3.9}$$

$$\nabla \cdot \nabla \times \Psi = 0 \tag{3.10}$$

$$\nabla \times \nabla \times A = \nabla(\nabla A) - \nabla^2 A \tag{3.11}$$

Applying the curl to (3.1):

$$\nabla \times \nabla \times H = \nabla \times J + \nabla \times \frac{\partial D}{\partial t} \tag{3.12}$$

Introducing (3.5) and (3.7):

$$\nabla \times \nabla \times H = \sigma \nabla \times E + \epsilon \frac{\partial \nabla \times E}{\partial t} \tag{3.13}$$

Introducing (3.2) from Maxwell equations into (3.13):

$$\nabla \times \nabla \times H = \sigma \left(-\frac{\partial B}{\partial t} \right) - \epsilon \frac{\partial}{\partial t} \frac{\partial B}{\partial t} \tag{3.14}$$

And using (3.6), we obtain a differential equation only dependent on H:

$$\nabla \times \nabla \times H = -\sigma\mu\frac{\partial H}{\partial t} - \epsilon\mu\frac{\partial^2 H}{\partial t^2} \tag{3.15}$$

Applying (3.3) and (3.11), we obtain:

$$\nabla \times \nabla \times H = \nabla(\nabla H) - \nabla^2 H = \nabla\left(\frac{1}{\mu}\underbrace{\nabla B}_{0}\right) - \nabla^2 H = -\nabla^2 H \tag{3.16}$$

And introducing (3.16) in (3.15):

$$\nabla^2 H = \sigma\mu\frac{\partial H}{\partial t} + \epsilon\mu\frac{\partial^2 H}{\partial t^2} \tag{3.17}$$

Similarly, the electric field vector can be obtained as:

$$\nabla^2 E = \sigma\mu\frac{\partial E}{\partial t} + \epsilon\mu\frac{\partial^2 E}{\partial t^2} \tag{3.18}$$

With equations (3.17) and (3.18), the electric and magnetic fields have been decoupled from their coupled formulation in the Maxwell equations (3.1) and (3.2).

Without loss of generality, we can assume simple harmonic form for time variation $E = E_0 e^{-j\omega t}$ [190]. The first and second derivatives are:

$$\frac{\partial E}{\partial t} = -j\omega E_0 e^{-j\omega t} = -j\omega E \tag{3.19}$$

$$\frac{\partial^2 E}{\partial t^2} = (-j\omega)(-j\omega)E_0 e^{-j\omega t} = -\omega^2 E \tag{3.20}$$

Introducing these in the wave equation for the electric field (3.18):

$$\nabla^2 E = -j\omega\sigma\mu E + -\omega^2\epsilon\mu E = -\omega^2\epsilon\mu\left(1 + \frac{\sigma}{\omega\epsilon}j\right)E = -k^2 E \tag{3.21}$$

Therefore, the wave equation for the electric and the magnetic field are as follows:

$$\nabla^2 E + k^2 E = 0 \tag{3.22}$$

$$\nabla^2 H + k^2 H = 0 \tag{3.23}$$

where

$$k^2 = \omega^2 \epsilon \mu \left(1 + \frac{\sigma}{\omega \epsilon} j\right) \tag{3.24}$$

Since the electric and magnetic field are determined by the same operator $(\nabla^2 + k^2)$ in (3.22)-(3.23), we can express the homogeneous scalar Helmholtz equation for any rectangular field component Ξ as:

$$\left(\nabla^2 + k^2\right) \Xi(x, y, z) = 0 \tag{3.25}$$

We can separate the propagation along z and the transverse field (x, y) as:

$$\Xi(x, y, z) = \Xi_t(x, y) e^{-j\beta z} \tag{3.26}$$

So that the Helmholtz or wave equation becomes:

$$\nabla^2 \Xi_t(x, y) e^{-j\beta z} + k^2 \Xi_t(x, y) e^{-j\beta z} = 0 \tag{3.27}$$

$$\left[\frac{\partial^2}{\partial x^2} + \frac{\partial^2}{\partial y^2} + \frac{\partial^2}{\partial z^2}\right] \Xi_t(x, y) e^{-j\beta z} + k^2 \Xi_t(x, y) e^{-j\beta z} = 0 \tag{3.28}$$

The target has become, then, to solve (3.28). We start by performing the derivatives. Since $\frac{\partial^2}{\partial z^2} \Xi_t(x, y) e^{-j\beta z} = \Xi_t(x, y)(-j\beta)^2 e^{-j\beta z}$, we obtain:

$$\left[\frac{\partial^2}{\partial x^2} + \frac{\partial^2}{\partial y^2} + k^2 - \beta^2\right] \Xi_t(x, y) e^{-j\beta z} = 0 \tag{3.29}$$

Now, we proceed to solve the Helmholtz equation by separation of variables [172]. We assume that the transverse field can be expressed as the product of x-dependence and y-dependence functions. This is an assumption and if we end up with a contradiction along the line then the assumption was wrong. If there is no contradiction then the assumption is valid. Thus, we seek a solution of the form:

$$\Xi_t(x, y) = f(x) g(y) \tag{3.30}$$

Differentiating we have:

$$\frac{\partial^2}{\partial x^2} \Xi_t(x, y) = g(y) \frac{\partial^2}{\partial x^2} f(x) \tag{3.31}$$

$$\frac{\partial^2}{\partial y^2} \Xi_t(x, y) = f(x) \frac{\partial^2}{\partial y^2} g(y) \tag{3.32}$$

Thus, the wave equation becomes:

$$g(y)\frac{\partial^2}{\partial x^2}f(x) + f(x)\frac{\partial^2}{\partial y^2}g(y) + (k^2 - \beta^2)f(x)g(y) = 0 \tag{3.33}$$

And dividing by the product f(x)g(y):

$$\frac{1}{f(x)}\frac{\partial^2}{\partial x^2}f(x) + \frac{1}{g(y)}\frac{\partial^2}{\partial y^2}g(y) + (k^2 - \beta^2) = 0 \tag{3.34}$$

With the notacion $\frac{\partial^2}{\partial x^2}f(x) = f''(x)$, and $\frac{\partial^2}{\partial y^2}g(y) = g''(y)$ the wave equation becomes:

$$\underbrace{\frac{f''(x)}{f(x)}}_{x\ dependence} + \underbrace{\frac{g''(y)}{g(y)}}_{y\ dependence} + \underbrace{(k^2 - \beta^2)}_{constant} = 0 \tag{3.35}$$

Each term must be equal to a constant since each term depends only on the corresponding variable:

$$\frac{f''(x)}{f(x)} = C_x \tag{3.36}$$

$$\frac{g''(y)}{g(y)} = C_y \tag{3.37}$$

Equations (3.36) and (3.37) are second order homogeneous ordinary differential equations (ODE) with constant coefficients. In these equations, the solution is a function whose derivatives keep the same form as the function itself. An elementary function which satisfies this restriction is the exponential function $e^{\lambda x}$. In order to solve this differential equation, we first calculate the characteristic equation of the ODE as (for x):

$$\lambda^2 - C_x = 0 \tag{3.38}$$

This characteristic equation has the solution $\lambda = \pm\sqrt{C_x}$. Where the choice in the sign depends on direction of the propagation constant either to $+x$ or $-x$. We can express it in a more convinient form if the constant $C_x = -k_x^2$. In this case, the solution becomes $\lambda = \pm jk_x$. Doing the same for the y-dependent ODE, we obtain the transverse field as (for simplicity we take positive sign of the propagation constants in both x and y):

$$\Xi_t(x, y) = f(x)g(y) = A_1 e^{jk_x x} A_2 e^{jk_y y} \tag{3.39}$$

Substituting in (3.29):

$$\left[\frac{\partial^2}{\partial x^2}+\frac{\partial^2}{\partial y^2}+k^2-\beta^2\right]e^{jk_x x}e^{jk_y y}e^{-j\beta z}=\left[-k_x^2-k_y^2+k^2-\beta^2\right]e^{jk_x x}e^{jk_y y}e^{-j\beta z}=0 \tag{3.40}$$

And then the constants k_x and k_y must satisfy:

$$\beta^2=k^2-k_x^2-k_y^2 \tag{3.41}$$

3.2.2 Modal analysis of lossless FSS and solution using MoM

Modal analysis is carried out now in order to obtain the IE of FSS arrays. The behavior of FSS is analyzed in terms of modes which may be propagating or evanescent depending on the physical dimensions of the array and any possible surrounding dielectrics. In this section, we present a step-by-step description on how to obtain the IE of an lossless FSS supported by a dielectric layer. First, the Floquet Theorem is explained and applied to obtained the propagation constants in periodic arrays (using the free-space wave-equation derived previously). A physical interpretation of the modes existing in FSS is also given. Second, a modal analysis is carried out and the vector Floquet modes obtained. Third, boundary conditions are applied to obtained the IE, which relates the incident plane-wave (illumination) and the currents induced in the elements of the FSS. Finally, the IE is solved using MoM and the S-parameter obtained. The notation taken throughout this section is as in [3, 191].

3.2.2.1 Floquet theorem for periodic systems

Periodic structures can be analyzed in a simple manner thanks to the French mathematician Gaston Floquet (1847-1920), who introduced the well-known Floquet theorem for the study of periodic systems. Such theorem states that "In a periodic system, for a given mode of propagation at a given steady-state frequency, the fields at one cross section differ from those one period (or an integer multiple of periods) away by only a complex constant" [192]. Essentially, this theorem tell us that we cannot distinguish between an infinite array and the same array displaced one or an integer multiples of periods.

For simplicity, consider first a 1D periodic system with period d as shown in Figure 3.1.

The periodicity in its geometry forces the field to be also periodic. If we define the field

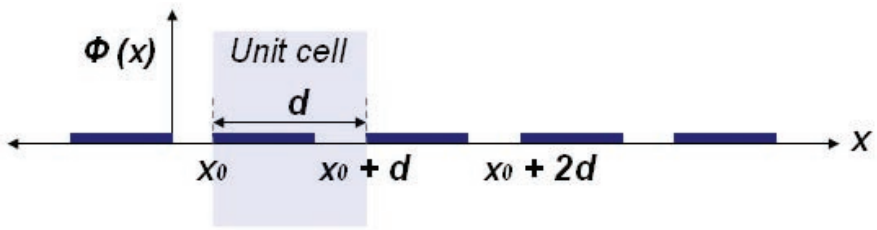

Figure 3.1: *1D periodic structure*

as $\phi(x)$, then the Floquet theorem tells us that the field in a period distance would differ only by a complex constant $\phi(x+d) = C\phi(x)$. If we move an integer number of periods m, the field becomes $\phi(x + md) = C^m\phi(x)$. In general, the complex constant C can be expressed as an exponential $e^{jk_{x_0}d}$, where k is a complex constant. The field relation between neighboring unit cells would then become:

$$\phi(x + d) = e^{jk_{x_0}d}\phi(x) \tag{3.42}$$

Now, we can define a periodic function:

$$P(x) = e^{-jk_{x_0}x}\phi(x). \tag{3.43}$$

To demonstrate that $P(x)$ is a periodic function, we proceed as follows:

$$P(x + d) = e^{-jk_{x_0}(x+d)}\phi(x + d) = e^{-jk_{x_0}x}e^{-jk_{x_0}d}e^{jk_{x_0}d}\phi(x) = e^{-jk_{x_0}x}\phi(x) = P(x) \tag{3.44}$$

Since $P(x)$ is a periodic function, it can be expressed as a Fourier series:

$$P(x) = \sum_{n=-\infty}^{\infty} a_n e^{j\frac{2\pi n}{d}x} \tag{3.45}$$

Substituting in (3.43), we obtain:

$$\phi(x) = e^{jk_{x_0}x}P(x) = e^{jk_{x_0}x}\sum_{n=-\infty}^{\infty} a_n e^{j\frac{2\pi n}{d}x} = \sum_{n=-\infty}^{\infty} a_n e^{jk_{x_0}x}e^{j\frac{2\pi n}{d}x} = \sum_{n=-\infty}^{\infty} a_n e^{jk_{x_n}x} \tag{3.46}$$

where

$$k_{x_n} = k_{x_0} + \frac{2\pi n}{d} \tag{3.47}$$

This description of the field for periodic systems is known as Floquet spatial harmonic expansion, and each term n represents a Floquet Space Harmonic (FSH). Floquet's theorem is essentially an extension of the Fourier theorem for periodic functions. Any function or field (e.g. $\phi(x)$) which repeats itself periodically except for a multiplicative exponential factor (e.g. $e^{jk_{x_0}d}$) can be expressed as an infinite set of modes (a_n). This formulation is adequate to describe the field in the vicinity of a planar 2D infinite periodic phased array with excitations of the unit cells which are uniform in amplitude and vary linearly in phase.

3.2.2.2 2D Periodic arrays formulation

Consider a periodic array of rectangular waveguides or dipole elements, as shown in Figure 3.2, which are excited with a uniform amplitude and a varying phase as required for the application of Floquet's theorem:

$$V_{00}e^{-j(d_xP_x+d_yP_y)} \tag{3.48}$$

where the inter-element phase shifts in the x- and y-directions (P_x and P_y, respectively) define the direction of propagation (θ and ϕ) of the radiated beam.

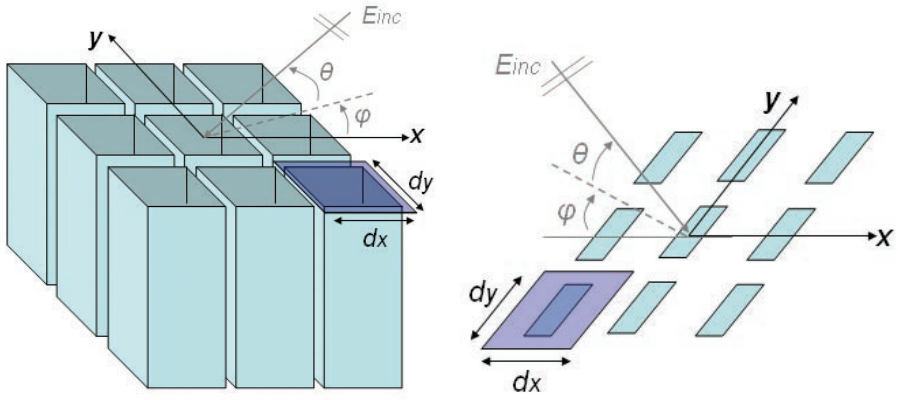

(a) Periodic waveguides (b) Periodic dipoles

Figure 3.2: *Periodic array of (a) rectangular waveguides and (b) dipoles*

$$P_x = k\sin\theta\cos\phi d_x = k_x^i d_x \tag{3.49}$$

$$P_y = k\sin\theta\sin\phi d_y = k_y^i d_y \tag{3.50}$$

And in free-space ($\sigma = 0,\ \epsilon = \epsilon_0,\ \mu = \mu_0$), $k = \omega\sqrt{\epsilon_0\mu_0} = \frac{2\pi f}{c} = \frac{2\pi}{\lambda}$.

The transverse field is periodic due to the periodic structure and the excitation given in (3.48), as described in [23]:

$$\Xi(x + d_x, y + d_y, z) = \Xi_t(x, y)e^{-j(P_x+P_y)}e^{-j\beta z} \tag{3.51}$$

We can now apply the Floquet spatial harmonic expansion, as explained previously in section 3.2.1.2. We will do so for each transverse direction (x, y) separately. We note that, for the x-dependence, if:

$$f(x + d_x) = f(x)e^{-jP_x} \tag{3.52}$$

then

$$F(x) = f(x)e^{j\frac{P_x}{d_x}x} \tag{3.53}$$

is a periodic function since

$$F(x+d_x) = f(x+dx)e^{j\frac{P_x}{d_x}(x+d_x)} = f(x)e^{-jP_x}e^{j\frac{P_x}{d_x}x}e^{j\frac{P_x}{d_x}d_x} = f(x)e^{j\frac{P_x}{d_x}x} = F(x) \tag{3.54}$$

Thus, $F(x)$ can be expressed as a Fourier series:

$$F(x) = \sum_{p=-\infty}^{\infty} a_p e^{j\left(\frac{2\pi p}{d_x}x\right)} \tag{3.55}$$

and, therefore, the x-dependence of the transverse field is expressed as an infinite sum of FSH, which represents a complete set of Floquet modes:

$$f(x) = \sum_{p=-\infty}^{\infty} a_p e^{j\left(\frac{2\pi p - P_x}{d_x}x\right)} \tag{3.56}$$

Since every mode satisfies (3.39), then we can obtain the propagation constants for each FSH in the x-direction as:

$$k_{x_p} = \frac{2\pi p - P_x}{d_x} = \frac{2\pi p}{d_x} - k\sin\theta\cos\phi\hat{x} \tag{3.57}$$

Following the same procedure, we can obtain the propagation constant in the

y-direction:

$$k_{y_q} = \frac{2\pi q - P_y}{d_y} = \frac{2\pi q}{d_y} - k \sin\theta \sin\phi \hat{y} \tag{3.58}$$

Hence the "modal field solution" of the wave equation (3.51) with the boundary condition set by the excitations in (3.48)-(3.50) is:

$$\Xi_{pq}(x, y, z) = e^{jk_{x_p}x} e^{jk_{y_q}y} e^{-j\beta_{pq}z} \tag{3.59}$$

where the propagation constants are related as in (3.41):

$$\beta_{pq} = \sqrt{k^2 - k_{x_p}^2 - k_{y_q}^2} = \sqrt{\left(\frac{2\pi}{\lambda}\right)^2 - \left(\frac{2\pi p - P_x}{d_x}\right)^2 - \left(\frac{2\pi q - P_y}{d_y}\right)^2} \tag{3.60}$$

With (3.59) and (3.60), any component of the electric or magnetic field can be calculated. For instance, for E_z we have:

$$E_z(x, y, z) = \sum_{p=-\infty}^{\infty} \sum_{q=-\infty}^{\infty} a_{pq} \Xi_{pq}(x, y, z) = \sum_{p=-\infty}^{\infty} \sum_{q=-\infty}^{\infty} a_{pq} e^{jk_{x_p}x} e^{jk_{y_q}y} e^{-j\beta_{pq}z} \tag{3.61}$$

where a_{pq} represents the amplitude of the Floquet mode pq.

3.2.2.3 Physical Interpretation

Each modal field solution (3.59) represents a plane wave propagating along the z-direction with a propagation constant defined in (3.60). If the propagation constant β is real, the modal solution represents a propagating wave.

$$If \quad k^2 > k_{x_p}^2 + k_{y_q}^2 \quad \rightarrow \quad \beta_{pq} \in \Re \quad and \quad \beta_{pq} > 0 \tag{3.62}$$

$$\Xi_{pq}(x, y, z) = \Xi_{t_{pq}}(x, y) e^{-j|\beta_{pq}|z} \tag{3.63}$$

In contrast, modal solutions with β imaginary are evanescent fields, which means that they are non-propagating waves, their amplitude decays exponentially and suffer no phase change in the z-direction.

$$If \quad k^2 < k_{x_p}^2 + k_{y_q}^2 \quad \rightarrow \quad \beta_{pq} \in \Im \quad and \quad \beta_{pq} < 0 \tag{3.64}$$

$$\Xi_{pq}(x, y, z) = \Xi_{t_{pq}}(x, y) e^{-j(-j|\beta_{pq}|)z} = \Xi_{t_{pq}}(x, y) e^{-|\beta_{pq}|z} \tag{3.65}$$

Figure 3.3 depicts the propagating and evanescent modes for an arbitrary free-standing FSS. The indexes $p, q = 0, 0$ represents the incident wave (forward scattering) and the specular reflected field (specular scattering) [1].

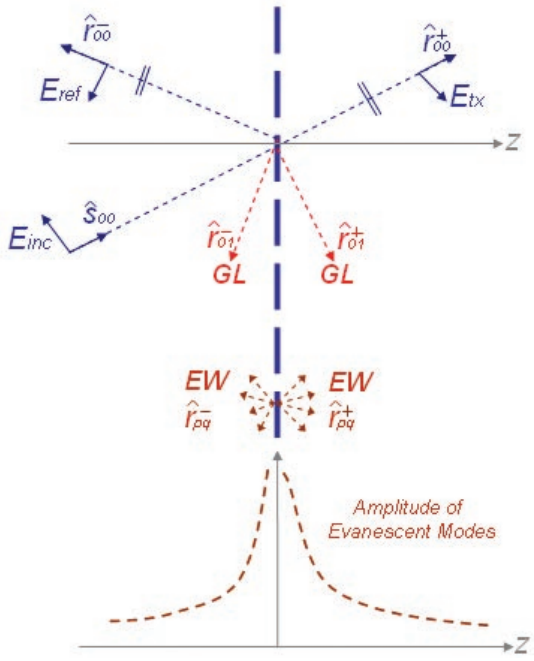

Figure 3.3: *Propagating and evanescent waves in FSS of arbitrary elements.*

For these propagating modes $(\pm\beta_{00})$, the propagating constant becomes:

$$\beta_{00} = \frac{2\pi}{\lambda}\sqrt{1 - (\sin\theta\cos\phi)^2 - (\sin\theta\sin\phi)^2} \tag{3.66}$$

It can be verified that

$$\left[(\sin\theta\cos\phi)^2 + (\sin\theta\sin\phi)^2\right] < 1, \quad \forall\theta, \phi \tag{3.67}$$

and, therefore, these propagating modes are always present for any periodic surface [1].

Higher order modes ($p \neq 0$ and/or $q \neq 0$), however, might be either evanescent or propagating waves depending on whether they exhibit real or imaginary propagation constant β. Such propagation constant (3.60) depends on the frequency (wavelength λ) and angle (θ, ϕ) of the incident wave, inter-element spacings (d_x, d_y) of the array

and order of the Floquet mode p, q. If we consider the incident wave normal to the array plane ($\theta = 0$), the propagation constant becomes:

$$\beta_{pq} = \sqrt{\left(\frac{2\pi}{\lambda}\right)^2 - \left(\frac{2\pi p}{d_x}\right)^2 - \left(\frac{2\pi q}{d_y}\right)^2} \tag{3.68}$$

Three observations can be made:

- For a fixed geometry d_x, d_y, higher order Floquet modes (p, q) will be propagating for increasing frequency (decreasing wavelength):

$$f \uparrow (\lambda \downarrow) \rightarrow \left(\frac{2\pi}{\lambda}\right)^2 > \left(\frac{2\pi p}{d_x}\right)^2 + \left(\frac{2\pi q}{d_y}\right)^2 \tag{3.69}$$

- The higher the order of the Floquet modes, the less likely to be propagating:

$$p, q \uparrow \rightarrow \left(\frac{2\pi}{\lambda}\right)^2 < \left(\frac{2\pi p}{d_x}\right)^2 + \left(\frac{2\pi q}{d_y}\right)^2 \tag{3.70}$$

- If the inter-element spacings are large enough, there might be additional values of p, q which produce a real β:

$$d_x, d_y \uparrow \rightarrow \left(\frac{2\pi}{\lambda}\right)^2 > \left(\frac{2\pi p}{d_x}\right)^2 + \left(\frac{2\pi q}{d_y}\right)^2 \tag{3.71}$$

Higher order Floquet modes which are propagating waves (real β) are denoted as grating lobes and their direction of propagation differs from the incident wave. The onset of grating lobes is defined when the propagating constant is zero, and therefore:

$$\left(\frac{2\pi}{\lambda}\right)^2 = \left(\frac{2\pi p}{d_x}\right)^2 + \left(\frac{2\pi q}{d_y}\right)^2 \tag{3.72}$$

Although evanescent modes are not propagating to the far-field, they need to be considered in a rigorous full-wave formulation of the IE. Evanescent near-fields represent the power stored in the vicinity of the array and, therefore, must be studied for FSS in applications such as imaging or sensing systems. The formulation of the Floquet modes presented in this Chapter is necessary for the following Chapters, where power stored, near-fields or induced currents are employed to investigate the Q-factors

in THz FSS as well as the FSS capabilities for sensing systems.

3.2.2.4 Modal solution for arbitrary lattice of the array

So far, we have accounted for arrays with rectangular lattice, where the elements are placed in columns and rows with rectangular angle (90 degrees). This represents the lattice configuration used throughout this thesis. However, here we generalize to arbitrary lattices in order to follow the same notation as in [3]. The modal solution for arrays with non-rectangular lattices can be generalized by means of a simple coordinates transformation. Assuming a lattice with unit vectors $\hat{u}$ and $\hat{v}$ and inter-element spacings D_u and D_v, as shown in Figure 3.4, the lattice vectors become:

$$\underline{D}_u = D_u(\cos\alpha_1\hat{x} + \sin\alpha_1\hat{y}) \tag{3.73}$$

$$\underline{D}_v = D_v(\cos\alpha_2\hat{x} + \sin\alpha_2\hat{y}) \tag{3.74}$$

and $\alpha_2 = \alpha + \alpha_1$

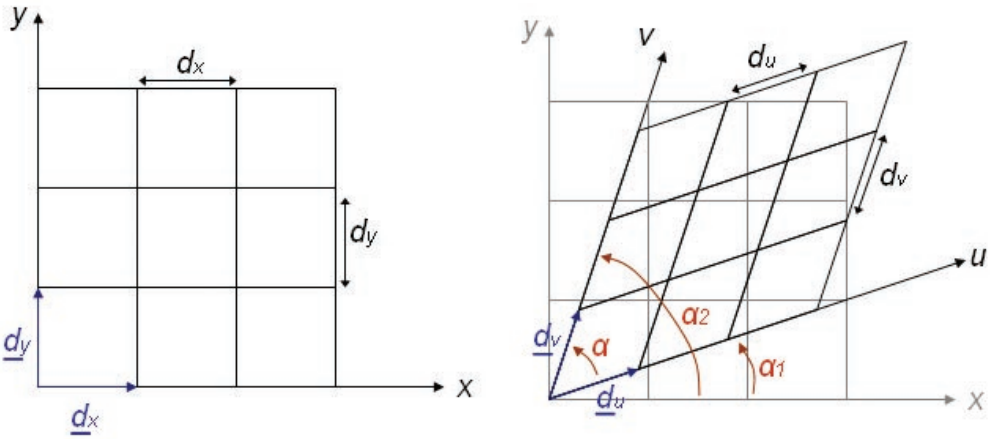

(a) Rectangular unit cell (b) Skewed unit cell

Figure 3.4: *Definition of parameters in rectangular (a), and skewed unit cell (b).*

The modal field from (3.59) can now be expressed as:

$$\Xi_{pq}(x,y,z) = e^{jk_{u_p}u}e^{jk_{v_q}v}e^{-j\underline{k}_{t00}\cdot r}e^{-j\beta_{pq}z} \tag{3.75}$$

where the incident wave component in the propagation constants (3.57)-(3.58) have been included in $\underline{k}_{t00}$, so then:

$$k_{u_p} = \frac{2\pi p}{d_u} \tag{3.76}$$

$$k_{v_q} = \frac{2\pi q}{d_v} \tag{3.77}$$

$$\underline{k}_{t00} = k\sin\theta\cos\phi\hat{x} + k\sin\theta\sin\phi\hat{y} \tag{3.78}$$

$$\underline{r} = x\hat{x} + y\hat{y} \tag{3.79}$$

We can now define a transverse propagating constant $\underline{k}_{t_{pq}}$ as follows:

$$\underline{k}_{t_{pq}} = \underline{k}_{t_{00}} + k_{u_p}u + k_{v_q}v \tag{3.80}$$

Since the projection of the coordinate system (u, v) onto (x, y) is given by:

$$\begin{pmatrix} u \\ v \end{pmatrix} = \frac{1}{\sin}\begin{pmatrix} \sin\alpha_2 & -\cos\alpha_2 \\ -\sin\alpha_1 & \cos\alpha_1 \end{pmatrix}\begin{pmatrix} x \\ y \end{pmatrix} \tag{3.81}$$

We can translate (3.80) to rectangular coordinates:

$$k_{u_p}u = \frac{2\pi p}{D_u}u = \frac{2\pi p}{D_u}\frac{1}{\sin\alpha}\left[\sin\alpha_2 x - \cos\alpha_2 y\right] \tag{3.82}$$

$$k_{v_q}v = \frac{2\pi q}{D_v}v = \frac{2\pi q}{D_v}\frac{1}{\sin\alpha}\left[-\sin\alpha_1 x + \cos\alpha_1 y\right] \tag{3.83}$$

And noticing the following expressions:

$$\hat{z}\times\underline{d}_v = \begin{vmatrix} x & y & z \\ 0 & 0 & 1 \\ d_v\cos\alpha_2 & d_v\sin\alpha_2 & 0 \end{vmatrix} = d_v(\sin\alpha_2\hat{x} - \cos\alpha_2\hat{y}) \tag{3.84}$$

$$\hat{z}\times\underline{d}_u = \begin{vmatrix} x & y & z \\ 0 & 0 & 1 \\ d_u\cos\alpha_1 & d_u\sin\alpha_1 & 0 \end{vmatrix} = d_u(\sin\alpha_1\hat{x} - \cos\alpha_1\hat{y}) \tag{3.85}$$

The transverse propagation constant can be expressed in a final form as:

$$\underline{k}_{t_{pq}} = k_{t_x}\hat{x} + k_{t_x}\hat{y} = \underline{k}_{t_{00}} + p\underline{k}_1 + q\underline{k}_2 \tag{3.86}$$

where

$$\underline{k}_1 = -\frac{2\pi}{A}\hat{z} \times \underline{d}_v \tag{3.87}$$

$$\underline{k}_2 = \frac{2\pi}{A}\hat{z} \times \underline{d}_u \tag{3.88}$$

$$A = d_u d_v \sin\alpha \tag{3.89}$$

3.2.2.5 Vector Floquet modes: TE and TM modes

In the most general case (non-rectangular lattice), the modal field solution was expressed as:

$$\Xi_{pq}(x,y,z) = e^{-j\underline{k}_{t_{pq}}\cdot\underline{r}} e^{-j\beta_{pq}z} \tag{3.90}$$

The transverse component of the field $\Psi_{pq} = e^{-j\underline{k}_{t_{pq}}\cdot\underline{r}}$ can be orthonormalized so that [3]

$$\Psi_{pq}(x,y,z) = \sqrt{\frac{1}{A}} e^{-j\underline{k}_{t_{pq}}\cdot\underline{r}} \tag{3.91}$$

$$\iint\limits_D \Psi_{pq}\Psi^*_{p'q'}\,dx\,dy = \delta_{pp'}\delta_{qq'} = \begin{cases} 1, & p = p' \text{ and } q = q' \\ 0, & otherwise \end{cases} \tag{3.92}$$

Equation (3.92) represents a set of orthogonal Floquet modes. From this, we can derive a complete set of vector TE and TM Floquet modes.

First, from source free ($\rho = 0, J = 0$) Maxwell's curl equations (3.1)-(3.2) in phasor form ($\frac{\partial}{\partial t} \to j\omega$) and the dependence $e^{-j\beta_{pq}z}$:

$$\nabla\bar{E}_{pq} = -j\omega\mu\bar{H}_{pq} \begin{cases} \frac{\partial E_{z_{pq}}}{\partial y} + j\beta_{pq}E_{y_{pq}} = -j\omega\mu H_{x_{pq}} \\ -j\beta_{pq}E_{x_{pq}} + \frac{\partial E_{z_{pq}}}{\partial x} = -j\omega\mu H_{y_{pq}} \\ \frac{\partial E_{y_{pq}}}{\partial x} - \frac{\partial E_{x_{pq}}}{\partial y} = -j\omega\mu H_{z_{pq}} \end{cases} \tag{3.93}$$

$$\nabla\bar{H}_{pq} = j\omega\epsilon\bar{E}_{pq} \begin{cases} \frac{\partial H_{z_{pq}}}{\partial y} + j\beta_{pq}H_{y_{pq}} = j\omega\epsilon E_{x_{pq}} \\ -j\beta_{pq}H_{x_{pq}} - \frac{\partial H_{z_{pq}}}{\partial x} = j\omega\epsilon E_{y_{pq}} \\ \frac{\partial H_{y_{pq}}}{\partial x} - \frac{\partial H_{x_{pq}}}{\partial y} = j\omega\epsilon E_{z_{pq}} \end{cases} \tag{3.94}$$

We can obtain the four transverse field components $(E_{x_{pq}}, E_{y_{pq}}, H_{x_{pq}}, H_{y_{pq}})$ in terms of the two longitudinal field components $(E_{z_{pq}}, H_{z_{pq}})$, taking into account that $\beta_{pq} =$

$\sqrt{k^2 - k_{t_{pq}}^2}$:

$$E_{x_{pq}} = \frac{-j}{k_{t_{pq}}^2}\left(\beta_{pq}\frac{\partial E_{z_{pq}}}{\partial x} + \omega\mu\frac{\partial H_{z_{pq}}}{\partial y}\right) \tag{3.95}$$

$$E_{y_{pq}} = \frac{j}{k_{t_{pq}}^2}\left(-\beta_{pq}\frac{\partial E_{z_{pq}}}{\partial y} + \omega\mu\frac{\partial H_{z_{pq}}}{\partial x}\right) \tag{3.96}$$

$$H_{x_{pq}} = \frac{j}{k_{t_{pq}}^2}\left(\omega\epsilon\frac{\partial E_{z_{pq}}}{\partial y} - \beta_{pq}\frac{\partial H_{z_{pq}}}{\partial x}\right) \tag{3.97}$$

$$H_{y_{pq}} = \frac{-j}{k_{t_{pq}}^2}\left(\omega\epsilon\frac{\partial E_{z_{pq}}}{\partial x} + \beta_{pq}\frac{\partial H_{z_{pq}}}{\partial y}\right) \tag{3.98}$$

- $\underline{TM\ \ modes}$: Transverse Magnetic (TM) modes are characterized by zero longitudinal magnetic field ($H_{z_{pq}} = 0$) and non-zero longitudinal electric field ($E_{z_{pq}} \neq 0$). Thus, Equations (3.95)-(3.98) are reduced to:

$$E_{x_{pq}} = \frac{-j}{k_{t_{pq}}^2}\left(\beta_{pq}\frac{\partial E_{z_{pq}}}{\partial x}\right) \tag{3.99}$$

$$E_{y_{pq}} = \frac{j}{k_{t_{pq}}^2}\left(-\beta_{pq}\frac{\partial E_{z_{pq}}}{\partial y}\right) \tag{3.100}$$

$$H_{x_{pq}} = \frac{j}{k_{t_{pq}}^2}\left(\omega\epsilon\frac{\partial E_{z_{pq}}}{\partial y}\right) \tag{3.101}$$

$$H_{y_{pq}} = \frac{-j}{k_{t_{pq}}^2}\left(\omega\epsilon\frac{\partial E_{z_{pq}}}{\partial x}\right) \tag{3.102}$$

And the transverse fields are derived from $E_{z_{pq}}$ as follows:

$$\underline{H}_{t_{pq}} = H_{x_{pq}}\hat{x} + H_{y_{pq}}\hat{y} = \frac{j\omega\epsilon}{k_{t_{pq}}^2}\frac{\partial E_{z_{pq}}}{\partial y}\hat{x} - \frac{j\omega\epsilon}{k_{t_{pq}}^2}\frac{\partial E_{z_{pq}}}{\partial x}\hat{y} = -\frac{j\omega\epsilon}{k_{t_{pq}}^2}\hat{z}\times\underline{\nabla}_t E_{z_{pq}} \tag{3.103}$$

$$\underline{E}_{t_{pq}} = E_{x_{pq}}\hat{x} + E_{y_{pq}}\hat{y} = -\frac{j\beta_{pq}}{k_{t_{pq}}^2}\frac{\partial E_{z_{pq}}}{\partial x}\hat{x} - \frac{j\beta_{pq}}{k_{t_{pq}}^2}\frac{\partial E_{z_{pq}}}{\partial y}\hat{y} = -\frac{j\beta_{pq}}{k_{t_{pq}}^2}\underline{\nabla}_t E_{z_{pq}} \tag{3.104}$$

where $\underline{\nabla}_t E_{z_{pq}} = \hat{x}\frac{\partial E_{z_{pq}}}{\partial x} + \hat{y}\frac{\partial E_{z_{pq}}}{\partial y}$ and $\hat{z}\times\underline{\nabla}_t E_{z_{pq}} = \hat{y}\frac{\partial E_{z_{pq}}}{\partial x} - \hat{x}\frac{\partial E_{z_{pq}}}{\partial y}$.

To obtain an orthonormalized vector mode we may define:

$$E_{z_{pq}}(x,y) = \frac{k_{t_{pq}}}{\beta_{pq}}\Psi_{pq}(x,y) \tag{3.105}$$

So that:

$$\underline{E}_{t_{pq}} = -\frac{j\beta_{pq}}{k_{t_{pq}}^2}\underline{\nabla}_t E_{z_{pq}} = -\frac{j\beta_{pq}}{k_{t_{pq}}^2}\left(\frac{k_{t_{pq}}}{\beta_{pq}}(jk_{tx}\hat{x} + jk_{ty}\hat{y})\Psi_{pq}(x,y)\right) = \underline{\kappa}_{1_{pq}}\Psi_{pq} \quad (3.106)$$

$$\underline{H}_{t_{pq}} = -\frac{j\omega\epsilon}{k_{t_{pq}}^2}\hat{z}\times\underline{\nabla}_t E_{z_{pq}} = -\frac{j\omega\epsilon}{k_{t_{pq}}^2}\hat{z}\times\left(\frac{k_{t_{pq}}}{\beta_{pq}}(jk_{tx}\hat{x} + jk_{ty}\hat{y})\Psi_{pq}(x,y)\right) = \eta_{1_{pq}}\hat{z}\times\underline{\kappa}_{1_{pq}}\Psi_{pq} \quad (3.107)$$

where

$$\underline{\kappa}_{1_{pq}} = \frac{k_{tx}\hat{x} + k_{ty}\hat{y}}{k_{t_{pq}}} \quad (3.108)$$

$$\hat{z}\times\underline{\kappa}_{1_{pq}} = \frac{k_{tx}\hat{y} - k_{ty}\hat{x}}{k_{t_{pq}}} \quad (3.109)$$

$$\eta_{1_{pq}} = \frac{\omega\epsilon}{\beta_{pq}} \quad (3.110)$$

The sub-index 1 denotes TM modes. $\eta_{1_{pq}}$ is the TM modal admittance for each p,q mode, and is obtained by $\underline{E}_{t_{pq}} = \frac{1}{\eta_{1_{pq}}}(\hat{z}\times\underline{H}_{t_{pq}})$. It can also be expressed in terms of wavenumber k and the free-space modal admittance ($\eta = \eta_{1_{00}} = \sqrt{\frac{\epsilon_0}{\mu_0}}$):

$$\eta_{1_{pq}} = \frac{k}{\beta_{pq}}\eta \quad (3.111)$$

- $\underline{TE\ modes}$: Transverse Electric (TE) modes are characterized by zero longitudinal electric field ($E_{z_{pq}} = 0$) and non-zero longitudinal magnetic field ($H_{z_{pq}} \neq 0$). Thus, Equations (3.95)-(3.98) are reduced to:

$$E_{x_{pq}} = \frac{-j}{k_{t_{pq}}^2}\left(\omega\mu\frac{\partial H_{z_{pq}}}{\partial y}\right) \quad (3.112)$$

$$E_{y_{pq}} = \frac{j}{k_{t_{pq}}^2}\left(\omega\mu\frac{\partial H_{z_{pq}}}{\partial x}\right) \quad (3.113)$$

$$H_{x_{pq}} = \frac{j}{k_{t_{pq}}^2}\left(-\beta_{pq}\frac{\partial H_{z_{pq}}}{\partial x}\right) \quad (3.114)$$

$$H_{y_{pq}} = \frac{-j}{k_{t_{pq}}^2}\left(\beta_{pq}\frac{\partial H_{z_{pq}}}{\partial y}\right) \quad (3.115)$$

And the transverse fields are derived from $H_{z_{pq}}$ as follows:

$$\underline{E}_{t_{pq}} = E_{x_{pq}}\hat{x} + E_{y_{pq}}\hat{y} = \frac{-j\omega\mu}{k_{t_{pq}}^2}\frac{\partial H_{z_{pq}}}{\partial y}\hat{x} + \frac{j\omega\mu}{k_{t_{pq}}^2}\frac{\partial H_{z_{pq}}}{\partial x}\hat{y} = \frac{j\omega\mu}{k_{t_{pq}}^2}\hat{z}\times\underline{\nabla}_t H_{z_{pq}} \tag{3.116}$$

$$\underline{H}_{t_{pq}} = H_{x_{pq}}\hat{x} + H_{y_{pq}}\hat{y} = \frac{-j\beta_{pq}}{k_{t_{pq}}^2}\frac{\partial H_{z_{pq}}}{\partial x}\hat{x} - \frac{j\beta_{pq}}{k_{t_{pq}}^2}\frac{\partial H_{z_{pq}}}{\partial y}\hat{y} = -\frac{j\beta_{pq}}{k_{t_{pq}}^2}\underline{\nabla}_t H_{z_{pq}} \tag{3.117}$$

As done for the TM modes previously, in order to obtain an orthonormalized set of TE vector modes, we can define:

$$H_{z_{pq}} = \frac{\eta k_{t_{pq}}}{k}\Psi_{pq} = \frac{k_{t_{pq}}}{\omega\mu}\Psi_{pq} \tag{3.118}$$

Using (3.118), the transverse fields of (3.116)-(3.117) become:

$$\underline{E}_{t_{pq}} = \frac{j\omega\mu}{k_{t_{pq}}^2}\hat{z}\times\underline{\nabla}_t H_{z_{pq}} = \frac{j\omega\mu}{k_{t_{pq}}^2}\hat{z}\times\left(\frac{k_{t_{pq}}}{\omega\mu}(jk_{tx}\hat{x} + jk_{ty}\hat{y})\Psi_{pq}\right) = \underline{\kappa}_{2_{pq}}\Psi_{pq} \tag{3.119}$$

$$\underline{H}_{t_{pq}} = -\frac{j\beta_{pq}}{k_{t_{pq}}^2}\underline{\nabla}_t H_{z_{pq}} = -\frac{j\beta_{pq}}{k_{t_{pq}}^2}\left(\frac{k_{t_{pq}}}{\omega\mu}(jk_{tx}\hat{x} + jk_{ty}\hat{y})\Psi_{pq}\right) = \eta_{2_{pq}}\underline{\kappa}_{1_{pq}}\Psi_{pq} = \eta_{2_{pq}}\hat{z}\times\underline{\kappa}_{2_{pq}}\Psi_{pq} \tag{3.120}$$

where

$$\underline{\kappa}_{2_{pq}} = -\hat{z}\times\frac{k_{tx}\hat{x} + k_{ty}\hat{y}}{k_{t_{pq}}} = \frac{k_{ty}\hat{x} - k_{tx}\hat{y}}{k_{t_{pq}}} \tag{3.121}$$

$$\hat{z}\times\underline{\kappa}_{2_{pq}} = \underline{\kappa}_{1_{pq}} = \frac{k_{tx}\hat{x} + k_{ty}\hat{y}}{k_{t_{pq}}} \tag{3.122}$$

$$\eta_{2_{pq}} = \frac{\beta_{pq}}{\omega\mu} = \frac{\beta_{pq}}{k}\eta \tag{3.123}$$

- $\underline{Electric\ and\ magnetic\ fields}$: The electric and magnetic fields can now be expressed as vector Floquet modes for TM and TE components, as follows:

$$\underline{E}(\underline{r}, z) = \sum_{pq} a_{1_{pq}}\Xi_{pq}\underline{\kappa}_{1_{pq}} + \sum_{pq} a_{2_{pq}}\Xi_{pq}\underline{\kappa}_{2_{pq}} = \sum_{mpq} a_{mpq}e^{\pm j\beta_{pq}z}\Psi_{pq}(\underline{r})\underline{\kappa}_{mpq} \tag{3.124}$$

$$\underline{H}(\underline{r}, z) = \mp\sum_{mpq}\eta_{mpq}a_{mpq}e^{\pm j\beta_{pq}z}\Psi_{pq}(\underline{r})\hat{z}\times\underline{\kappa}_{mpq} \tag{3.125}$$

3.2.2.6 Fields as reflected and transmitted waves

In order to analyze an specific FSS, we need to separate the solution region along the z direction into various subregions. Here, we show the solution for an FSS supported by a dielectric substrate, as shown in Figure 3.5, although the same procedure can be applied to any multilayered configuration. The space is separated into three regions $(-, 1, +)$, and the fields inside these regions will be derived as a function of incident, reflected and transmitted waves.

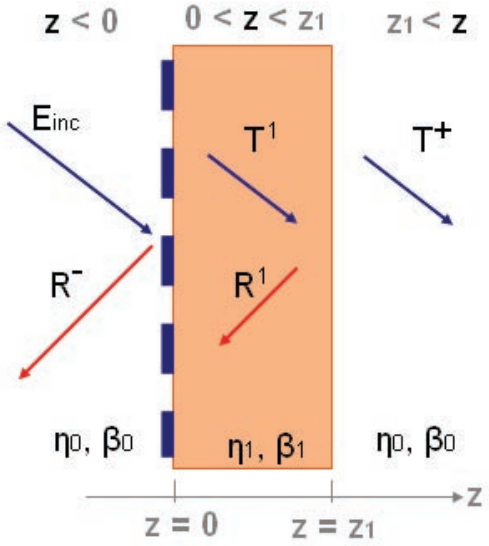

Figure 3.5: *Field regions of an FSS supported by a dielectric layer*

$z < 0$

$$\underline{E}^{-}(\underline{r}, z) = \underline{E}^{inc} + \sum_{mpq} R^{-}_{mpq} e^{j\beta^{0}_{pq} z} \Psi_{pq}(\underline{r}) \underline{\kappa}_{mpq} \tag{3.126}$$

$$\underline{H}^{-}(r, z) = \underline{H}^{inc} - \sum_{mpq} \eta^{0}_{mpq} R^{-}_{mpq} e^{j\beta^{0}_{pq} z} \Psi_{pq}(\underline{r}) \cdot \hat{z} \times \underline{\kappa}_{mpq} \tag{3.127}$$

$0 < z < z_1$

$$\underline{E}^{1}(\underline{r}, z) = \sum_{mpq} \left(T^{1}_{mpq} e^{-j\beta^{1}_{pq} z} + R^{1}_{mpq} e^{j\beta^{1}_{pq} z} \right) \Psi_{pq}(\underline{r}) \underline{\kappa}_{mpq} \tag{3.128}$$

$$\underline{H}^{1}(r, z) = \sum_{mpq} \eta^{1}_{mpq} \left(T^{1}_{mpq} e^{-j\beta^{1}_{pq} z} - R^{1}_{mpq} e^{j\beta^{1}_{pq} z} \right) \Psi_{pq}(\underline{r}) \cdot \hat{z} \times \underline{\kappa}_{mpq} \tag{3.129}$$

$z > z_1$

$$\underline{E}^{+}(\underline{r}, z) = \sum_{mpq} T^{+}_{mpq} e^{-j\beta^{0}_{pq} z} \Psi_{pq}(\underline{r}) \underline{\kappa}_{mpq} \tag{3.130}$$

$$\underline{H}^{+}(r, z) = \sum_{mpq} \eta^{0}_{mpq} R^{-}_{mpq} e^{j\beta^{0}_{pq} z} \Psi_{pq}(\underline{r}) \cdot \hat{z} \times \underline{\kappa}_{mpq} \tag{3.131}$$

where the incident wave is expressed as the 0^{th} Floquet harmonic:

$$\underline{E}^{inc} = \sum_{m=1}^{2} T^{inc}_{m00} e^{-j\beta^{0}_{00} z} \Psi_{00}(\underline{r}) \underline{\kappa}_{m00} \tag{3.132}$$

$$\underline{H}^{inc} = \sum_{m=1}^{2} \eta^{0}_{m00} T^{inc}_{m00} e^{-j\beta^{0}_{00} z} \Psi_{00}(\underline{r}) \cdot \hat{z} \times \underline{\kappa}_{m00} \tag{3.133}$$

and R and T represent reflection and transmission coefficients for the different sub-regions and Floquet modes.

3.2.2.7 Boundary Conditions

Once the electric and magnetic fields are obtained throughout the space, we proceed to match the fields at the boundaries of our structure, namely the dielectric-air interface ($z = z_1$) and the array ($z = 0$).

1. - $\underline{Dielectric - air \;\; interface}$

The tangential component of the electric field must be continuous:

$$\underline{E}^{1}(\underline{r}, z_1) = \underline{E}^{+}(\underline{r}, z_1) \tag{3.134}$$

So then:

$$\sum_{mpq} \left(T^{1}_{mpq} e^{-j\beta^{1}_{pq} z} + R^{1}_{mpq} e^{j\beta^{1}_{pq} z} \right) \Psi_{pq}(\underline{r}) \underline{\kappa}_{mpq} = \sum_{mpq} T^{+}_{mpq} e^{-j\beta^{0}_{pq} z} \Psi_{pq}(\underline{r}) \underline{\kappa}_{mpq} \tag{3.135}$$

By multiplying both sides by $\Psi^{*}_{lm}(\underline{r}) \underline{\kappa}_{mpq}$, integrating over the unit cell (A), and using orthogonality between Floquet modes $\iint\limits_{A} \Psi^{*}_{pq}(\underline{r}) \Psi^{*}_{lm}(\underline{r}) \, ds = A \cdot \delta_{pl} \cdot \delta_{qm}$, we obtain:

$$T^{1}_{mpq} e^{-j\beta^{1}_{pq} z} + R^{1}_{mpq} e^{j\beta^{1}_{pq} z} = T^{+}_{mpq} e^{-j\beta^{0}_{pq} z} \tag{3.136}$$

Similarly for the H-field:

$$\underline{H}^1(\underline{r}, z_1) = \underline{H}^+(\underline{r}, z_1) \tag{3.137}$$

And then:

$$\eta^1_{mqp} T^1_{mpq} e^{-j\beta^1_{pq} z} - \eta^1_{mqp} R^1_{mpq} e^{j\beta^1_{pq} z} = \eta^0_{mqp} T^+_{mpq} e^{-j\beta^0_{pq} z} \tag{3.138}$$

2. - $\underline{At\ \ the\ \ array}$

Similarly to the previous boundary, at the array the electric field must be continuous:

$$\underline{E}^-(\underline{r}, 0) = \underline{E}^1(\underline{r}, 0) \tag{3.139}$$

So then:

$$\sum_{m=1}^{2} T^{inc}_{m00} e^{-j\beta^0_{00} z} \Psi_{00}(\underline{r}) \underline{\kappa}_{m00} + \sum_{mpq} R^-_{mpq} e^{j\beta^0_{pq} z} \Psi_{pq}(\underline{r}) \underline{\kappa}_{mpq} =$$

$$= \sum_{mpq} \left(T^1_{mpq} e^{-j\beta^1_{pq} z} + R^1_{mpq} e^{j\beta^1_{pq} z} \right) \Psi_{pq}(\underline{r}) \underline{\kappa}_{mpq} \tag{3.140}$$

Using orthogonality:

$$T^{inc}_{m00} \cdot \delta_{p0} \cdot \delta_{q0} + R^-_{mpq} = T^1_{mpq} + R^1_{mpq} \tag{3.141}$$

On the other hand, currents are induced in the elements of the FSS array, so that the magnetic field is discontinuous. If $\underline{J}(\underline{r}, 0)$ is the surface-current density:

$$\underline{H}^-(\underline{r}, 0) = \underline{H}^1(\underline{r}, 0) + \hat{z} \times \underline{J}(\underline{r}, 0), \qquad \underline{r} \in A \tag{3.142}$$

and then:

$$\sum_{m=1}^{2} \eta^0_{m00} T^{inc}_{m00} e^{-j\beta^0_{00} z} \Psi_{00}(\underline{r}) \cdot \times \underline{\kappa}_{m00} - \sum_{mpq} \eta^0_{mpq} R^-_{mpq} e^{j\beta^0_{pq} z} \Psi_{pq}(\underline{r}) \cdot \hat{z} \times \underline{\kappa}_{mpq} =$$

$$= \hat{z} \times \underline{J}(\underline{r}, 0) + \sum_{mpq} \eta^1_{mpq} \left(T^1_{mpq} e^{-j\beta^1_{pq} z} - R^1_{mpq} e^{j\beta^1_{pq} z} \right) \Psi_{pq}(\underline{r}) \cdot \hat{z} \times \underline{\kappa}_{mpq} \tag{3.143}$$

Using orthogonality:

$$\eta^0_{m00} T^{inc}_{m00} \delta_{p0} \delta_{q0} - \eta^0_{mpq} R^-_{mpq} = \frac{\tilde{J}_{mpq}}{A} + \eta^1_{mpq} T^1_{mpq} - \eta^1_{mpq} R^1_{mpq} \tag{3.144}$$

Where the current is:

$$\tilde{J}_{mpq} = \underline{\tilde{J}}_{pq} \cdot \underline{\kappa}_{mpq} \tag{3.145}$$

and we have used the Floquet transformation of current as:

$$\underline{\tilde{J}}_{pq} = \iint_{A'} \underline{J}(\underline{r}) \cdot \Psi^*_{pq}(\underline{r})\, ds = \langle \underline{J}(\underline{r}), \Psi_{pq}(\underline{r}) \rangle_{A'} \tag{3.146}$$

where A' is the surface of the metallic element.

3. - *Electric Field boundary condition*

Now, we can impose the electric field boundary condition. For perfect electric conductors (PEC) the electric field is zero on the metallic surfaces

$$\underline{E}^-(\underline{r}, 0) = 0, \quad \underline{r} \in A' \tag{3.147}$$

So then:

$$E^{inc} + \sum_{mpq} R^-_{mpq} e^{j\beta^0_{pq} z} \Psi_{pq}(\underline{r}) \underline{\kappa}_{mpq} = 0 \tag{3.148}$$

and

$$\sum_{m=1}^{2} T^{inc}_{m00} \Psi_{00}(\underline{r}) \underline{\kappa}_{m00} + \sum_{mpq} R^-_{mpq} e^{j\beta^0_{pq} z} \Psi_{pq}(\underline{r}) \underline{\kappa}_{mpq} = 0 \tag{3.149}$$

Summarizing the relations found after applying the boundary conditions at both interfaces (dielectric-air and array), and considering perfect conductors, we obtained:

$$T^1_{mpq} e^{-j\beta^1_{pq} z} + R^1_{mpq} e^{j\beta^1_{pq} z} = T^+_{mpq} e^{-j\beta^0_{pq} z} \tag{3.150a}$$

$$\eta^1_{mqp} T^1_{mpq} e^{-j\beta^1_{pq} z} - \eta^1_{mqp} R^1_{mpq} e^{j\beta^1_{pq} z} = \eta^0_{mqp} T^+_{mpq} e^{-j\beta^0_{pq} z} \tag{3.150b}$$

$$T^{inc}_{m00} \cdot \delta_{p0} \cdot \delta_{q0} + R^-_{mpq} = T^1_{mpq} + R^1_{mpq} \tag{3.150c}$$

$$\eta^0_{m00} T^{inc}_{m00} \delta_{p0} \delta_{q0} - \eta^0_{mpq} R^-_{mpq} = \frac{\tilde{J}_{mpq}}{A} + \eta^1_{mpq} T^1_{mpq} - \eta^1_{mpq} R^1_{mpq} \tag{4.150d}$$

$$\sum_{m=1}^{2} T^{inc}_{m00} \Psi_{00}(\underline{r}) \underline{\kappa}_{m00} + \sum_{mpq} R^-_{mpq} e^{j\beta^0_{pq} z} \Psi_{pq}(\underline{r}) \underline{\kappa}_{mpq} = 0 \tag{4.150e}$$

3.2.2.8 Electric Field Integral Equation, EFIE

Now we seek for relating the electric field and the surface-current density by means of formulating the Electric Field Integral Equation (EFIE). For doing so, we first relate the reflected and transmitted field amplitude inside and outside the dielectric.

1. $\underline{Inside\ \ the\ \ dielectric}$

Dividing (3.150a) by (3.150b), we can relate the transmitted (T^1_{mpq}) and reflected (R^1_{mpq}) fields inside the dielectric:

$$\frac{T^1_{mpq}e^{-j\beta^1 z_1} + R^1_{mpq}e^{j\beta^1 z_1}}{\eta^1_{mpq}(T^1_{mpq}e^{-j\beta^1 z_1} - R^1_{mpq}e^{j\beta^1 z_1})} = \frac{T^+_{mpq}e^{-j\beta^0 z_1}}{\eta^0_{mpq}T^+_{mpq}e^{-j\beta^0 z_1}}$$

$$\frac{T^1_{mpq}e^{-j\beta^1 z_1} + R^1_{mpq}e^{j\beta^1 z_1}}{T^1_{mpq}e^{-j\beta^1 z_1} - R^1_{mpq}e^{j\beta^1 z_1}} = \frac{\eta^1_{mpq}}{\eta^0_{mpq}} \tag{3.150}$$

If we define the coefficient ρ^1_{mpq} to relate the transmitted and reflected wave:

$$R^1_{mpq} = \rho^1_{mpq}T^1_{mpq} \tag{3.151}$$

Then we obtain:

$$\frac{T^1_{mpq}e^{-j\beta^1 z_1} + \rho^1_{mpq}T^1_{mpq}e^{j\beta^1 z_1}}{T^1_{mpq}e^{-j\beta^1 z_1} - \rho^1_{mpq}T^1_{mpq}e^{j\beta^1 z_1}} = \frac{\eta^1_{mpq}}{\eta^0_{mpq}}$$

$$\eta^1_{mpq}e^{-j\beta^1 z_1} - \eta^1_{mpq}\rho^1_{mpq}e^{j\beta^1 z_1} = \eta^0_{mpq}e^{-j\beta^1 z_1} + \eta^0_{mpq}\rho^1_{mpq}e^{j\beta^1 z_1}$$

$$(\eta^1_{mpq} - \eta^0_{mpq})e^{-j\beta^1 z_1} = \rho^1_{mpq}e^{j\beta^1 z_1}(\eta^1_{mpq} + \eta^0_{mpq})$$

$$\rho^1_{mpq} = \frac{(\eta^1_{mpq} - \eta^0_{mpq})}{(\eta^1_{mpq} + \eta^0_{mpq})}e^{-2j\beta^1 z_1} \tag{3.152}$$

2. $\underline{Outside\ \ the\ \ dielectric\ \ (specular\ \ scattering)}$

Using the reflection coefficient in the dielectric-air interface obtained in (3.152), we can express (3.150c) and (3.150d) as follows:

$$T^{inc}_{m00}\cdot\delta_{p0}\cdot\delta_{q0} + R^-_{mpq} = (1+\rho^1_{mpq})T^1_{mpq} \tag{3.153}$$

$$\eta^0_{m00}T^{inc}_{m00}\delta_{p0}\delta_{q0} - \eta^0_{mpq}R^-_{mpq} = \eta^1_{mpq}(1-\rho^1_{mpq})T^1_{mpq} + \frac{\tilde{J}_{mpq}}{A} \tag{3.154}$$

Dividing (3.150d) by (3.150c), we obtain the reflected wave in the specular scattering (R^-_{mpq}):

$$\frac{\eta^0_{m00}T^{inc}_{m00}\delta_{p0}\delta_{q0} - \eta^0_{mpq}R^-_{mpq} - \frac{\tilde{J}_{mpq}}{A}}{T^{inc}_{m00}\cdot\delta_{p0}\cdot\delta_{q0} + R^-_{mpq}} = \frac{\eta^1_{mpq}(1-\rho^1_{mpq})T^1_{mpq}}{(1+\rho^1_{mpq})T^1_{mpq}} = \eta^1_{mpq}\zeta^1_{mpq} \tag{3.155}$$

where

$$\zeta^1_{mpq} = \frac{1-\rho^1_{mpq}}{1+\rho^1_{mpq}} \tag{3.156}$$

Isolating the reflected wave in the specular scattering (R^-_{mpq}), we obtain:

$$\eta^0_{m00}T^{inc}_{m00}\delta_{p0}\delta_{q0} - \eta^0_{mpq}R^-_{mpq} - \frac{\tilde{J}_{mpq}}{A} = \eta^1_{mpq}\zeta^1_{mpq}T^{inc}_{m00}\delta_{p0}\delta_{q0} + \eta^1_{mpq}\zeta^1_{mpq}R^-_{mpq}$$

$$(\eta^0_{mpq} + \eta^1_{mpq}\zeta^1_{mpq})R^-_{mpq} = (\eta^0_{mpq} - \eta^1_{mpq}\zeta^1_{mpq})T^{inc}_{m00}\delta_{p0}\delta_{q0} - \frac{\tilde{J}_{mpq}}{A}$$

$$R^-_{mpq} = \frac{(\eta^0_{mpq} - \eta^1_{mpq}\zeta^1_{mpq})}{(\eta^0_{mpq} + \eta^1_{mpq}\zeta^1_{mpq})}T^{inc}_{m00}\delta_{p0}\delta_{q0} - \frac{1}{(\eta^0_{mpq} + \eta^1_{mpq}\zeta^1_{mpq})}\frac{\tilde{J}_{mpq}}{A} \tag{3.157}$$

And defining ρ^0_{mpq}:

$$\rho^0_{mpq} = \frac{(\eta^0_{mpq} - \eta^1_{mpq}\zeta^1_{mpq})}{(\eta^0_{mpq} + \eta^1_{mpq}\zeta^1_{mpq})} \tag{3.158}$$

We finally obtain:

$$R^-_{mpq} = \rho^0_{mpq}T^{inc}_{m00}\delta_{p0}\delta_{q0} - \frac{1}{(\eta^0_{mpq} + \eta^1_{mpq}\zeta^1_{mpq})}\frac{\tilde{J}_{mpq}}{A} \tag{3.159}$$

3. $\underline{Outside\ the\ dielectric\ (forward\ scattering)}$

Using the reflection coefficient in (3.152), (3.150a) and (3.150c) can be expressed as follows:

$$T^1_{mpq}(e^{-j\beta^1_{pq}z} + \rho^1_{mpq}e^{j\beta^1_{pq}z}) = T^+_{mpq}e^{-j\beta^0_{pq}z} \tag{3.160}$$

$$T^{inc}_{m00}\cdot\delta_{p0}\cdot\delta_{q0} + R^-_{mpq} = T^1_{mpq}(1+\rho^1_{mpq}) \tag{3.161}$$

Dividing (3.162) by (3.161):

$$\frac{T^1_{mpq}(e^{-j\beta^1_{pq}z} + \rho^1_{mpq}e^{j\beta^1_{pq}z})}{T^1_{mpq}(1+\rho^1_{mpq})} = \frac{T^+_{mpq}e^{-j\beta^0_{pq}z}}{T^{inc}_{m00}\cdot\delta_{p0}\cdot\delta_{q0} + R^-_{mpq}} \tag{3.162}$$

Defining the transmission coefficient (τ^1_{mpq}) as:

$$\tau^1_{mpq} = \frac{e^{-j\beta^1_{pq}z} + \rho^1_{mpq}e^{j\beta^1_{pq}z}}{1+\rho^1_{mpq}} \tag{3.163}$$

we can obtain the transmitted wave in the forward scattering T^+_{mpq} as:

$$T^+_{mpq}e^{-j\beta^0_{pq}z} = \tau^1_{mpq}\left[T^{inc}_{m00}\cdot\delta_{p0}\cdot\delta_{q0} + R^-_{mpq}\right] \tag{3.164}$$

and using (3.160), the final expression for T^+_{mpq} becomes:

$$T^+_{mpq}e^{-j\beta^0_{pq}z} = \tau^1_{mpq}\left[(1+\rho^0_{mpq})T^{inc}_{m00}\delta_{p0}\delta_{q0} - \frac{1}{(\eta^0_{mpq}+\eta^1_{mpq}\zeta^1_{mpq})}\frac{\tilde{J}_{mpq}}{A}\right] \tag{3.165}$$

4. $\underline{Electric Field Integral Equation (EFIE)}$

Using (3.159) and (3.150e), we obtain the EFIE:

$$\sum_{m=1}^{2} T^{inc}_{m00}\Psi_{00}(\underline{r})\underline{\kappa}_{m00} = -\sum_{mpq} R^-_{mpq}\Psi_{pq}(\underline{r})\underline{\kappa}_{mpq} =$$

$$= -\sum_{mpq}\left[\rho^0_{mpq}T^{inc}_{m00}\Psi_{00}(\underline{r})\underline{\kappa}_{m00} - \frac{1}{(\eta^0_{mpq}+\eta^1_{mpq}\zeta^1_{mpq})}\frac{\tilde{J}_{mpq}}{A}\Psi_{pq}(\underline{r})\underline{\kappa}_{mpq}\right]$$

$$\sum_{m=1}^{2}(1+\rho^0_{m00})T^{inc}_{m00}\Psi_{00}(\underline{r})\underline{\kappa}_{m00} = \sum_{mpq}\frac{1}{(\eta^0_{mpq}+\eta^1_{mpq}\zeta^1_{mpq})}\frac{\tilde{J}_{mpq}}{A}\Psi_{pq}(\underline{r})\underline{\kappa}_{mpq} \tag{3.166}$$

3.2.2.9 Solution of the EFIE by MoM

In (3.166) together with the definition of the currents (3.145)-(3.146), we have obtained an integral equation for each Floquet mode p, q and for each polarization $m = 1, 2$=TM,TE. This integral equation provide the currents induced in the elements $(\tilde{J}_{mpq})$ due to certain incident wave $(T^{inc}_{m00}\Psi_{00}(\underline{r})\underline{\kappa_{m00}})$. From the EFIE and Table 3.2, the units of the transformed current $\tilde{J}_{mpq}$ are readily seen to be $(A\cdot m)$.

We proceed now to apply the MoM for solving the EFIE derived in the previous section. As explained in Chapter 2, the MoM consists of transforming an integral equation (2.6) into a matrix equation (2.13) by expanding the unknown parameter, i.e. surface

Parameter	T^{inc}_{mpq}	A	η^0_{mpq}	η^1_{mpq}	ρ^0_{mpq}	ζ^1_{mpq}	$\Psi_{pq}(\underline{r})$	$\underline{\kappa}_{mpq}$
Units	V/m	m^2	Ω^{-1}	Ω^{-1}	dls	dls	dls	dls

Table 3.2: *Units of parameters in the EFIE (*dls = dimensionless).*

currents $\underline{J}(\underline{r})$ in our case, as a summation of basis functions $\underline{h}_n(\underline{r}_n)$, and taking the inner product with a test function $\underline{h}_i(\underline{r}_i)$.

1. Expanding the currents $\underline{J}(\underline{r}) = \sum_{n=1}^{N} c_n \underline{h}_n(\underline{r}_n)$:

$$\tilde{J}_{mpq} = \underline{\tilde{J}}_{pq} \cdot \underline{\kappa}_{mpq} = \iint\limits_A \underline{J}(\underline{r}) \Psi^*_{pq}(\underline{r}) \underline{\kappa}_{mpq}\, ds = \iint\limits_A \sum_{n=1}^{N} c_n \underline{h}_n(\underline{r}_n) \Psi^*_{pq}(\underline{r}) \underline{\kappa}_{mpq}\, ds = \sum_{n=1}^{N} c_n \tilde{h}_n(\underline{r}_n) \tag{3.167}$$

The EFIE becomes:

$$\sum_{m=1}^{2} (1 + \rho^0_{m00}) T^{inc}_{m00} \Psi_{00}(\underline{r}) \underline{\kappa}_{m00} = \sum_{mpq} \frac{1}{A(\eta^0_{mpq} + \eta^1_{mpq}\zeta^1_{mpq})} \left(\sum_{n=1}^{N} c_n \tilde{h}_n(\underline{r}_n) \right) \Psi_{pq}(\underline{r}) \underline{\kappa}_{mpq} \tag{3.168}$$

2. And taking the inner product with the test function $\iint\limits_A (\ )\underline{h}^*_i(\underline{r}_i)\, ds$, we obtain:

$$\sum_{m=1}^{2} (1 + \rho^0_{m00}) T^{inc}_{m00} \left(\iint\limits_A \underline{h}^*_i(\underline{r}_i) \Psi_{00}(\underline{r}) \underline{\kappa}_{m00}\, ds \right) =$$

$$= \sum_{mpq} \frac{1}{A(\eta^0_{mpq} + \eta^1_{mpq}\zeta^1_{mpq})} \sum_{n=1}^{N} c_n \left(\iint\limits_A \tilde{h}_n(\underline{r}_n) \underline{h}^*_i(\underline{r}_i) \Psi_{pq}(\underline{r}) \underline{\kappa}_{mpq}\, ds \right) \tag{3.169}$$

3. Taking the Floquet transformation of the test functions:

$$\sum_{m=1}^{2} (1 + \rho^0_{m00}) T^{inc}_{m00} \tilde{h}^*_i(\underline{r}_i) = \sum_{mpq} \frac{1}{A(\eta^0_{mpq} + \eta^1_{mpq}\zeta^1_{mpq})} \sum_{n=1}^{N} c_n \tilde{h}_n(\underline{r}_n) \tilde{h}^*_i(\underline{r}_i) \tag{3.170}$$

This integral equation (3.170) can be expressed in matrix form similar to the matrix equation of (2.13) as follows:

$$[Z_{in}][c_n] = [\tilde{E}_i] \tag{3.171}$$

where:

- Z_{in} is a matrix of dimension $I \times N$ equal to:

$$Z_{in} = \begin{bmatrix} Z_{11} & \cdots & Z_{1N} \\ \vdots & \ddots & \vdots \\ Z_{I1} & \cdots & Z_{IN} \end{bmatrix} = \sum_{mpq} \frac{1}{A(\eta^0_{mpq} + \eta^1_{mpq}\zeta^1_{mpq})} \sum_{n=1}^{N} c_n \tilde{h}_n(\underline{r}_n)\tilde{h}^*_i(\underline{r}_i) \tag{3.172}$$

- c_n is a vector of dimension N with the unknown current coefficients:

- $\tilde{E}_i$ is a vector of dimension I resulting from the inner product of the incident wave and the testing basis functions:

$$\sum_{m=1}^{2} (1 + \rho^0_{m00}) T^{inc}_{m00} \tilde{h}^*_i(\underline{r}_i) \tag{3.173}$$

The test functions are chosen to be equal to the basis functions (Garlekin method). The method employed for the estimation of the coefficients c_n is by matrix inversion. As mentioned before, when the MoM was introduced in Chapter 2, the higher the number of basis functions N used, the more accurate the results obtained. However, the inversion of matrices of increasing size entails higher computational cost and may lead to rounding errors. The choice of the basis functions, therefore, is important when analyzing FSS in terms of accuracy and computacional cost. We can categorize the basis functions under two main groups, namely entire-domain or subdomain. If a priori estimation of the current distribution is possible, entire-domain basis functions may be employed. For instance, thin dipoles can be assumed to exhibit zero ended current with no variation along the width. Simple sinusoidal entire-domain basis functions (3.174)-(3.175) can be used to simulate the current induced in thin dipoles, as shown in Figure 3.6.

$$\underline{h}^c_n(\underline{r}) = \sqrt{\frac{2}{wL}} \cos\left(\frac{n\pi y}{L}\right) \tag{3.174}$$

$$\underline{h}^s_n(\underline{r}) = \sqrt{\frac{2}{wL}} \sin\left(\frac{n\pi y}{L}\right) \tag{3.175}$$

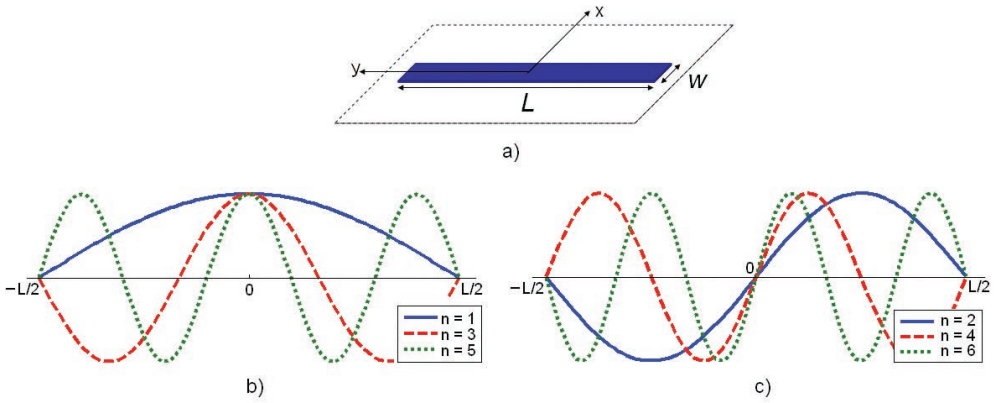

Figure 3.6: *a) Dipole FSS, b) cosine and c) sine entire-domain basis functions*

The Floquet transformation of these basis/test functions are as follows [3]:

$$\tilde{h}_n^c = \iint_A \underline{h}_n^c(\underline{r}) \cdot \Psi_{pq}^*(\underline{r})\, ds = \hat{y}\sqrt{\frac{2}{wL}} \frac{\sin\left(k_x \frac{w}{2}\right)}{k_x \frac{w}{2}} \cdot \left\{ \frac{\sin\left[\left(\frac{n\pi}{L} - k_y\right)\frac{L}{2}\right]}{\left(\frac{n\pi}{L} - k_y\right)} + \frac{\sin\left[\left(\frac{n\pi}{L} + k_y\right)\frac{L}{2}\right]}{\left(\frac{n\pi}{L} + k_y\right)} \right\} \tag{3.176}$$

$$\tilde{h}_n^s = \iint_A \underline{h}_n^s(\underline{r}) \cdot \Psi_{pq}^*(\underline{r})\, ds = \hat{y} \cdot j \cdot \sqrt{\frac{2}{wL}} \frac{\sin\left(k_x \frac{w}{2}\right)}{k_x \frac{w}{2}} \cdot \left\{ \frac{\sin\left[\left(\frac{n\pi}{L} - k_y\right)\frac{L}{2}\right]}{\left(\frac{n\pi}{L} - k_y\right)} - \frac{\sin\left[\left(\frac{n\pi}{L} + k_y\right)\frac{L}{2}\right]}{\left(\frac{n\pi}{L} + k_y\right)} \right\} \tag{3.177}$$

The units of the basis functions are $(1/m)$, while the transformed functions exhibit (m) units. Thus, the unit of the unknown current coefficients c_n are (A). The surface current $\underline{J}(\underline{r})(A/m)$ is therefore calculated as (using cosine basis functions):

$$\underline{J}(\underline{r}) = \sum_{n=1}^{N} c_n \underline{h}_n(\underline{r}_n) = c_1\sqrt{\frac{2}{wL}}\cos\left(\frac{\pi}{L}y\right) + c_2\sqrt{\frac{2}{wL}}\cos\left(\frac{3\pi}{L}y\right) + c_3\sqrt{\frac{2}{wL}}\cos\left(\frac{5\pi}{L}y\right) + \ldots \tag{3.178}$$

More complicated elements require more sophisticated entire domain basis functions, such as Chebyshev functions for patch elements [5]. Yet for arbitrary shapes of the elements, subdomain basis functions such as rooftop functions must be employed. Rooftop functions exhibit a triangular dependence in the direction of the current and step-wise constant dependence in the orthogonal direction, as shown in Figure 3.7. Complex elements can be meshed and the currents expressed in terms of these rooftop functions (this is the technique employed in commercial simulator Ansoft Designer).

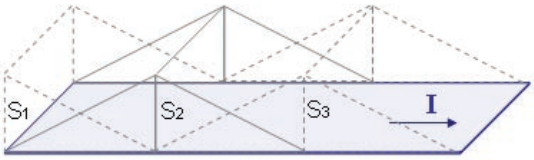

Figure 3.7: *Example of 1D rooftop subdomain basis functions. S_1, S_2, and S_3 represent three elements of the mesh*

3.2.2.10 Obtaining parameters of interest: S-parameters

After obtaining the coefficients of the Fourier expansion of the currents, we have all the information needed for the calculation of the reflection and transmission coefficients. As shown in Figure 3.5, the coefficients of the reflected modes back from the FSS array ($z = 0$) and the transmitted modes forward from the interface dielectric-air ($z = z_1$) are represented by R^-_{mpq} and T^+_{mpq}, respectively. Therefore, the transverse reflected field can be calculated at the array as:

$$\underline{E}^r(\underline{r}, z = 0) = \sum_{mpq} R^-_{mpq} e^{+j\beta_{pq} z_0} \Psi_{pq}(\underline{r}) \underline{\kappa}_{mpq} \tag{3.179}$$

and the transverse transmitted field from the dielectric-air interface:

$$\underline{E}^t(\underline{r}, z = z_1) = \sum_{mpq} T^+_{mpq} e^{+j\beta_{pq} z_2} \Psi_{pq}(\underline{r}) \underline{\kappa}_{mpq} \tag{3.180}$$

For an arbitrary propagation mode pq, either propagating or evanescent, the total reflection and transmission field of such mode is calculated adding the transverse and longitudinal components:

$$\underline{E}^{rT} = \underline{E}^r + E^r_z \hat{z} \tag{3.181}$$

$$\underline{E}^{tT} = \underline{E}^t + E^t_z \hat{z} \tag{3.182}$$

And therefore:

$$\underline{E}^{rT}(\underline{r}, z = 0) = (R^r_x \hat{x} + R^r_y \hat{y} + R^r_z \hat{z}) e^{+j\beta_{pq} z_0} \Psi_{pq}(\underline{r}) \tag{3.183}$$

$$\underline{E}^{tT}(\underline{r}, z = 0) = (R^r_x \hat{x} + R^r_y \hat{y} + R^r_z \hat{z}) e^{+j\beta_{pq} z_0} \Psi_{pq}(\underline{r}) \tag{3.184}$$

where:

$$R_x^r = R_{mpq}^- \underline{\kappa}_{m00x}; \;\; T_x^t = T_{mpq}^- \underline{\kappa}_{m00x} \tag{3.185}$$

$$R_y^r = R_{mpq}^- \underline{\kappa}_{m00y}; \;\; T_y^t = T_{mpq}^- \underline{\kappa}_{m00y} \tag{3.186}$$

$$R_z^r = -\frac{R_x^r \sin\theta\cos\phi + R_y^r \sin\theta\sin\phi}{\cos\theta}; \;\; T_z^t = -\frac{T_x^t \sin\theta\cos\phi + T_y^t \sin\theta\sin\phi}{\cos\theta} \tag{3.187}$$

and the z-components E_z^r and E_z^t are calculated using the divergence theorem $\nabla \cdot \underline{E} = 0$.

Finally, the complex reflection and transmission coefficients S_{11} and S_{21} are calculated as the projections of the total reflection and transmission fields (3.183)-(3.184) on to the incident field direction $\underline{B}^i$, as follows:

$$S_{11} = \frac{\underline{E}^{rT}(\underline{r}, z=0)}{\underline{E}^{inc}(\underline{r}, z=0)} = R_x^r B_x^{inc} + R_y^r B_y^{inc} + R_z^r B_z^{inc} \tag{3.188}$$

$$S_{21} = \frac{\underline{E}^{tT}(\underline{r}, z=z_1)}{\underline{E}^{inc}(\underline{r}, z=z_1)} = T_x^t B_x^{inc} + T_y^t B_y^{inc} + T_z^t B_z^{inc} \tag{3.189}$$

Since the total field is projected to the incident-wave direction, (3.188)-(3.189) are relative to the copolar component. The crosspolar component of the reflection and transmission coefficients may be obtained by projecting to a unit vector perpendicular to the incident-wave direction.

In the following table, the steps to obtain the S-parameters of FSS are summarized:

Step	Concept	Parameters
0a	Incident wave	θ,ϕ, V_{00}, f
0b	FSS geometry	d_x,d_y,L,w,t_{die},ϵ_r
1	Modal solution	$E(x,y)$, β_{pq}
2	Floquet TE/TM modes	$\Psi(r)\kappa(r)$
3	Tx/Rx fields	E^-,E^1,E^+
4	Boundary conditions	$E(z=z_1), E(z=0), H(z=z_1), H(z=0)$
5	Current's Floquet transf.	$\tilde{J}_{mpq}$
6	EFIE and MoM	c_n,E_i,Z_{in}
7	Tx/Rx coefficients	S_{11},S_{21}

Table 3.3: *Summary of the steps for the analysis of lossless FSS*

3.3 Analysis of FSS with ohmic losses

The formulation for the analysis of FSS explained before can be adapted to account for ohmic or dielectric losses by simply modifying the boundary condition of zero electric field at the array. In this thesis, the formulation presented before is employed solely for the analysis of FSS in the absence of losses, and specially for the calculations of induced currents, near-fields or power stored in the vicinity of the FSS. However, thermal losses due to the finite conductivity of the metallic elements and lossy dielectric layers must be accounted at THz frequencies. For doing so, commercial simulators Ansoft Designer and HFSS are employed.

In this section, the issue of metallic losses is firstly investigated from a general point of view. The interaction of light with matter is revised and the different models for conducting materials compared. Theoretical models for the behavior of metals are assessed with respect to available experimental data. A detailed description of the modeling of FSS in the commercial simulators Ansoft Designer and HFSS, which are employed to analyze lossy FSS, is also given, including periodic, radiation and finite conductivity boundary conditions.

Structure analyzed	Propagation dependence
Lossy homogeneous medium	Material properties dependency (no geometry)
Lossy FSS	Geometry and material properties dependency

Table 3.4: *Propagation dependence of lossy homogeneous medium and lossy FSS*

3.3.1 Interaction of THz radiation with matter: material models

In this subsection, homogeneous materials exhibiting losses are modeled as a function of their EM properties. First, the macroscopic EM properties of a material (complex dielectric permittivity and magnetic permeability) are derived from Maxwell equations and their meaning described. After, materials are classified under conducting or dielectric, and modeled by their intrinsic impedance. Finally, we focus on the interaction of conducting materials with light, and investigate the different metal models throughout the THz regime of the EM spectrum.

3.3.1.1 Macroscopic properties of matter

The interaction of electromagnetic (EM) waves with matter is well understood through the Maxwell equations. The microscopic form of Maxwell equations in Gaussian units is as follows [193]:

$$\nabla \cdot e(r,t) = 4\pi\rho_{micro} \tag{3.190}$$

$$\nabla \times e(r,t) = -\frac{1}{c}\frac{\partial b(r,t)}{\partial t} \tag{3.191}$$

$$\nabla \cdot b(r,t) = 0 \tag{3.192}$$

$$\nabla \times b(r,t) = \frac{1}{c}\frac{\partial e(r,t)}{\partial t} + \frac{4\pi}{c} j_{micro} \tag{3.193}$$

Where $e(r,t)$ and $b(r,t)$ represent the microscopic electric and magnetic fields, and ρ_{micro} and j_{micro} correspond to the microscopic charge and current densities, respectively.

The microscopic form of Maxwell equations might be useful to study systems of few particles involved. In order to study the properties of matter which contains of the order of 10^{22} electrons per cm^3, Maxwell equations can be rewritten in their macroscopic form as follows:

$$\nabla \cdot E = 4\pi\rho^{total} \tag{3.194}$$

$$\nabla \times E = -\frac{1}{c}\frac{\partial B}{\partial t} \tag{3.195}$$

$$\nabla \cdot B = 0 \tag{3.196}$$

$$\nabla \times B = \frac{1}{c}\frac{\partial E}{\partial t} + \frac{4\pi}{c} J^{total} \tag{3.197}$$

Where $E = E(r,t)$ and $B = B(r,t)$ represent the electric field strength and magnetic induction, respectively, while ρ^{total} and J^{total} correspond to the total charge and current density, respectively.

From the viewpoint of an EM wave with wavelength λ of the order of the dimensions of a volume element of a solid ΔV containing millions of atoms, the solid can be treated as continuous, and therefore, the macroscopic quantities can be derived by integrating the microscopic quantities over such a volume ΔV [193].

$$E(r,t) = \int_{\Delta V} e(x+dx, y+dy, z+dz, t)dxdydz \tag{3.198}$$

$$B(r,t) = \int_{\Delta V} b(x+dx, y+dy, z+dz, t)dxdydz \tag{3.199}$$

$$\rho^{total}(r,t) = \int_{\Delta V} \rho_{micro}(x+dx, y+dy, z+dz, t)dxdydz \tag{3.200}$$

$$J^{total}(r,t) = \int_{\Delta V} \mathrm{J}_{micro}(x+dx, y+dy, z+dz, t)dxdydz \tag{3.201}$$

The total charge density ρ^{total} is a consequence of both the polarization of atoms ρ^{pol} in the presence of an electric field (i.e. displacement of the electronic charge distribution) and the possible introduction of any net extra charge density from an external source (ρ^{ext}) [193]. ρ^{pol} can be expressed as:

$$\rho^{pol} = -\nabla \cdot P \tag{3.202}$$

where the polarization P represent the dipole moment per unit volume. The total charge density can thus be expressed as follows:

$$\rho^{total} = \rho^{pol} + \rho^{ext} = -\nabla \cdot P + \rho^{ext} \tag{3.203}$$

The total current density J^{total}, on the other hand, is originated from four different mechanisms [193]. A first contribution is due to time-variant electric field, which produced a localized motion of the electrons bound to the nuclei J^{pol}.

$$J^{pol} = \frac{\partial P}{\partial t} \tag{3.204}$$

In addition, a time-variant magnetic field modifies the electron spin and gives rise to time-dependent magnetization M, defined as the magnetic dipole moment per unit volume, resulting in a second contribution J^{mag} for the total current density.

$$J^{mag} = c\nabla \times M \tag{3.205}$$

The current density contributions from magnetization and polarization arise from electrons bound to the nuclei $J^{bound} = J^{pol} + J^{mag}$. The third and fourth contributions, however, are due to the motion of conduction electrons throughout the solid in the presence of an electric field J^{cond} and by any external source J^{ext}. The total current,

therefore, can be expressed as the summation of these four contributions:

$$J^{total} = J^{pol} + J^{mag} + J^{cond} + J^{ext} = \frac{\partial P}{\partial t} + c\nabla \times M + J^{cond} + J^{ext} \tag{3.206}$$

Using (3.203) into (3.194), we obtain:

$$\nabla \cdot E = 4\pi\rho^{pol} + 4\pi\rho^{ext} = -4\pi\nabla \cdot P + 4\pi\rho^{ext}$$

$$\rightarrow \quad \nabla \cdot (E + 4\pi P) = 4\pi\rho^{ext} \tag{3.207}$$

and we can define the electric displacement field D as follows:

$$D = E + 4\pi P \tag{3.208}$$

Likewise, using (3.206) into (3.197), we obtain:

$$\nabla \times B = \frac{1}{c}\frac{\partial E}{\partial t} + \frac{4\pi}{c}J^{pol} + \frac{4\pi}{c}J^{mag} + \frac{4\pi}{c}J^{cond} + \frac{4\pi}{c}J^{ext} =$$

$$= \frac{1}{c}\frac{\partial E}{\partial t} + \frac{4\pi}{c}\frac{\partial P}{\partial t} + \frac{4\pi}{c}c\nabla \times M + \frac{4\pi}{c}J^{cond} + \frac{4\pi}{c}J^{ext}$$

$$= \frac{1}{c}\frac{\partial (E + 4\pi P)}{\partial t} + 4\pi\nabla \times M + \frac{4\pi}{c}J^{cond} + \frac{4\pi}{c}J^{ext}$$

$$\rightarrow \quad \nabla \times (B - 4\pi M) = \frac{1}{c}\frac{\partial (E + 4\pi P}{\partial t} + \frac{4\pi}{c}J^{cond} + \frac{4\pi}{c}J^{ext} \tag{3.209}$$

and we can define the magnetic field strength H as follows:

$$H = B - 4\pi M \tag{3.210}$$

Introducing the previous definitions of D and H into the Maxwell equations, we obtain:

$$\nabla \cdot D = 4\pi\rho^{ext} \tag{3.211}$$

$$\nabla \times E = -\frac{1}{c}\frac{\partial B}{\partial t} \tag{3.212}$$

$$\nabla \cdot B = 0 \tag{3.213}$$

$$\nabla \times H = \frac{1}{c}\frac{\partial D}{\partial t} + \frac{4\pi}{c}J^{cond} + \frac{4\pi}{c}J^{ext} \tag{3.214}$$

The polarization P can be expressed as a power series:

$$P_i = \sum_j \chi_{ij} E_j + \sum_{j,k} \gamma_{ijk} E_j E_j + \dots \tag{3.215}$$

Since for isotropic media non-linear effects can be neglected, we can reduce the previous expression to:

$$P = \chi_e E \tag{3.216}$$

Or for the magnetization M:

$$M = \chi_m H \tag{3.217}$$

Where χ_e is the electric susceptibility and χ_m is the magnetic susceptibility. Likewise, the conduction current can be approximated through the conductivity σ as:

$$J^{cond} = \sigma E \tag{3.218}$$

The macroscopic quantities χ_e, χ_m and σ characterize the properties of a medium. However, two other macroscopic quantities are commonly employed for describing a medium, namely, the dielectric permittivity ϵ and the magnetic permeability μ, which relate to the previous quantities as follows:

$$\epsilon = 1 + 4\pi\chi_e \tag{3.219}$$

$$\mu = 1 + 4\pi\chi_m \tag{3.220}$$

and therefore:

$$D = \epsilon E \tag{3.221}$$

$$B = \mu H \tag{3.222}$$

Maxwell equations (in Gaussian units) can then be expressed in terms of these macroscopic quantities as:

$$\nabla \cdot (\epsilon E) = 4\pi\rho^{ext} \tag{3.223}$$

$$\nabla \times E = -\frac{\mu}{c}\frac{\partial H}{\partial t} \tag{3.224}$$

$$\nabla \cdot (\mu H) = 0 \tag{3.225}$$

$$\nabla \times H = \frac{1}{c}\frac{\partial(\epsilon E)}{\partial t} + \frac{4\pi\sigma}{c}E + \frac{4\pi}{c}J^{ext} \tag{3.226}$$

Or in the international system of units (SI):

$$\nabla \cdot (\epsilon E) = \rho^{ext} \tag{3.227}$$

$$\nabla \times E = -\frac{\partial(\mu H)}{\partial t} \tag{3.228}$$

$$\nabla \cdot (\mu H) = 0 \tag{3.229}$$

$$\nabla \times H = \frac{\partial(\epsilon E)}{\partial t} + \sigma E + J^{ext} \tag{3.230}$$

3.3.1.2 Material classification and intrinsic impedance

We assume from now on that there is not external source of either charge or current density $\rho^{ext} = J^{ext} = 0$. According to Maxwell's equations (3.227)-(3.30), the curl sources of the magnetic field are the conduction current ($J = \sigma E$) and a variable displacement current or electric field ($\partial D/\partial t$), while the curl source of the electric field is a variable magnetic field ($\partial B/\partial t$). For a linearly y-polarized plane wave propagating in the x-direction, these equations are expressed in phasor-form as:

$$\frac{\partial H_z}{\partial x} = j\omega D + J^{cond} = j\omega\epsilon E_y + \sigma E_y = (j\omega\epsilon + \sigma)E_y \tag{3.231}$$

$$\frac{\partial E_y}{\partial x} = -j\omega\mu H_z \tag{3.232}$$

Materials can be classified depending on which phenomenon dominates the space rate of change of the magnetic field [190]. When the displacement current is much greater than the conduction current ($\sigma/\omega\epsilon < 1/100$), the materials behave as dielectric ($\sigma = 0$ indicates lossless dielectric). In contrast, when the conduction current is dominant ($\sigma/\omega\epsilon > 100$), the material is conductor. In any other case, the material can be considered poor conductor or high lossy dielectric, known as quasi-conductor.

From (3.231)-(3.232) we can obtain the wave equation for a y-polarized plane-wave propagating along the x-direction:

$$\frac{\partial E_y}{\partial x^2} - (j\omega\mu\sigma - \omega^2\mu\epsilon)E_y = 0 \tag{3.233}$$

It is well known that free space or, in general, any medium can be seen as an array of field-cell transmission lines [190] as shown in Figure 3.8, and therefore we can relate the field quantities (ϵ, μ, σ, E and H) with circuit or distributed quantities (series inductance $L = \mu(H/m)$, shunt capacitance $C = \epsilon(F/m)$, shunt conductance $G = \sigma(\Omega/m)$, series resistance $R = \omega\mu''(\Omega/m)$, potential difference $V = E_y h(V)$, and current $I = H_x w(A)$).

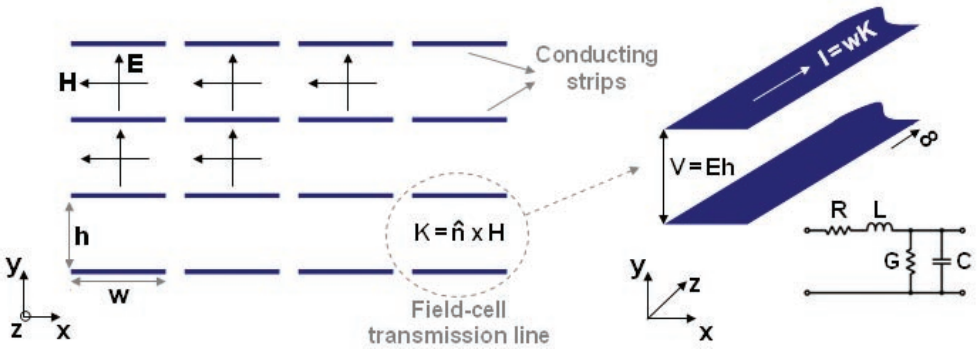

Figure 3.8: *"Field-cell transmission lines" equivalence of space and schematic representation of an infinitesimally short segment of one field cell consisting of parallel conducting strips (adapted from [190]).*

Therefore, the wave equation of (3.233)(for the voltage) becomes:

$$\frac{\partial V}{\partial x^2} - (R + j\omega L)(G + j\omega C)V = 0 \tag{3.234}$$

Defining $Z = R + j\omega L$ and $Y = G + j\omega C$ as the series impedance and shunt admittance, respectively, the previous equation can be simplified as:

$$\frac{\partial V}{\partial x^2} - ZYV = 0 \tag{3.235}$$

The characteristic impedance of the transmission line can then be obtained as:

$$Z_0 = \frac{V}{I} = \sqrt{\frac{Z}{Y}}(\Omega) \tag{3.236}$$

Which reduces to $Z_0 = \sqrt{\frac{L}{C}}$ in the absence of losses ($R = G = 0$).

From the characteristic impedance in the transmission line, we can obtain the intrinsic

impedance of the medium in its more general expression as:

$$Z_0 = \sqrt{\frac{\mu}{\epsilon}}(\Omega) \tag{3.237}$$

Where ϵ and μ are in general complex values:

$$\epsilon = \epsilon' - j\left(\epsilon'' + \frac{\sigma}{\omega}\right) \tag{3.238}$$

$$\mu = \mu' - j\mu'' \tag{3.239}$$

3.3.1.3 Skin depth and impedance approximations

The electric field inside a conducting medium decays with a rate determined by the real part of the propagation constant γ, as obtained from the wave equation for conducting materials [190]:

$$\frac{\partial^2 E_y}{\partial x^2} - \gamma E_y = 0 \quad \rightarrow E_y = E_0 e^{-\gamma x}, \;\; \gamma = j\omega\mu\sigma - \omega^2\mu\epsilon \tag{3.240}$$

When a plane electromagnetic wave impinges a conducting medium the electric field inside the conductor is not zero. Beer's law [194] describes the rate of signal attenuation with distance in a certain medium as:

$$E(z,t) = e^{-\alpha_{abs} z/2}\Re\Big(E_0 e^{j(kz-\omega t)}\Big) \tag{3.241}$$

where α_{abs} is the attenuation coefficient and k the angular wavenumber ($k = 2\pi/\lambda$). The depth of penetration at which the electric field $E(z,t)$ decays $1/e$ of its initial value E_0 is called skin depth δ_{skin} and can be obtained as [**?**, 190]:

$$\delta_{skin} = \frac{2}{\alpha_{abs}} = \sqrt{\frac{1}{\mu\sigma\pi f}} \tag{3.242}$$

According to this formulation, the skin depth for Al (DC conductivity $\sigma_{Al} = 3.8 \cdot 10^7 S/m$ at room temperature [65]) ranges from $0.8\mu m$ at $10GHz$ to $8nm$ at $100THz$. However, this formulation for the skin depth is valid only near DC and breaks down the closer we get to the plasma frequency ($\sim 15eV$ or $3.6PHz$ for metals). A more accurate

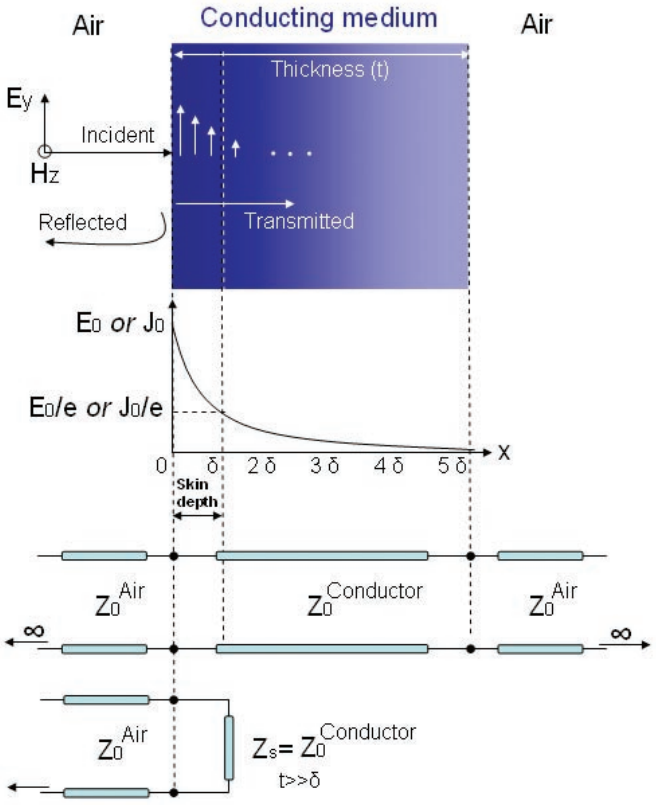

Figure 3.9: *Linearly y-polarized plane wave normally incident to a conducting medium and penetrating according to the skin depth effect, and equivalent transmission line problem*

expression can be derived from Beer's law by taking a complex index of refraction [195]. First, let's take a complex (angular) wavenumber $\tilde{k}$:

$$E(z,t) = \Re\Big(E_0 e^{j(\tilde{k}z-\omega t)}\Big) \tag{3.243}$$

where

$$\tilde{k} = k + j\frac{\alpha_{abs}}{2} = \frac{2\pi}{\lambda} + i\frac{\alpha_{abs}}{2} \tag{3.244}$$

Defining now an index of refraction $n = ck/\omega$, or in its complex form:

$$\tilde{n} = c\frac{\tilde{k}}{\omega} = n + jk_{ext} \tag{3.245}$$

where k_{ext} is the extinction coefficient. Then, we obtain:

$$E(z,t) = \Re\Big(E_0 e^{j\omega((\tilde{n}z/c)-t)}\Big) \tag{3.246}$$

where:

$$\Re(\tilde{n}) = n = \frac{ck}{\omega}, \quad \Im(\tilde{n}) = k_{ext} = \frac{c}{\omega}\frac{\alpha_{abs}}{2} = \frac{c}{\omega}\frac{1}{\delta_{skin}} \tag{3.247}$$

And, therefore, the skin depth is related to the extinction coefficient as follows:

$$\delta_{skin} = \frac{c}{\omega k_{ext}} = \frac{c}{2\pi f k_{ext}} \tag{3.248}$$

This expression (3.248) represents a more accurate formulation for the skin depth than the traditional form (3.242). The consequence of using (3.242) is that the skin depth of metals at higher frequencies will be larger than if calculated using (3.248), as shown in Figure 3.10 (e.g. at 100THz the skin depth is 8nm or 15nm using (3.248) or (3.242), respectively).

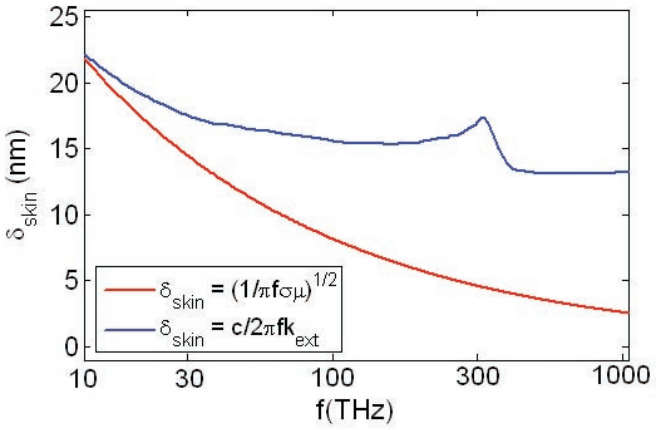

Figure 3.10: *Skin depth comparison between the two formulations*

In any case, the underlying physics of δ_{skin} reveals that as the frequency is increased, the current is more confined to the surface of the conductor. When the thickness is comparable to the skin depth, the propagation inside the conductor must be considered. However, for conductors much thicker than the skin depth (which is the common situation at THz frequencies), the propagation inside the conductor can be accurately modeled by a surface impedance Z_s with value equal to the intrinsic impedance inside the conductor Z_0 (3.237)-(3.239). In general, the equivalent surface impedance of a metallic sheet varies with its thickness as well as the frequency. The equivalent surface impedance of a metallic sheet as a function of the thickness and frequency can be

approximated by [7, 194]:

$$Z_s = \frac{1+j}{\sigma\delta}\coth t\frac{1+j}{\delta} \tag{3.249}$$

When the skin depth δ is greater than the thickness t, the surface impedance can be approximated to the DC limit ($Z_s = 1/\delta t$) [7]. In this case, the surface impedance is inversely proportional to thickness t of the conducting medium until the skin depth is reached. However, for metal thickness t greater than the skin depth, the surface impedance is no longer dependent on the thickness, and can be approximated by a resistive model as follows:

$$Z_s = (1+j)\frac{1}{\sigma\delta} \tag{3.250}$$

3.3.1.4 Metal conductivity at THz frequencies

Real conductors exhibit non-zero intrinsic impedance and can be modeled as "lossy dielectric" [190]. As we have seen before, for good conductors ($\sigma/\omega\epsilon > 100$), the surface impedance can be approximated by the resistive model of equation (3.249). However, for increasing frequency this approximation does not hold and the more general classical model (3.236)-(3.238) repeated again in equation (3.250) must be employed [190].

$$Z_0 = \frac{E}{H} = \sqrt{\frac{\mu}{\epsilon}},\ \ \epsilon = \epsilon' - j\left(\epsilon'' + \frac{\sigma}{\omega}\right),\ \ \mu = \mu' - \mu'' \tag{3.251}$$

where μ, ϵ and σ represent the complex magnetic permeability, the complex dielectric permittivity, and the complex conductivity of the metal, respectively. For non-magnetic materials the permeability becomes that in free-space ($\mu = \mu_0$). Assuming the metal behavior related solely to conduction electrons (Drude or free electron model for metals), we have $\epsilon' = \epsilon_0$ and $\epsilon'' = 0$. In addition, for sufficiently low frequencies the conductivity can be approximated to the DC conductivity.

As the frequency is increased, the value of the frequency-independent real DC conductivity is no longer applicable and the complex frequency-dependent AC conductivity must be employed [6, 65, 193, 195–197]:

$$\sigma_{AC} = \frac{\sigma_{DC}}{1 - j\omega\tau} \tag{3.252}$$

where τ represents the Drude relaxation time or damping constant. At even higher frequencies another effect, known as anomalous skin depth effect [193, 198, 199], occurs. When the skin depth is comparable to the mean free path of electrons, the assumption that the electrons velocity, and hence the current density, depends on the electric field at the observation point alone does not hold. Therefore, the conduction current is not directly proportional to a local electric field, but is a nonlocal function of the electric field distribution in the conductor.

In general, the energy dissipated in metals accounted by the free electron model is solely due to collisions. This mechanism for the dissipation of energy is present at all frequencies and, therefore, does not produce fast frequency-dependent variations of the metal properties. However, abrupt changes of the properties of measured real metals versus frequency and significant disparity between different metals are evident [195, 196]. These strong frequency-dependent variations in the measured properties are due to the onset of new mechanisms for absorption of energy, such as interband transitions (e.g. Al exhibits interband excitation of valence electrons for incident radiation with wavelength around $0.8\mu m$) [195, 196].

Experimental data from measured bulk or thin-film samples can be employed to determine accurately the properties of real metals (complex ϵ, μ, and σ), taking into account all previous effects. The measured properties of metals are commonly obtained in the form of the power reflectance Γ_p and/or the complex index of refraction $\hat{n} = n + j \cdot k_{ext}$, where n and k_{ext} are the index of refraction and the extinction coefficient, respectively [195]. The surface resistance can then be calculated accurately from the experimental data according to:

$$\Gamma_p = \left| \frac{R_s - \eta_0}{R_s + \eta_0} \right|^2 , \quad or \quad R_s = Re \sqrt{\frac{\mu_0}{\epsilon}} , \quad \epsilon = \epsilon_1 + j\epsilon_2 = \sqrt{\hat{n}} \tag{3.253}$$

where $\eta_0 = 120\pi$ represents the intrinsic impedance of free space.

Figure 3.11 shows the power reflectance (green dash-dot line) in comparison to the surface resistance (black dotted line), using experimental data for Al from [195]. In order to examine different conductor models and their accuracy throughout the THz region, Figure 3.11 also presents the surface resistance as obtained from the classical models (red dashed and blue solid lines), described by equations (3.249)-(3.250). The

graph is subdivided into different THz regions, namely Far, Mid and Near Infrared (IR), optics and ultraviolet (UV).

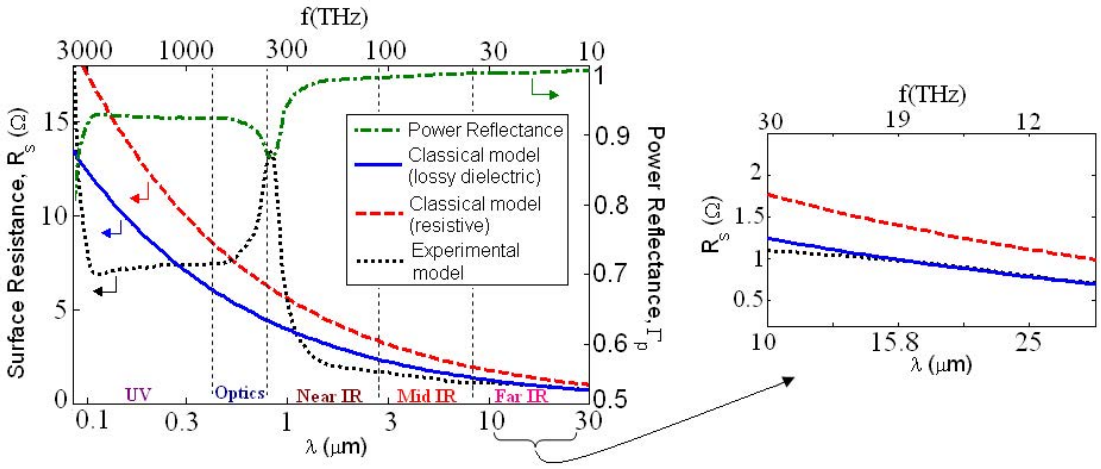

Figure 3.11: *Power reflectance (green dash-dot line and right y-axis) and surface resistance for Al (left y-axis) using the experimental model (3.253) in black dotted line and classical models (3.250)-(3.251) in red dashed and blue solid lines, respectively. The inset zooms in the far-IR band and shows just the Rs*

As shown, most of the infrared band exhibits near total reflection and low surface resistance. However, in the near IR and optics region, the reflectance drops significantly due to the onset of interband transitions around $0.8\mu m$. The classical models do not account for these effects and, therefore, fail to estimate accurately the surface resistance in conductors for higher frequency. In the near-IR and optics, the surface resistance is mostly underestimated by the classical models (which do not account for the drop in reflectivity around $0.8\mu m$). In the mid-IR band, the classical models slightly overestimate the surface resistance. On the other hand, for the far-IR, which is the frequency region of interest (5THz-30THz), the classical model defined in (3.250) (lossy dielectric) accurately estimates the surface resistance and fits well the experimental model, while the approximation of a good conductor (3.249) (resistive model) overestimates the surface resistance of Al by a factor of about 1.41 in this region of frequencies.

3.3.2 Analysis of lossy FSS using commercial softwares

The introduction of losses in the analysis of FSS includes two parts. First, non-zero loss tangent (non-zero conductivity) in the propagation constant (along the z-direction) in dielectric layers, as shown in (3.24), where now σ is not zero. This adds a attenuation factor α of a wave propagating inside a lossy medium. Second, the PEC boundary condition described in section 3.2.1.8 must be replaced by finite conductivity boundary condition. In the presence of ohmic losses, i.e. finite conductivity of the metallic layer, the tangential component of the electric fields is no longer zero, but it is calculated following the expression:

$$E_t = Z_s(\hat{n} \times H_t) \tag{3.254}$$

where E_{tan} and H_{tan} are the electric and magnetic field components tangential to the surface, respectively. Z_s corresponds to the surface impedance of the boundary explained in the previous sections.

This would modify the boundary condition (BC) of (3.150e) and, therefore, the EFIE of (3.166). The introduction of finite conductivity in the elements modify the induced currents [1]. The distribution of these currents in infinitely long dipoles, and lossless and lossy dipoles of finite length are shown in the following figure.

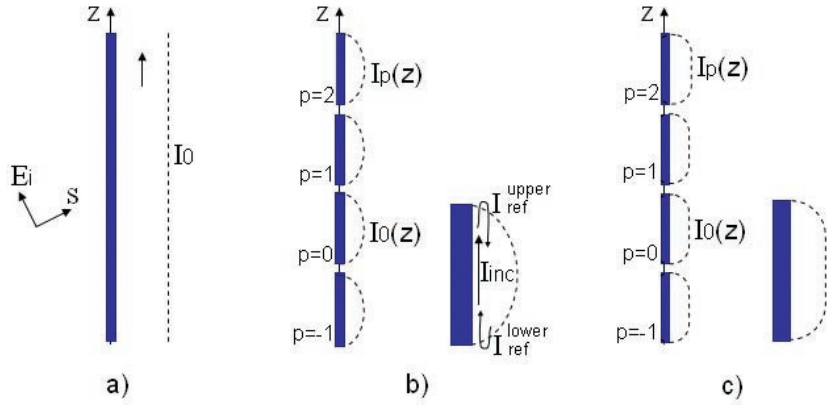

Figure 3.12: *a) Infinitely long wires, b) lossless, and c) lossy dipoles of finite length. Adapted from [1]*

As we can see, when an incident plane-wave impinges on infinitely long lossless dipoles, there will be an induced current propagating upwards ($I(z) = I_0 e^{-j\beta z s_z}$). When the length of the dipoles is not infinite, the induced current flowing upwards reflects at

both the upper and lower tips of the dipole, giving rise to a sinusoidal distribution of the total current ($I_p(z) = I_0(z)e^{-j\beta pD_z s_z}$). If the dipoles consist of very lossy materials, this distribution is modified [1]. Current waves traveling through lossy elements will be attenuated and, thus, the current distribution and amplitude changes. The higher the losses, the more affected is the distribution of the currents. In general, however, for small losses (e.g. good conductors), the distribution of the currents can be approximated to that of lossless FSS, and only a small decrease of the currents amplitude will occur (as will be shown in the next Chapter 4).

The following table summarizes the main effects of the introduction of losses in the FSS:

	Prop. constant	BC at the array	Currents distribution
Lossless FSS	$\beta_{pq} = \sqrt{k_0^2 - k_{tpq}^2}$	$E_t = 0$	Sinusoidal
Lossy FSS	$\beta_{pq} + j\alpha_{pq} = \sqrt{k(\sigma)^2 - k_{tpq}^2}$	$E_t = Z_s(\hat{n} \times H_t)$	Trapezoidal

Table 3.5: *Effects of the introduction of losses in the FSS*

Commercial softwares are employed when these effects are considered throughout this thesis. Particularly, Ansoft Designer and HFSS are used. A detailed description of the modeling and analysis of lossy FSS in these two simulators is given next, with special attention to periodic, radiation and finite conductivity boundary conditions.

3.3.2.1 Ansoft Designer

Ansoft Designer is a 2.5D circuit and planar EM simulator based on the MoM. Ansoft Designer is employed throughout this thesis for accounting for metallic losses in FSS, so that a brief description of the characteristics of this simulator is given. The analysis technique used by Ansoft Designer to analyze EM structures is based on the mixed potential integral equation (MPIE) solved using the MoM. The MPIE expresses the electric and magnetic field as a combination of a vector and a scalar potential, as follows [200]:

$$\hat{n} \times (-j\omega A - \nabla\Phi) = \hat{n} \times Z_s J \tag{3.255}$$

where $\hat{n}$ is a unit vector normal to the face of the mesh elements (e.g. triangles), ω the angular frequency, A the magnetic vector potential, Φ the electric potential, and Z_s the surface impedance.

The MoM is employed to solve the current distribution on a 3D surface mesh of the EM structure. Other results such as S-parameters or radiated fields are calculated from the current distribution J [200]. Ansoft Designer meshes automatically the surface of the geometry to be analyzed, using an iterative process in which a mesh consisting on triangular elements is refined until an accurate solution is reached. At high frequencies the skin depth is small, so that Ansoft Designer only generates a mesh in the surface of the geometry, and not inside the structure [200]. Both 2D and 3D views of a four-legged FSS modeled in Ansoft Designer are shown in Figure 3.13. An example of the mesh used is also shown. The components of the current normal to the edges of the elements are stored. The value of the current inside the basis elements is the superposition of these normal values [200], as shown in Figure 3.13d.

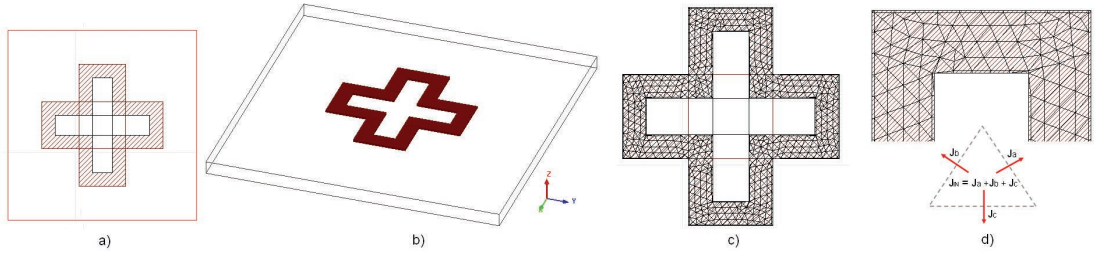

Figure 3.13: *a) Planar 2.5D model of a four-legged FSS, b) 3D view of the FSS on a substrate, c) mesh of the element, and d) zoom in the mesh, where the currents normal to the edges of triangular elements are calculated and the current inside the element is obtained as superposition of the normal currents*

For solving the currents, Ansoft Designer employs zero-order normal element basis functions. The elements have one unknown for each edge in the mesh. Testing functions equal to the basis functions are used, therefore the Garlekin method as explained before is utilized.

3.3.2.2 Ansoft HFSS

HFSS (High Frequency Structure Simulator) is a 3D full-wave frequency domain EM solver based on the FEM. HFSS is employed at various points throughout this thesis, so that here we provide a brief description on the design of FSS in HFSS. Figure 3.14 depicts the FSS design, its boundaries and excitation. The design consists of an FSS supported by a dielectric substrate. Only a unit cell needs to be designed (e.g. a perturbed FSS in the figure) embedded within various boundaries and excited by an incident wave. For FSS elements sensitive to the polarization of the incident wave, such as parallel dipoles, it is important to define the incident wave parallel to the element length $E_0 = \hat{y}$. The direction of propagation of the incident wave is also set ($k_0 = -z$ in this case).

Radiation boundaries are useful to simulate open EM problems radiating infinitely far, such as antenna and scattering problems. The radiation boundaries mimics free space and avoids any undesired reflected wave from the finite dimension of the simulated problem. Radiation boundaries are applied at the top and bottom surfaces of the FSS structure, as shown in Figure 3.14c. In addition to applying radiation boundary conditions, HFSS offers a further option 'Reference for FSS', so that the radiation boundary surface becomes the input surface for calculations of reflection/transmission coefficients as well [201]. The other radiation surface automatically becomes the output for such calculations. PML represent another option for radiation boundaries, particularly for oblique angles of incidence. Radiation boundaries must be placed at least $\lambda/4$ away from the radiating surface and are most efficient for normal incident waves, while PML boundaries may be placed anywhere (although it requires meshing) [202]. Another alternative is the Floquet Ports. In this case, HFSS performs a modal decomposition that provides further information, where the fields in the port are represented by a set of Floquet modes, similarly to the modes in waveguide structures, with their respective cut-off frequencies and propagation constants [203]. Master and slave boundaries, on the other hand, enable us to simulated periodic arrays by just modeling the unit cell. The electric field at each point of the slave is forced to be equal in amplitude with a phase difference to each corresponding point in the master. This is a simple implementation to the Floquet Theorem. Figure 3.14d depicts the boundary assignment in an FSS structure.

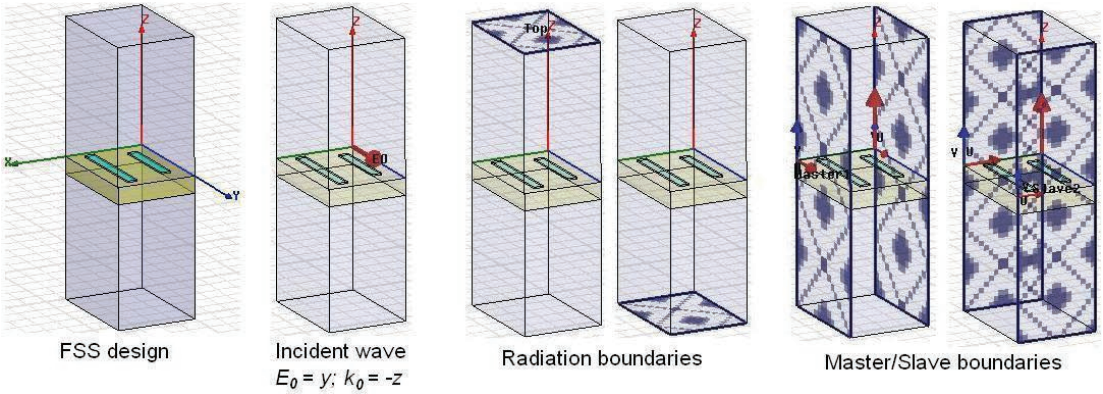

Figure 3.14: *HFSS FSS analysis steps, FSS drawing, incident wave, radiation boundaries, and master/slave boundaries*

As we discussed before, FEM requires meshing the solution region in order to calculate the fields in the different elements. HFSS generates an initial mesh according to the different surfaces of the EM problem. It further refines the mesh at the ports and subsequently compute the fields in the structure at the solution frequency. The mesh in regions of the problem with high errors are further refined iteratively until the solution converges or the maximum number of iterations is reached. It is important to highlight when doing frequency sweeps that HFSS only refines the mesh at the solution frequency and calculates the rest of the frequencies with the same mesh. Thus, the solution frequency must be set equal to the higher frequency of interest. Figure 3.15 shows an example of the mesh generated for a perturbed FSS on a dielectric.

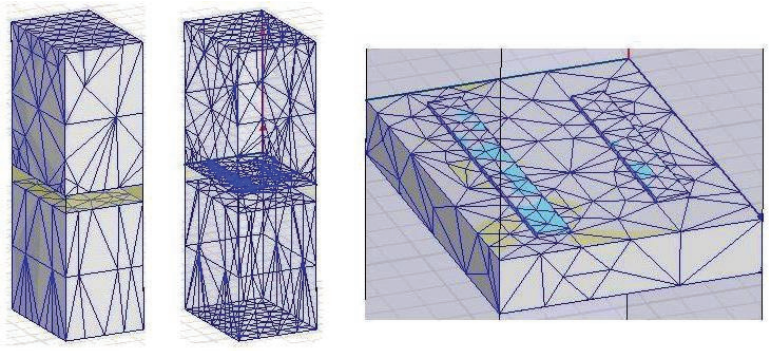

Figure 3.15: *Example of mesh of an FSS in HFSS*

HFSS provides a wide range of materials for the design of our EM structure, including dielectric and metals. For metallic components, various boundaries might

be selected. Perfect E boundaries rendered the selected metallic component in a perfectly conducting surface ($\sigma = \infty$). This is useful for simulating lossless FSS. However, imperfect conductors with finite conductivity can be set by selecting Finite Conductivity boundaries. At this boundaries, the condition shown in (3.254)-(3.255) is employed. When this option is selected, HFSS does not compute the field inside the material. Thus, this boundary is only valid for good conductors, i.e. metal thickness greater than the skin depth at the frequency of interest. If the thickness is in the range of the skin depth, another boundary must be used, namely layered impedance [201]. Surface roughness may be also included when applying Finite Conductivity boundary. It is also important to comment that frequency dependence can be set in the properties of the materials. This is of paramount importance when dispersive material are used.

3.4 Fabrication Process

3.4.1 General considerations

The fabrication of FSS operating at THz frequencies requires microfabrication equipment and materials compatible with the processes/chemicals involved during the fabrication. In this section we develop a fabrication scheme for the prototyping of THz FSS on a thin dielectric substrate. There are fundamental constraints/requirements that must be taking into account when developing the fabrication process. These requirements concern mainly the dielectric substrate material and its thickness, and the metal used for the FSS elements.

a) *Materials consideration*

The thickness of the dielectric substrate must be kept thick enough so as to provide mechanical integrity for the entire device, and it must be minimized in order to reduce dielectric losses and dispersion as much as possible, and avoid the appearance of secondary resonances due to the dielectric (this is investigated in Chapter 5). The thickness employed in the fabricated prototypes throughout the thesis will be around $1.7\mu m$, which is well below the operation wavelength ($\approx 15\mu m$), and strong enough to be free-standing on a thicker hollowed substrate.

The material of the substrate must be as transparent as possible and exhibit acceptable

absorption at the window of frequencies of interest. The frequency of operation and the amount of losses permitted are related to the particular application of the FSS. For instance, FSS as filters for thermal conversion systems would require very low absorption and focus on the near-IR (from 1 to $10\mu m$). In this thesis, the frequency of operation will be between 3THz and 30THz, and the absorption is not an issue as long as it is not extremely high. The frequency range restriction is determined in the higher limit (30THz) by the minimal size feature which we are able to pattern using optical lithography with equipment at the SMC, and is set to $1\mu m$ approximately. The lower limit is fixed by the minimum frequency that we can measure using the FT-IR equipment available (3THz). In addition, the material used as a substrate must be compatible and chemically insensitive to common microfabrication processes and chemicals involved.

Silicon (Si) substrates exhibit excessive losses at mid/far-IR. In order to reduce free carrier loss, high resistivity silicon (HRS) can be employed. HRS has been used successfully in the (sub) mm-wave region [118] and exhibits average transparency $(50-60\%)$ in most of the THz regime [204, 205]. However, the transmittance of HRS wafers decrease significantly in the THz region 5-30THz [204,205]. On the other hand, polymer materials, such as polyimide (PI), have shown good transparency at these frequencies [13]. Besides, PI can be spun readily onto silicon wafers and its thickness can be controlled easily, which is important due to the influence of the substrate on the FSS performance [1]. Moreover, PI is a good candidate for curved FSS/metamaterials [206] and multilayered FSS [207] (as interlayer between FSS). PI is therefore chosen as the supporting material, particularly PI2525 from HDMicroSystems.

The metal used for the FSS elements is Aluminum (Al), which has high conductivity (low ohmic losses), it is easily deposited, readily available and cheap.

b) *Aimed prototype*

The idea is to construct an FSS on a thin substrate as shown in Figure 3.16a. However, since the thin dielectric substrate has a thickness of $1.7\mu m$, we need a further thick substrate to provide mechanical strength, as shown in Figure 3.16b. The thick substrate must be hollowed under the FSS in order not to interfere with the propagation of electromagnetic waves and deteriorate the FSS characteristics. Therefore, the final prototype will consist of an FSS on a free-standing PI membrane placed on a hollowed

thick Silicon (Si) substrate.

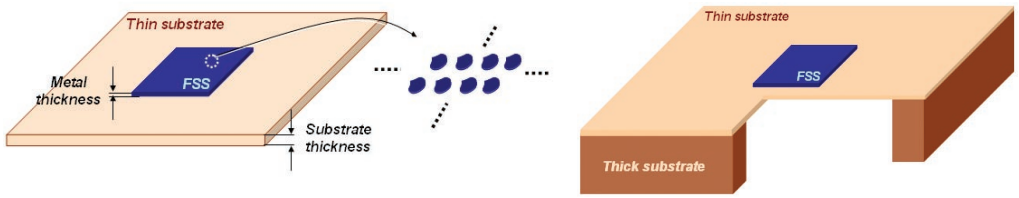

(a) Ideal FSS on thin substrate

(b) Real FSS on thin substrate and hollowed thick substrate

Figure 3.16: *FSS on a thin substrate(a), supported by a hollowed thicker substrate (b)*

c) *Fabrication process*

The general idea for the fabrication of the structure shown in Figure 3.16b is described next. The starting point is a Si wafer onto which a thin PI layer is spin-coated, thin film Al deposited and patterned with the FSS geometry. After this, we need to etch the Si under the PI, obtaining the final patterned FSS on the free-standing PI membrane supported by a thick hollowed Si substrate. There are several options for the deposition, pattern and etch steps, as explained in Chapter 2. There are also incompatibilities between the material used and the processes available. FSS elements made of Al are incompatible with wet etching such as KOH etching. Such technique for deep etching the Si thick substrate is then not used. Instead, dry etching based on the Bosch process in ICP equipment is used. Yet another problem arises when using the Bosch process due to the use of O_2 in the Si etching recipe. The problem of using O_2 is that it attacks PI (and polymers in general), so we need to add a protection layer under the PI membrane to stop the deep etching before it reaches the PI layer. The protection layer consists of a SiO_2 film. After the deep-etch is finished, the SiO_2 protection layer is wet etched with an etchant which does not attack either Al or PI. The detailed fabrication flow and a bird-view scheme of the final device are shown in Figure 3.17 and 3.18, respectively.

In the following subsections, each step is described separately and in more details.

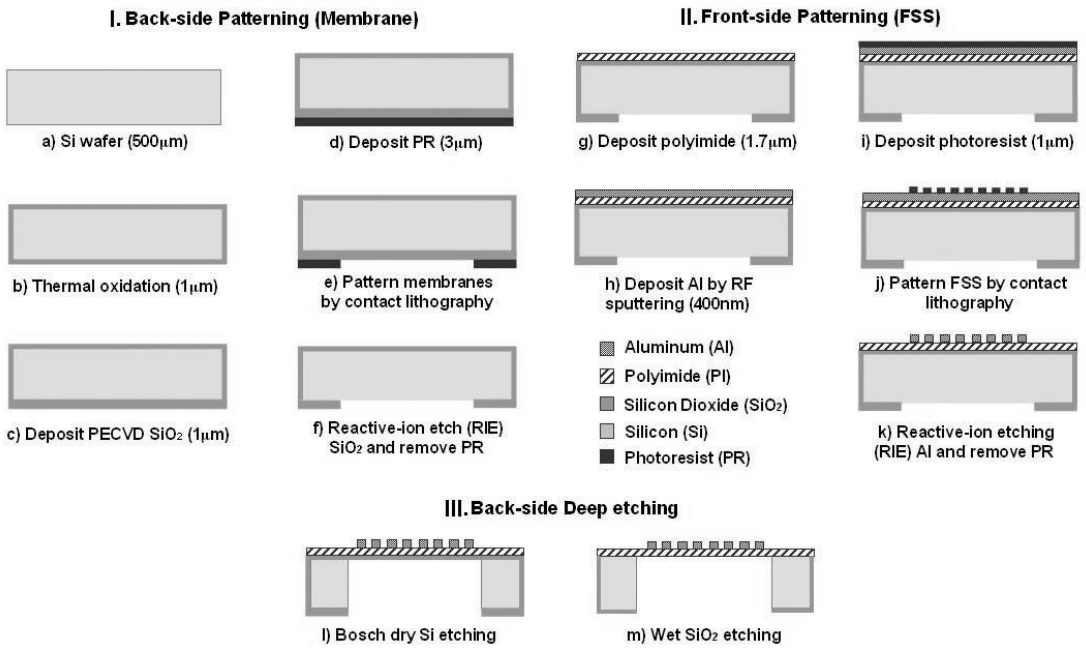

Figure 3.17: *Fabrication process develop in this thesis for the fabrication of THz FSS*

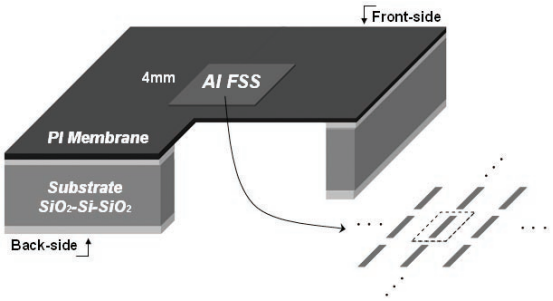

Figure 3.18: *Bird view of FSS*

3.4.2 SiO_2-Si-SiO_2 substrate

For the fabrication of FSS on freestanding PI membranes, $100mm$ diameter double-side polished sacrificial Si wafers are employed as rigid substrate for mechanical strength during and after processing. $1\mu m$ of silicon dioxide SiO_2 is thermally grown at both sides of the wafer in a furnace using the recipe shown in Table 3.6a. An additional $1\mu m$ SiO_2 was deposited on the back side of the wafer using PECVD with the recipe shown in Table 3.6b. On the front side of the wafer, the thermal oxide acts as a stop layer during the deep etching step and protects the following PI membrane from being damaged. Only thermal oxide was employed on this side of the wafer in order to enhance the flatness of the following PI layer. On the back side of the wafer, a thicker oxide layer is

employed as a mask during the deep Si etching step. Inspection of the thickness of the deposited oxide using Nanospec was carried out to confirm the deposition thickness.

(a) LPCVD oxide (thermal)

Gases	N_2
T^a	1100°C
Oxid. rate	$1\mu m$/2.5hrs

(b) PECVD

Pressure	900mTorr
Gases	N_2 392sccm (25%)
	N_2O 1420sccm (25%)
	SiH_4 10sccm (25%)
Power	30W
$T^a(^\circ C)$	300°C (platten)
	250°C (showerhead)
Dep. rate	33nm/min

Table 3.6: *Recipes for thermal and PECVD oxide employed for the fabrication of the SiO_2-Si-SiO_2 substrate*

3.4.3 Patterning process

After the SiO_2-Si-SiO_2 substrate is prepared, the back side of the wafer is processed. Positive photoresist SPR 220.7 from MicroChem Corp. was spun in the manual spinner of Figure 2.15. in two steps, namely $30sec$ at $700r.p.m.$ and $1min$ at $4000r.p.m.$, in order to obtain a $6\mu m$ thick layer. Prior to the photoresist spin-coating, the wafer was exposed to HMDS to promote the adhesion of the photoresist, as explained in Chapter 2. Due to the thickness of the resist, the wafer with the photoresist is pre-baked for $2min$ at $90^\circ C$, and a further $2min$ at $110^\circ C$. After, in order to avoid the wafer to stick to the mask during lithography, the wafer is immersed in developer MF-26A from MicroChem Corp. during $1min$, rinsed with DI water and dried with a N_2 gun. The wafer is then loaded (proximity and spacer) into the optical lithography equipment (KarlSuss of Figure 2.18) and exposed for $45sec$ through a chrome mask containing the membrane patterns, as shown in Figure 3.19a. After exposure, the wafer is developed using the same MF-26A developer during $2min$, rinsed, dried, and post-bake at $110^\circ C$ during $2min$. The pattern in the photoresist is then transferred to the oxide layer (Figure 3.19b) by dry etching in RIE equipment (Plasmatherm from Oxford Labs. or JLS) using either recipe shown in Table 3.7.

(a) Plasmatherm		(b) JLS	
Pressure	72mTorr	Pressure	20mTorr
Gases	CF_4 60sccm	Gases	CHF_3 17.7sccm
	H_2 10sccm		Ar 20.1sccm
Power	750W	Power	750W (200V bias)
Etch rate	33nm/min	Etch rate	50nm/min

Table 3.7: *Recipes for RIE oxide etching using Plasmatherm and JLS*

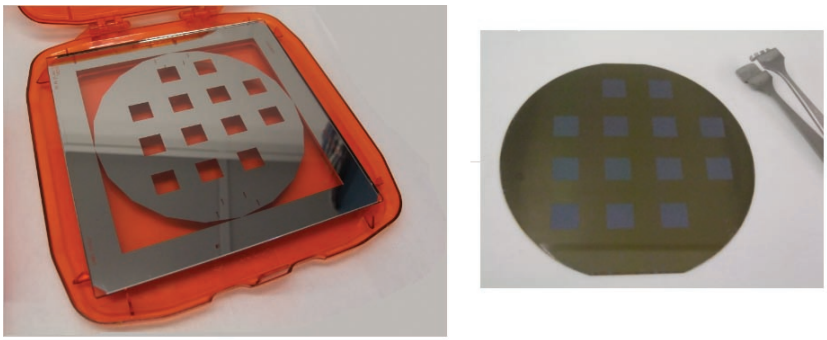

a) b)

Figure 3.19: *Chrome mask containing the membrane patterns and patterned oxide*

Subsequently, the front side of the wafer is processed. Liquid form PI (PI2525 from MicroChemicals) is spun onto the wafer in two steps. First, a polyimide primer consisting of 2% solution of VM361 from MicroChemicals in DI water is laid onto the wafer during $20sec$ and spun at $2500r.p.m.$ during $1min$. Second, the viscous PI is spun during $30sec$ at 700r.p.m. and a further $1min$ at $4000r.p.m.$ in order to obtained a $1.7\mu m$ thick film. The spun PI is then thermally cured at 200^oC during $30min$ in order to achieve the desired mechanical, thermal, and electrical properties. Afterwards, RF sputtering is used to deposit a $300nm$ Al thin film. Positive photoresist SPR-350 is spun onto the wafer (previously exposed to HMDS for $10min$) at $4500r.p.m.$ during $1min$ in order to obtain a very thin resist layer of approximately $1\mu m$ thickness. This is important for achieving high resolution in optical lithography as shown in equation (2.23) in the previous chapter. The exposure, through the mask shown in Figure 3.20a, and developing times for such thin resists are 6sec and $1min$, respectively. It is important to mention that when very small features ($\approx 1\mu m$) are targeted, excesive developing of the resist may lead to pealing off the thin resist patterns. The pattern in the photoresist is then transferred to the Al layer (Figure 3.20b-c) by using RIE etching

with the recipe shown in Table 3.8. The maximum error for patterning features above $1\mu m$ is less than $0.2\mu m$. Thus, the corners in very small rectangular features (around $1\mu m$) can be slightly rounded, as shown in Figure 3.20.

Pressure	100mTorr
Gases	$SiCl_4$ 37sccm
	Ar 14.5sccm
Power	60W
Etch rate	25nm/min

Table 3.8: *Recipes for RIE etching of Al*

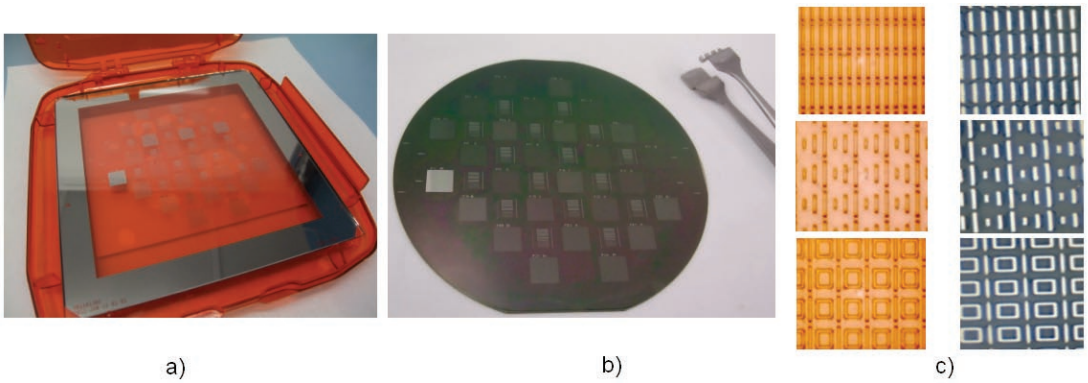

Figure 3.20: *a) Cr mask of FSS patterns, b) patterned wafer and c) zoom in patterned FSS before (left) and after (right) etching*

3.4.4 Deep-etching step

After patterning both sides of the wafer, the substrate is ready for the deep etching step. The process selected was the $DRIE$ Bosch process consisting of alternative etch and passivation steps. During the passivation step, C_4F_8-based plasma is employed to deposit conformally a thin polymer layer. During the etch step, the plasma is switched to SF_6/O_2 and the plate is DC biased giving rise to ion bombardment onto the surface of the wafer. The polymer parallel to the surface of the wafer is removed much faster than the polymer deposited on the walls, so that a directional etching of the silicon is achieved. The actual recipe of the Bosch process used is described in Table 3.9.

(a) Etch step		(b) Passivation step	
Time	13sec	Time	7sec
Pressure	94mTorr	Pressure	94mTorr
He flow	40sccm, 9.9Torr	He flow	40sccm, 9.9Torr
	20mTorr/min Max He leak		20mTorr/min Max He leak
Gases	SF_6 130sccm	Gases	C_4F_8 143sccm
	O_2 13sccm	Power	600W (coil)
Power	600W (coil)		0W (platen)
	15W (platen)	Etch rate	0nm/min
Etch rate	$1.5\mu m/min$		

Table 3.9: *Etching and passivation steps in DRIE Bosch process*

After the Si is removed, a freestanding $SiO_2 - PI$ layer is obtained, as shown in Figure 3.21.

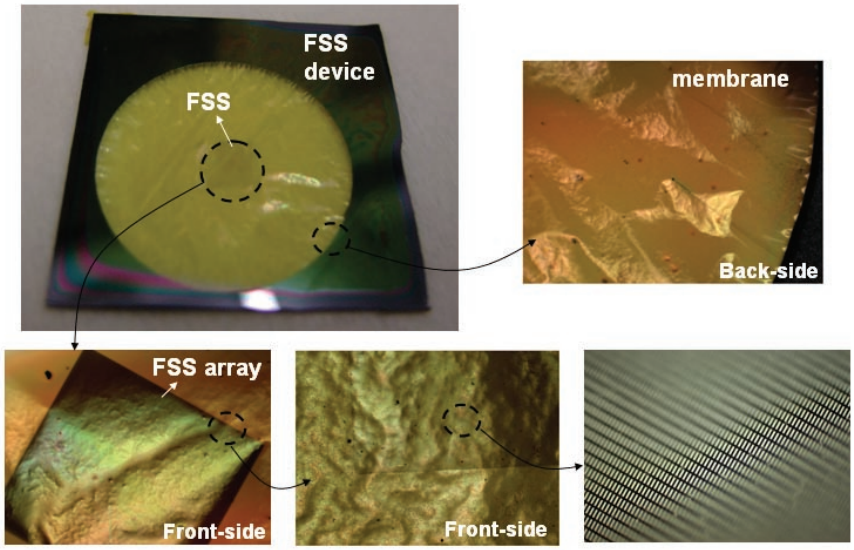

Figure 3.21: *Patterned FSS on rough PI-SiO_2 membrane after DRIE etching*

Since SiO_2 exhibits low transparency at far/mid-IR, and the $SiO_2 - PI$ layer exhibits undesired roughness due to mechanical stress between both materials, a solution of 50% ammonium fluoride, NH_4F, and 50% acetic acid, HAc, is employed to wet etch the SiO_2, resulting in the final freestanding PI layer, as shown in Figure 3.22.

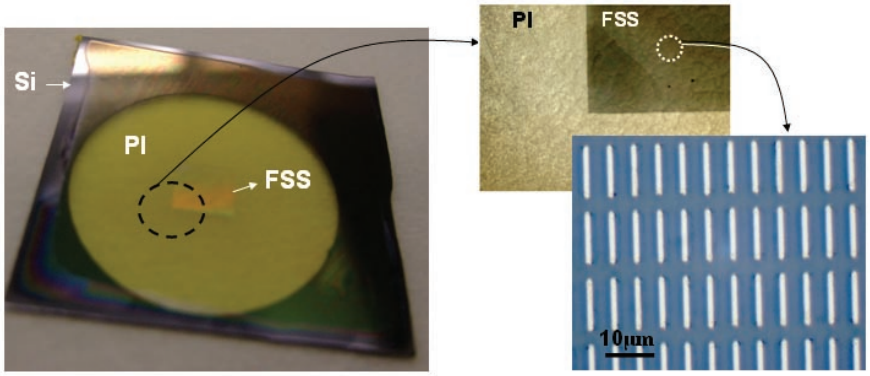

Figure 3.22: *Flat membrane*

A double reaction takes place when the oxide layer is in contact to the aquaseous solution, as follows:

$$NH_4F + HAc \rightarrow \text{HF+NH}_4Ac \text{ (dissolved in water)}$$
$$HF + SiO_2 \rightarrow \text{SF}_4 \text{ (volatile)} + H_2O$$

The etch rate of thermal oxide using this etchant is found to be approximately $50nm$ at room temperature, as shown in Figure 3.23. Increasing the T^a lead to a higher etch rate, although it also affect PI and Al more readily.

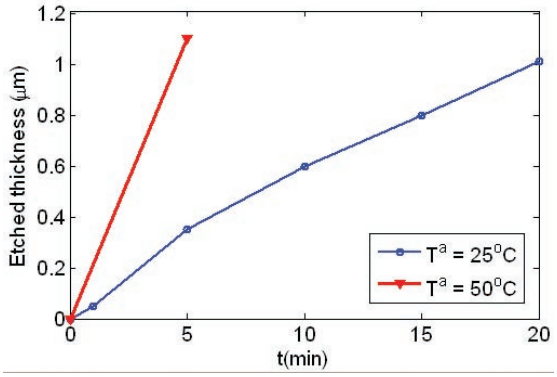

Figure 3.23: *Study on the oxide etch-rate for ammonium fluoride and acetic acid*

3.5 Measurement Scheme: FTIR equipment and set-up

Two FTIR equipment are used for the measurements of prototyped FSS in this thesis, namely a Perkin Elmer Spectrum 100FT-IR from the University of Murcia (Spain) and a Bruker IFS 120HR from the Science and Technology Facilities Council (STFC) at Oxford (U.K.). The Perkin Elmer FTIR is cheaper and easier to use, while the Bruker FTIR is a more expensive and accurate tool. In this section, detailed information about both equipments, and the measurement procedure for the characterization of FSS is given.

I. Perkin Elmer FTIR

The characteristics of the Perkin Elmer Spectrum 100FTIR are shown in Table 3.10. The available beam-splitter (KBr) and detector (DGTS) define the lowest measurable wavenumber at 250cm^{-1}, that is a wavelength of 40μm, and a frequency of 7.5THz. This entails a limit in the maximum size of the FSS geometry in order to exhibit a resonance in a frequency higher than 7.5THz. Only FSS with a resonance higher than 7.5THz can be measured with this FTIR. Although the resolution is not high for detecting very narrow peaks, it is more than enough for the measurement of broadband FSS resonances.

Beam-splitter	KBr
IR detector	DGTS
Range	250-4000cm^{-1}
Resolution	4cm^{-1} (0.25cm retardation)

Table 3.10: *Perkin Elmer FTIR characteristics*

The following two steps are carried out for the measurement of FSS arrays. First, a metallic sheet with an aperture of size equal to the size of the FSS array area is used to obtain the background measurement that defines the conditions in which the FSS are measured. By doing so, the diameter of the IR beam is reduced to match the FSS array area. This is necessary to ensure that all the energy is transmitted from the IR source through the FSS array area to the detector. Second, as shown in Figure 3.24, the FSS spectrum is subsequently obtained by placing the FSS after the metallic aperture. The transmission parameter (S_{21}) is computed by dividing the sample measurement by the background one.

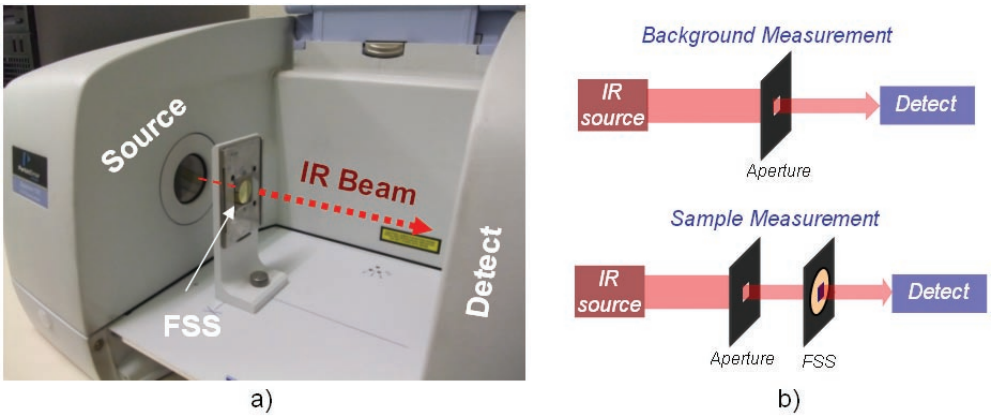

Figure 3.24: *a) Set-up for measuring FSS with the Perkin Elmer FTIR (University of Murcia, Spain), and b) measuring scheme*

II. Bruker FTIR

The Bruker FTIR, which characteristics and schematic are shown in Figure 3.25, exhibits further capabilities.

Beam-splitter	Mylar
	KBr/Ge
IR detector	far-IR DTGS
	mid-IR MCT
Range	100-600cm^{-1} (DGTS)
	500-4000cm^{-1} (MCT)
Resolution	up to 0.001cm^{-1}

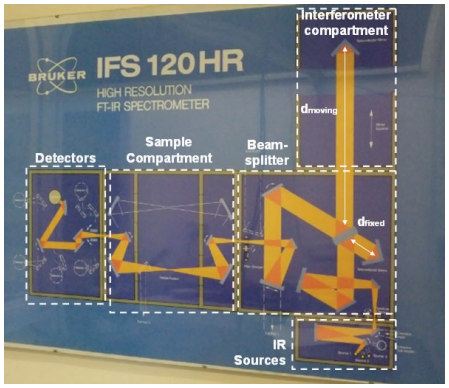

Figure 3.25: *Schematic of Bruker 120HR (STFC, Oxford)*

Far-IR and mid-IR measurements are possible by using DTGS and MCT detectors, respectively. The detectors and beam-splitters frequency windows are shown in Figure 3.26. The MCT/KBr detector/beam-splitter combination can only measure from 500cm^{-1} (15THz), while the DGTS/Mylar combination exhibits a measuring window from 100 to 600cm^{-1} (3-18THz) and, therefore, is more suitable for the FSS studied in this thesis. The absorption bands in 600cm^{-1} and 700cm^{-1} are due to the Mylar substrate.

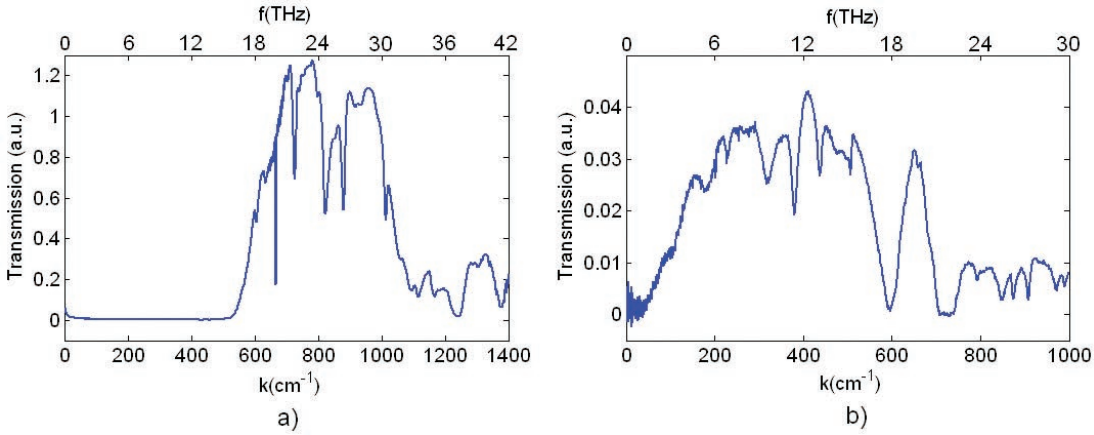

Figure 3.26: *Measurement frequency range using a) MCT detector and KBr-Ge beam-splitter, b) DGTS detector and Mylar beam-splitter*

A larger interferometer compartment, shown in Figure 3.27, also provides higher resolution (larger displacement of the scan mirror), at the expense of slower measurements. The sample and interferometer compartments are vacuum-pumped, so that undesired absorption peaks from the atmosphere gases are avoided.

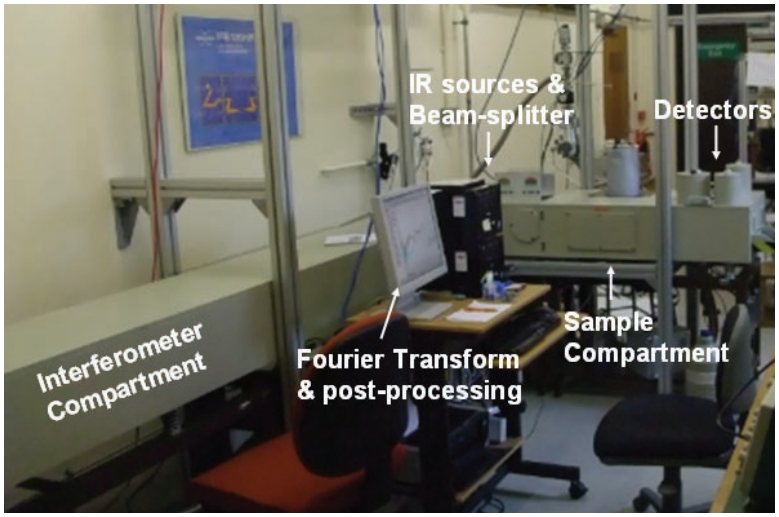

Figure 3.27: *General view of Bruker 120HR (STFC, Oxford)*

The procedure for the measurement of the spectral signature of FSS is the same as the one described for the Perkin Elmer FTIR, and a picture of the set-up is shown in Figure 3.28.

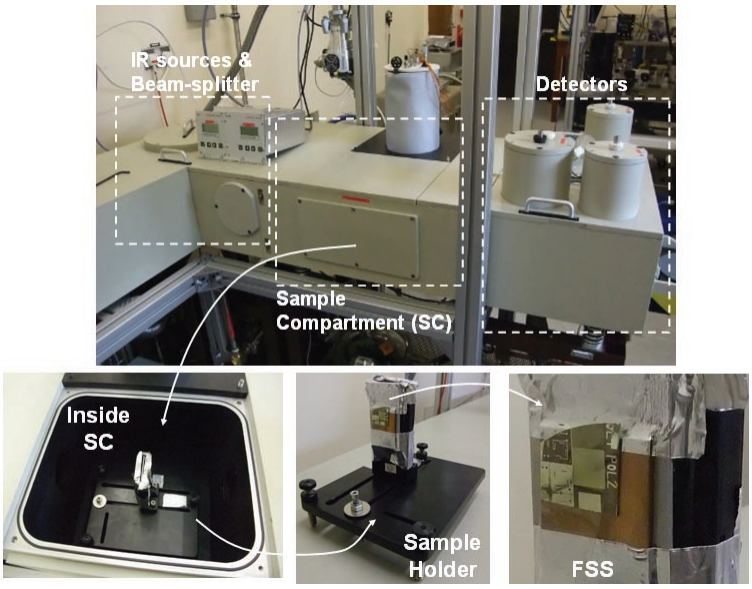

Figure 3.28: *Close look at sample, detectors and beam-splitter compartments of Bruker 120HR (STFC, Oxford)*

The interferograms are obtained in each scan (position of the scan mirror) as shown in Figure 3.29a. Then, the Fourier Transform is performed with all the interferograms, as explained in Chapter 2, giving rise to the spectrum shown in Figure 3.29b for a background measurement (blue line), i.e. without FSS, and a sample measurement (red line), i.e. with an FSS. The transmission in percentage or in terms of the S_{21} parameter is obtained by dividing the sample measurement by the background measurement, as shown in Figure 3.29c-e for different number of scans.

The number of scans carried out in each measurement determines the signal-to-noise (S/N) ratio, and the time cost. Measurements using 100, 50 and 10 scans are shown in Figure 3.29c-e, where the S/N ratio decreases as the number of scans decreases. The higher the number of scans we carried out, however, the slower the measurement. Each scan takes about 12sec, so that a total of 100scans take as much as 20min.

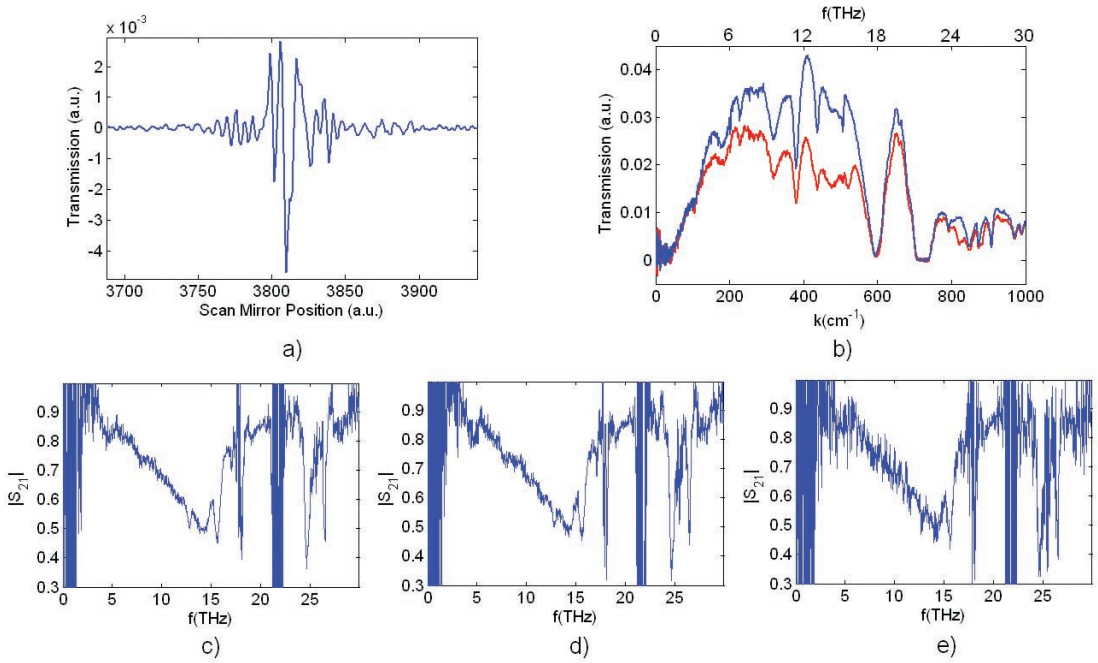

Figure 3.29: *a) Interferogram, b) energy at the detector without and with FSS, c)-e) transmission (energy with/energy without) of the FSS for 100, 50, and 10scans, respectively*

3.6 Conclusions

This chapter has presented a thorough and accurate description of the analytical tools, fabrication process and measurement set-ups developed in this thesis for the analysis, fabrication and measurement of FSS at THz frequencies. A brief remark on the main contributions of this chapter are outlined as follows:

- Physical insight on the Floquet theory for analyzing periodic structures and assessment on the validity of various ohmic losses for its application to lossy periodic arrays

The first part of the chapter has been devoted to description of Floquet theory and method of moments applied to analyzing periodic structures. In addition, the dissipation factors in FSS have been addressed. Theoretical and experimental models of ohmic losses were investigated and their range of applicability deduced in the THz regime of the EM spectrum. It has been found that metals can be accurately modeled by the intrinsic impedance of lossy dielectrics up to approximately 30THz, from which

frequency models derived from measured data must be used.

- Development of a fabrication scheme for manufacturing micron-scale FSS operating at THz

A fabrication scheme using standard microfabrication techniques has been developed for the prototyping of THz FSS. A silicon wafer has been employed as a hard substrate for the processing and it has been etched at the end of the process using dry DRIE, leading to a thin polyimide substrate supporting the FSS. The advantages of our approach, in contrast to other suggested approaches such as KOH wet etching, are avoiding damage in the thin membrane when removing protective masks/layers in wet etching, and materials incompatibilities. For instance, Al bond pads are rapidly attacked and damaged by KOH, causing problems in fabricating other potential configurations such as the electronically tunable FSS proposed in chapter 7.

- Development of a measurement scheme for testing FSS operating at THz

In the last part of the chapter, a far-infrared measurement scheme, using an FTIR spectrometer, has been set up for testing prototyped THz FSS. Detailed description of the measurement procedure and the key components in the measurement system has been presented. In addition, a comparison between the technology offered by a PerkinElmer and a Bruker FTIR has been given.

Chapter 4
Energy storage, dissipation and quality factors of FSS at THz frequencies

4.1 Introduction

In the microwave regime, metallic elements in FSS can be assumed to be nearly perfect conductors (without ohmic losses), because dielectric losses are the main source of thermal power dissipation [8]. However, ohmic losses become more significant at higher frequencies and can no longer be neglected [6,8]. The study of the FSS response in relation to power dissipation is motivated by the increased ohmic loss of conductors at THz [6, 8]. In addition, unique issues arising at higher frequencies (e.g. THz regime) in conducting mediums, such as conductivity dispersion, surface roughness and anomalous skin depth effect, might contribute to add further ohmic losses and must be considered [65, 193, 195–197, 208].

In resonant systems, such as FSS, thermal power dissipation is described conveniently by the quality factor, which represents the ratio of the reactive power stored over power dissipated. Normally, the quality factor definition is restricted in the literature to the loaded quality factor, and it is estimated through the far-field response by the inverse of the fractional -3dB bandwidth [7]. However, it is well-known from filter theory that in any resonator we can identify three quality factors [209], namely, unloaded (resonator in isolation), loaded (coupled to the in/out ports) and external (regarding only the coupling with the environment). The extraction of the unloaded quality factor has not been done before because at lower frequencies the external quality factor can be accurately approximated by the loaded quality factor (unloaded quality factor becomes infinite in the lossless case). Generally, the quality factor can be defined as the ratio of the power stored over the power loss by the resonator. A rigorous study of the reactive power stored in the vicinity of FSS would typically require detailed investigation of the

near fields and has yet to appear. As a result, a study of the quality factors of FSS is still missing from the literature. The importance in extracting the unloaded quality factor from the stored and dissipated power lies in the ability to access the intrinsic quality factor of the resonator, which would facilitate better analysis and design of FSS in near-field enhancement and sensing applications. The sensors capability is proportional to the amplitude of the near-fields, so that FSS with higher near-fields will lead to higher sensitivity devices [11, 12, 169, 171, 210, 211].

This chapter presents a thorough study of the quality factors of FSS at THz frequencies and, therefore, deals also with the problem of analyzing the stored power in the near-field (electric and magnetic) of the FSS and the dissipated power due to the flow of the current through the metallic FSS elements with finite conductivity. In the first part of the chapter (section 4.2), the influence of metal properties, such as conductivity, thickness and surface roughness, in the FSS performance is addressed. In section 4.3, a novel FSS circuital model that includes ohmic losses is introduced and validated by means of rigorous full-wave Method of Moments (MoM), which formulation was described in detail in chapter 3, and by Ansoft Designer which includes both dielectric and metallic losses. The definition of the different quality factors as well as their underlying physics are also presented. In section 4.4, we describe the techniques to obtain the stored power in the near-fields of the FSS by two means, namely, the volume integral of the FSS near-fields and the equivalent circuit. We carry out a parametric study (varying the FSS dimensions) of the power stored for a dipole-based FSS as well as the dissipated power and quality factors. We concentrate our study on free-standing FSS in order to focus on the power dissipated solely by the ohmic losses arising from the finite conductivity of the metallic strips. Subtrate effects will be analyzed in detail in the next chapter.

4.2 Material considerations

In this section, the effects of the materials employed in free-standing FSS are addressed. First, ohmic and dielectric losses are compared throughout the EM spectrum in order to observe the dominant source of thermal dissipation in each frequency region. Subsequently, the effects of thickness of the metallic elements and surface roughness on the performance of free-standing FSS is investigated at THz

frequencies.

4.2.1 Metal and dielectric dissipation

The properties of homogeneous materials as a function of the complex dielectric permittivity were addressed in Chapter 2. In this subsection, we analyze the sources of losses in FSS arrays, namely dielectric and ohmic losses. Losses are commonly quantify by the absorption coefficient $Abs = 1 - S_{11}^2 - S_{21}^2$ as the power which is neither reflected S_{11} nor transmitted S_{21}. The absorption coefficient is, then, also defined as the ratio between the dissipated and incident power $P_{dis} = Abs \cdot P_{inc}$. Before the onset of grating lobes, these losses represent solely thermal losses, that is, heat dissipation due to the currents flowing through real (non-perfect) conductors and EM waves propagating through lossy dielectrics. The heat dissipation of an EM waves propagating inside a dielectric (dielectric losses) depends on the dielectric volume considered (e.g. the unit cell (u.c.) size (d_x, d_y) and the thickness of the dielectric t_{die}, $V = d_x \cdot d_y \cdot t_{die}$), the loss tangent ($tan\delta = \epsilon''/\epsilon'$), the frequency f and the amplitude of incident wave $|E|$, as shown in the electrical power dissipation density $P_d(W/m^3)$ expression [190]:

$$P_{u.c.} = \iiint_V P_d \, dV = P_d \cdot d_x \cdot d_y \cdot t_die \; ; \quad P_d = 2\pi f \epsilon_0 \underbrace{\epsilon' tan\delta}_{\epsilon''} E^2 \tag{4.1}$$

The higher the loss tangent $tan\delta$, the more energy can be absorbed in the material, and the higher the permittivity ϵ', the more the material can be polarized (also allowing more heat dissipation).

On the other hand, power dissipated due to Joule effect in lossy metals depends on the current $J(r)$ flowing through the metal (area S) and the surface resistance R_s of the metal, as shown in the following expression [190]:

$$P_{u.c.} = R_s \iint_S J(r)^2 \, dS \tag{4.2}$$

The value of the surface resistance can be obtained using any of the models shown in section 2.2.2, while the current excited in the FSS elements may be obtained through the FSS formulation in section 2.1.2.

In order to analyze the type of losses which dominates in different regions of the

spectrum, Figure 4.1 shows the absorption of an FSS resonating from a few GHz up to tens of THz. The dimensions of the FSS are $L = 9X$, $w = 1X$, $d_x = 8X$, $d_y = 11X$ (μm) supported by a dielectric with permittivity $\epsilon_r = 3.5$ and thickness $t_{die} = 1.7X$, where X is a scaling factor to scale the dimensions of the FSS and its substrate to resonate at the different regions of the spectrum (e.g. $X = 1$, 10, 100, 10^3, 10^4 lead to FSS resonating at $11.5THz$, $1.15THz$, $115GHz$, $11.5GHz$, and $1.15GHz$, respectively). The green and red lines show the absorption only due to dielectric (loss tangent $tan\delta = 0.008$) or ohmic losses (conductivity $\sigma = 3.8 \cdot 10^6 S/m$ and lossy dielectric metal model used), respectively. For simplicity, in this general study we assumed that $tan\delta$ is constant over the entire range of frequencies. The solid blue line represents both ohmic and dielectric losses present simultaneously. The dotted blue line shows the addition of ohmic and dielectric losses obtained separately. The green area shows the absorption area limited by dielectric-only losses with loss tangent equal to 0.01 (higher limit) and 0.005 (lower limit). The blue area shows the absorption due to both dielectric and ohmic losses with the same limits as the green area.

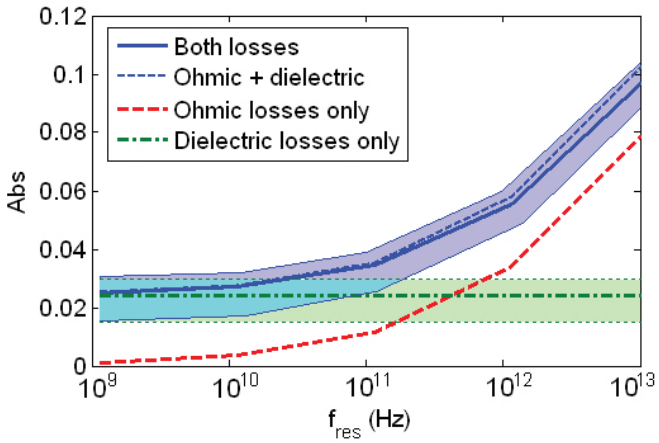

Figure 4.1: *Absorption of FSS at resonance for various frequency regions. The green and red lines show the absorption due to dielectric-only and ohmic-only losses, respectively. The solid blue line represents both ohmic and dielectric losses present simultaneously. The dotted blue line shows the addition of ohmic and dielectric losses obtained separately.*

As we can see, the ohmic losses are increasing with frequency, as a consequence of an increase in the surface resistance (inversely proportional to frequency, as previously demonstrated in (3.239) and (3.231)). This will be seen in next section 4.2.2 in more detail. On the other hand, the dielectric losses remain constant throughout

the whole spectrum. Although the dissipated power in the dielectric is proportional to the frequency (multiplicative factor X), the thickness of the dielectric was scaled down (dividing factor X) together with the unit cell dimensions. Thus, the increase of frequency ($f_{1THz} = 1000 f_{1GHz}$) is compensated by the decrease in the dielectric thickness ($t_{die}^{1THz} = 1/1000 t_{die}^{1GHz}$), and the absorption in the dielectric remains constant.

The figure above shows clearly the dominant source of losses within each region of the EM spectrum. At lower frequencies (a few GHz), the metal can be approximated to be nearly perfect conductor and, therefore, ohmic losses are negligible. Dielectric losses represent the main source of losses at this frequency regime. However, as the resonant frequency increases (FSS size is reduced), the metallic elements can no longer be approximated as perfect conductors, introducing increasing ohmic losses. For the case shown in Figure 4.1., ohmic losses become as important as dielectric losses at 412GHz for the values of conductivity, loss tangent and dielectric permittivity defined above. From that frequency onwards, the main source of losses become the metallic components. For this reason, throughout this chapter, only ohmic losses are taken into account in free-standing FSS, leaving the effects of substrates for the next chapter.

4.2.2 Metal thickness

The thickness of the FSS elements is normally much greater than the skin depth, and therefore it is usually neglected. In this section, we investigate the influence of the metal thickness in the FSS performance. For doing that, we first analyze the surface resistance in a metallic sheet of various thickness. Figure 4.2 shows the variation of the surface resistance of Al films versus frequency for different thicknesses using (3.238). The skin depth is calculated using (3.237) and its value at different frequencies is also shown. For comparison, the R_s for 25nm thick Al layer is also plotted using the skin depth in (3.231), confirming its inaccuracy of as we move towards higher frequencies.

The surface impedance is shown to vary with the metal thickness as expected. At frequencies in which the metal thickness is lower than the skin depth, the surface impedance increases with the metal thickness. At frequencies in which the metal thickness is higher than the skin depth, the surface impedance is constant and does not depend on the metal thickness. For instance, at $1THz$ ($\delta = 80nm$) the surface resistance decreases from 1.05Ω for $t = 25nm$ to 0.32Ω for $t = 100nm$, and then it

remains constant at 0.32Ω for greater thickness ($t = 200nm$, $400nm$, and $1\mu m$).

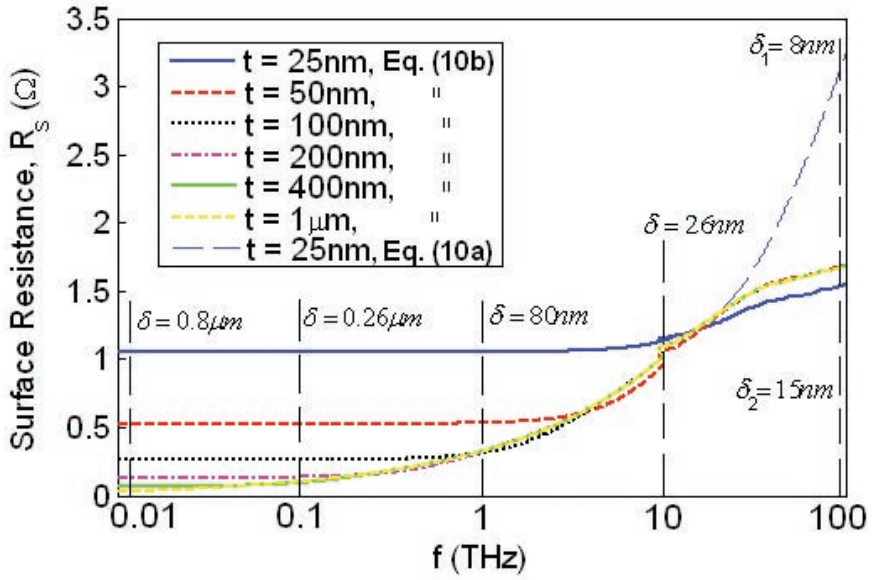

Figure 4.2: *Surface resistance (3.238) versus frequency of Al films with varying thickness. The skin depth at each frequency is also shown for reference. At 100THz two values of skin depth are shown δ_1 and δ_2 corresponding to (3.231) and (3.237), respectively.*

In order to investigate the influence of the metal thickness in the FSS response, the reflection coefficient of a dipole-based FSS ($d_x = 8\mu m$, $d_y = 11\mu m$, $L = 9\mu m$, and $w = 1\mu m$) is obtained for variable metal thicknesses in the range $t = [150nm, 1\mu m]$, which is well above the skin depth and below the operation wavelength. Commercial HFSS software based on Finite Element Method (FEM) is employed in this study. Surface impedance boundaries were used, where Z_s was calculated from the classical model (3.240), which agrees well with the values of Z_s obtained from real optical properties at the frequencies simulated. The fields inside the structure are not solved, but this is a reasonable approximation because the thickness of the conductor is much larger than the skin depth at the frequencies simulated.

As shown in Figure 4.3 and 4.4, the thickness of the elements has, in fact, an effect in the FSS performance even for thicknesses well above the skin depth ($\delta = 19.8nm$ for Al at 17THz). For thin films with thickness well below the operation wavelength ($t < 0.1\lambda$), three effects can be identified, namely, a drop in the absorption, a shift

towards higher frequencies and an increase of the bandwidth. These results are in agreement with similar results previously reported in [7, 212, 213]. As it will be shown in section 4.4 when studying the induced currents in FSS, the changes in absorption and bandwidth in FSS are strongly related to changes in the amplitude and distribution of the induced currents in the FSS elements.

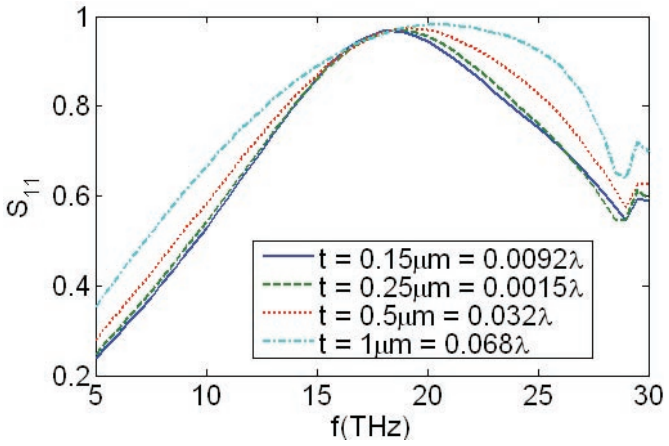

Figure 4.3: *Reflection parameter for variable thickness of the elements (thin metal).*

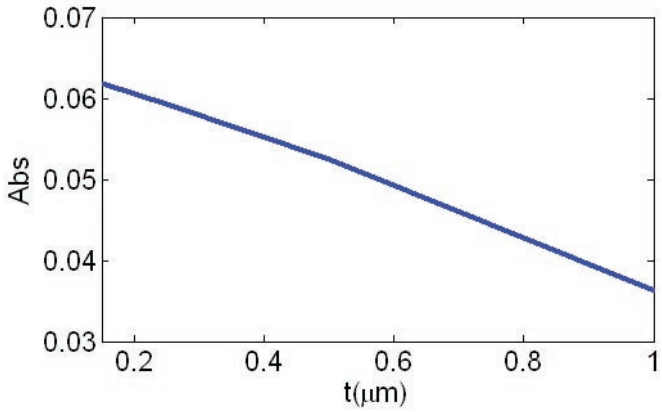

Figure 4.4: *Absorption for variable thickness of the elements (thin metal).*

For even thicker FSS (thickness approaching $\lambda/2$) the fundamental FSS resonance vanishes and a sharp transmission emerges as a consequence of guided propagation through the walls of the elements. Figure 4.5 shows the transmission characteristics of very thick FSS and Figure 4.6 depicts the guiding effect of thick FSS as compared to the resonant behavior of thin FSS.

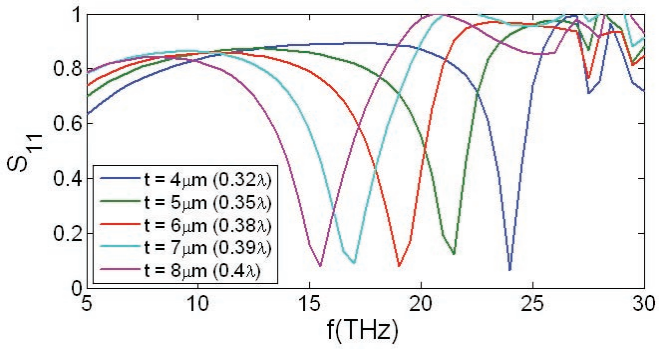

Figure 4.5: *Reflection parameter for variable thickness of the elements (thick FSS).*

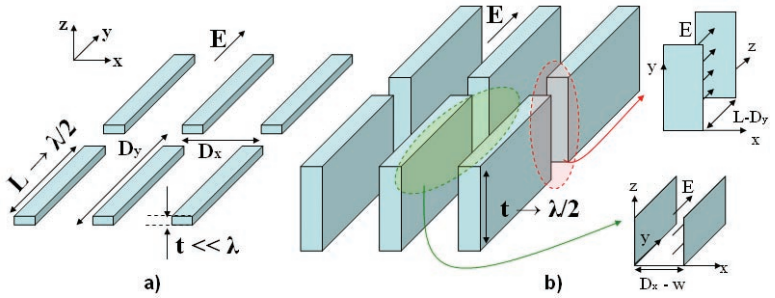

Figure 4.6: *Representation of a) thin FSS, and b) thick FSS*

4.2.3 Surface roughness and native oxide

At frequencies where the wavelength is in the order of centimeters or millimeters, any metallic film can be considered to be perfectly flat, since small defects (a few, tens or even hundreds of nanometers) in the morphology of the surface do not have any noticeable effects on the value of the conductivity. However, at higher frequencies surface roughness is responsible for scattering and coupling to surface plasmons, which gives rise to an additional drop in the power reflectance [195]. As noted before, this drop in the reflectance corresponds to an increase in the surface resistance, which is produced by a decrease in the conductivity. The conductivity of a rough surface can be approximated by the following expression [208]:

$$\sigma_{rs} = \frac{\sigma_{fs}}{1 + e^{-\frac{\delta}{2s}}} \tag{4.3}$$

where σ_{rs} and σ_{fs} denote the conductivity with a rough and a flat surface, respectively, s represents the surface roughness, and δ is the skin depth.

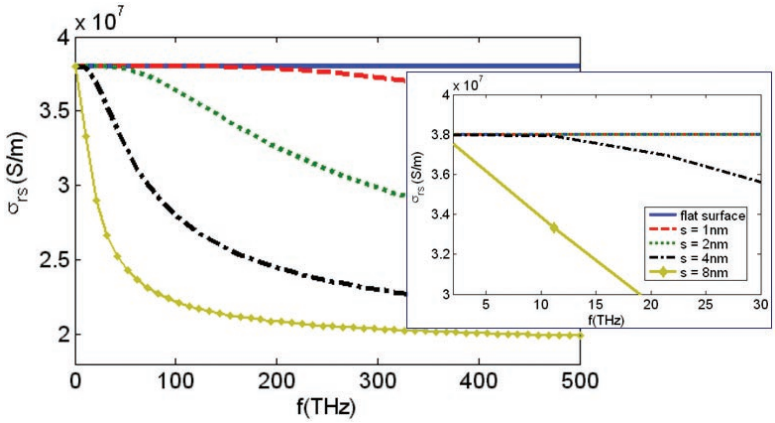

Figure 4.7: *Conductivity of Al films ($\sigma_{bulk} = 3.8 \cdot 10^7 S/m$) versus frequency for variable surface roughness. The inset zooms in the FIR frequency regime.*

As shown in Figure 4.7, in the near infrared, optical frequencies and beyond, the effect is significant even for a surface roughness as low as $2nm$. However, in the far IR there is not a great impact for low surface roughness. For instance, the conductivity at 15THz with a surface roughness of $5.5nm$ decreases just 5% from that of a flat surface. The same roughness gives rise to a 35% decrease in the conductivity at 150THz. Current metal deposition methods are capable of exhibiting surface roughness in pure Al thin films as low as $1.2nm$ [214] and $5.5nm$ [215]. Further Al alloys can improve surface roughness even below $1nm$ [216].

In addition to the surface roughness, Al thin-films (like other metals) are susceptible to the formation of a very thin layer of native oxide (Al_2O_3 for Al), even in high vacuum conditions, that could reduce the power reflectance of the Al thin-film [195], thus increasing the surface resistance. The thickness of the native oxide varies depending of the conditions that the thin-film has been exposed to. For instance, evaporated films exposed to normal atmosphere conditions may exhibit between 2 and $5.5nm$ thick native oxide, while this thickness can be fairly increased in moist environments [195]. However, at far/mid-IR the native oxide thickness is much lower than the wavelength of operation and its influence is negligible. Moreover, Al_2O_3 is highly transparent at wavelengths from $6\mu m$ to $180nm$, and, therefore, has little influence in the near-IR, optics and, part of ultraviolet [195].

4.3 Resonant Characteristics of FSS

4.3.1 Circuital model of FSS

In isolation, a resonator can be typically modeled by an RLC circuit [7] and can be characterized by its resonant frequency and its reactance slope parameter [217]. The inductance L and capacitance C are associated with the power stored in the magnetic and electric field respectively, while the resistance R is associated with dissipated power in the form of thermal losses or absorption. In the absence of thermal dissipation, the equivalent impedance of the resonator is purely reactive.

When in free space and illuminated by a plane wave, an FSS consisting of isolated perfect metallic conductors (capacitive screen) can be represented by the circuit of Figure 4.8, where $Z_a = R_a + jX_a$ represents the terminal impedance of the array [1].

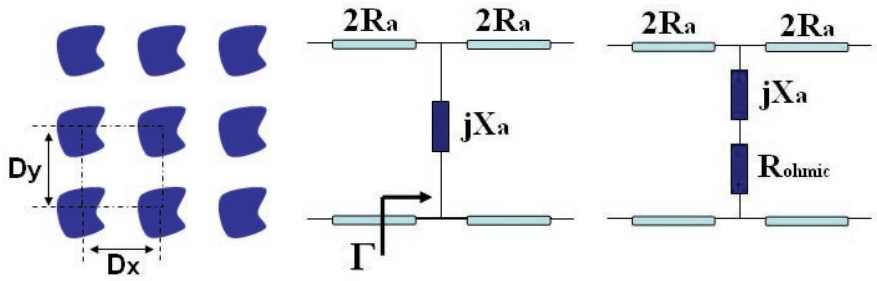

(a) (b) (c)

Figure 4.8: *Equivalent circuits of capacitive FSS with arbitrary shape (a), in the lossless (b) and the lossy case (c)*

The shunt reactance X_a is associated with the reactive energy stored in the FSS. The resistance R_a is associated with the power exchange between the FSS and free space, and is not related to dissipated losses. In the vicinity of the resonance, it is a good approximation to assume that the real and imaginary parts of the terminal impedance are constant and linear with frequency, respectively [1].

$$Z_a(f) = R_a(f) + jX_a(f) \begin{cases} R_a(f) \approx R_a \\ X_a(f) \propto (f - f_{res}) \end{cases} \tag{4.4}$$

The terminal reactance can therefore be expressed as:

$$X_a = Af - B = Af - Af_{res} = A(f - f_{res}) \tag{4.5}$$

where A (Ω/Hz) and B (Ω) are constants employed to describe the variation of X_a with frequency. Using the expressions given in [1], full-wave calculations are used to accurately obtain R_a and X_a.

The reactance slope parameter for a series-type resonator is defined as [217]:

$$x = \frac{\omega_{res}}{2} \frac{dX_a}{d\omega}\bigg|_{\omega_{res}} \tag{4.6}$$

and to a good approximation can be assumed to be constant in the vicinity of the resonance ($x(f) \approx x$).

In the presence of finite conductivity, a further resistance R_{ohmic} is introduced to model the power dissipated on the metallic elements. The equivalent circuit of Fig 4.8b [1] is then modified to that of Figure 4.8c. In this case, R_{ohmic} is calculated by matching the S-parameter as obtained by the lossy circuital model and the full-wave results using Ansoft Designer. The usefulness of obtaining these electrical parameters (Z_a and R_{ohminc}) lies in the fact that they provide a valuable insight on the operation of the FSS under investigation. The equivalent circuit does no intend to substitute the full-wave analysis, but to complement it.

The performance characteristics of the FSS with ohmic losses can be then modeled through this equivalent circuit. The reflection, transmission and the absorption coefficients can be readily obtained as follows:

$$S_{11} = \frac{-R_a}{Z_a + R_{ohmic}} = \frac{-R_a}{(R_a + R_{ohmic}) + jX_a} = \frac{-1}{(1+\kappa) + j\left(\frac{X_a}{R_a}\right)} \tag{4.7}$$

$$S_{21} = \frac{R_{ohmic} + jX_a}{Z_a + R_{ohmic}} = \frac{R_{ohmic} + jX_a}{(R_a + R_{ohmic}) + jX_a} = \frac{\kappa + j\left(\frac{X_a}{R_a}\right)}{(1+\kappa) + j\left(\frac{X_a}{R_a}\right)} \tag{4.8}$$

$$A = 1 - S_{11}^2 - S_{21}^2 = \frac{2R_aR_{ohmic}}{(R_a + R_{ohmic})^2 + X_a^2} = \frac{2\kappa}{(1+\kappa)^2 + \left(\frac{X_a}{R_a}\right)^2} \tag{4.9}$$

where $\kappa = R_{ohmic}/R_a$. At resonance ($X_a = 0$) the transmission, reflection and absorption coefficients become:

$$S_{11}\Big|_{res} = \frac{-1}{(1+\kappa)} \tag{4.10}$$

$$S_{21}\Big|_{res} = \frac{\kappa}{(1+\kappa)} = \frac{1}{\left(1+\frac{1}{\kappa}\right)} \tag{4.11}$$

$$A\Big|_{res} = \frac{2\kappa}{(1+\kappa)^2} \tag{4.12}$$

The lossless case is represented by $\kappa = 0$. Resonance occurs when the reactive impedance is zero ($X_a = 0$), and in the absence of ohmic loss ($R_{ohmic} = 0$), the reflection coefficient becomes -1. However, in the presence of losses ($R_{ohmic} > 0$), the ratio $\kappa = R_{ohmic}/R_a$ is responsible for decreasing the amplitude of the reflection coefficient, allowing some transmitted wave and giving rise to power dissipated. Normally, R_{ohmic} is much lower than R_a and the factor κ remains small (e.g. $\kappa < 0.1$). Figure 4.9 depicts the FSS behavior in terms of the circuital model.

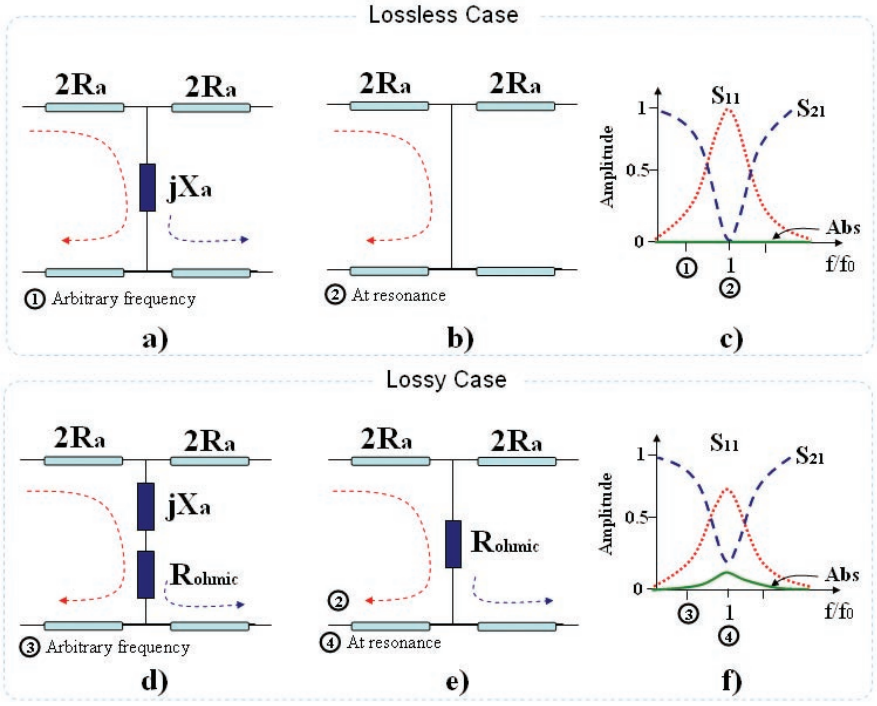

Figure 4.9: *Equivalent circuit and far-field response of FSS a-c) in the absence of losses and d-f) in the presence of losses.*

In addition to the effects of ohmic loss previously commented (reduce reflection amplitude, allow certain tramitted energy and thermal dissipation), the introduction of R_{ohmic} also broadens the bandwidth of the reflection/transmission curves around the resonant frequency. The 3dB bandwidth (Δf) of a capacitive FSS can be defined by the lower and upper cut-off frequencies in which the reflection coefficient drops 3dB from the maximum reflected amplitude (at resonance):

$$\Delta f = f_{-3dB}^{upper} - f_{-3dB}^{lower} \approx 2(f_{-3dB}^{upper} - f_{res}) \approx 2(f_{res} - f_{-3dB}^{lower}) \tag{4.13}$$

The reflection coefficient in the cut-off frequencies can be obtained as follows:

$$S_{11}\Big|_{-3dB} = \frac{S_{11}^{max}\Big|_{fres}}{\sqrt{2}} = \frac{-R_a}{(R_a + R_{ohmic}) + jX_a\Big|_{-3dB}} \tag{4.14}$$

And using the linear approximation of (4.5) for the terminal reactance:

$$\frac{S_{11}^{max}\Big|_{fres}}{\sqrt{2}} = \frac{-R_a}{(R_a + R_{ohmic}) + jA(f_{-3dB} - f_{res})} = \frac{-R_a}{(R_a + R_{ohmic}) + jA\Delta f/2} \tag{4.15}$$

Taking the module and squaring each side of the equation:

$$\frac{(S_{11}^{max})^2}{2} = \frac{R_a^2}{(R_a + R_{ohmic})^2 + \Delta f^2 A^2/4} \tag{4.16}$$

We can then calculate the bandwidth by isolating it to one side of the equation:

$$\Delta f^2 = \left(\frac{R_a^2}{\frac{(S_{11}^{max})^2}{2}} - (R_a + R_{ohmic})^2 \right) \frac{1}{A^2/4} \tag{4.17}$$

Since $S_{11}^{max} = \frac{1}{(1+\kappa)}$ and $\kappa = R_{ohmic}/R_a$, the bandwidth can be simplify as:

$$\Delta f^2 = \frac{\left(\frac{2}{\frac{1}{(1+\kappa)^2}} - (1+\kappa)^2 \right) R_a^2}{A^2/4} = \frac{(1+\kappa)^2 R_a^2}{A^2/4} \tag{4.18}$$

In the absence of losses, $\kappa = 0$, so then the bandwidth is directly proportional to the terminal resistance R_a and inversely proportional to the slope of the terminal reactance

A, as shown in the next equation:

$$\Delta f_{lossless} = \sqrt{\Delta f^2} = \frac{2R_a}{A} \tag{4.19}$$

On the other hand, the bandwidth in the presence of losses also depends on the ratio κ, and can be expressed as a function of the bandwidth in the lossless case, as follows:

$$\Delta f_{lossy} = (1+\kappa)\frac{2R_a}{A} = (1+\kappa)\Delta f_{lossless} \tag{4.20}$$

where $(1+\kappa) > 1$, so then in the presence of losses the bandwidth is always increased for a fixed geometry as compared to the same geometry in the absence of losses.

Therefore, various effects on the far-field response are directly related to the introduction of R_{ohmic}, which models the finite conductivity of the FSS metallic elements. The amplitude of the reflected wave is decreased ($|S_{11}| < 1$), the transmitted wave and absorption are no longer null ($|S_{21}| > 0$ and $Abs > 0$), and the resonance is broadened ($\Delta f_{lossy} > \Delta f_{lossless}$). These effects are summarize in Table 4.1.

	Lossless	Lossy
Reflection $S_{11}\big\|_{res}$	-1	$\frac{-1}{1+\kappa}$
Transmission $S_{21}\big\|_{res}$	0	$\frac{1}{1+\frac{1}{\kappa}}$
Absorption $Abs\big\|_{res}$	0	$\frac{2\kappa}{(1+\kappa)^2}$
Bandwidth Δf	$\frac{2R_a}{A}$	$(1+\kappa)\frac{2R_a}{A}$

Table 4.1: *Summary of the performance of capacitive FSS*

4.3.2 Definitions of the quality factors in FSS

An important parameter of a resonant circuit is the quality factor [209]. The quality factor Q is defined generally as the ratio between the average reactive energy stored

over the power loss in a resonator in a period of oscillation:

$$Q = \omega \frac{Energy_{stored}}{Energy_{loss}\ per\ second} = \omega \frac{W_m + W_e}{P_{loss}} \tag{4.21}$$

Since at resonance both the electric W_e and magnetic W_m energy stored are equal, the quality factor can be expressed as follows:

$$Q = \omega \frac{W_m + W_e}{P_{loss}} = \omega_{res} \frac{2W_m}{P_{loss}} = \omega_{res} \frac{2W_e}{P_{loss}} \tag{4.22}$$

Equation (4.21) is a general expressions for the quality factor. However, we can identify different definitions of quality factor depending on whether we consider intrinsic properties of the resonator or coupled to the environment, and in the presence or absence of losses. In this sense, we can identify three quality factors, namely, unloaded, loaded and external. The unloaded quality factor Q_U refers to the resonator in isolation. In the definition of Q_U, the power loss is therefore associated solely with the power loss by thermal dissipation.

When the resonator is coupled to its environment, some energy transfer occurs between the resonator and the input/output ports (power radiated). With reference to the resonator, this is additional to any thermal dissipation and is experienced as increased power loss. In this case, the loaded quality factor Q_L is employed, which is also defined by (4.21) but now the power loss also includes the power coupled to the input and output port (or power radiated) [217]. It can be demonstrated that within certain approximations, the loaded quality factor Q_L can be obtained from the 3dB fractional bandwidth [209, 217].

$$Q_L = \frac{f_{res}}{\Delta f_{-3dB}} \tag{4.23}$$

The loaded and unloaded quality factors are related through the external quality factor Q_e by [209]:

$$\frac{1}{Q_L} = \frac{1}{Q_U} + \frac{1}{Q_e} \tag{4.24}$$

The external quality factor Q_e is associated solely with the apparent loss due to the power transfer to the input/output as well as the power stored in the resonator.

- Lossless case:

In the absence of ohmic losses ($R_{ohmic} = 0$), the unloaded quality factor Q_U is infinite

since no dissipation takes place ($P_{loss} = 0$):

$$Q_U = \omega_{res} \frac{2W_e}{\underbrace{P_{loss}}_{0}} = \infty \tag{4.25}$$

Therefore, the overall or loaded quality factor Q_L is directly equal to the external quality factor Q_e, as obtained by using (4.24)-(4.25).

$$Q_L = Q_e, \quad if \;\; \kappa = 0 \tag{4.26}$$

The loaded quality factor can be obtained in different ways and all of them lead to the same expression. We can use the definition (4.21), the reactance slope parameter x (4.6) and the far-field response (4.23).

a) Q_L *calculation from the definition*

In order to obtain the loaded quality factor $Q_L = Q_e$ through the definition, the energy stored needs to be calculated. We can do so by means of a volume integration of the electric/magnetic near-fields. This will be done in a later section 4.4.1. Instead, here we will use the circuital formulation and estimate the values of the equivalent inductance L and capacitance C associated to the terminal reactance X_a. Since X_a was assumed linear (4.4)-(4.5), it can be approximated to the linear component of the Taylor expansion of the reactance of a LC series circuit (4.27), which is an acceptable approximation near the resonance, as shown in Figure 4.13.

$$\begin{aligned} X_a(f)\Big|_{LC\ series} &= \omega L - \frac{1}{\omega C} = \frac{\omega^2 LC - 1}{\omega C} \\ X_a(f)\Big|_{Taylor} &= X_a(f_{res}) + \underbrace{\frac{X_a'(f_{res})}{1!}(f - f_{res})}_{linear\ component} + \frac{X_a''(f_{res})}{2!}(f - f_{res})^2 + \cdots \\ \rightarrow X_a(f)\Big|_{Linear\ approx.} &= \frac{4\pi^2 f_{res}^2 LC + 1}{4\pi^2 f_{res}^2 C}(f - f_{res}) \end{aligned} \tag{4.27}$$

By solving (4.5) and (4.27), and known the resonant frequency of a LC series circuit

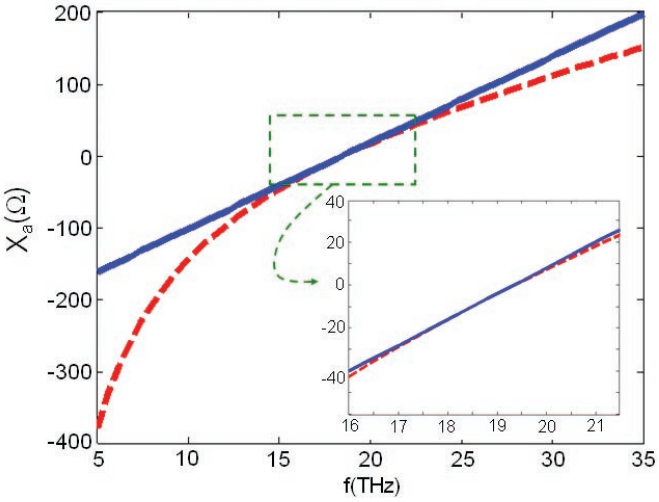

Figure 4.10: *Terminal reactance calculated with MoM formulation (blue straight line) and Taylor approximation (red dashed line) for FSS resonant at 18.5THz.*

to be $f_{res} = 1/2\pi\sqrt{LC}$, we can obtain the equivalent inductance and capacitance as:

$$C = \frac{1}{A\pi f_{res}^2} \; ; \quad L = \frac{A}{4\pi} \tag{4.28}$$

Thus, the loaded quality factor Q_L in the absence of losses (equal to the external quality factor Q_e) can be obtained from the circuital model as:

$$Q_L = Q_e = \omega_{res} \frac{2W_e}{P_{loss}}\Big|_{\omega=\omega_{res}} = \omega_{res} \frac{2\left(\frac{1}{2}L|I_X|^2\right)}{\left(\frac{1}{2}R_a|I_R|^2\right)}\Big|_{I_X=I_R} = \frac{\omega_{res}L}{R_a} = \frac{1}{\omega_{res}CR_a} \tag{4.29}$$

b) *Q_L calculation through the reactance slope parameter x.*

The loaded quality factor Q_L can also be calculated through the reactance slope parameter using the following expression in [217]:

$$Q_L = \frac{x}{R_a} \tag{4.30}$$

where the reactance slope parameter x can be obtained by means of taking the derivative of the reactance X_a (series LC circuit) [217] and is equal to the inductive (or capacitive) reactance at resonance:

$$x = \frac{\omega_{res}}{2}\frac{\partial X_a}{\partial \omega}\Big|_{\omega_{res}} = \frac{\omega_{res}}{2}\frac{\omega_{res}^2 LC^2 + C}{\omega_{res}^2 C^2} = \frac{\omega_{res}}{2} 2L = \omega_{res}L \tag{4.31}$$

Which is equivalent to the Taylor approximation of the linear component of the reactance of a LC series circuit, described before (4.29). The reactance slope parameter and the external quality factor can therefore be calculated as:

$$x = \omega_{res} L = \frac{A f_{res}}{2} \quad \rightarrow \quad Q_e = \frac{x}{R_a} = \frac{\omega_{res} L}{R_a} = \frac{A f_{res}}{2 R_a} \tag{4.32}$$

c) Q_L *calculation through the far-field expression*.

Yet another way of obtaining Q_L is from the far-field results by the definition of the quality factor in terms of the 3dB bandwidth (4.23) and using (4.19):

$$Q_e = \frac{f_{res}}{\Delta f_{lossless}} = \frac{f_{res}}{2R_a/A} = \frac{A f_{res}}{2 R_a} \tag{4.33}$$

- Lossy case:

In the presence of losses ($R_{ohmic} > 0$), the unloaded quality factor Q_U is no longer infinite and, in turn, the loaded quality factor Q_L is no longer equal to the external quality factor Q_e.

In terms of the equivalent circuit, it can be noticed that the current induced in the shunt FSS is reduced in the presence of the ohmic resistance, as depicted in Figure 4.11. At resonance, the circuital model is shorted in the absence of losses, so that the entire incoming current/wave is reflected. In contrast, in the presence of losses, a current divider is observed so that the incoming current (incident wave) is split into an outgoing current (transmitted wave) and a current flowing through the shunt FSS with ohmic resistance R_{ohmic}, which will cause some thermal absorption and a reflected current/wave.

From the definition (4.21), the loaded quality factor can be expressed as follows:

$$Q_L = \omega_{res} \frac{2W_e}{P_{loss}}\Big|_{\omega=\omega_{res}} = \omega_{res} \frac{2W_e}{P_{rad}^{R_a^{IN}} + P_{rad}^{R_a^{OUT}} + P_{dis}^{R_{ohmic}}}\Big|_{\omega=\omega_{res}} =$$

$$= \frac{\omega_{res} L |I_{FSS}|^2}{\frac{1}{2} 2R_a |I_{IN}|^2 + \frac{1}{2} 2R_a |I_{OUT}|^2 + R_{ohmic} |I_{FSS}|^2} \tag{4.34}$$

Where I_{IN}, I_{OUT} and I_{FSS} represent the currents flowing in the equivalent circuit, as

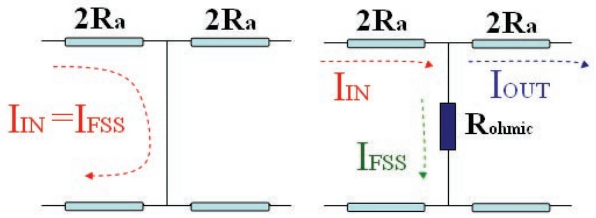

Figure 4.11: *Currents flowing in the equivalent circuit at resonance in a) lossless FSSs and b) lossy FSSs*

shown in (4.35) and Figure 4.11.

$$I_{IN} = I_{OUT} + I_{FSS} \tag{4.35}$$

While in the lossless case the incident wave (I_{IN}) is entirely reflected at resonance by the shunt FSS ($I_{IN} = I_{FSS}$ and $I_{OUT} = 0$), in the presence of R_{ohmic} certain power is transmitted (I_{OUT}), so that the reflected field is no longer equal to the incident field ($I_{FSS} < I_{IN}$, and $I_{OUT} \neq 0$). Using (4.34)-(4.35), the loaded Q-factor can be operated as follows:

$$Q_L = \frac{\omega_{res} L}{R_a \left(\frac{|I_{IN}|^2}{|I_{FSS}|^2} + \frac{|I_{OUT}|^2}{|I_{FSS}|^2} \right) + R_{ohmic}} = \frac{\omega_{res} L}{R_a \Delta I + R_{ohmic}} = \frac{Q_e}{\Delta I + \kappa} \tag{4.36}$$

Where the factor ΔI accounts for the change in the induced currents in the presence of losses, and is near the unity. This can be seen also as a change in the terminal resistance ($R_a^{lossy} = R_a^{lossless} \Delta I$). As explained before, a decrease in the induced current implies an increase in the terminal resistance, and vice versa. If we assume that the currents induced in the dipoles (or the terminal resistance) do not change when we include ohmic losses, which is the same as assuming that the external quality factor do not change when we introduce losses:

$$\Delta I \;\rightarrow\; 1 \;;\left(\frac{|I_{IN}|^2}{|I_{FSS}|^2} \;\rightarrow\; 1,\; \frac{|I_{OUT}|^2}{|I_{FSS}|^2} \;\rightarrow\; 0 \right) \;;\; R_a^{lossless} \rightarrow R_a^{lossy} \tag{4.37}$$

then the loaded quality factor would be expressed as:

$$Q_L = \frac{Q_e}{\Delta I + \kappa}\Big|_{\Delta I = 1} = \frac{Q_e}{1 + \kappa} \tag{4.38}$$

Resulting in the same expression as obtained from the far-field approximation by using (4.20) and (4.23):

$$Q_L = \frac{f_{res}}{\Delta f} = \frac{f_{res}}{\frac{2R_a}{A}(1+\kappa)} = \frac{\omega_{res} L}{R_a(1+\kappa)} = \frac{Q_e}{1+\kappa} \tag{4.39}$$

In any case, the loaded quality factor Q_L is always decreased in the presence of losses, as shown in (4.36).

The unloaded quality factor can be calculated using (4.24):

$$Q_U = \frac{Q_e \cdot Q_L}{Q_e - Q_L} = \frac{Q_e \cdot \frac{Q_e}{\Delta I+\kappa}}{Q_e - \frac{Q_e}{\Delta I+\kappa}} = \frac{Q_e}{(\Delta I - 1)+\kappa} \tag{4.40}$$

Again, assuming that the currents do not change in the presence of losses $(\Delta I \rightarrow 1)$, the unloaded quality factor can be approximated as:

$$Q_U = \frac{Q_e}{\kappa} \tag{4.41}$$

In general, the assumption that the induced currents are equal in the absence and presence of losses may be useful for obtaining Q_L since $\Delta I \approx 1 >> \kappa$. However, this assumption significantly deviates from the exact solution when calculating Q_U since $(\Delta I - 1) \approx \kappa$. Table 4.2 summarizes the quality factor formulation.

	Lossless	Lossy (exact)	Lossy $(approx.\ \Delta I = 1)$
External Q_e		$\frac{x}{R_a} = \frac{\omega_{res} L}{R_a} = \frac{A f_{res}}{2R_a}$	
Loaded Q_L	Q_e	$\frac{Q_e}{\Delta I+\kappa}$	$\frac{Q_e}{1+\kappa}$
Unloaded Q_U	∞	$\frac{Q_e}{(\Delta I-1)+\kappa}$	$\frac{Q_e}{\kappa}$

Table 4.2: *Summary of the quality factors of FSS in the presence and absence of losses*

4.4 Q-factors and powers assessment in free-standing FSS

In the following we proceed to estimate the stored and dissipated power and the quality factors for capacitive FSS at IR. We employ the working example shown in Figure 4.12 consisting of an FSS based on dipoles of length $L = 9\mu m$, width $w = 1\mu m$, and thickness $t = 250nm$ (so that no thickness effects are present). The unit cell length along the y-axis is fixed at $d_y = 11\mu m$. At seen before, the main source of thermal absorption comes from the ohmic losses on the conductors [6, 8]. We therefore concentrate our studies assuming only ohmic losses, that is free-standing FSS.

We commence our investigation by studying the FSS in the absence of ohmic losses. For this case we extract the equivalent circuit parameters and the reactive power stored in the array. Using these results, we proceed to account for the effect of losses on the Q-factor. The study is undertaken initially for periodicity along the x-axis (dx) varying in the region $6\mu m$-$14\mu m$. The effects of variable width w and length L of dipole will also be briefly discussed.

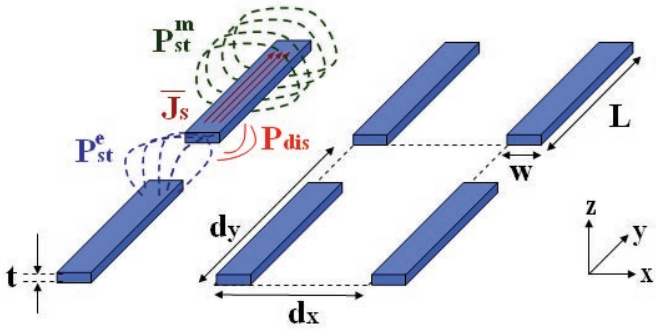

Figure 4.12: *Capacitive FSS based on parallel strip of length L, width w and thickness t. The strips are periodically arranged at a distance d_x and d_y from each other. J_s, P_{dis} and P_{st} represent the surface current density induced in the dipoles, the dissipated power and the stored power (either in the electric or magnetic field), respectively.*

4.4.1 Power stored in FSS (no ohmic losses)

The far-field reflection coefficient of the FSS of Figure 12 under normally incident plane wave as obtained by the full-wave MoM code described in Chapter 3 is shown in Figure 4.13 for three different values of periodicity d_x. For this study, zero ohmic losses are assumed so that the dissipated power P_{dis} is zero. The far-field reflection can also be

predicted by the EC model of Figure 4.8a using (4.7) and the method described in [1], and is superimposed for comparison with MoM results in Figure 4.13.

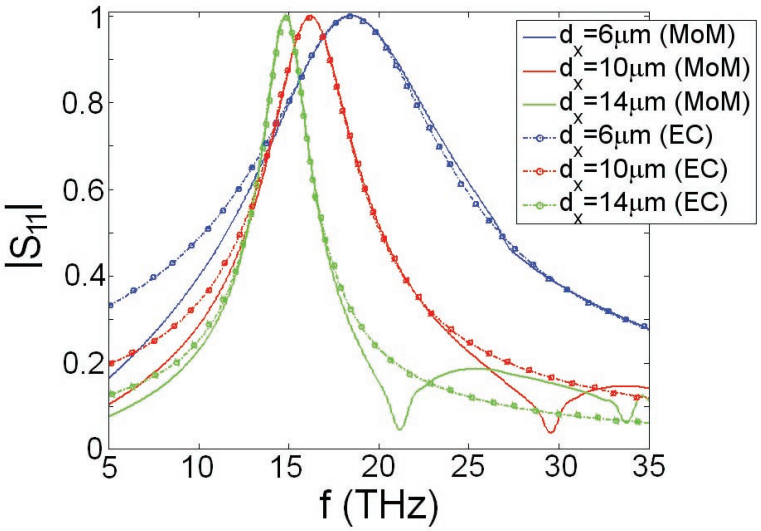

Figure 4.13: *Reflection coefficient of the lossless FSS depicted in Figure 4.12 with dimensions $L = 9\mu m$, $w = 1\mu m$, $d_y = 11\mu m$ and varying d_x as calculated by MoM and EC.*

Good agreement between the MoM and EC results is observed, with the exception of the grating lobes which manifest as dips in the full-wave results. When grating lobes occur, part of the energy is directed in other angles, leading to an apparent power loss at the direction of incidence [1]. Multi-modal behavior occurs when a grating lobe is present and therefore the RLC circuit fails.

The average currents I_{av} excited on the elements as calculated by the full-wave method (4.42) and (3.178) are shown in Figure 4.14. Likewise, the average currents obtained from the EC are superimposed in Figure 4.14. As we can see, the current distribution exhibits a higher amplitude and narrower width for shorter dipoles, while longer dipoles give rise to weaker excitations of the currents (lower amplitude and wider width). Comparing the current distribution with the reflection parameter, it can be easily verified that the way that the incoming wave excite currents in the FSS (depending on its shape) determines the reflection characteristic of the FSS.

Assuming $J(r)$ the surface-current density on the dipole within the unit cell as in

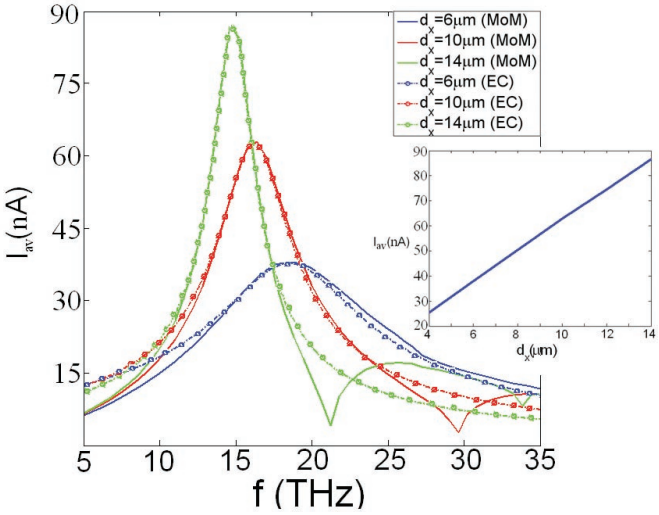

Figure 4.14: *Average current induced in the dipoles in the lossless FSS of Figure 4.13 calculated by MoM and EC various d_x. The inset shows the peak value of the average current induced in the dipoles versus the periodicity.*

(3.178), the averaged current along the dipole is obtained as:

$$I_{av} = \frac{1}{L} \int_{-L/2}^{L/2} \int_{0}^{w} J(r)\, dx\, dy \tag{4.42}$$

The basis functions used to calculate the currents with the code described in Chapter 3 are simple sinusoidal functions along y, while the current density is assumed constant along the width of the dipoles. Five coefficients are employed (c_1, c_2, c_3, c_4, and c_5) to obtain the surface-current density along the length of the dipole. The current density obtained by these means is an effective current density that provides an accurate solution, even for wide dipoles (e.g. patches). However, the current density does vary along the width of the dipole. Ansoft Designer is employed to simulate the currents of the same FSS with width equal to 0.1, 0.5, and $1\mu m$. Ansoft Designer uses sub-domain basis functions and the dipoles is meshed into smaller elements, so that a precise distribution of the currents can be obtained also along the width, as shown in Figure 4.15. As shown in Figure 4.15a, the current exhibit a sinusoidal distribution along the length of the dipole, and tend to flow close to the edges of the dipole. In narrow dipoles, the current distribution along the width is almost constant, while in wide dipoles the current exhibits a minimum in the center of the dipole and a maximum at the edges. The results obtained with the code described in Chapter 3 (using entire domain basis

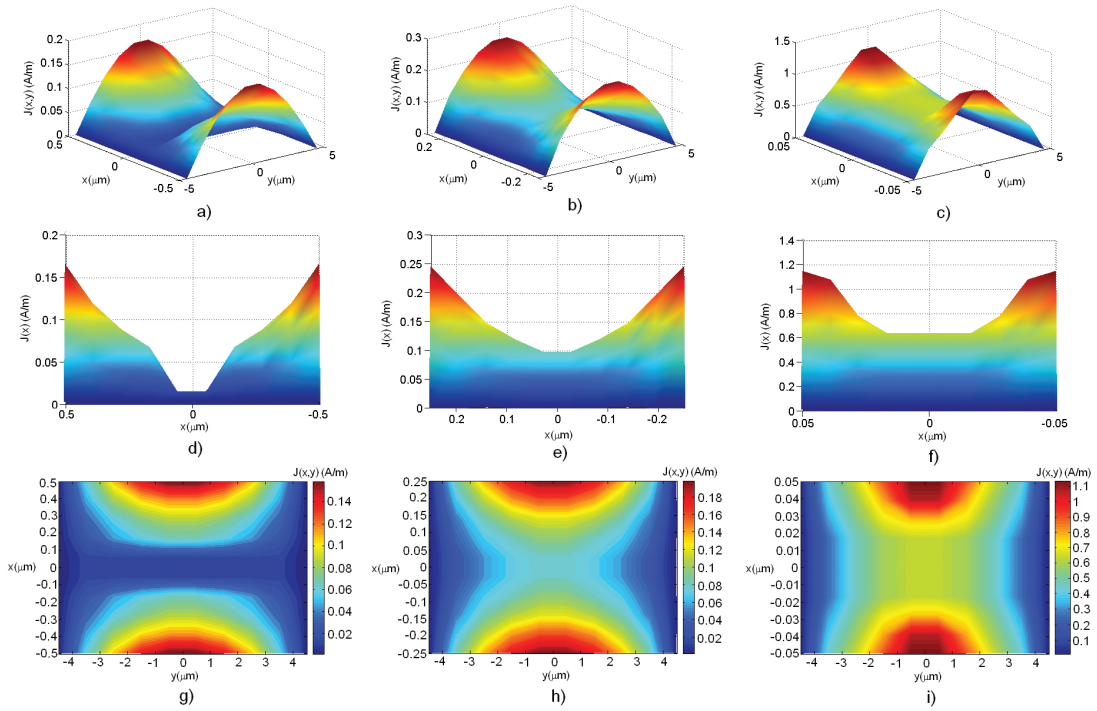

Figure 4.15: *Surface-current densities for lossless FSS with variable width (*$1, 0.5$*, and* $0.1\mu m$*) and dimensions* $L = 9\mu m$*,* $dx = 8\mu m$*,*$dy = 11\mu m$*. a-c) Bird's view, d-f) view along the width, and g-i) top view.*

functions) are accurate as compared to the results obtained with Ansoft Designer (using sub-domain basis functions).

The values of the terminal resistance R_a and reactance slope parameter x can be obtained using the equivalent circuit and are plotted in Figure 4.16 as a function of the periodicity d_x. As observed in Figure 4.14-4.15, the resonant frequency of the array drops with increasing periodicity and tends to approach the $\lambda/2$ resonance of the dipole elements. This is due to the fact that more closely packed dipoles interact more strongly. Hence, the resonance of the dipole elements in the array deviates more from the resonance of the free-standing element for small spacings. In addition, sparser arrays experience a lower load R_a leading to sharper resonant features (stronger currents at resonance and higher loaded quality factors).

Since the reflection coefficient from the FSS at resonance in the lossless case is exactly equal to -1, the power transfered from the FSS to free-space per unit cell is equal to the power incident on each unit cell. The power transfered can be obtained through a

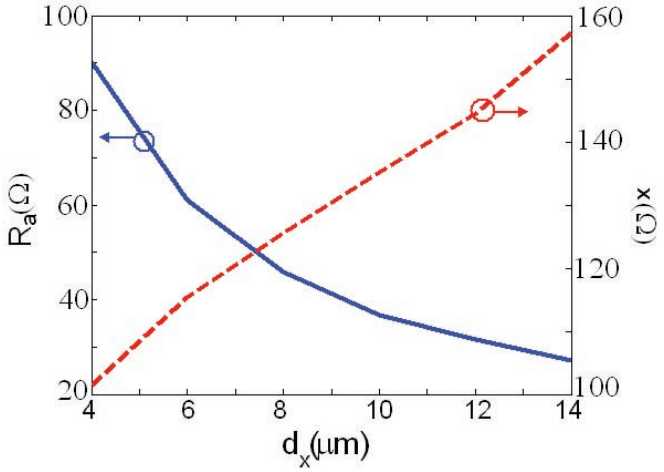

Figure 4.16: *Terminal resistance (left y-axis) and reactance slope parameter (right y-axis) for the FSS of Figure 4.13 and different values of periodicity d_x.*

surface integral of the Poynting vector of the incoming plane-wave along the unit cell:

$$P_{rad} = \frac{1}{2}\oint_A \bar{S}\cdot d\bar{s} = \frac{1}{2}\oint_A \bar{E}\times\bar{H}^*\cdot d\bar{s} = \frac{1}{2\eta}\iint_A \bar{E}\cdot\bar{E}\cdot d\bar{s} \tag{4.43}$$

where the plane of integration is normal to the direction of the incoming wave. For a normally incident plane wave in free space with $1V/m$ y-polarized electric field, the power incident on the FSS unit cell is:

$$P_{rad}(pW) = \frac{|E|^2\,A}{2\eta} = \frac{1(V^2m^{-2})\cdot d_x(\mu m)\cdot d_y(\mu m)}{240\pi(\Omega)} \tag{4.44}$$

The power radiated to free space can also be calculated by the EC as the power consumed on the terminal resistance R_a at resonance:

$$P_{rad} = \frac{1}{2}2R_aI_{av}^2 = R_aI_{av}^2 \tag{4.45}$$

The average reactive power stored in the near field of the FSS can be estimated from the EC as the reactive power stored at the terminal at resonance:

$$P_{st} = xI_{av}^2 \tag{4.46}$$

where I_{av} is the amplitude of the average current excited on the dipole at resonance, as shown in Figure 4.14. The power stored can also be calculated from the volume

integral of the near-fields (evanescent modes) as:

$$P_{st} = f_{res} \cdot \epsilon_0 \iiint_V \left| \bar{E} \cdot \bar{E}^* \right| \, dV \tag{4.47}$$

$$P_{st} = f_{res} \cdot \epsilon_0 \iiint_V \left| \sum_{mpq} R^-_{mpq} \cdot \bar{\kappa}_{mpq} \cdot \Psi_{pq}(\bar{r}) \cdot e^{-j\beta^0_{pq} z} \right| \, dx \, dy \, dz \tag{4.48}$$

where E represents the reactive field in the vicinity of the array at resonance. Assuming operation below the grating-lobe regime, E can be obtained by the MoM formulation as the total contribution of all but the propagating Floquet Space Harmonic. The volume V is defined in the transverse plane by the unit cell dimensions (d_x and d_y) and along the normal of the array it is truncated to at the distance V_z from the array surface where the contribution from the slowest decaying Floquet space harmonic (usually the TE_{00} mode) drops below 1% from its maximum value. In addition, in order to ensure convergence in the near-field estimation, FSH which contribute up to 5% of the TE_{00} mode at the array level have been considered [218]. The truncation of the volume is depicted in Figure 4.17.

The average reactive energy stored in the near field of the FSS unit cell at resonance as well as the power radiated to free space in a unit cell are plotted in Figure 4.18. Both MoM and EC results are shown. The average current and terminal impedance depicted in Figure 4.14 and Figure 4.16, respectively, were utilized in applying (4.45) and (4.46). The agreement observed validates the circuit model. The power radiated by the unit cell at resonance increases linearly with the FSS periodicity in accordance with the unit cell area. The average energy stored increases with the periodicity of the FSS more rapidly than the power radiated, reflecting the sharper resonance characteristics observed in Figure 4.13-4.14.

4.4.2 Power dissipated (ohmic losses)

Taking into consideration the material properties discussed in the previous Chapter 3 (section 3.3) and this Chapter 4 (section 4.2), we proceed now to calculate the ohmic resistance R_{ohmic} and the power dissipated P_{dis} in lossy FSS. The experimental model (3.242) is employed for the surface resistance of Al throughout this section. The thickness of the metallic elements is set to be well above the skin depth at these

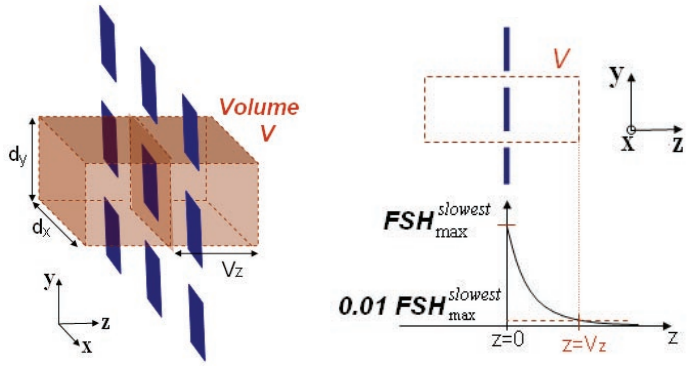

(a) (b)

Figure 4.17: *a) Bird's and b) side view of the dimensions of the integral volume for calculating the power stored*

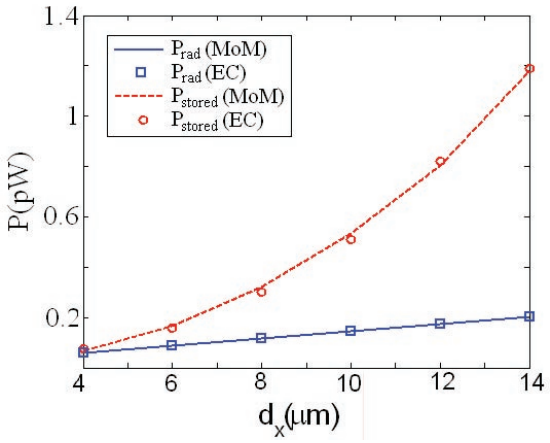

Figure 4.18: *Power radiated from the FSS of Figure 4.13 to free space at resonance using (4.44)-(4.45) and power stored at the same FSS at resonance using (4.46)-(4.47) for varying periodicities d_x.*

frequencies ($t = 300nm$, $\delta_{5THz} = 36.5nm$) and well below the operation wavelength ($\lambda \sim 20\mu m$). The surface roughness is neglected at these frequencies, as discussed previously. Figure 4.19 shows the full-wave simulations of Figure 4.13, where now ohmic losses are present using Ansoft Designer. Figure 4.19 also shows the reflection characteristics obtained from the circuit of Figure 4.8c.

The values of R_a and X_a shown in Figure 4.16 have been employed, making the slight current correction ΔI due to the presence of losses. In order to match the absorption levels, the ohmic resistance R_{ohmic} varies as shown in Figure 4.20. The good agreement between the full-wave and circuit results validates the circuital model. Again, grating

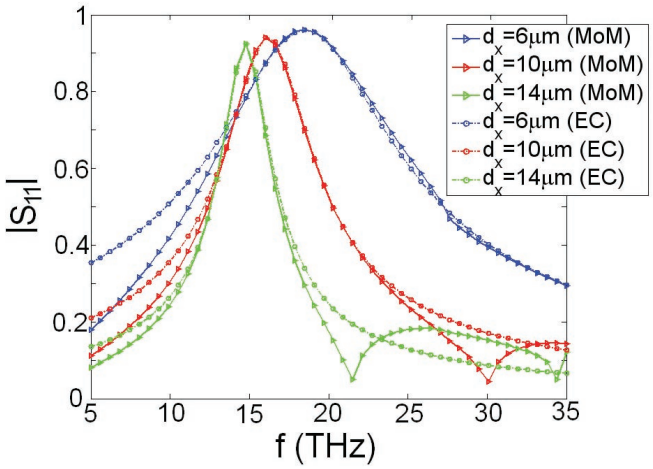

Figure 4.19: *Reflection coefficient of the FSS of Figure 4.13 where the metallic elements are fabricated using aluminum calculated by MoM and EC for different periodicities* d_x.

lobes appears as dips in the reflection and are not described by the EC.

As noted previously, a small correction in the currents ΔI was taking into account to calculate the far-field reflection coefficient of Figure 4.19. Using Ansoft Designer we can investigate in more details the effects of the presence of ohmic losses (e.g. finite conductivity) on the surface-current density. In Figure 4.21, the 2D distribution of the current density is shown in the presence of ohmic losses. In addition, the distribution along the length of the dipole is plotted at four different values of the width, namely $x = \pm w/2$ (edges of the dipole), $x = \pm w/2.4$, $x = \pm w/4$, and $x = 0$ (center of the dipole), and for different values of the metal conductivity, namely $\sigma = \infty, 3.8, 1, 0.55 MS/m$.

As we can see, there exist a decrease in the induced current when the quality of the conductor (conductivity) decreases. This is significant at the edges of the dipole, while it remains insignificant towards the center of the dipole.

The distribution in frequency of the induced currents is also changed by the introduction of losses. Figure 4.22 shows the maximum amplitude $(y = 0, x = \pm w/2)$ and corresponding phase of the induced current density versus frequency. As we can see, the resonant frequency is not changed significantly when losses are introduced (only slightly towards lower frequencies due to the presence of the imaginary part of the surface impedance, $Z_s = R_s + jX_s$.). However, the maximum of the current is slightly reduced throughout the spectra, particularly at resonance and at the edges of the dipole

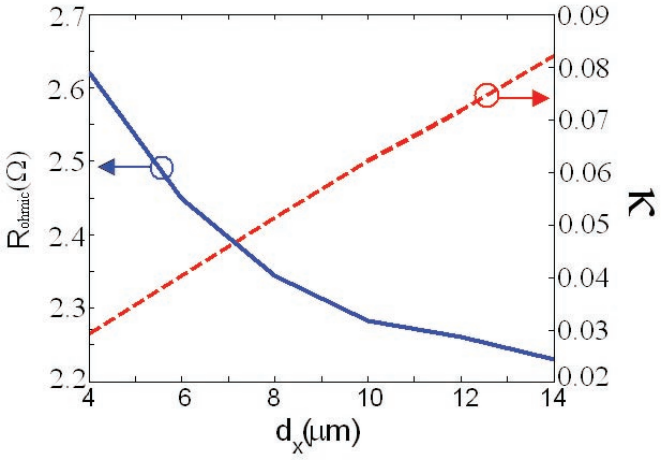

Figure 4.20: *Ohmic resistance R_{ohmic} (left y-axis) and ratio $\kappa = R_{ohmic}/R_a$ (right y-axis) of the FSS of Figure 4.19 for different periodicities d_x.*

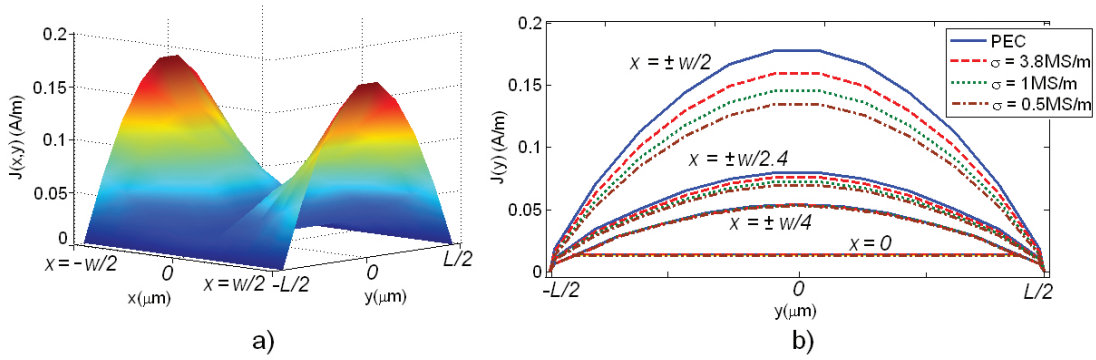

Figure 4.21: *Surface currents for variable conductivities*

$(x = \pm w/2)$. This reduction of the current maximum at resonance is responsible for stronger thermal absorption when the metal conductivity is reduced.

The absorption coefficient can be obtained from (4.9) and is plotted in Figure 4.23 using both the full-wave results as well as the EC model. For clarity, only one conductivity is shown, corresponding to that of Al ($\sigma_{Al} = 3.8MS/m$). Good agreement between the two methods is observed until the fictitious absorption corresponding to the grating lobes is observed in the full-wave results towards higher frequencies (e.g. at $21THz$ for $d_x = 14\mu m$).

The dissipated power ($P_{dis} = P_{inc} \cdot Abs$) at resonance for increasing array periodicity is summarized in Figure 4.24. Interestingly, the power dissipation is increased for increasing periodicity, in opposite trend to the ohmic resistance. This is due to the

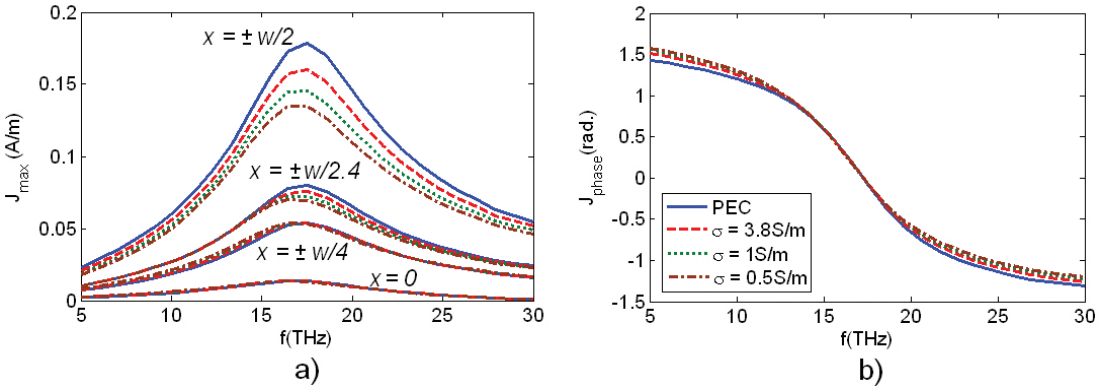

Figure 4.22: *Surface currents (maximum amplitude and phase) vs frequency for variable conductivities*

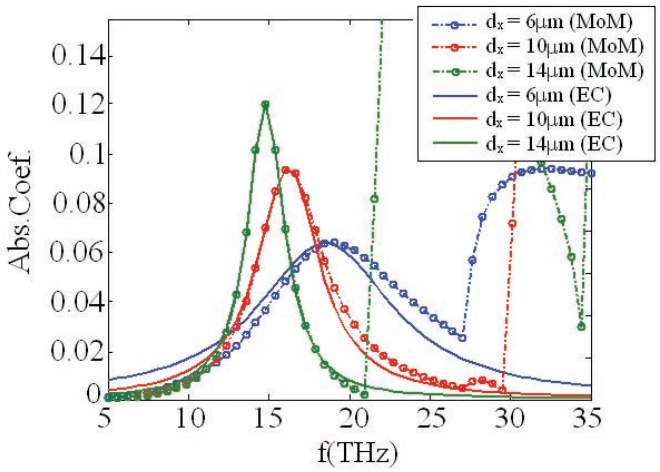

Figure 4.23: *Absorption coefficient of the FSS of Figure 19 as calculated by MoM and EC for different periodicities d_x.*

fact that the terminal resistance R_a decreases more rapidly with periodicity than the ohmic resistance R_{ohmic} and hence the ratio $\kappa = R_{ohmic}/R_a$ (also plotted in Figure 4.20) increases with periodicity.

4.4.3 External, Loaded and Unloaded Quality Factors

The external quality factor Q_e can be obtained by the definition (4.21), where the power radiated from the FSS to free space is assumed in the denominator (as power loss). It can also be derived from the EC according to (4.30). In the absence of power dissipation, Q_U is infinite, and according to (4.24) $Q_L = Q_e$. Therefore, the external quality factor in the lossless case can be obtained from the loaded quality factor, which

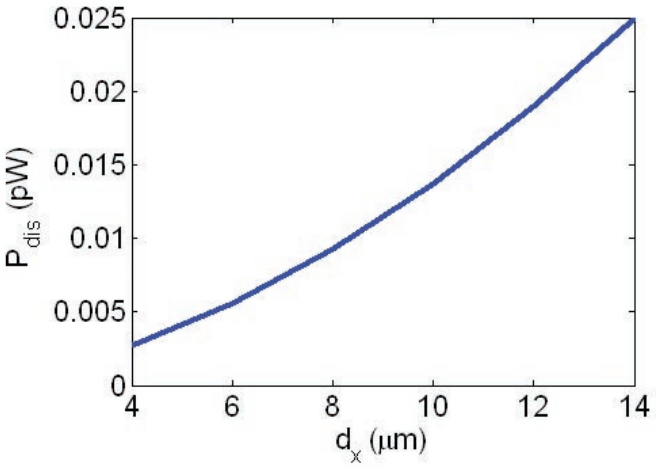

Figure 4.24: *Power dissipated at resonance for the FSS of Figure 19 for varying periodicity* d_x.

can be approximated by the inverse of the $3dB$ fractional bandwidth (4.23).

Figure 4.25 shows the external quality factor Q_e as calculated by the definition, by the EC and by the inverse fractional bandwidth. Good agreement is observed between the three methods. As shown, the external quality factor Q_e increases with increasing periodicity. This suggests a weaker coupling of the incident plane-wave to the resonating array. This value can be employed in (4.24) to extract the unloaded quality factor Q_U.

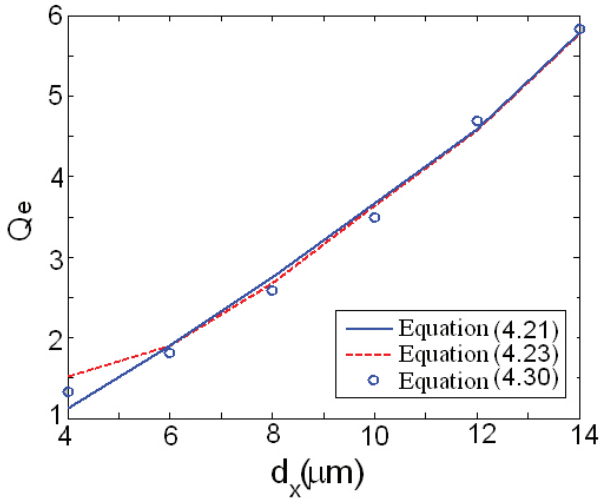

Figure 4.25: *External quality factor in the lossless FSS of Figure 13 calculated by the definition, EC, and the inverse of the* $3dB$ *fractional bandwidth for different periodicities* d_x.

The loaded quality factor Q_L can be estimated as the $3dB$ fractional bandwidth of the reflection curves shown in Figure 4.19 for the lossy FSS. As expected from (4.24), the loaded quality factor in the presence of losses is always lower than the external quality factor, as shown in Figure 4.26a. The extracted Q_U is plotted in Figure 4.26b. As shown, Q_U increases linearly with increasing periodicity despite the increased absorption shown in Figure 4.24. This is because higher reactive power levels are stored in the array as d_x increases (see Figure 4.18). In addition, we can see that the unloaded quality factor is nearly an order of magnitude higher than the loaded quality factor. This is because Q_U represents the intrinsic or near-field quality factor of the FSS as a resonator in isolation, without interacting with the in/output ports.

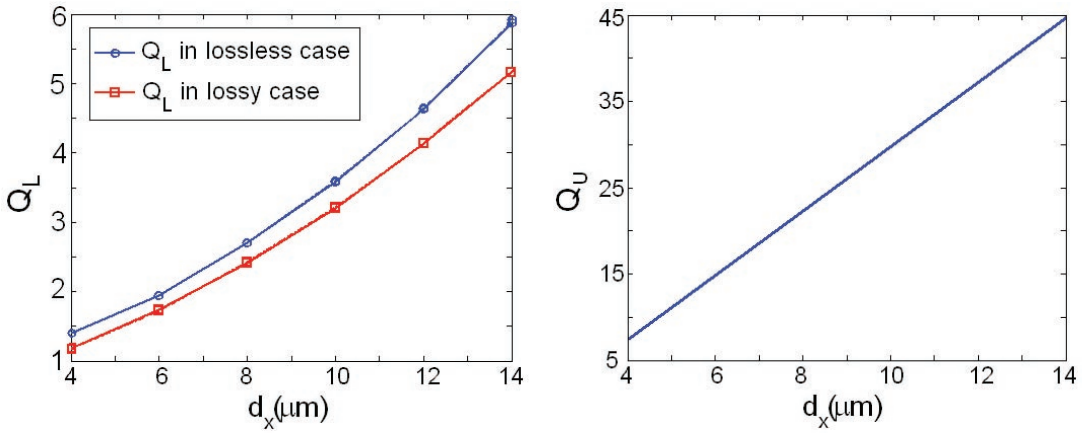

(a) (b)

Figure 4.26: *a) Loaded quality factor for the FSS of Figure 4.13 (lossless) and Figure 4.19 (lossy) for varying periodicity d_x. b) Unloaded quality factor for the FSS of Figure 4.19 for varying periodicities d_x.*

4.4.4 Influence of varying length and width of the dipoles

Identical studies have been performed for variable length and width of the dipoles. For these studies the periodicity d_x is fixed at $8\mu m$, while the length varies from $5\mu m$ to $10\mu m$, and the width ranges from $0.5\mu m$ to $3\mu m$. It was found that the reactive stored power increases in shorter and narrower strips, due to stronger induced currents. Stronger induced currents are also responsible for the increased dissipated power observed in shorter and narrower strips, in spite of exhibiting lower ohmic resistance. The loaded and external quality factor has also been found to increase for

shorter and narrower strips, which are sign of weaker coupling between the FSS and the environment. The intrinsic unloaded quality factor is found to decrease for longer and wider dipoles. Figure 4.27 and 4.28 shows the reflection coefficient, induced currents and Q-factors as a function of length and width of the dipoles, respectively.

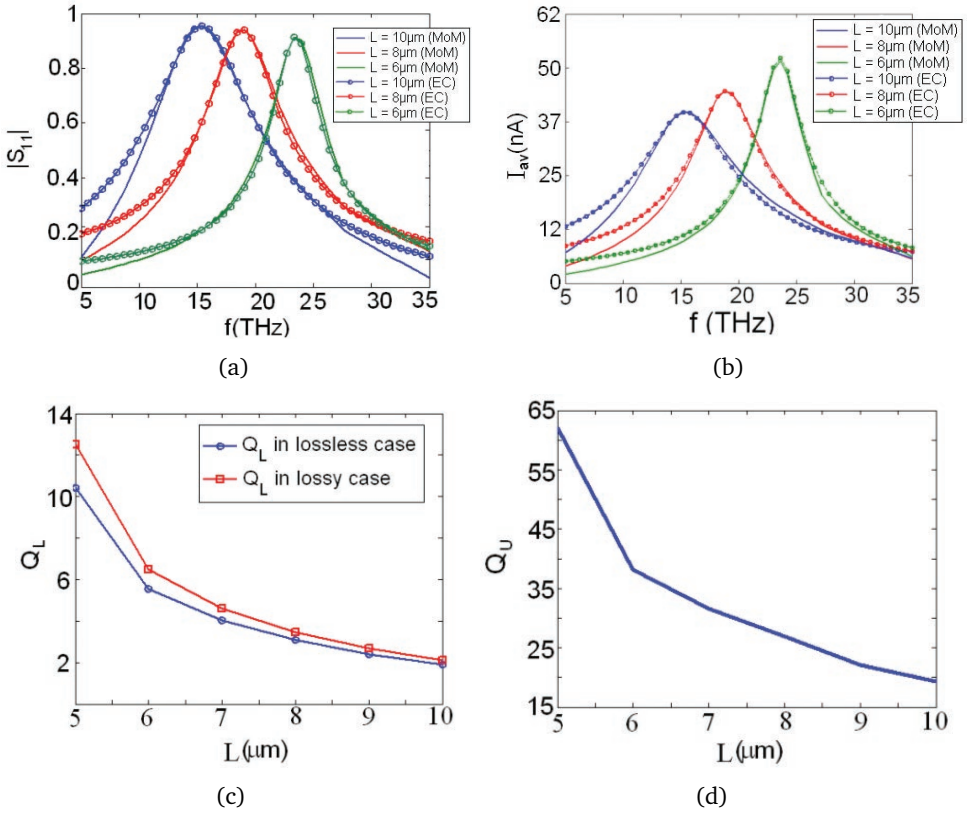

Figure 4.27: *a) Reflection coefficient, b) averaged induced currents, c) loaded and external q-factors, and d) unloaded q-factor of FSS with varying length L*

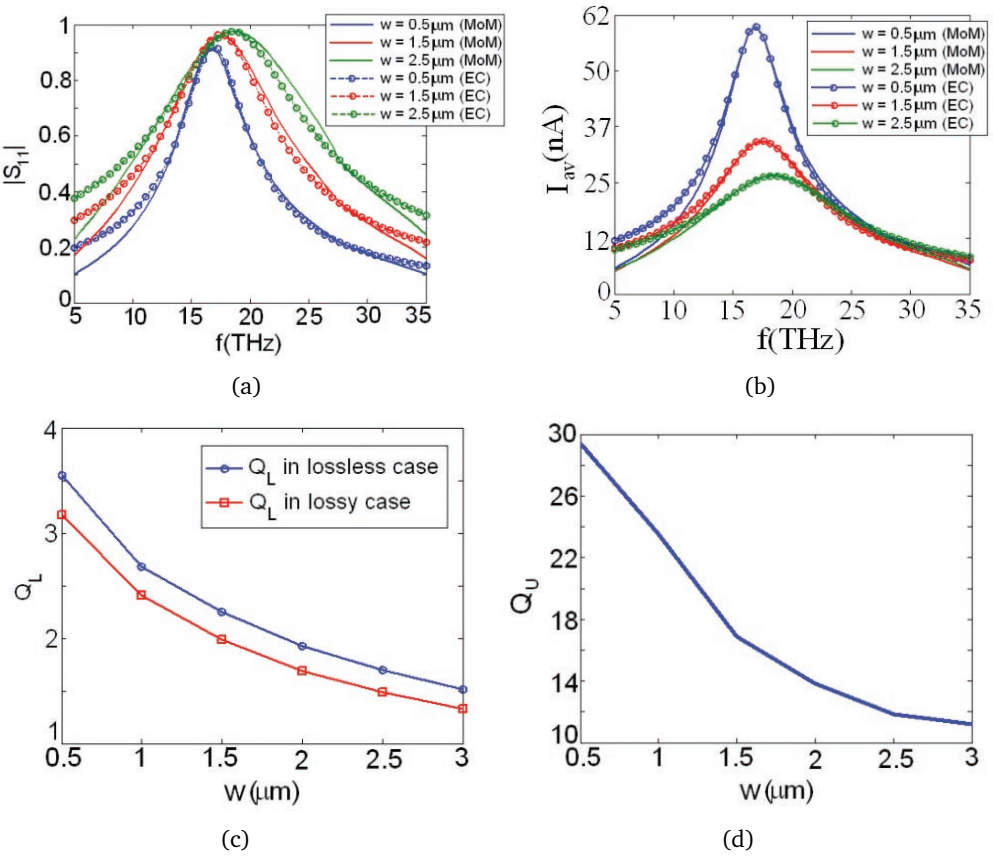

Figure 4.28: *a) Reflection coefficient, b) averaged induced currents, c) loaded and external q-factors, and d) unloaded q-factor of FSS with varying width* w

4.5 Conclusions

The quality factors in FSS operating at THz frequencies have been investigated in this chapter by rigorous full-wave analysis based on the method of moments (described in chapter 3) and validated equivalent circuits. The importance of analyzing the quality factors lies in the fact that it includes information on the powers dissipated in the form of heat and stored in the form of reactive near-fields. This is, in turn, directly related to the FSS induced currents and performance. In order to recapitulate the novelty of this chapter, the major contributions are highlighted as follows:

- Development of a single-mode circuital model based on the terminal impedance of the FSS, accounting for ohmic losses, for the analysis of unloaded and loaded quality factors in free-standing configurations.

A circuital model consisting of the terminal impedance of the FSS, i.e. terminal

reactance X_a and resistance R_a, was extended to account for ohmic losses by introducing an ohmic resistance R_ohmic. This ohmic resistance depends on both the geometry of the FSS unit cell and the surface resistance R_s, which only depends on the properties of the metal used. The equivalent circuit was validated by means of full-wave analysis based on the MoM. The usefulness of such circuital model is twofold, providing suitable physical insight and offering design guidelines.

- Calculation, for the first time, of the reactive power stored in the vicinity of FSS.

To the best of our knowledge, the calculation of the reactive power stored has not been done before because near-fields of FSS are not generally used in any specific application. However, the use of FSS as sensors at THz frequencies has led to the need of addressing the interaction of the near-fields of the FSS and any substance placed on its vicinity. In this chapter, the energy stored in the vicinity of a free- standing FSS is obtained by using two methods, namely, integrating the evanescent Floquet-modes in the FSS near-field, and using the circuital model. Results from both methods have been shown to be in agreement.

- Details of the source of power dissipated in FSS operating at THz frequencies as well as influence of metallic properties.

First, it was demonstrated that in the microwave regime metallic elements in FSS can be assumed to be nearly perfect conductors (without ohmic losses), because dielectric losses are the main source of thermal power dissipation at these frequencies. However, ohmic losses are shown to increase significantly at higher frequencies and can no longer be neglected. In addition, other issues arising at THz frequencies in conducting mediums, such as surface roughness and conductivity dispersion, are confirmed to contribute to add further ohmic losses and must be considered. Surface roughness has been found to dramatically drop the conductivity for increasing frequency. While a surface roughness of 5.5nm produces a 5% drop in the conductivity at 15THz, the same roughness gives rise to a 35% decrease in the conductivity at 150THz. The thickness of the metallic elements has been also analyzed, and it has been revealed that thicker elements lead to wider bandwidth and lower losses. For very thick elements, waveguide-like transmissions were observed due to guiding effects.

The power dissipated due to the finite conductivity of the metallic elements of the

FSS has been thoroughly investigated. A useful parameter κ has been introduced relating the two fundamental factors controlling the power dissipation, namely the terminal resistance and the ohmic resistance. The resonance properties of the FSS have been found to be the key parameter determining the thermal losses by means of the amplitude and frequency-distribution of the current induced in the elements.

- Calculations, for the first time, of unloaded, external and loaded quality factors referred to resonant arrays such as FSS.

The definitions of unloaded, loaded and external quality factors have been applied, for the first time, in the analysis of FSS in order to offer information not only on the far-field properties (FSS coupled to the environment), but also on the near-field or intrinsic properties (FSS in isolation).

Parametric studies for varying periodicity, length and width of the strips have been carried out in order to investigate the influence of the geometry on the electrical parameters of the FSS array (terminal impedance and ohmic resistance), induced currents, resonance properties (resonant frequency and bandwidth), power stored and dissipated. With all that information, an assessment study has been performed on the quality factors. FSS with increased periodicity have been found to give rise to higher thermal absorption and higher unloaded quality factor. In contrast, FSS consisting of larger or wider strips exhibit lower unloaded, despite exhibiting lower thermal absorption. This is because higher reactive power levels are stored in the array as the length or width of the elements increases. In addition, the unloaded quality factor is shown to be nearly an order of magnitude higher than the loaded quality factor, because it represents the intrinsic or near-field quality factor of the FSS as a resonator in isolation, without interacting with the in/output ports.

Chapter 5
Substrate effects in FSS at THz frequencies

5.1 Introduction

Although FSS may be designed/fabricated free-standing (i.e. without any sub/superstrate) [219], the absence of any dielectric might not only be unrealistic for the mechanical integrity of the structure (particularly for capacitive FSS), but also undesirable from a design point of view. Although the choice of the shape and size of the elements represents the most important design parameter (the array of elements are, after all, responsible for the resonance behavior of the structure), dielectrics surrounding the FSS screen can be added to gain design capabilities [1]. For instance, the design of band-pass filters with constant bandwidth for all angles of incidence and polarization (which plays a key role in phased arrays) can be achieved by embedding an inductive FSS in a dielectric layer [1]. Higher bandwidth (although generally with worst flatness) or frequency tuning are also possible with the addition of dielectric layers [1]. FSS with anisotropic substrates [220] or substrate integrated waveguide (SIW) technology [221] have also been investigated. In addition to design possibilities in passive FSS, the inclusion of dielectric layers whose properties can be tuned by an externally applied magnetic field (magnetic permeability in ferrite materials), electric field (dielectric permittivity in liquid crystals) or optical light (conductivity in semiconductors) can be employed in the design of tunable FSS [17, 79, 90].

The importance/usefulness of employing dielectric layers is well understood and the influence of dielectric layers on the transmission, reflection and absorption properties of the FSS have been widely investigated in the microwave regime [1, 63]. At these frequencies, the dielectric losses are the main source of thermal absorption, and the ohmic losses introduced by the finite conductivity of the metallic elements is negligible [6, 8]. However, power dissipation at higher frequencies is dramatically increased by

ohmic losses [6, 8]. It is readily understood that at higher frequencies, where ohmic losses can no longer be neglected, the total dissipated power is therefore the sum of ohmic and dielectric losses. However, the inclusion of dielectric layers in FSS operating at THz frequencies will not only increase thermal absorption due to the addition of dielectric losses to ohmic losses, but also leads to changes in the amplitude/distribution of the currents induced in the metallic elements as well as their near-fields. In turn, these changes will also affect the ohmic losses. A rigorous study of the dissipated power in free-standing FSS at THz frequencies was presented in Chapter 4. Following similar procedures, the influence of dielectric surrounding on the performance of FSS working at THz frequencies will be investigated.

In this chapter, the circuital model of Chapter 4 for a free-standing FSS will be extended to account for the presence of a dielectric substrate, providing interesting information on the influence of dielectric-loading on the resonance frequency and bandwidth, obtaining similar results as in [63] at microwave frequencies. These effects on the resonance are also investigated from the perspective of the variation in the currents induced in the FSS elements and the amplitude of evanescent Floquet modes. Next, a detailed investigation on the power stored is carried out in three different scenarios, namely in the presence of ohmic and dielectric losses separately, and simultaneously. By doing this, we can understand and quantify the contribution of each type of losses to the overall dissipated power. All these studies are performed under the assumption of dispersionless dielectrics. The influence of dielectric dispersion is briefly revised.

5.2 FSS operation in the presence of dielectrics

5.2.1 Circuital model of FSS with a dielectric loading

The behaviour of a free-standing FSS under plane-wave illumination can be well understood through the equivalent circuits shown in Figure 5.1a-c. The terminal impedance $Z_{a0} = R_{a0} + jX_{a0}$ and an additional ohmic resistance R_{ohmic} represent an accurate model before the onset of grating lobes [1]. The terminal or radiation resistance R_{a0} is associated with the power radiated from the FSS (exchange with the environment), the terminal reactance X_{a0} represents the power stored in the FSS, and the ohmic resistance R_{ohmic} embodies the ohmic losses due to the finite conductivity

of the metallic elements of the FSS [1] (see chapter 4). In the presence of a dielectric substrate supporting the FSS, the equivalent circuit become that of Figure 5.1d-f, where the radiation resistances R_{a0} and R_{a1} are those of an FSS immersed in free-space and an infinite dielectric with the properties of the substrate, respectively [1]. The electrical

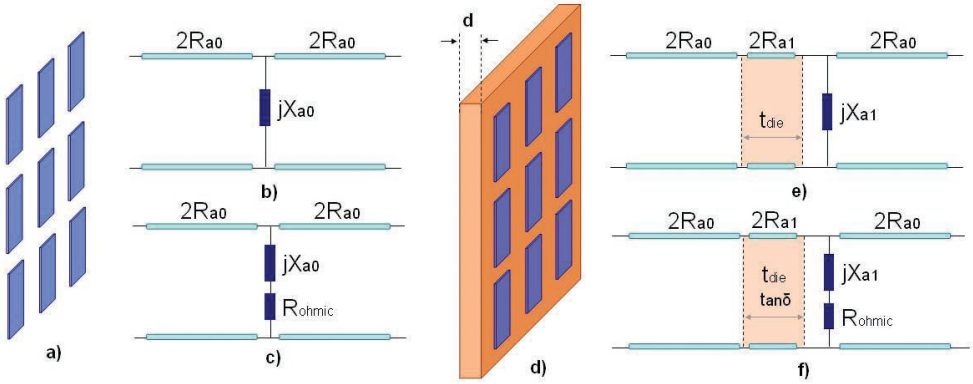

Figure 5.1: *Free-standing capacitive FSS consisting of dipoles (a), and its equivalent circuit based on the terminal impedance $Z_{a0} = R_{a0} + jX_{a0}$ in the presence (b) and absence (c) of ohmic losses. Capacitive FSS on a dielectric substrate (d), and its equivalent circuit based on the terminal impedances Z_{a0} (free-standing FSS) and Z_{a1} (FSS immersed in an infinite dielectric) in the presence (e) and absence (f) of ohmic and dielectric losses.*

length of the transmission line is given as [1]:

$$t_{die} = d \cdot r_{1z} = d \cdot \sqrt{1 - \left(s_{1x} + k\frac{\lambda}{d_x}\right) - \left(s_{1y} + n\frac{\lambda}{d_y}\right)} \tag{5.1}$$

Where r_{1y} is the direction of propagation of the plane-wave spectrum from the FSS, $s = s_{1x}\hat{x} + s_{1y}\hat{y} + s_{1z}\hat{z}$ is the direction of propagation of the incidence wave, d_x and d_z are the periodicities in the x and z axis, $\{k, n\}$ the order of the Floquet modes and λ the wavelength of operation. For normal incidence $(s_{1x} = s_{1z} = 0)$ and propagation below the onset of trapped or free-space grating lobes $(k = n = 0)$, the electrical length of the transmission line is equal to the physical length of the substrate $t_{die} = d(r_{1y} = 1)$.

The complex propagation constant for a lossy dielectric is equal to:

$$\gamma_{die} = \alpha + j\beta = \frac{\pi\sqrt{\epsilon_r}}{\lambda} + j\frac{2\pi\sqrt{\epsilon_r}}{\lambda} \tag{5.2}$$

where α and β are the attenuation (for small losses) and phase constant, respectively, ϵ_r the dielectric permittivity, $tan\delta$ the loss tangent and λ the operation wavelength.

From the point of view of the terminal reactance X_{a1}, the lossy dielectric layer transforms the real terminal impedance $2R_{a0}$ into a complex impedance $Z_t = R_t + jX_t$ (Figure 5.2a) [63]. In general, this complex impedance has both resistive and reactive components and, therefore, can influence the resonance and modify its shape/location from that of the free-standing configuration. The reactance X_{a1} in an inductive FSS

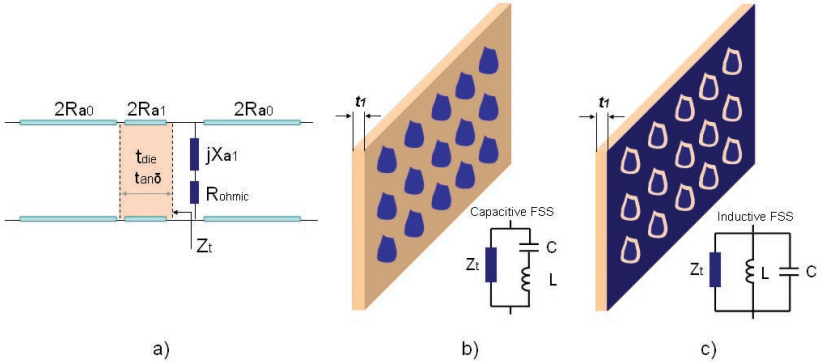

Figure 5.2: *a) Transmission-line model for FSS loaded with a dielectric substrate. Equivalent impedance of a capacitive (b), and inductive (c) FSS.*

consists of a parallel LC (Figure 5.2c). The addition in parallel of a further reactance from the complex impedance Z_t may lead to a significant change of the resonance frequency. Only thicknesses multiple of $\lambda/4$ (Z_t remains purely real) will not alter the resonance frequency. On the other hand, the reactance of a capacitive FSS consists of a series LC (Figure 5.2b). In this case, the complex impedance Z_t does not alter the resonance frequency, which is still determined by the terminal reactance X_{a1}, although it may produced changes in the shape of the resonance [63]. For the sake of brevity, here we limit our study to capacitive FSS, which requires a dielectric substrate for its fabrication and cannot be made free-standing [219].

The reflection, transmission and absorption coefficients for a capacitive FSS supported by a dielectric layer can readily be calculated as:

$$S_{11} = \frac{Z_{in} - 2R_{a0}}{Z_{in} + 2R_{a0}} \tag{5.3}$$

$$S_{21} = \frac{2Z_{in}}{Z_{in} + 2R_{a0}} \tag{5.4}$$

$$Abs = \frac{8R_{a0}Z_{in} - 4Z_{in}^2}{(Z_{in} + 2R_{a0})^2} \tag{5.5}$$

Where the input impedance Z_{in} is the parallel combination of the transformed impedance Z_t and the terminal reactance X_{a1} in series with the ohmic resistance R_{ohmic}:

$$Z_{in} = \frac{Z_t(R_{ohmic} + jX_{a1})}{Z_t + R_{ohmic} + jX_{a1}} \tag{5.6}$$

And the transformed impedance is:

$$Z_t = 2R_{a1}\frac{2R_{a0} + 2R_{a1}tanh(\gamma \cdot t_{die})}{2R_{a1} + 2R_{a0}tanh(\gamma \cdot t_{die})} \tag{5.7}$$

In the absence of losses ($X_t = R_{ohmic} = 0$), and for thickness t_{die} multiple of $\lambda/2$ ($R_t = 2R_{a0}$), the effect of the substrate is merely that of shifting the frequency downwards, and the equivalent circuit of Figure 5.1f) becomes that of Figure 5.1b), but with terminal reactance jX_{a1}. In this case, the reflection and transmission characteristics simplify to:

$$S_{11} = \frac{-R_{a0}}{R_{a0} + jX_{a1}} \; ; \quad S_{21} = \frac{jX_{a1}}{R_{a0} + jX_{a1}} \tag{5.8}$$

The variation of the resonant characteristics from a lossless free-standing FSS to a lossy FSS supported by a lossy dielectric substrate is shown in Figure 5.3 in four steps. Results from both rigorous analyses based on MoM and approximated circuital models shown in Figure 5.1 are employed. First, a lossless free-standing FSS is characterized in Figure 5.3a, where R_{a0} and X_{a0} extracted as in chapter 4. An FSS immersed in infinitely thick lossless dielectric of permittivity equal to 2 is also shown, from which R_{a1} and X_{a1} may be extracted. Second, the reflection of a lossy free-standing FSS is plotted in Figure 5.3b, where R_{ohmic} is extracted. Third, the resonance of a lossless FSS supported by a lossless dielectric substrate is shown in Figure 5.3c for a given thickness of the dielectric ($t_{die} = 1.7\mu m$). Four and last, a lossy FSS supported by a lossy dielectric ($tan\delta = 0.008$) is characterized in Figure 5.3d.

5.2.2 Substrate effects on the resonance shape and location

As shown in Figure 5.3, it is clear that the resonant characteristics of FSS are greatly influenced by the dielectric surroundings of the FSS. In this subsection, we revised the main consequences of the presence of the dielectric on the shape and location of the resonance. For this purpose, the reflection coefficient in dB of a lossless FSS supported by a dielectric layer ($\epsilon_r = 2$) is investigated as a function of frequency

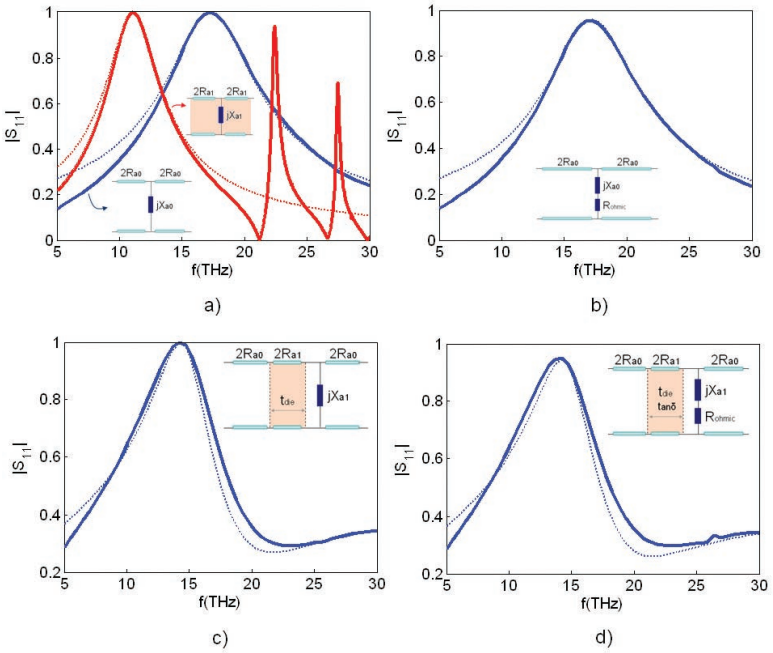

Figure 5.3: *Influence of the dielectric on capacitive FSS reflection obtained by full-wave MoM (solid lines) and EC (dotted lines). a) Free-standing lossless FSS ($L = 9\mu m$, $w = 1\mu m$, $d_x = 10\mu m$, $d_y = 11\mu m$) (blue line) and FSS immersed in an infinite dielectric of permittivity equal to 2 (red line); b) free-standing lossy FSS ($s = 3.810^6 S/m$); c) lossless FSS on lossless substrate ($t_{die} = 1.7\mu m$); and d) lossy FSS on lossy substrate ($tan\delta = 0.008$). The inset shows the circuital models employed in each subfigure. R_{a0}, R_{a1}, and R_{ohmic} employed are 36.82, 26.03 and 1.52Ω, respectively. The reactance slope parameter corresponding to X_{a0} and X_{a1} are 92.13 and 70.42Ω, respectively.*

and thickness of the dielectric substrate, and is shown in the following contour figure (Figure 5.4). The contour figure shows the value of the reflection coefficient in dB versus thickness $t = t_{die}$ (horizontal axis) and frequency (vertical axis). The black solid-line indicates total reflection, i.e. 0dB. The grey dashed-lines show the location of dielectric-only transmission peaks, which influence mainly the Q-factor of capacitive FSS. The contour figure shows at one glance information of the properties (resonant frequency and bandwidth) of the spectral signature of FSS supported by dielectric of various thicknesses. For a fixed value of dielectric thickness, we obtain the S_{11} versus frequency, as shown in Figure 5.6 for thickness 20, 22.5 and $25\mu m$. The dotted lines of Figure 5.4 are shown in Figure 5.6, corresponding to the dielectric-only ridges (dielectric electrical thickness of $\lambda/2$, λ, $3\lambda/2$).

The first aspect worth mentioning is the decrease in the resonance frequency as the

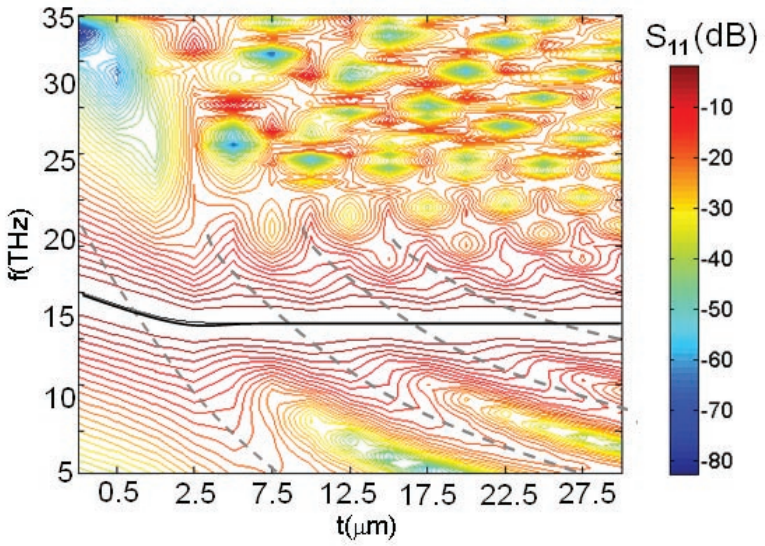

Figure 5.4: *Contour plot of the reflection coefficient of an FSS with dimensions $L = 9\mu m$, $w = 1\mu m$, $d_x = 10\mu m$, $d_y = 11\mu m$. The horizontal and vertical axis represent the thickness $t = t_{die}$ and the frequency, respectively. The black solid-line corresponds to the resonant frequency and the grey dashed-lines represent secondary resonances due to the presence of the dielectric.*

thickness is increased, approaching the well-known value for FSS supported by a semi-infinite dielectric. This shift in the resonance is caused by the interaction of the near-fields with the surrounding dielectric material [63], point at which we will return in a following section.

The Q-factor also suffers a variation in the presence of a dielectric support. For thin substrates, where a decrease in the resonant frequency is evident, the bandwidth remains unchanged. However, thicker substrates providing a constant resonant frequency give rise to variable bandwidth versus thickness. This is due to the emergence of secondary resonances in the dielectric and coinciding with the frequencies at which the thickness is a multiple of $\lambda/2$, as shown in the grey dashed-lines of Figure 5.4. Due to the reflective nature of capacitive FSS, the effects of the dielectric resonances are stronger out-of-resonance when the FSS allows more energy to pass through. This means that the bandwidth at $-3dB$ is more affected than the bandwidth at $-1dB$. Therefore, the dielectric is shown to affect the bandwidth in two manners. When the dielectric resonances take place away from the FSS resonance, ripples can be observed in the reflection characteristic, as shown in Figure 5.6 for three different thicknesses (regions $t_{die} = \lambda/2$ and $3\lambda/2$). When these secondary resonances

lie near the resonance, the bandwidth is either widened or made narrower (region $t_{die} = \lambda$).

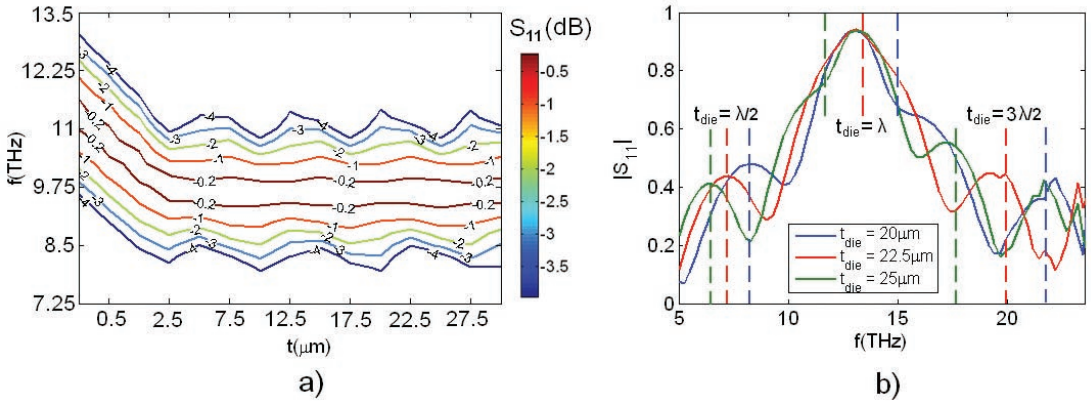

Figure 5.5: *a) Zoom in the contour plot of Figure 5.4. The frequency range is reduced to cover between* 7.25 *and* $13.5THz$*, and the contour lines of the reflection are focused on the range from* 0.2 *to* $-4dB$*. b) Reflection coefficient for the FSS of Figure 5.4 versus frequency at three particular thicknesses, namely* 20*,* 22.5 *and* $25\mu m$*. The effect of secondary dielectric resonances is evident.*

The bandwidth varies due to the presence of a dielectric support. Figure 5.5 shows a zoom in the contour plot of Figure 5.4 near the resonance. For thin substrate, where a decrease in the resonant frequency is evident, the bandwidth remains unchanged. However, thicker substrates providing a constant resonant frequency give rise to variable bandwidth versus thickness. This is due to the secondary resonances in the dielectric and coinciding with the frequencies at which the thickness is a multiple of $\lambda/2$, as shown in the grey dashed-lines of Figure 5.4. Due to the reflective nature of capacitive FSS, the effects of the dielectric resonances are stronger out-of-resonance when the FSS allows more energy to pass through. This means that the bandwidth at $-3dB$ is more affected than the bandwidth at $-1dB$, as seen in Figure 5.5.

Therefore, the dielectric is shown to affect the bandwidth in two manners. When the dielectric resonances take place away from the FSS resonance, ripples can be observed in the reflection characteristic, as shown in Figure 5.6 for three different thicknesses (regions $t_{die} = \lambda/2$ and $3\lambda/2$). When these secondary resonances lie near the resonance, the bandwidth is either expanded or contracted (region $t_{die} = \lambda$).

5.3 Currents and Near-Field excited in FSS supported by a dielectric substrate

In the vicinity of the FSS (near-field) energy is not radiated, but evanescent with distance ($1/r^2$ or $1/r^3$). This energy is transferred back and forth from the FSS (currents and voltage) to the reactive near-field (magnetic and electric near-fields). The currents excited in the FSS elements and the associated near-fields will depend on the substrate thickness and dielectric permittivity. As we have shown before, this has a clear effect on the resonance frequency and the bandwidth. In this section, we investigate the changes observed in the currents and the amplitude of the low-order Floquet modes.

5.3.1 Induced currents

In the previous section, we have observed that the presence of a supporting layer for the FSS has the significant effect of shifting the frequency and varying the bandwidth of the resonance. Since the far-field reflection and transmission coefficients are determined by the currents induced on the FSS elements, we would expect a similar behavior of the currents. Figure 5.6a-b depicts the averaged currents (as defined in Chapter 4) versus frequency for various thickness of the supporting dielectric layer t_{die}, and permittivity $\epsilon_r = 2$. As we can see, in Figure 5.6 for thin dielectrics, the main effect is a shift in the resonance frequency downwards due to the interaction of the near-fields with the substrate (air-dielectric interface). Also, sharp resonances appear near the region of grating lobes. For thicker dielectrics (Figure 5.6b), the resonance location remains almost constant, but the bandwidth of the resonance exhibit certain ripples. In addition, the number of sharp resonances near the grating lobe region increases considerably. While the shift in resonance frequency is due to the dielectric-loading effect [63], the other two effects arise as a consequence of two different phenomena. On the one hand, ripples in the bandwidth appears from the dielectric-only resonances, as explained earlier. On the other hand, the sharp resonances at higher frequencies not only represent the onset of free-space grating lobes (similar to what happened in free-standing FSS), but are also a consequence of surface-waves or trapped grating lobes propagating within the dielectric and finally escaping to the free space [1]. As the thickness of the dielectric increases, more trapped grating lobes are able to propagate within the dielectric, eventually escaping to free-space.

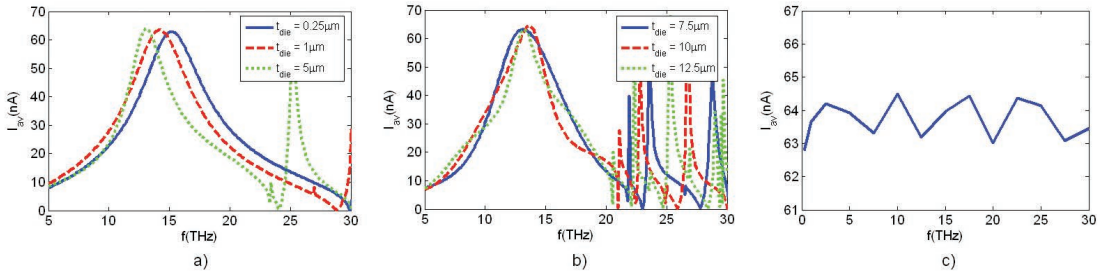

Figure 5.6: *Averaged currents induced in the FSS for varying thickness and dielectric permittivity* $\epsilon_r = 2$

In Figure 5.6c, we can see how the amplitude of the induced currents remain almost constant regardless the thickness of the dielectric substrate, exhibiting only a small variation. This small variation does, however, have a slight influence on the power dissipated as we shall see in the following sections. In order to evaluate also the effect of the value of the dielectric permittivity, Figure 5.7a shows the averaged induced currents versus frequency for various permittivities. As we can see also in Figure 5.7b, increasing permittivity gives rise to higher induced currents. The increase in the amplitude of the excited currents leads to a narrower width (versus frequency) of the current distribution. As a consequence, an FSS loaded by a dielectric permittivity will exhibit a lower bandwidth in its reflection or transmission characteristic (higher Q-factor). This decrease in bandwidth when an FSS is supported or embedded by a dielectric is similar to the bandwidth loss experienced in an antenna when is loaded by a dielectric.

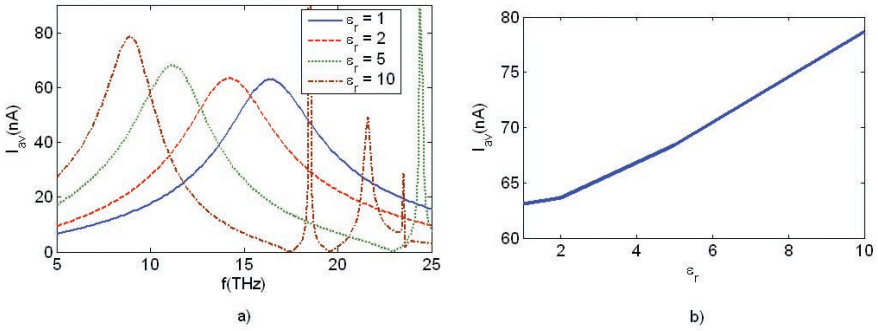

Figure 5.7: *Averaged currents induced in the FSS for varying dielectric permittivity and thickness* $t_{die} = 1\mu m$

5.3.2 Floquet modes excitation

A shift in resonance frequency as the dielectric thickness increases was observed earlier in the chapter. This resonance shift is determined by the interaction of the evanescent Floquet modes excited at the array with the interface air-dielectric ($z = t_{die}$). The rate at which the resonance shifts reduces for increasing dielectric thickness (see Figure 5.4). This is due to the fact that the amplitude of the evanescent Floquet modes arriving at the air-dielectric interface reduces considerably as such interface moves away from the array (i.e. thickness increases). Hence, from a certain thickness of the dielectric, the resonance remain constant, and the only effect of the dielectric is to modify the shape of the resonance, i.e. bandwidth. In Figure 5.8a-b, the evolution of the slowest-decaying evanescent Floquet mode along the propagation direction z is shown for various thickness and permittivities. The step seeing for the value $z = t_{die}$ is due to the air-dielectric interface.

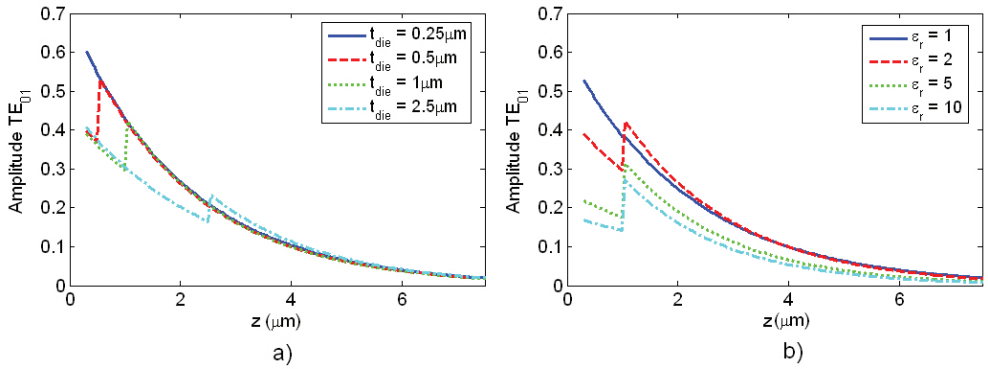

Figure 5.8: *Amplitude of the slowest decaying Floquet mode TE_{01} for various thickness (fixed $\epsilon_r = 2$) (a) and permittivity (fixed thickness $t_{die} = 1\mu m$) (b)*

5.4 Dielectric behavior at THz frequencies

So far we have considered lossless FSS. From this section we introduced losses both in the metallic elements of the FSS and the dielectric supporting layer. Before starting the investigation of the dielectric effects on the power dissipated, however, we discuss briefly another important issue when working at THz frequencies, namely the dispersion. Particularly, here we focus on the dispersion in the electric permittivity of the dielectric substrate. We refer to Chapter 3 for details on the effects of the dispersion in the conductivity of the metallic elements of the FSS.

In general, the permittivity of any material is a complex frequency-dependent value. The real and imaginary parts of the permittivity are related to the energy storage and dissipation, respectively. There exist various dielectric mechanisms contributing to the overall permittivity, from the lower-frequency slow relaxation effects related to orientation polarization to the higher-frequency faster resonant effects associated to electronic and atomic polarization.

In order to investigate the effects of permittivity dispersion on the FSS resonance, we compare in Figure 5.9 and 5.10 the reflection characteristic of an FSS supported by a lossless dielectric with various dispersive features, namely dispersionless, linear dispersion and sinusoidal dispersion.

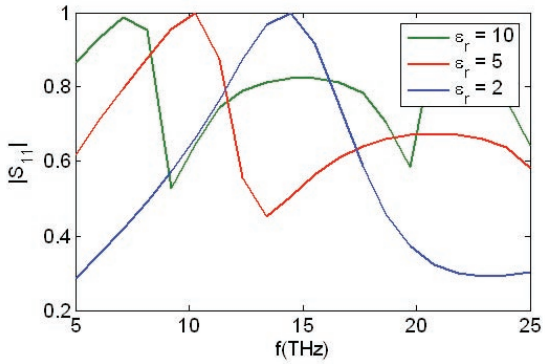

Figure 5.9: *Dispersion study of the reflection coefficient of a lossless FSS supported by a dielectric substrate with no dispersion*

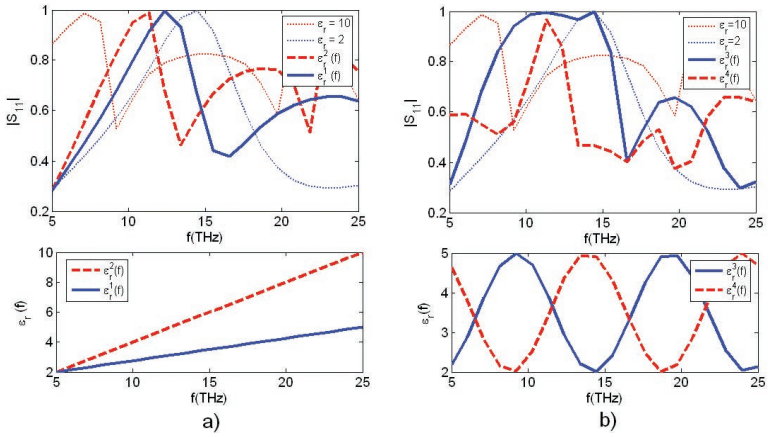

Figure 5.10: *Dispersion study of the reflection coefficient of a lossless FSS supported by a dielectric substrate with a) linear and b) sinusoidal dispersion*

The effect of dispersionless dielectric is shifting downwards the resonant frequency and increasing the reflection in the out-of-band frequencies. Slow variations in the value of electrical permittivity, such as the linear dispersion in Figure 5.10b, are shown not to modify significantly the FSS response, whereas fast variations, such as the sinusoidal dispersion in Figure 5.10c, lead to strongly modified reflection characteristics by contracting or expanding the bandwidth. From Figure 5.10a, we can identify FSS resonating at 10THz and 15THz for permittivity equal to 5 and 2, respectively. For a dispersion function such as $\epsilon_r^3(f)$, where the value of the permittivity varies from 5 to 2 in the frequency range between 10THz and 15THz, the bandwidth of the FSS resonance is expanded and covers the entire range between 10 and 15THz. On the contrary, the dispersion function $\epsilon_r^4(f)$ gives rise to a contracted bandwidth.

In general, however, some materials may be assumed dispersionless in a narrow band of frequencies. For instance, polyimide has been shown to exhibit a fairly constant index of refraction around 1.8 in the frequency range between 16 and 30THz (wavelengths between 10 and $18\mu m$), whereas Si_3N_4 exhibits fast variations of index of refraction from 0.9 through 3.1 to 2.2 in the same frequency region [222].

5.5 Power dissipated in the presence of a substrate

In order to investigate the influence of a dielectric substrate on the dissipation that takes place in resonant FSS, we carried out a parametric study varying the thickness of a dielectric supporting an FSS with same dimensions as in Figure 5.4. The thickness is varied from 0 to $30\mu m$ and a dispersionless permittivity is considered constant to 2. The study is done in the separated and combined presence of dielectric and ohmic losses. When dielectric losses are included, the loss tangent is set at 0.008, and when ohmic losses are considered the classical 'lossy dielectric' ohmic model with finite conductivity of the metals equal to $3.8 \cdot 10^7 S/m$ is employed, which represent a good approximation at the frequencies investigated (see Chapter 3).

5.5.1 Ohmic losses only

The reflection and absorption coefficients for thin and thick dielectric substrates in the sole presence of ohmic losses $(tan\delta = 0)$ are shown in Figure 5.11-12. The reflection

and absorption peaks are zoomed in near the resonance on the right-hand side of each figure. A frequency shift downwards is evident for thin substrates, remaining constant at $13THz$ for thickness higher than $2.5\mu m$. The bandwidth is shown to be constant for thin substrate, while ripples arousing from secondary dielectric resonances appears for thicker substrates.

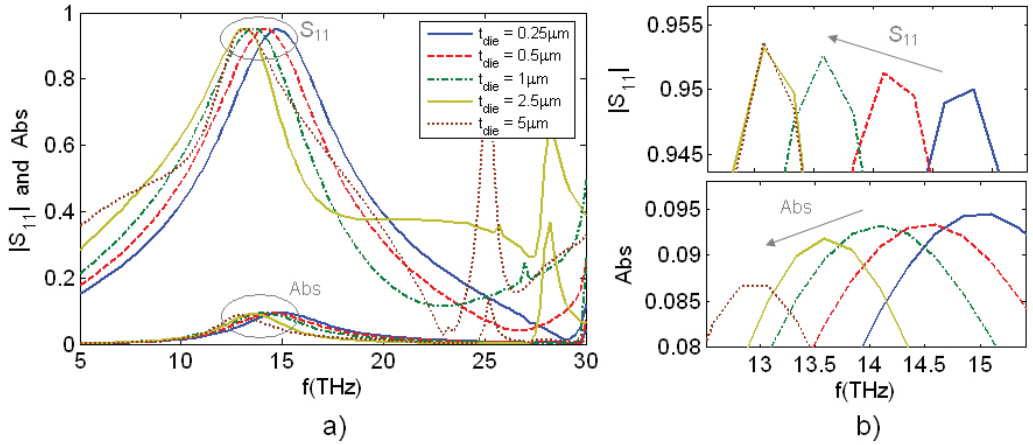

Figure 5.11: *Reflection coefficient versus frequency for low values of thickness of the substrate ($0.25\mu m$ to $5\mu m$). On the right-hand side, the reflection and absorption near the resonance is zoomed in. FSS with same dimensions as in Figure 5.4 and only ohmic losses.*

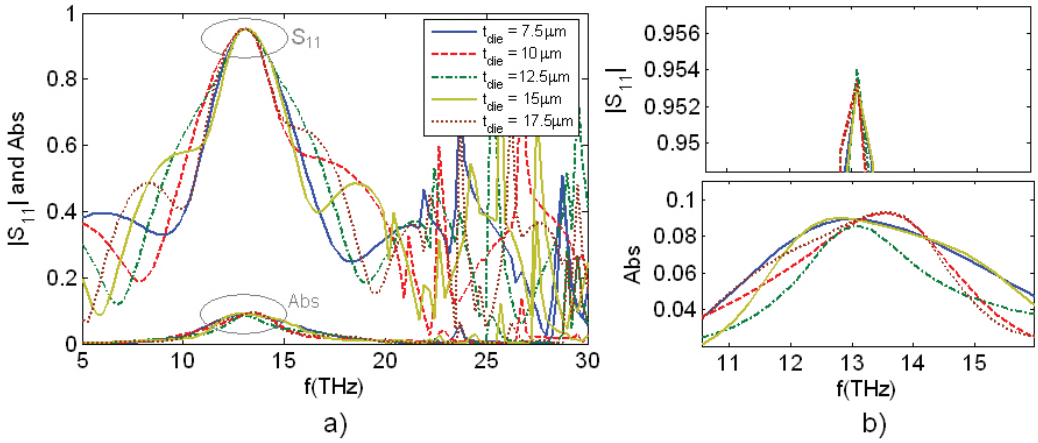

Figure 5.12: *Reflection coefficient versus frequency for thick substrates ($7.5\mu m$ to $17.5\mu m$). On the right-hand side, the reflection and absorption near the resonance is zoomed in. FSS with same dimensions as in Figure 5.4 and only ohmic losses.*

Interestingly, the absorption at resonance is shown to decrease as the thickness increases for thin substrates. This follows the same trend as the amplitude of the induced currents shown in Figure 5.6. Since the surface resistance remains invariable (FSS dimensions are fixed), the power dissipation is proportional to the amplitude of the currents flowing through the metallic elements, as inferred from the expression.

As the thickness of the substrate is increased, however, the expansion and contraction of the FSS resonance due to the presence of dielectric secondary resonances leads to an oscillation in the absorption observed at the resonant frequency. Figure 5.13 shows the evolution of absorption with thickness of the dielectric. The two effects commented above are clearly identified, namely 1) decrease of the absorption from 0.095 to 0.0875 for thin substrate and 2) oscillatory behavior around 0.0875 for thicker substrates. The absorption oscillations (< 0.005) are, however, small as compared to the total absorption (> 0.085).

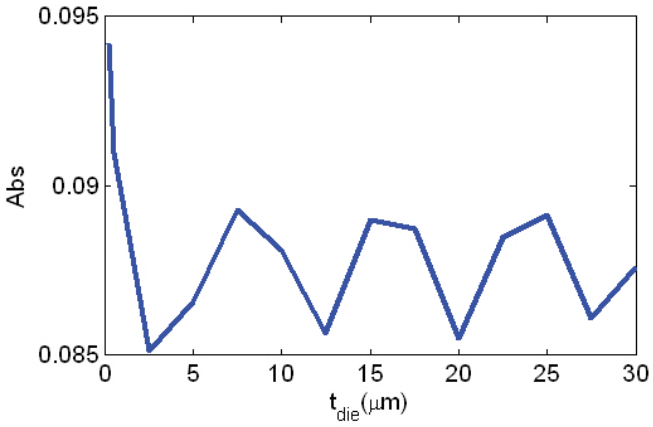

Figure 5.13: *Absorption coefficient versus thickness of the supporting dielectric layer t_{die}. FSS with same dimensions as in Figure 5.4 and only ohmic losses.*

The contour Figure 5.14 shows the variation of the absorption as a function of thickness not only at resonance, but in a wider range of frequencies. The usefulness of Figure 5.14 relies on the fact that we can see the all the substrate effects in the presence of only ohmic losses at one glance, namely frequency shift and oscillatory behavior of bandwidth and absorption. In addition, the absorption are concentrated near the resonance.

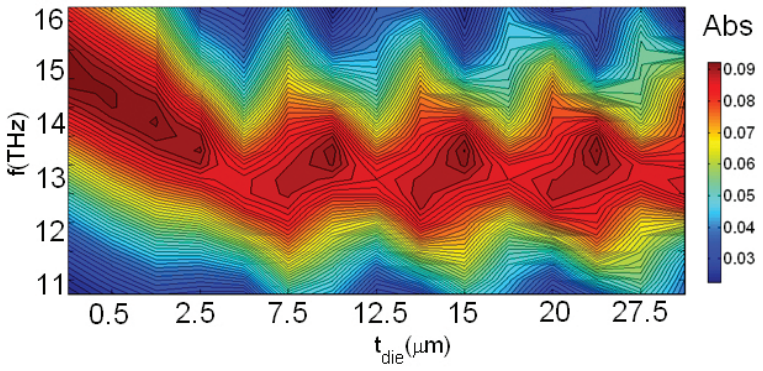

Figure 5.14: *Contour plot of the absorption coefficient versus thickness of the supporting dielectric layer t_{die} and frequency. FSS with same dimensions as in Figure 5.4 and only ohmic losses.*

5.5.2 Dielectric losses only

The reflection and absorption coefficients for thin and thick dielectric substrates in the sole presence of dielectric losses (infinite conductivity of metals, $\sigma = \infty$, and constant loss tangent across all frequencies equal to 0.008) are shown in Figure 5.15-16. The reflection and absorption peaks are zoomed in near the resonance on the right-hand side of each figure. As before, the frequency shift and the characteristic ripples from secondary dielectric resonances are identified. The absorption at resonance due to the lossy dielectric layer, in opposite trend to the ohmic losses, increases for thicker substrates and reaches a fairly constant absorption (around 0.03) from thickness higher than 5. This is due to the fact that the evanescent near-fields amplitude decays in the direction normal to the FSS and, therefore, the amount of heat dissipation taking place from the interaction between the near-fields and the dielectric also decays. As the thickness increases, the contribution of the evanescent modes lessens and the increase rate of the dielectric losses decline, approaching a limiting value (0.03). For these thicker substrates the higher order evanescent Floquet modes have decayed to near zero amplitude at the air/substrate boundary, and do not add further dielectric losses from these higher order modes.

It is interesting to notice that for thick substrates, higher absorption appears away from the resonance (Figure 5.16, right bottom) as a consequence of the secondary dielectric resonances (wavelengths multiple of $\lambda/2$), where multiple reflections inside

the dielectric lead to higher absorption.

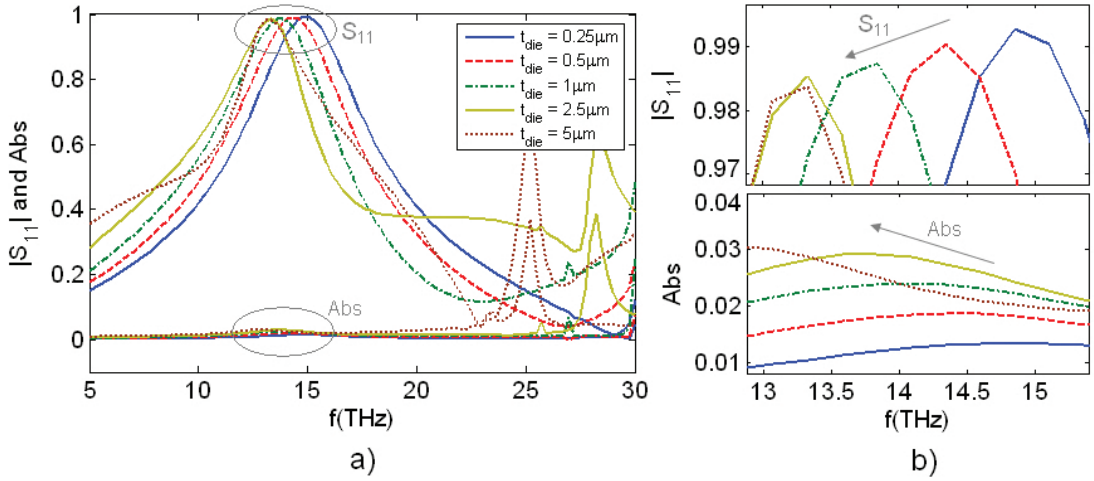

Figure 5.15: *Reflection coefficient versus frequency for low values of thickness of the substrate ($0.25\mu m$ to $5\mu m$). On the right-hand side, the reflection and absorption near the resonance is zoomed in. FSS with same dimensions as in Figure 5.4 and only dielectric losses.*

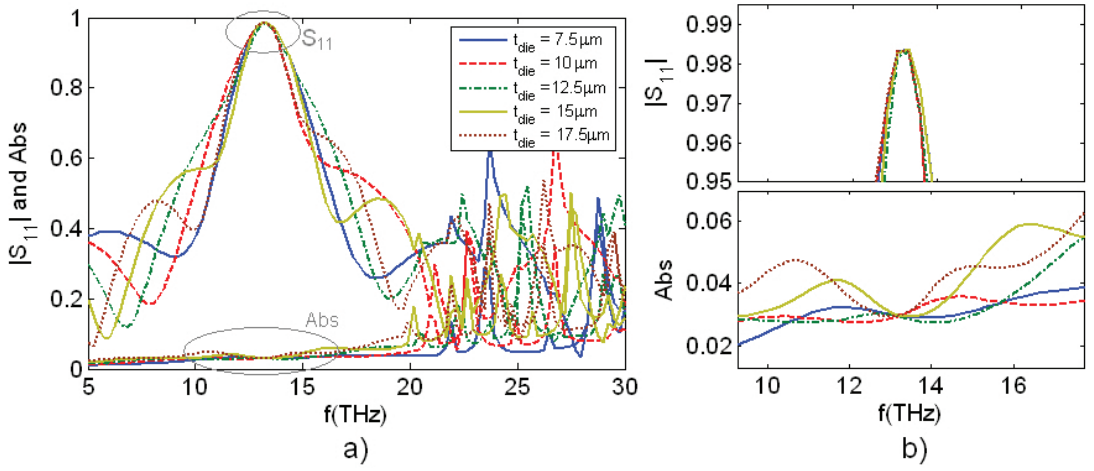

Figure 5.16: *Reflection coefficient versus frequency for thick substrates (7.5um to 17.5um). On the right-hand side, the reflection and absorption near the resonance is zoomed in. FSS with same dimensions as in Figure 5.4 and only dielectric losses.*

Figure 5.17 shows the evolution of absorption with thickness of the dielectric. Two

of the effects commented above are readily perceived, namely (1) increase of the absorption from 0 (lossless) to 0.03 for thin substrates and (2) apparently constant amount of absorption (0.03) for thick substrates with an insignificant oscillation (< 0.0015). For thick substrates, although evanescent higher-order modes do not contribute further to the absorption, this apparently constant absorption is actually very slowly increasing because of the absorption due to the propagating mode.

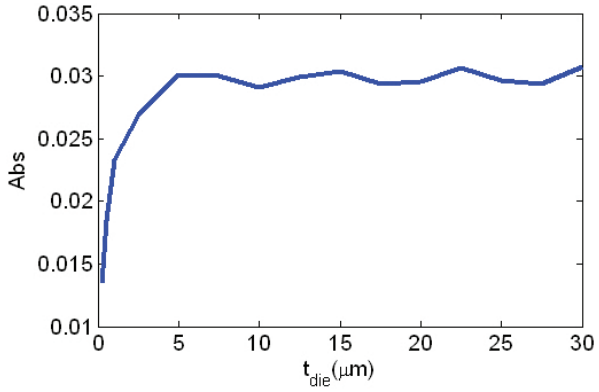

Figure 5.17: *Absorption coefficient versus thickness of the supporting dielectric layer t_{die}. FSS with same dimensions as in Figure 5.4 and only dielectric losses.*

The other effect related to higher absorption observed away from resonance can be seen in the contour Figure 5.18. An almost constant absorption around 0.03 at resonance is observed from $5\mu m$ thickness of the dielectric layer onwards. For thicker substrates, however, higher absorption appears away from the resonance, due to the dielectric-only resonances.

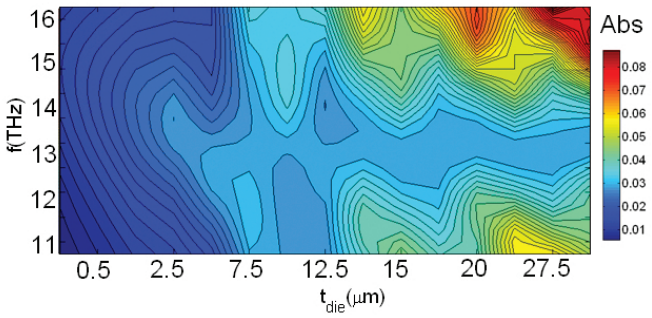

Figure 5.18: *Contour plot of the absorption coefficient versus thickness of the supporting dielectric layer t_{die} and frequency. FSS with same dimensions as in Figure 5.4 and only dielectric losses.*

5.5.3 Dielectric and ohmic losses

The result of including both dielectric and ohmic losses is presented in Figure 5.19-5.20. As we can see, the losses arising from both dissipation mechanisms are added. Comparing the contour plots in Figure 5.19 (both losses) and Figure 5.14 (only ohmic), we can notice a broadening of the absorption due to the introduction of significant dielectric losses away from resonance.

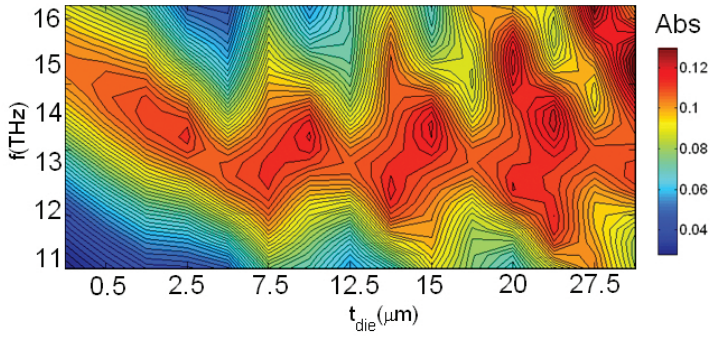

Figure 5.19: *Contour plot of the absorption coefficient versus thickness of the supporting dielectric layer t_{die} and frequency. FSS with same dimensions as in Figure 5.4 and both dielectric and ohmic losses.*

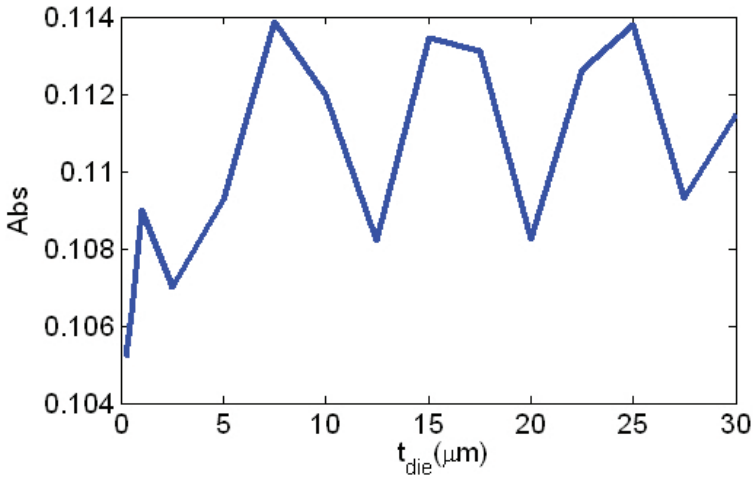

Figure 5.20: *Absorption coefficient versus thickness of the supporting dielectric layer t_{die}. FSS with same dimensions as in Figure 5.4 and both dielectric and ohmic losses.*

In order to readily compare the two sources of power dissipation, Figure 5.21 shows

the absorption versus thickness of the dielectric for the four possible scenarios, namely lossless, only ohmic losses, only dielectric losses, and both ohmic and dielectric losses. We can observe how the dissipation due to the finite conductivity of the metals is higher that dissipation arising from the dielectric, and therefore ohmic losses are the main contribution of dissipated energy at these frequencies. Interestingly, the introduction of a dielectric has an obvious effect in the dielectric losses and an indirect effect on the ohmic losses. On the one hand, from a free-standing FSS with no dielectric losses ($t_{die} = 0$), as we increase the thickness of the dielectric layer, dielectric losses are certainly increased and become almost constant with a certain ripple (dielectric-only resonances) as we keep increasing the dielectric. The main contribution of dielectric losses are the strong evanescent near-fields in the vicinity of the array. As we move further from the array, the amplitude of these near-fields decreases (see Figure 5.8), and the dielectric-losses contribution lessens. On the other hand, an FSS on a thin dielectric substrate is observed in Figure 5.21 to exhibit lower ohmic losses than a free-standing FSS. As the dielectric thickness increases, the ohmic losses varies around a constant value. As explained earlier, this can be explained by means of changes in the currents due to the presence of the dielectric.

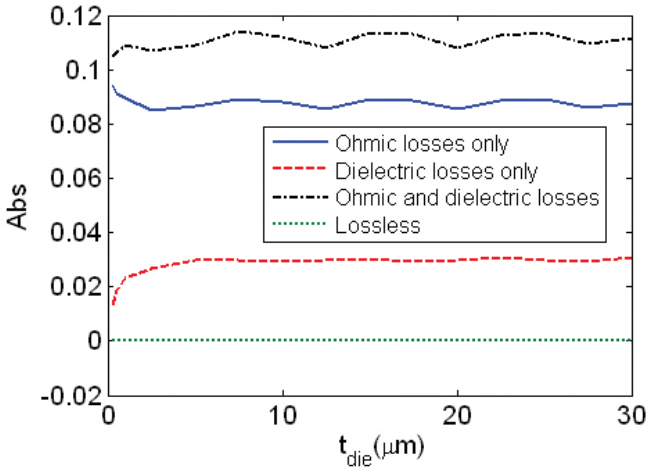

Figure 5.21: *Summary of absorption contributions from ohmic and dielectric losses.*

5.6 Conclusions

While in the previous chapter free-standing THz FSS were considered, this chapter has been devoted to the analysis of THz FSS supported by a dielectric substrate. In the

past, various studies of the influence of dielectrics in the vicinity of the FSS has been carried out accurately in the microwave regime and, generally, in the absence of losses. However, the issue of dielectric and ohmic losses, as well as the currents induced on the elements of the FSS under the presence of a nearby dielectric layer is missing in the literature. In the following, we proceed to highlight the main contributions of this chapter:

- Extension of the equivalent circuit based on the terminal impedance of the FSS, accounting for losses, for modeling dielectric-loaded FSS

The circuital model introduced in chapter 4, consisting of the terminal impedance of the FSS, was extended to model the presence of dielectric layers in the vicinity of the array, and validated by full-wave analysis. This equivalent circuit offers a clear view of the effects of the dielectric-loading on the main resonance characteristics of the FSS, namely resonance shift and variation of bandwidth.

- Calculation, for the first time, of the induced currents on the elements of dielectric- loading FSS

As shown in previous chapters, the scattering characteristics of FSS are determined by the way that the incident field induces currents on the elements. Different currents distributions are obtained in different types of elements, leading to different frequency selectivity of the re-radiated field. In addition to the type of FSS, the medium in which the FSS is immersed also determines the currents induced on the elements. This substrate effects on the currents have been, for the first time, presented in this thesis. The currents have been investigated for thin and thick dielectric substrates. Two different phenomena dominate in the presence of thin and thick substrates. For thin substrates, a shift in resonance frequency (e.g. frequency of maximum current) is evident. This has been explained in terms of the the evanescent Floquet modes. The dielectric-loading effect pulling the resonance downwards in frequency depends on the amplitude of the evanescent Floquet modes at the air-dielectric interface. For thick substrates, however, this pulling effect is vanished due to the fact that the amplitude of the evanescent Floquet modes at the air-dielectric interfaces fades away with increasing thickness of the dielectric. The phenomenon dominating in the presence of thick substrates is the appearance of dielectric-only resonances at thicknesses equal

to odd multiples of $\lambda/2$. When this resonances lie in the vicinity of the resonance, the bandwidth of the FSS is affected, either widening or making it narrower.

- *Calculation, for the first time, of the power dissipated by dielectric-loading FSS, distinguishing between dielectric and ohmic losses*

The losses arising from the finite and non-zero electrical conductivity of metallic and dielectric materials, respective, have been analyzed in FSS arrays supported by a dielectric substrate, for the first time. Ohmic and dielectric losses and their effects have been studied independently and simultaneously. Ohmic losses have been shown to be the dominant source of losses at these frequencies. Interestingly, it has been shown that ohmic losses are subject to the thickness of lossless dielectric. Ohmic losses decrease with thickness of the substrate for thin substrates, stabilizing with an

oscillatory behaviour for thicker substrates. Pulling of the maximum ohmic losses towards lower frequencies has been observed corresponding to the same shift in the currents induced on the elements. Certainly, dielectric losses are also dependent on the thickness of the substrate. As the substrate thickness increases, the dielectric losses increases, stabilizing for thicker substrates due to the exponentially decreasing amplitude of the evanescent Floquet modes interacting with the nearby dielectric layer. It has been shown that higher dielectric losses are found at odd multiples of $\lambda/2$, due to the dielectric-only resonances, than at the FSS resonance.

Chapter 6
Single-screen FSS for filters and sensing components at THz frequencies

6.1 Introduction

The advent of microfabrication techniques have facilitated an increase interest in exploring the operation of FSS at THz frequencies. The main difference of FSS working at THz frequencies with respect to those working at microwave frequencies lies in the introduction of ohmic losses due to the finite conductivity of the metallic elements of the array. This issue was thoroughly covered in Chapter 4, and the introduction of dielectric effects was also analyzed in Chapter 5. Traditional elements such as those shown in Chapter 2, in single-screen configurations and under normal incidence, exhibit solely a fundamental resonance or even mode before the onset of grating lobes [1]. Various type of elements have been studied in the past working at THz frequencies and in relation with ohmic losses and currents induced [6]. Different designs have also been proposed to achieve multiband operation in the microwave regime of the spectrum [14, 50, 51, 69–73]. Only fractal designs, however, have been scaled to work at THz frequencies in multiband filters. Although fractal FSS exhibit good multiband performance, the design of such fractal FSS using genetic algorithms is a time-consuming and non-intuitive procedure, which may become more a more complicated if we include additional dielectric or FSS layers. Fractal FSS also lack direct relation between the shape of its elements and its spectral response in terms of key filtering parameters such as resonant frequency, absorption and quality factors. On the other hand, perturbed FSS have been shown to exhibit dual-band characteristics in the microwave and represent a good approach to reach multiband performance [14]. In addition, owing to the peculiar modes of currents induced in its elements, perturbed FSS show interesting properties for its use in multiband absorbing screens [223]

as well as sensing systems [170]. Periodic arrays based on asymmetric elements exhibiting spectral features at THz frequencies are attracting increasing attention for their capability to detect, distinguish or identify materials in their surroundings [170].

In the first part of this chapter, various FSS consisting of traditional elements working at THz frequencies and exhibiting single-band performance are briefly described in relation to its absorption and currents induced. Subsequently, the main part of the chapter devotes to investigate FSS consisting of perturbed elements for its use in multiband and sensing applications. The operation of perturbed FSS (free-standing to isolate from dielectric effects and only consider ohmic losses) in the far- and near-field is examined and the underlying physics behind its behavior described. On the one hand, perturbed FSS are designed to exhibit dual-, tri- and quad-band characteristics. Introducing two type of elements, each of them sensitive to a different polarization, dual-band dual-polarized FSS are also designed. On the other hand, perturbed FSS are studied for its potential application in sensing systems. The currents induced in the elements as well as the near-fields are examined. The sensing performance of perturbed FSS for various types (quantity and permittivity) of sensed material is investigated. Finally, perturbed FSS are demonstrated experimentally using the techniques explained in Chapter 3.

6.2 Conventional-elements FSS for single-band applications

In this section, a brief analysis of various single-screen FSS working at THz frequencies is carried out, concentrating upon their induced current distribution and absorption levels. Ansoft Designer is employed to obtain the S-parameter and surface-density current $J(A/m)$ under vertical polarization, unless stated otherwise. Details of the simulations carried out with this software were given previously in section 3.3.2.1. All FSS are supported by a lossy dielectric ($\epsilon = 3.5$, $tan\delta = 0.008$) of thickness $t_{die} = 1.7\mu m$. The metallic elements are considered infinitely thin (no thickness effects considered for simplicity) with conductivity of Al $\sigma = 3.8 \cdot 10^7 S/m$, and the 'lossy dielectric' model (3.251) is employed to calculate the surface resistance R_s and, therefore, the ohmic losses.

The starting point for the design of single-screen FSS is the array of infinitely-long

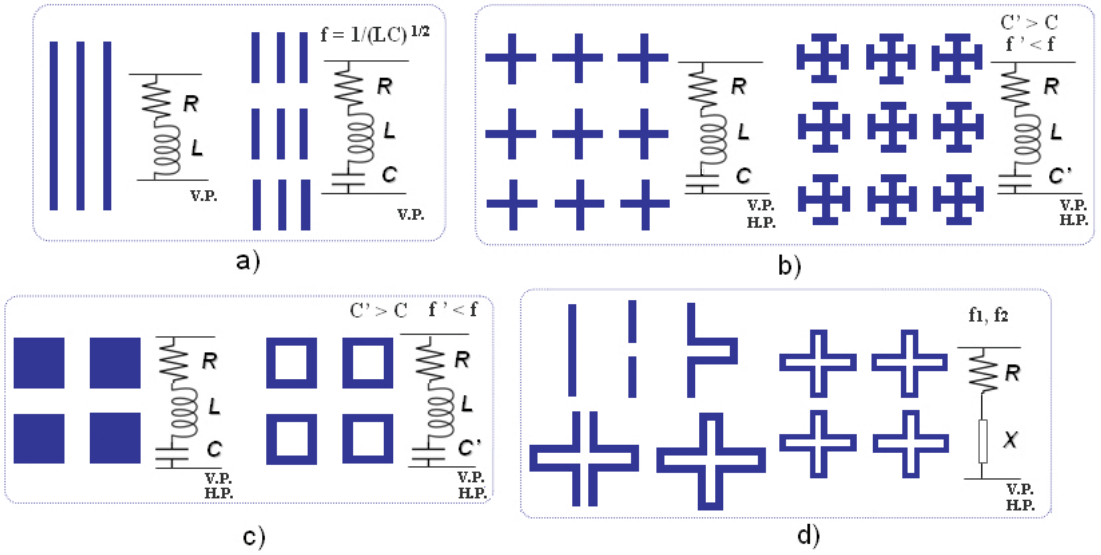

Figure 6.1: *Derivation of different types of elements from the array of infinitely-long dipoles. a) finite-length dipoles, b) crossed-dipoles and Jerusalem crosses, c) plate and loop-type elements, and d) four-legged loaded elements.*

dipoles, as shown in Figure 6.1, where various traditional elements are derived from such array. Infinitely long dipoles act as inductors, so that the array exhibits a high-pass filtering characteristic (only total reflection at DC), as shown in Figure 6.2. In such array, the current induced in the dipoles flow upwards and with approximately constant amplitude along the vertical axis, since there is no discontinuity. This array is non-resonant and its equivalent circuit consists of an inductance L in series with a resistance R. The inductance determines the transition frequency of the high-pass characteristic, while the resistance and the induced currents determine the absorption due to ohmic losses. The losses for a non-resonant FSS are quite low ($\approx 3.5\%$ in the example shown in Figure 6.2) due to the low value of the induced currents.

In order to render the array resonant, a capacitance C can be included by substituting the infinitely-long dipoles to finite-length dipoles, as shown in Figure 6.1a, so that a gap between the dipoles produces the needed capacitance. By doing so, the equivalent circuit changes to a resonant series RLC circuit with stop-band characteristic, as obtained in Figure 6.3. In such case, as shown in Chapter 4, the current induced in the dipoles exhibits a sinusoidal distribution along the length of the dipole, maximum at the center and minimum at the ends, and concentrates at the edges of the dipole along the width. The losses are increased substantially as compared to the non-resonant

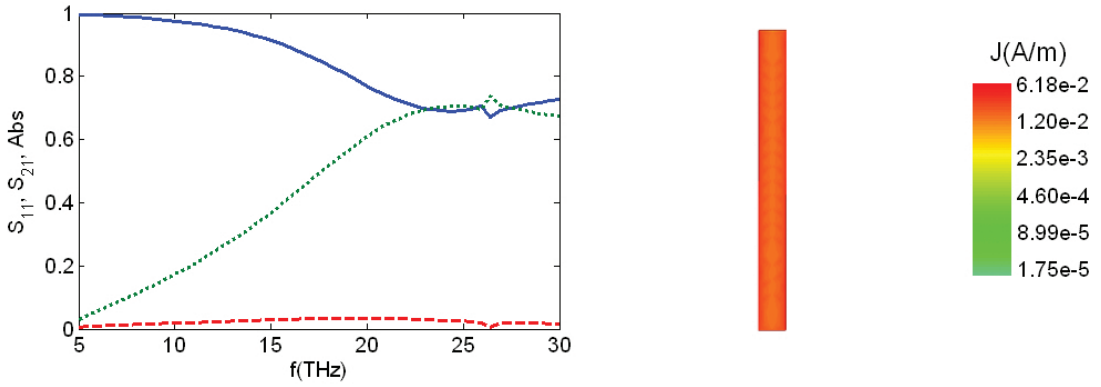

Figure 6.2: *Reflection and absorption characteristic (left) and amplitude of induced current (right) of polarizer with dimensions* $w = 1.5\mu m$, $d_x = 3\mu m$.

array ($\approx 10\%$ in the example given in Figure 6.3). As shown in Chapter 4, increasing separation, and decreasing length and width give rise to stronger induced currents and, therefore, higher levels of thermal absorption.

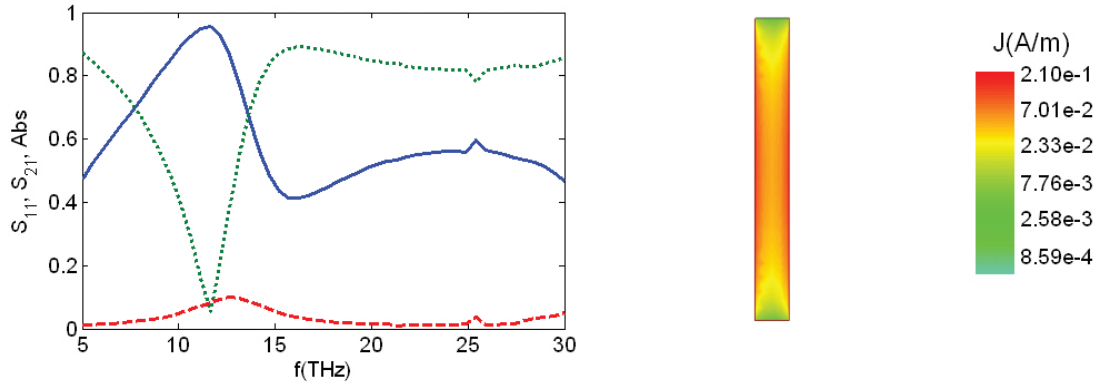

Figure 6.3: *Reflection and absorption characteristic (left) and amplitude of induced current (right) of dipole FSS with dimensions* $L = 14\mu m$, $w = 2\mu m$, $d_x = 10\mu m$, $d_y = 20\mu m$.

So far, non-resonant infinitely-long dipoles exhibiting high-pass characteristic (Figure 6.2) have been converted to resonant finite-length dipoles exhibiting band-pass characteristic (Figure 6.3). With the addition of a horizontal dipole of the same length superimposed over the vertical dipole, a crossed-dipole FSS (Figure 6.1b) exhibits similar band-pass characteristic not only for vertical polarization, but also for horizontal polarization, as shown in Figure 6.4 for vertical polarization. In Figure 6.4 we can also observe similar distribution of the current along the length of the vertical dipole with a small perturbation from the horizontal dipole, which give rise to a drop

in the current at the center of the dipole and to some current flowing on the horizontal dipole near the center. The total effect is a slight increase in the thermal absorption ($\approx 12.5\%$). Likewise, length, width, and separation of the dipoles further tailor the resonance characteristics of the crossed-dipole FSS.

An capacitive loading can be added in the crossed-dipole element giving rise to the Jerusalem cross element, as shown in Figure 6.1b. The main effect of the introduction of a capacitive loading is a shift of the resonance towards lower frequencies and an increase of the bandwidth, while the losses remain similar, i.e. 12.5% for the example given in Figure 6.5.

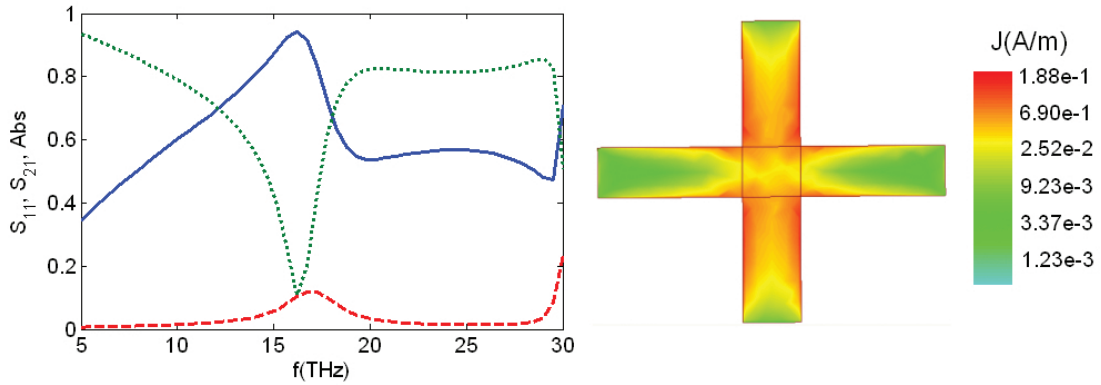

Figure 6.4: *Reflection and absorption characteristic (left) and amplitude of induced current (right) of cross-dipole FSS with dimensions* $L = 10\mu m$, $w = 2\mu m$, $d_x = 16\mu m$, $d_y = 16\mu m$.

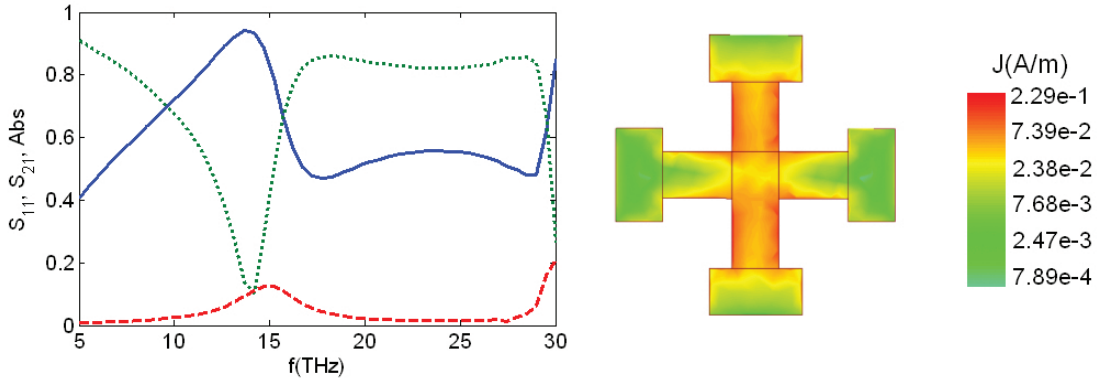

Figure 6.5: *Reflection and absorption characteristic (left) and amplitude of induced current (right) of Jerusalem-cross FSS with dimensions* $L = 8\mu m$, $w = 2\mu m$, $d_x = 16\mu m$, $d_y = 16\mu m$, $L_{load} = 4\mu m$.

FSS sensitive to both vertical and horizontal polarization can be also made of tripole elements, as shown in Figure 6.6. In this case, the losses decrease slightly to $\approx$

8.2%. As we can see, under vertical polarization, the surface-current density is mostly concentrated on the sides of the vertical arm and slightly on the other arms inclined $\pm 120deg$. Although the maximum amplitude of the current seems slightly greater than that of the crossed-dipole, the losses are lower due to smaller size of the element where the current is flowing (recall Eq.(4.2) in Chapter 4). Apart from this, earlier onset of grating lobes are observed for the case shown in Figure 6.6. The onset of grating lobes can be delayed, however, by close-packing the elements.

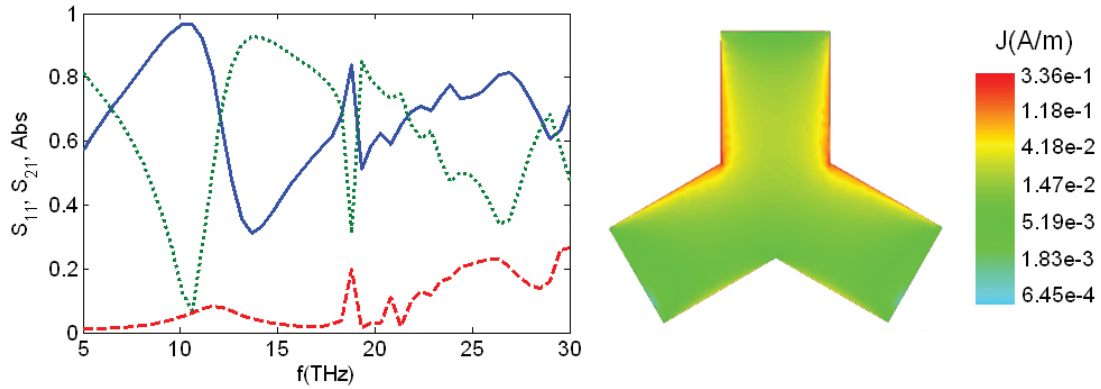

Figure 6.6: *Reflection and absorption characteristic (left) and amplitude of induced current (right) of tripole FSS with dimensions* $L_{leg} = 5.15\mu m$, $w = 4\mu m$, $d_x = 16\mu m$, $d_y = 16\mu m$.

Another type of element that can be derived from the dipole is the patch element, giving rise to the plate or solid elements (e.g. rectangular, circular, hexagonal). In the case of a rectangular plate, the dipole width becomes the same as the dipole length, as shown in Figure 6.1c. The characteristics of the resonance produced by these type of elements, however, are not very attractive because the resonance always appears close to the onset of grating lobes [1], and there are few designing parameters. The array resonates when the dimensions of the plate are $\lambda/2$ across the element approximately. This is due to the fact that plate elements exhibit a very low inductance L (or a very low capacitance C in aperture elements) so that the resonance frequency is very high and close to the onset of the grating lobes. In order to increase the inductance, and therefore lower the resonance frequency away from the grating lobes, the plates can be perforated as shown in Figure 6.1c. In the aperture case, the aperture can be filled to increase the overall capacitance. By doing so, the FSS with solid elements are transformed into the loop-type FSS. In such case, the array resonates when the averaged circumference of the element is λ.

Examples of the resonance of arrays with rectangular- and (octagonal)circular-loop elements are shown in Figure 6.7 and Figure 6.8, respectively. Due to the vertical polarization of the incident wave, the current is induced in the vertical sides of the loops, exhibiting the maximum amplitude in the center of element along the vertical axis and concentrated at the edges along the width. The amount of losses are slightly lower than for the dipoles or crossed-dipoles ($\approx 8.5\%$ for both square- and ring-loop elements). This is due to the fact that loop-type elements exhibit a wider distribution of the currents versus frequency, leading to wider bandwidth and lower absorption, similarly to what was explained in Chapter 4 for the case of dipoles with various separations.

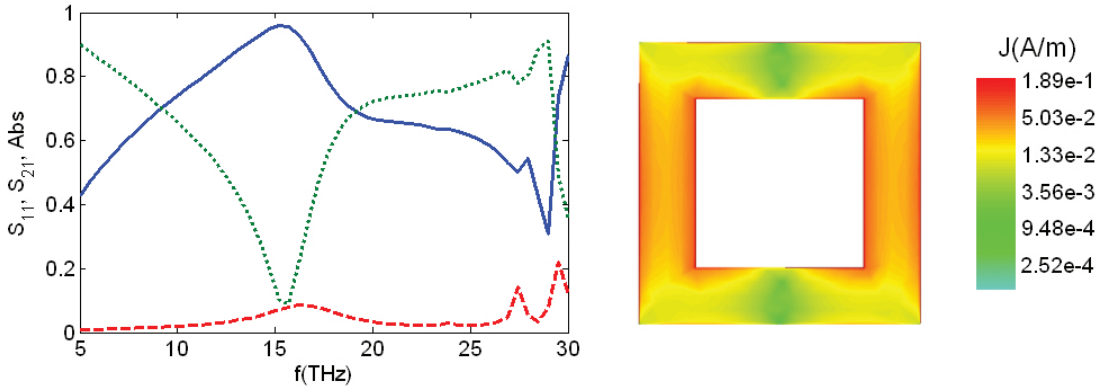

Figure 6.7: *Reflection and absorption characteristic (left) and amplitude of induced current (right) of square-loop FSS with dimensions* $L_{max} = 12\mu m$, $L_{min} = 8\mu m$, $d_x = 20\mu m$, $d_y = 20\mu m$, $w = 2\mu m$.

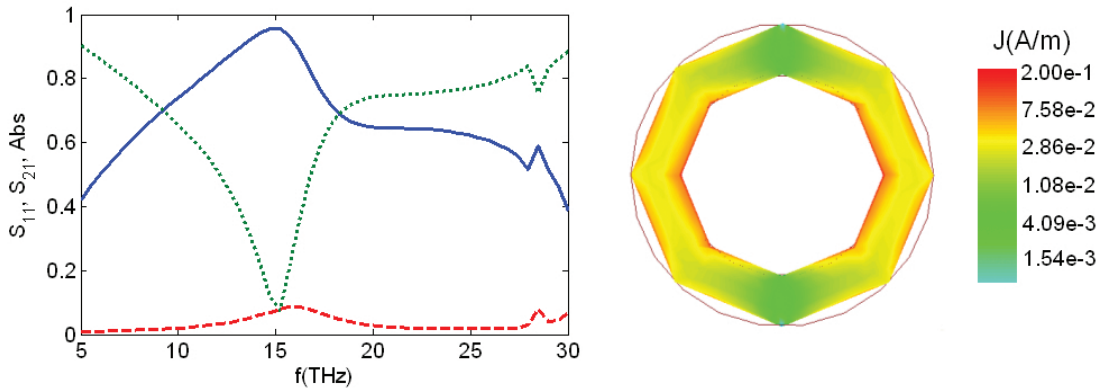

Figure 6.8: *Reflection and absorption characteristic (left) and amplitude of induced current (right) of ring FSS with dimensions* $r_{max} = 5\mu m$, $r_{min} = 3\mu m$, $d_x = 12\mu m$, $d_y = 20\mu m$, $w = 2\mu m$.

Finally, we investigate the performance of the four-legged loaded element, which

derivation from the simple dipole is shown in Figure 6.1d. Briefly, the dipole of length $\lambda/2$ is first shortened to a $\lambda/4$ length, so that capacitively loaded. Subsequently, the $\lambda/4$ dipole is inductively loaded by a two wire-transmission line ($Z_L = jZ_0 tan\beta l$), recovering then the original resonant frequency. Finally, two elements are placed side by side and, because they exhibit the same potential at their ends, they can be connected.

As shown in Figure 6.9 (left), four-legged loaded elements exhibit two resonances under normal incidence. The explanation for the excitation of an additional mode can be well understood by looking into the currents induced on the elements, as shown also in Figure 6.9 (right). At the first resonance ($\approx 10THz$), the currents flow upwards in the same manner as in the previous examples, due to the vertical polarization of the incidence wave. At this frequency, the terminal impedance of the dipoles alone is capacitive, while the load impedance Z_L due to the wire-transmission lines is inductive, giving rise to a resonance. After this resonance, a null known as 'load null' [1] appears at a frequency in which the length of the loaded transmission line is $\lambda/4$ and the load impedance goes to infinity, preventing any current to flow in the loaded transmission lines. After this load null, the impedance of the dipoles alone is inductive, while the load impedance is capacitive, giving rise to a second resonance around $20THz$. At this frequency, the currents in the elements and the loads flow in opposite directions, as shown in Figure 6.9. At this frequency, the loads do not act like loads any more, and therefore the resonant frequency of this mode ($\lambda/4$) is doubled compared to the first mode ($\lambda/2$).

As far as the thermal losses is concerned, both resonances exhibit higher absorption than previous elements, giving rise to around 20% absorption in the example of Figure 6.9, which doubles the absorption obtained for a simple dipole. The four-legged loaded elements consist basically of two connected dipoles (i.e. twice the length of simple dipoles), so that it can be readily understood that the aborption becomes higher than for the simple dipoles.

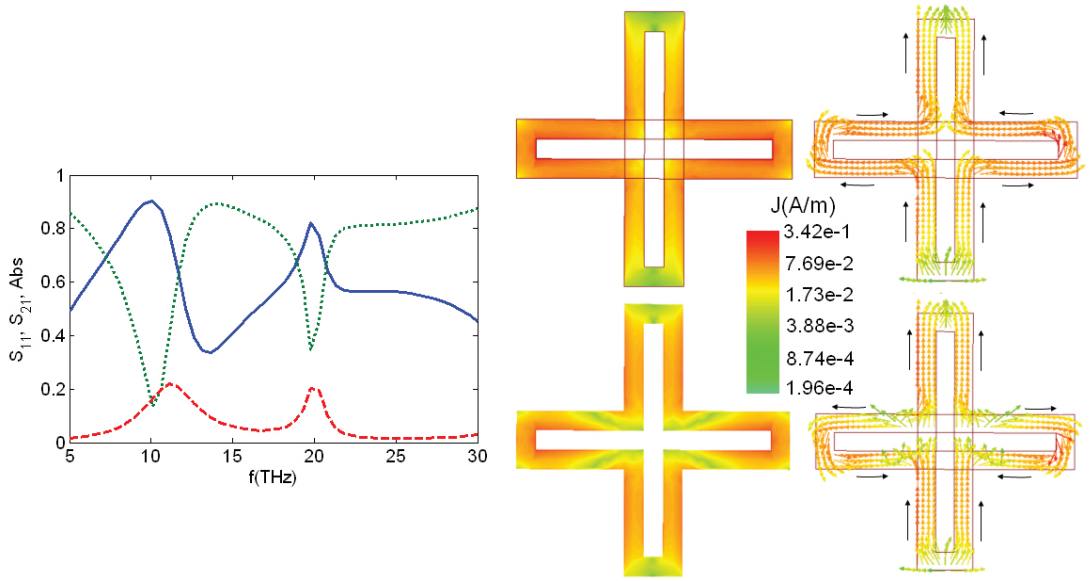

Figure 6.9: *Reflection and absorption characteristic (left) and amplitude of induced current (right) of four-legged FSS with dimensions* $L_{max} = 14\mu m$, $L_{min} = 3\mu m$, $d_x = 28\mu m$, $d_y = 28\mu m$, $w = 2\mu m$.

6.3 Perturbed FSS for multiband and sensing applications

After studying the characteristics of single-band traditional FSS in terms of their S-parameters, absorption and induced currents, now we focus on the investigation of perturbed FSS consisting mainly of dipoles with length perturbation. This configuration was first suggested in [14] for the design of dual-band FSS at microwave frequencies. Here, we design perturbed FSS, as the one shown in Figure 6.10b, working at THz frequencies for multiband and sensing applications. This section first describes the operation of perturbed-dipoles FSS in terms of their terminal impedance and induced currents. Secondly, multiband FSS are designed achieving dual-, tri- and quad-band characteristics as well as dual-band dual-polarized performance by combining dipoles and square-loops or rings. Thirdly, FSS with perturbed elements are investigated for its application in sensing nearby materials.

6.3.1 Perturbed FSS operation

The perturbed array shown in Figure 6.10 can be conveniently described as two coupled unperturbed sub-arrays [14]. One sub-array consists of larger dipoles and is therefore inductively loaded with respect to the unperturbed array ($L_1 > L$). The terminal

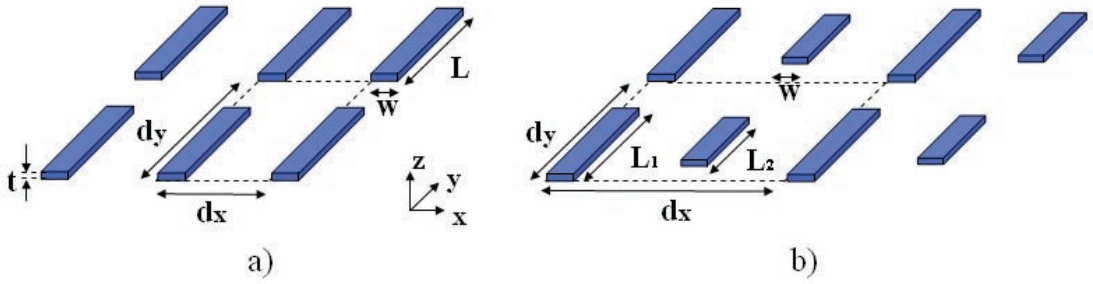

Figure 6.10: *a) Unperturbed FSS ($L_1 = 9\mu m$, $w = 1\mu m$, $d_x = 8\mu m$, and $d_y = 11\mu m$), and b) simply perturbed FSS ($L_2 = 9\mu m$, $L_2 = 7um$, $w = 1\mu m$, $d_x = 8\mu m$, and $d_y = 11\mu m$).*

impedance of this sub-array is $Z_{11} = Ra + j(X_a + \Delta X)$, where $+\Delta X$ represents the inductive electrical loading associated to the increase of length of the sub-array with respect to the unperturbed array. The other sub-array formed by shorter dipoles is capacitively loaded ($L_2 < L$), and its terminal impedance is $Z_{22} = Ra + j(X_a - \Delta X)$. In addition to the self-impedances of the sub-arrays, there is a mutual impedance representing the coupling between both sub-arrays, $Z_{12} = Z_{21} = R_a + jX_m$ for normal incidence, where X_m represents the mutual reactance between the two sub-arrays. The impedance matrix for the perturbed FSS is therefore:

$$\begin{bmatrix} Z_{11} & Z_{12} \\ Z_{21} & Z_{22} \end{bmatrix} = \begin{bmatrix} R_a + j(X_a + \Delta X) & Ra + jX_m \\ R_a + jX_m & R_a + j(X_a - \Delta X) \end{bmatrix} \tag{6.1}$$

The perturbed array in the absence of losses can still be modeled by the circuital equivalence of Figure 4.8b (Chapter 4, section 4.3.1), where now the terminal reactance X_a^p becomes [14]:

$$X_a^p = \frac{X_m^2 - X_a^2 + \Delta X^2}{2(X_a - X_m)} \tag{6.2}$$

The fundamental consequence of perturbing an array is the appearance of a pole $X_a = X_m$, and two zeros $X_a = \pm\sqrt{X_m^2 + \Delta X^2}$ in the reactance X_a^p. The zeros and poles of the reactance correspond to resonances in the perturbed array, exhibiting total or zero reflections, zeros and poles, respectively. Attending to the far-field response, element length perturbation of the FSS produces two reflection bands and a null between them and, therefore, can be applied in dual-band FSS [14].

As we know from Chapter 3, the FSS far-field characteristics (S-parameters) are

determined by the near-field and currents induced in the elements. The currents induced in the perturbed FSS can be obtained by solving Ohm's law in the following matrix form:

$$[Z][I] = [V] \tag{6.3}$$

The impedance matrix is shown in (6.1), while the the current and voltage matrices are the transpose of $[I] = [I_1 \;\; I_2]$ and $[V] = [V_1 \;\; V_2]$. The voltage can be assumed equal to that in unperturbed FSS (V_0) for small perturbations [14]. Upon solving (6.3) at the perturbed FSS resonances, we can identify the nature of the currents induced in the dipoles of each subarray. The system of linear equations given by (6.3) is:

$$\begin{cases} Z_{11}I_1 + Z_{12}I_2 = V_0 \\ Z_{21}I_1 + Z_{22}I_2 = V_0 \end{cases} \tag{6.4}$$

Solving for I_1 and for normal incidence $Z_{12} = Z_{21}$, we obtain:

$$I_1 = \frac{Z_{22} - Z_{12}}{Z_{11}Z_{22} - Z_{12}^2}V_0 \tag{6.5}$$

Using (6.1), the current in the first dipole becomes:

$$I_1 = \frac{R_a + j(X_a - \Delta X) - (R_a + jX_m)}{(R_a + j(X_a + \Delta X))(R_a + j(X_a - \Delta X)) - (R_a + jX_m)^2}V_0 \tag{6.6}$$

and simplifying we obtain:

$$I_1 = \frac{j(X_a - \Delta X - X_m)}{j2R_aX_a - X_a^2 + \Delta X^2 - j2R_aX_m + X_m^2}V_0 \tag{6.7}$$

Similarly for I_2:

$$I_2 = \frac{j(X_a + \Delta X - X_m)}{j2R_aX_a - X_a^2 + \Delta X^2 - j2R_aX_m + X_m^2}V_0 \tag{6.8}$$

We can confirm that for $X_m = \Delta X = 0$, we obtain the currents for the unperturbed FSS, i.e. $I_1 = I_2 = V_0/(2R_a + jX_a)$, and at resonance ($X_a = 0$) the currents are equal to $V_0/2R_a$.

I. Reactance zeros

The reflection resonances in the perturbed FSS are determined by the zeros in the

reactance X_a^p, i.e. $X_a = \pm\sqrt{X_m^2 + \Delta X^2}$. Substituting in (6.7)-(6.8):

$$I_1 = \frac{V_0}{2R_a}\frac{\pm\sqrt{X_m^2+\Delta X^2}-\Delta X - X_m}{\pm\sqrt{X_m^2+\Delta X^2}-X_m} = \frac{V_0}{2R_a}\left[1+\frac{\Delta X}{\mp\sqrt{X_m^2+\Delta X^2}+X_m}\right] \tag{6.9}$$

$$I_2 = \frac{V_0}{2R_a}\frac{\pm\sqrt{X_m^2+\Delta X^2}+\Delta X - X_m}{\pm\sqrt{X_m^2+\Delta X^2}-X_m} = \frac{V_0}{2R_a}\left[1+\frac{\Delta X}{\pm\sqrt{X_m^2+\Delta X^2}-X_m}\right] \tag{6.10}$$

Taking into account that X_m is normally negative and that for small perturbations ΔX is much smaller than X_m [14], the currents for the positive sign of the square roots corresponding to one of the two reactance zeros become:

$$I_1 \approx \frac{V_0}{2R_a}\left[1+\frac{-\Delta X}{2X_m}\right] \approx \frac{V_0}{2R_a} \tag{6.11}$$

$$I_2 \approx \frac{V_0}{2R_a}\left[1+\frac{\Delta X}{2X_m}\right] \approx \frac{V_0}{2R_a} \tag{6.12}$$

which appears to be of the same nature as the resonance of the unperturbed array, i.e. currents flowing parallel and of identical amplitude. This resonance represents the fundamental or *even mode*.

If we now take the negative sign of the square root, we obtain:

$$I_1 \approx \frac{V_0}{2R_a}\left[1+\frac{1}{\Delta X}\right] \approx \frac{V_0}{2R_a}\frac{1}{\Delta X} \tag{6.13}$$

$$I_2 \approx \frac{V_0}{2R_a}\left[1+\frac{1}{-\Delta X}\right] \approx -\frac{V_0}{2R_a}\frac{1}{\Delta X} \tag{6.14}$$

As we can see, the currents in the dipoles flow anti-parallel and exhibit a much stronger amplitude (inversely proportional to ΔX) at this reflection resonance, corresponding to an *odd mode* of propagation.

II. Reactance pole

Consider now the currents at the reactance pole, i.e. $X_a = X_m$. In this case, the currents in (6.7)-(6.8) become:

$$I_1 = \frac{-j\Delta X}{\Delta X^2}V_0 = -\frac{jV_0}{\Delta X} \tag{6.15}$$

$$I_1 = \frac{j\Delta X}{\Delta X^2} V_0 = \frac{jV_0}{\Delta X} \tag{6.16}$$

Similar to the case of the reactance zero with negative sign of the square root, at the reactance pole the currents induced in the dipoles also flow anti-parallel, exhibit much stronger amplitude and represent an odd mode of propagation.

As we will investigate later in section 6.3.3, the excitation of the odd mode in perturbed FSS will not only offer the possibility of achieving single-screen multiband FSS, but also provide interesting near-field properties, particularly in the field of near-field enhancement for sensing applications.

6.3.2 Multiband perturbed FSS

Firs, we investigate the influence of the FSS perturbation on the far-field characteristic for its viability in multiband applications. Following the design of dual-band FSS, we extend the FSS performance to achieve tri- and quad-band characteristics by adding two and three perturbations, respectively. We further employ two different elements in each sub-array in order to obtain dual-band dual-polarized FSS.

Figure 6.11 shows MoM results for the far-field reflection coefficient of an FSS based on parallel dipoles with length perturbation, as depicted in Figure 6.10. The incident wave is set to be vertically polarized. The unit cell of the array consists of vertical d_y and horizontal d_x dimensions fixed at $11\mu m$ and $8\mu m$, respectively. The width w is fixed at $1\mu m$. The length of the dipoles of the subarray 1 (L_1) is fixed at $9\mu m$, while the length of the dipoles of the subarray 2 (L_2) ranges from $9\mu m$ to $3\mu m$. In the unperturbed case, $L_1 = L2 = 9\mu m$ and only one resonance appears at $14.5THz$ (reflection band 1). When the array is perturbed by decreasing the length L_2, even and odd modes are present, giving rise to two reflections (bands 2 and 3) and a modal-interaction null (bands 4).

It can be seen that the lower resonant frequency in the perturbed case is almost constant at $10.5THz$ (reflection bands 2), while the location of the upper resonant frequency (reflection bands 3) increases as the L_2 is decreased. Intuitively, this is due to the fact that the lower resonance is dominated by the subarray 1 (dipole with fixed length at $L_1 = 9\mu m$) and the upper resonances are mainly due to the subarray 2 (dipoles with varying length L_2 from $7\mu m$ to $3\mu m$). The increase in the upper resonant frequency

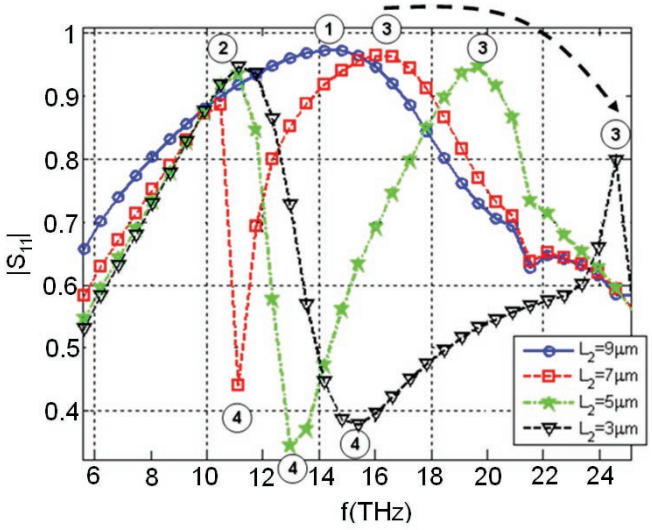

Figure 6.11: *Far-field reflection coefficient of perturbed FSS vs frequency for length of the dipoles of subarray 1 fixed at $9\mu m$ and subarray 2 ranging from $L_2 = 9$ to $3\mu m$. The numbers in the figure indicates the various resonances of each case. 1 indicates the even mode in unperturbed FSS. 2, 3, and 4 indicate the odd mode, even mode and interaction null in perturbed FSS, respectively.*

for varying L_2 is because shorter dipoles exhibit lower value of equivalent capacitance between collinear elements. In the most extreme case (L_2 approaching $0\mu m$), the upper resonance would disappear, giving rise to an unperturbed FSS with double horizontal dimension of the unit cell and resonance fixed by L_1.

This intuitive understanding of the behavior of the FSS is a simple approximation, but it is not really the mechanism underlying the appearance of the new resonance. The behavior of perturbed FSS was accurately described in section 6.3.1. The two reflection bands separated by a null are a consequence of the excitation of two propagation modes, even and odd modes, in which the currents induced in the dipoles flow parallel and anti-parallel, respectively, as shown in Figure 6.12. A rigorous analysis of the induced currents will be carried out in the following section when analyzing perturbed FSS for sensing applications.

The lengths of the dipoles mainly control the location of the two resonances. The length-difference roughly determines the bandwidth (and Q-factor) of the two resonances. For instance, small perturbations ($L_2 \approx L_1$, that is $\Delta L \rightarrow 0$) gives rise to one sharper and another broader resonance. As the perturbation increases, the bandwidths of both resonances even up. In the limit, when the length difference ΔL

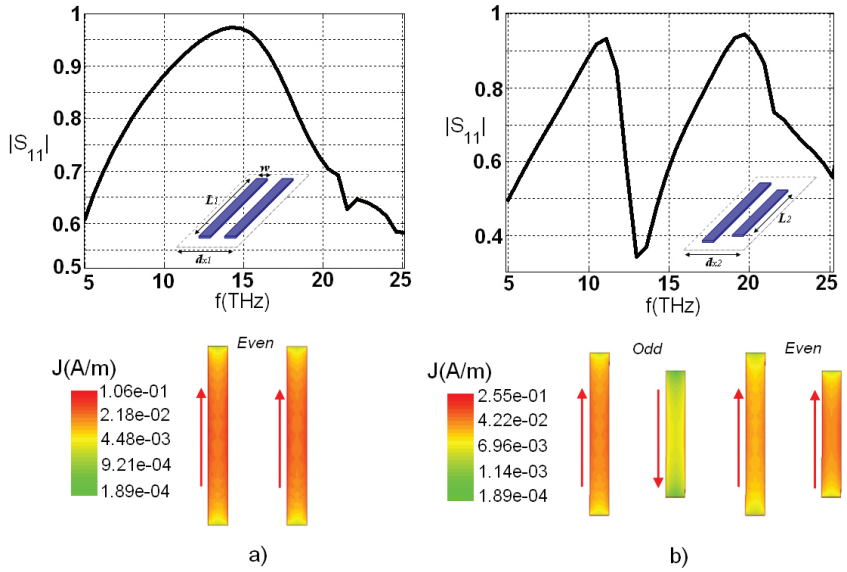

Figure 6.12: *Simulated reflection coefficient versus frequency by full-wave MoM of a) unperturbed FSS ($L_1 = 9\mu m$, $w = 1\mu m$, $d_x = 8\mu m$, and $d_y = 11\mu m$), and b) simply perturbed FSS ($L_2 = 9\mu m$, $L_2 = 7\mu m$, $w = 1\mu m$, $d_x = 8\mu m$, and $d_y = 11\mu m$). The magnitude and direction of the currents at the even and/or odd modes are also shown.*

is close to L_1, the higher resonance disappears. Also, it is important noticing that the periodicity must be kept small enough to avoid the onset of grating lobes around the upper resonance.

This perturbation principle has been extended to reach tri- and quad-band responses by introducing two and three perturbations, respectively. Figure 6.13 plots the simulated reflection coefficients of doubly and triply perturbed FSS. The addition of perturbations gives rise to additional resonances corresponding to odd modes in which the amplitude and direction of the induced currents varies as shown in Figure 6.13.

For doubly-perturbed FSS, three modes are identified, one even mode and two odd modes. In the even mode (higher frequency), the currents in the three dipoles flow parallel and exhibit similar magnitude. In the odd modes (lower and middle frequency), however, the magnitude of the currents is dominated by one of the dipoles, and the currents do not flow parallel in all dipoles. In the first odd mode (lower frequency), the longer dipole exhibit higher current flowing anti-parallel to the shorter dipoles. In the second odd mode (middle frequency), the current induced on the middle dipole is significantly higher than the others and flows parallel to the longer dipole and

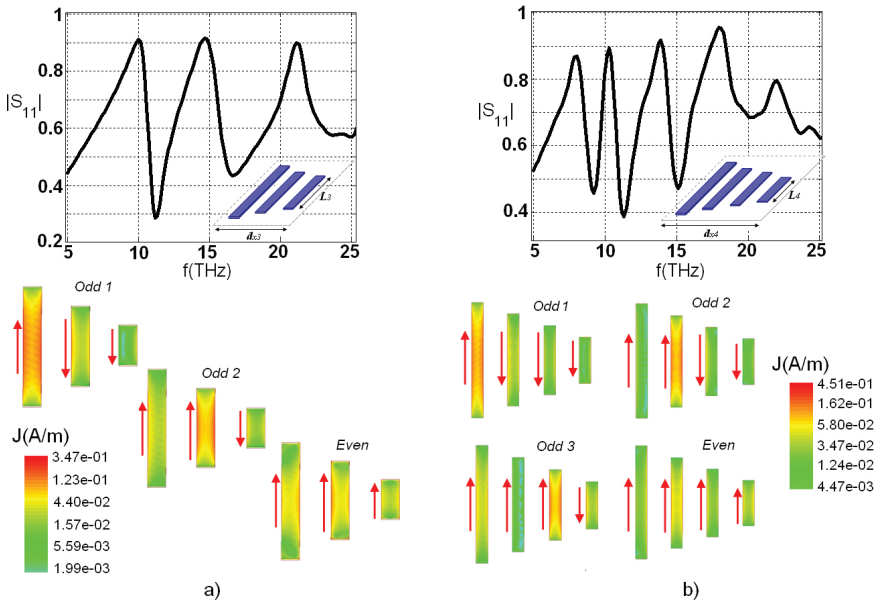

Figure 6.13: *Simulated reflection coefficient versus frequency by full-wave MoM of a) doubly perturbed FSS ($L_1 = 9\mu m$, $L_2 = 7\mu m$, $L_3 = 5\mu m$, $w = 1\mu m$, $d_x = 12\mu m$, and $d_y = 11\mu m$), and c) triply perturbed FSS ($L_1 = 10\mu m$, $L_2 = 8.5\mu m$, $L_3 = 7\mu m$, $L_4 = 5.5\mu m$, $w = 1\mu m$, $d_x = 16\mu m$, and $d_y = 11\mu m$). The magnitude and direction of the currents at the even and/or odd modes are also shown.*

anti-parallel to the shorter dipole. The triply-perturbed FSS, shown in Figure 6.13b, gives rise to an additional odd mode, which amplitude and direction follow the same principle as the other odd modes.

In addition to the linearly-polarized perturbed FSS shown before, dual-band dual-polarized strip-ring configurations have been designed where one sub-array is made of dipoles, while another sub-array consists of circular loops or rings, as shown in Figure 6.14. In this case, at the dipole's resonance (8THz), only vertical polarization is reflected, while both vertical and horizontal polarizations are reflected at the ring's resonance (11.5THz).

In this section, the use of simply perturbed FSS in dual-band plane-wave filters have been reported. Multiband and dual-band dual-polarized performance have been demonstrated by adding more perturbations and including different element types, respectively. In the following section, we turn our attention to the use of perturbed FSS as components for sensing systems.

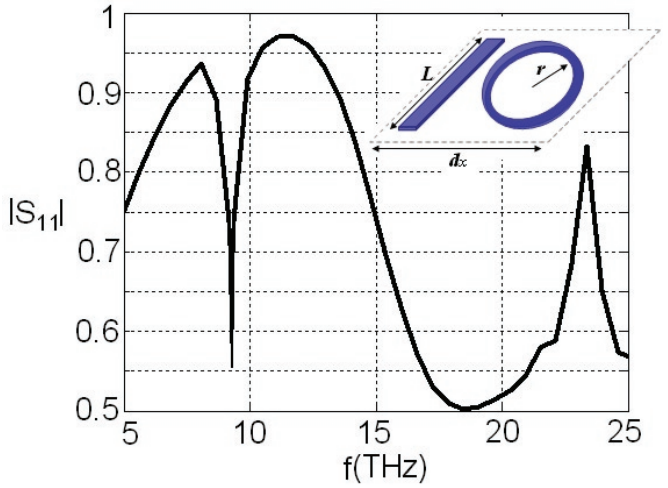

Figure 6.14: *Reflection coefficient of a dipole-ring FSS ($L = 9\mu m$, $w = 1\mu m$, $d_x = 8\mu m$, $d_y = 16\mu m$, and $r = 4\mu m$).*

6.3.3 Sensing using perturbed FSS

As explained in Chapter 2, periodic metallo-dielectric arrays have been thoroughly investigated over the last few years across a wide frequency spectrum and applied in filtering components, electromagnetic absorbers, radiating structures and guiding systems [1, 3, 64, 224]. Recently, the study of the interaction of the near-fields of resonant planar arrays such as FSS with chemical or biochemical materials has led to increasing interest towards using these arrays in sensing components [11, 170]. The capability of resonant systems for storing energy allows enhanced interaction between the near-fields of the array and any material in the vicinity of the array. The sensing performance for a sensor based on resonant structures is often determined by the steepness of its frequency response. This is quantified in terms of the quality factor (see Chapter 4), which, in turn, is associated with the magnitude of the electric/magnetic field at the probing point. In such a scheme, sensing is often based on the shift of the transmission/reflection frequency response induced by the presence of the sensed material [11,170]. A lossless resonator decoupled from any input or output ports would exhibit infinite quality factor (i.e. a single spectral line of zero bandwidth). However the spectral response of practical FSS broadens due to both the coupling with the input and outgoing propagating waves as well as the thermal losses (see Chapter 4). Maximizing the stored power and minimizing the dissipated power represent the two targets when designing FSS as sensors.

6.3.3.1 Near-field enhancement

The study performed in Chapter 4 reveals that unperturbed FSS may be employed as sensing components. However, the degree of freedom for tuning the dimensions in unperturbed FSS faces limitations which are inherent in periodic resonant arrays. For instance, the periodicity must be kept small enough to push the onset of grating lobes away from the FSS main resonance. Moreover, the dimensions of the elements can be decreased up to the point that the main resonance is distorted, disappeared or shifted near the onset of grating lobes.

An alternative technique to enhance the power stored in FSS is based on perturbation of the array, as shown in Figure 6.10. This length perturbation represents a particular case of generally perturbed FSS with certain asymmetry in the elements, similar to the work done before by [11, 170]. The most apparent effect of perturbing an array is the modification of its spectral signature. The reflection response shown in Figure 6.15 for the perturbed and unperturbed array manifests this effect. Two frequency points of full reflection can be identified corresponding to the two zeros of the equivalent terminal reactance (even and odd modes) [14]. Moreover, one reflection null is observed resultant of the pole found in the perturbed terminal reactance. The new resonance, around 17THz, which appears by effect of the perturbation, represents a sharper spectral response than the unperturbed resonance at 23THz superimposed here for comparison and, thus it seems more suitable for sensing systems.

To probe into the effect observed in the far-field, a thorough investigation of the perturbation effects on the near-fields and the currents induced on the two dipoles is carried out. Figs. 6.16a-d show the magnitude and phase of the currents in both dipoles within the unit cell of same dimensions as in Figure 6.15. The amplitude of the currents significantly increases within the frequency range 16.5 and 18.1THz which coincides with the sharp resonance observed in the reflection response. Moreover, in this frequency range, the currents in the two dipoles flow out-of phase with the incident field (odd mode). In contrast in the unperturbed case, 23THz, the currents in both dipoles have comparable magnitudes and are in phase with the incident field (even mode).

Figure 6.17a-b shows the longitudinal component of the magnetic field H_z at the plane

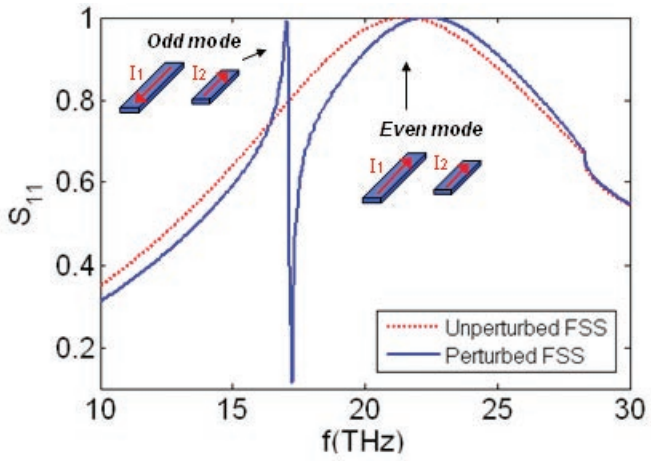

Figure 6.15: *Reflection coefficient S_{11} versus frequency for the perturbed FSS of Figure 6.10, with L_1 = 8.2μm, L_2 = 7.5μm, w = 0.5μm, d_y = 10.6μm, and d_x = 7.7μm. For comparison the S_{11} for an unperturbed FSS with the same dimensions and L = 8.2μm is added.*

of the array, XY, at 17.34GHz (odd mode and modal interaction null frequency) and at 23THz (even mode). Since the currents of both dipoles flow parallel at the even mode, following the right-hand's rule, the magnetic field normal to the plane of the array, along the z-axis, produced by one dipole is opposing that produced by the nearby dipole canceling in the area between. However, at the odd mode the anti-parallel current flow leads to constructive interference in the area between them exhibiting an enhanced near-field. The near-field can be enhanced nearly two orders of magnitude by appropriately tailoring the FSS dimensions.

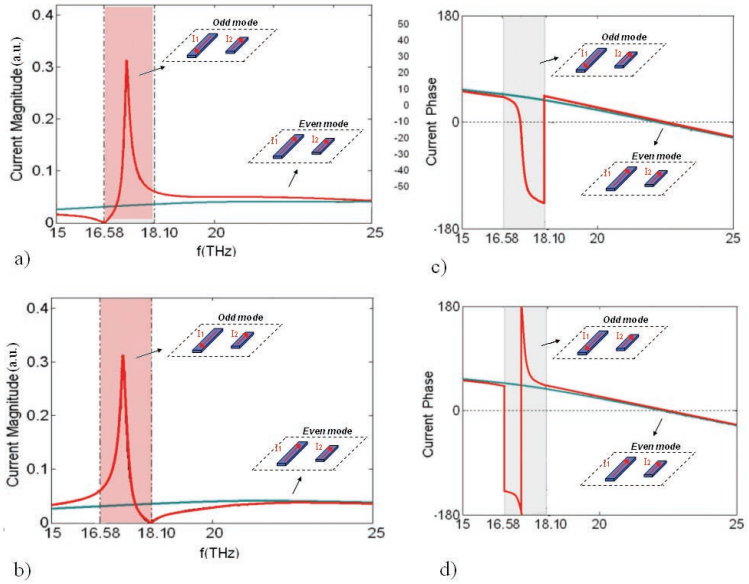

Figure 6.16: *a-b) Magnitude of current induced on the long and short dipole, respectively. c-d) Phase of current induced on the long and short dipole, respectively. The dimensions of the FSS are those employed in Figure 6.15.*

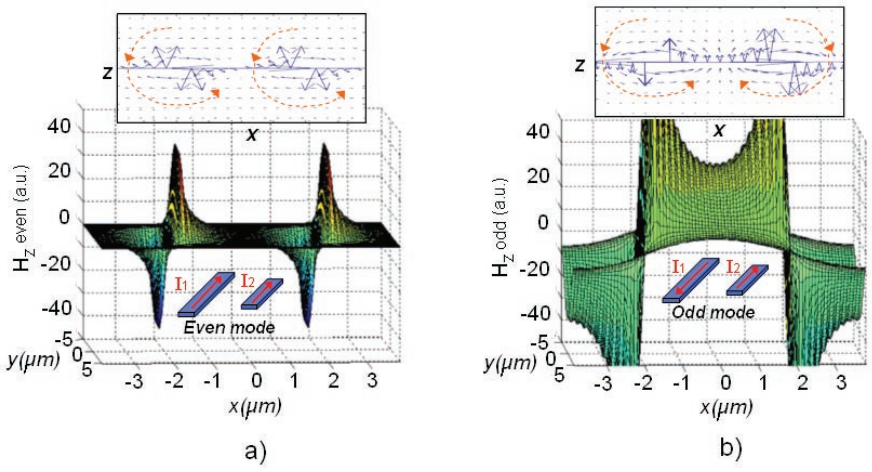

Figure 6.17: *a-b) z-component of magnetic near-field for the even and odd modes, respectively. The dimensions of the FSS are those employed in Figure 6.15.*

In order to provide guidelines for the design of perturbed FSS sensors, the loaded Q-factor in the presence and the absence of losses for variable length L_2 is shown in Figure 6.18, where the Q_L for an unperturbed FSS with L=8.2μm is also plotted for comparison.

The quality factor shown in Figure 6.18 for both lossless and lossy perturbed FSS requires special attention. Ideally in the absence of losses the perturbed FSS exhibits an exponentially increasing Q_L as L_2 approaches L_1. The smaller the perturbation, the stronger the induced currents and near-fields of the odd mode, which represents a higher quality factor. However, since stronger currents entail also higher absorption in the presence of losses, the smallest perturbation achieved when L_2 tends to L_1, does not lead to the highest Q_L. The optimum length of the shorter dipole L_2 that achieves the maximum value of Q_L for the dimensions considered here (d_x, d_y, L_1, w) is found to be about 6.7μm. This corresponds to a decrease of 18.3% in the length of every second dipole. Thus, there is a trade-off between thermal losses and loaded Q-factor, which did not appear in the unperturbed arrays.

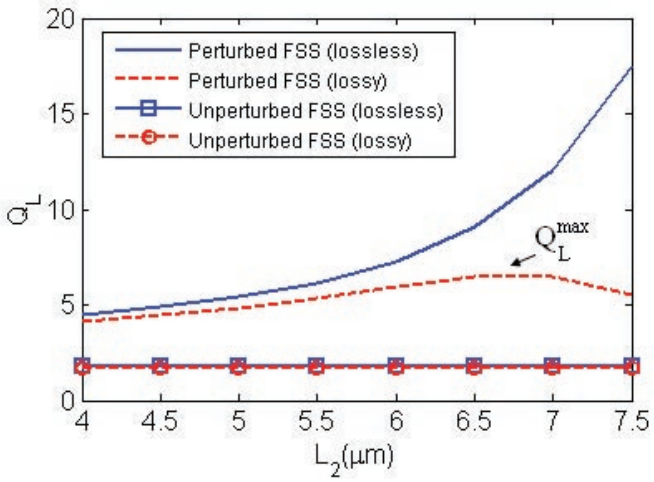

Figure 6.18: *Loaded Q-factor Q_L as a function of L_2 for the perturbed FSS of Figure 6.10, with L_1 = 8.2μm, w = 0.5μm, d_y = 10.6μm, and d_x = 7.7μm. For comparison the Q_L for an unperturbed FSS with the same dimensions and L = 8.2μm is added.*

6.3.3.2 Sensing performance

A perturbed FSS supported by a dielectric layer of thickness $t_{die} = 1.7\mu m$, permittivity 3.5, and loss tangent 0.008 is considered for sensing a slab of certain material under investigation. The slab is adjacent to the FSS array as shown in the inset of Figure 6.19. For simplicity, the electrical properties of the material under investigation are considered dispersionless. Its loss tangent is assumed 0.008, while the permittivity ϵ_r and thickness t_{mat} are varying. Figure 6.19 shows the far-field response and electric

near-field of the perturbed FSS within a unit cell. The enhanced electric near-field corresponding to the odd mode at 10.5THz is found at the top and bottom edges of the dipoles. In Figure 6.20, the frequency shift due to the presence of a material on the FSS is obtained for various thicknesses and permittivity of such material.

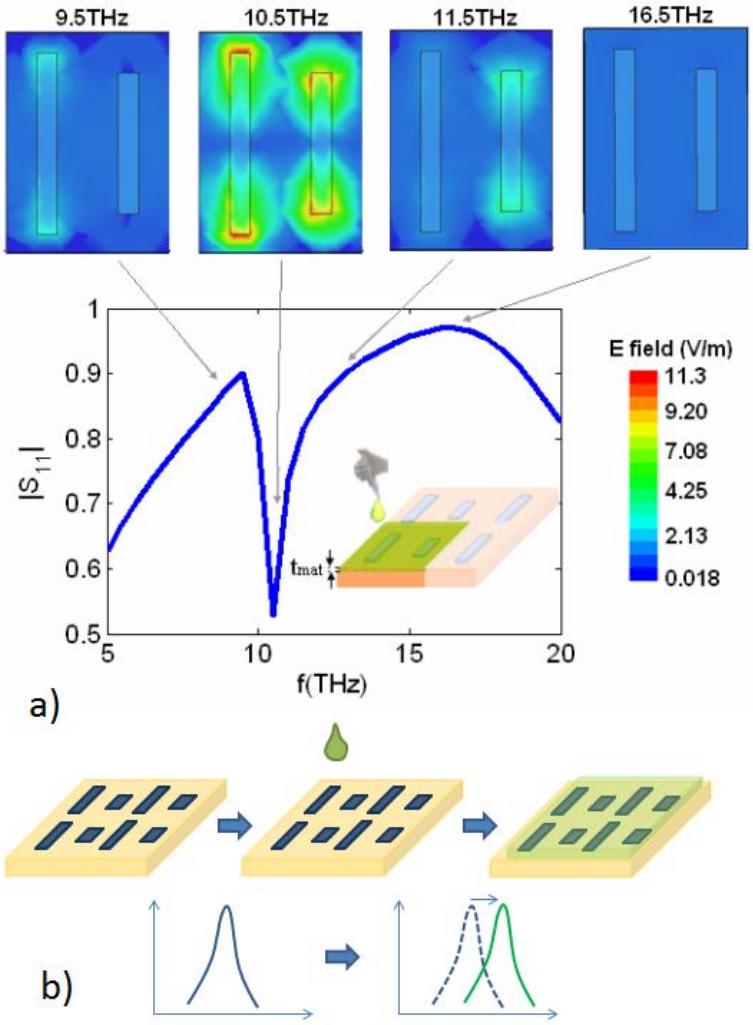

Figure 6.19: *a) Magnitude of electric field in the unit cell of a perturbed FSS (L_1 = 9μm, L_2 = 7μm, w = 1μm, d_y = 8μm, d_x = 10μm) supported by a dielectric layer (t_{die} = 1.7μm, ϵ_r = 3.5, $tan\delta$ = 0.008). b) Scheme of the sensing mechanism, showing the expected measured resonant shift after the sensed material is deposited on the FSS.*

As defined in [170], the sensitivity can be calculated as the shift in resonance wavelength per unit change of the refractive index $(\mu m/RIU)$. The sensitivity of our system is not entirely linear; it depends on the properties of the material sensed (i.e.

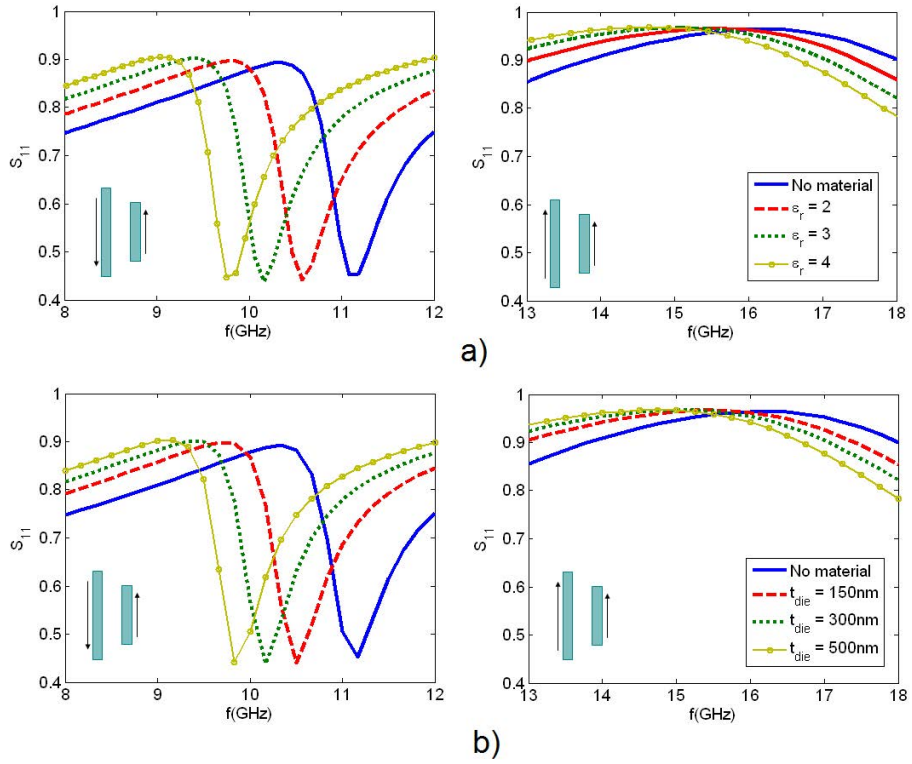

Figure 6.20: *Frequency shift for a) 300nm of a material with variable permittivity ϵ_r, and b) various thicknesses t_{mat} of a material of $\epsilon_r = 3$. The shift is shown for both the odd (left) and even (right) modes*

refractive index), due to non-linear dielectric-loading effects [63]. The higher the index of refraction, the more sensitive the system is. However, this is not an issue, since it is an expected and predictable behavior, which can readily be taken into account.

For clarity, we can distinguish between two definitions of the sensitivity, depending on the use of the sensing system. For detection or characterization of materials, the resonance wavelength λ_1 produced by the FSS with the sensing material n_1 is compared to the resonance wavelength λ_0 produced by the FSS with no sensing material $n_0 = 1$, and the sensitivity is defined as:

$$S_{det} = \frac{\lambda_1 - \lambda_0}{n_1 - 1} \tag{6.17}$$

When the sensing system is used to differentiate two materials (n_1, n_2), the sensitivity is generalized as:

$$S_{diff} = \frac{\lambda_2 - \lambda_1}{n_2 - n_1} \tag{6.18}$$

Here, the formulation for material characterization (only one sensing material) is employed. The calculated sensitivity for a $300nm$ thick sensing material of refractive index $n_1 = 1.41$ is $2.5\mu m/RIU$ approximately (Figure 6.20). This sensitivity improves to $4.88\mu m/RIU$ for sensing materials with higher refractive index ($n_1 = 2$) due to the non-linearity mentioned before. The figure of merit FOM, defined as the sensitivity divided by the linewidth at half-maximum [170] ($\approx 2\mu m$ in this case), ranges from 1.24 ($n_1 = 1.41$) to 2.44 ($n_1 = 2$).

In addition, as shown in Figure 6.20b, the increase in the amount of sensing material deposited can lead to a significant increase in the sensitivity of the system due to higher interaction with the near-fields of the FSS. For instance, the sensitivity for a sensing material of refractive index $n_1 = 1.73$ improves from $2.86\mu m/RIU$ ($FOM = 1.7$) for $300nm$ deposited material to $4.8\mu m/RIU$ ($FOM = 2.4$) and $8.7\mu m/RIU$ ($FOM = 4.35$) for $500nm$ and $1\mu m$ deposited material, respectively. Therefore, in spite of the non-linearity related to the substrate-loading effect in resonant arrays, the values of sensitivity and FOM are fairly good as compared to other sensing devices [170]. The sensitivity is still improved in differentiation applications. For instance, the sensitivity for distinguishing two materials ($300nm$ thick) of $n_1 = 1.73$ and $n_2 = 2$ is $10.378\mu m/RIU$ ($FOM = 5.18$).

6.4 Experimental validation of perturbed FSS

In this section, we demonstrate experimentally the excitation of the even and odd mode in a perturbed FSS working at THz frequencies. The fabrication of the FSS and the measurements were carried out following the fabrication process and measurement set-up detailed in Chapter 3.

The FTIR measurement of the transmission S_{21} of $1.7\mu m$ PI membranes is shown in Figure 6.21. Besides the reflection peaks due to its internal bonds, PI thin membranes exhibit around 70% of transmission.

The measurement of the unperturbed FSS with $L = 7\mu m$, $w = 1\mu m$, $d_x = 8\mu m$, and $d_y = 11\mu m$ in comparison with the simulated transmission and normalized with the PI-only response is plotted in Figure 6.22a. The resonant frequency obtained at 14.13THz, corresponding to the even mode, is in good agreement with the simulated

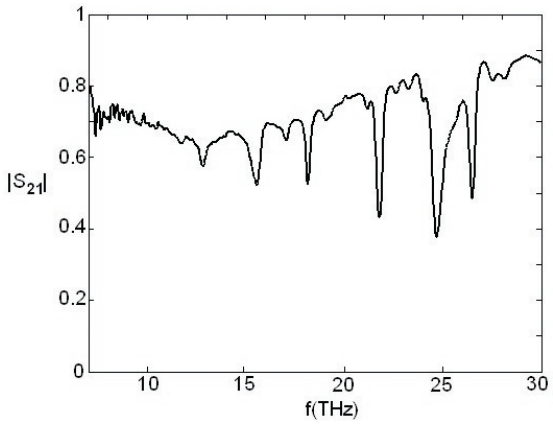

Figure 6.21: *Transmission FTIR measurements of* $1.7\mu m$ *thick PI membrane.*

responses. However, the amplitude of the measured transmission in the reflection band is higher than that from the simulation under vertically polarized incident wave. This is because the IR source of the FTIR is not vertically polarized, but unpolarized. Therefore, only the vertical component is reflected by the FSS (since y-oriented dipoles are sensitive solely to the vertical polarization), resulting in energy transmitted in the horizontal component to the IR detector which did not occur in the simulated response. Simulations of the transmission under elliptically polarized incident wave (polarization ratio between vertical and horizontal polarization of 1.5) have been performed and the result is superimposed in Figure 6.22a for comparison. The simulated response under elliptical polarization shows an increase in the amplitude of the transmission at resonance, similar to the measured amplitude response. Elliptical polarization, corresponding to a defined state of polarization, is different to unpolarized radiation, which exhibits rapid and random changes of polarization with time. However, it can be seen that FSS simulated under elliptical polarization represents a closer situation to the measurement set-up than FSS simulated under purely vertical polarization, thus confirming the impact of the unpolarized nature of the FTIR source (i.e. decreased coupling between the electric field of the incident wave and the metallic strips of FSS).

Figure 6.22b shows the measured transmission of simply perturbed FSS with $L_1 = 9\mu m$, $L_2 = 5\mu m$, $w_1 = w_2 = 1\mu m$, $d_x = 8\mu m$, and $d_y = 11\mu m$. Two resonances at 11THz and 20THz can be identified, in agreement with the superimposed simulated responses, and corresponding to the odd and even modes, respectively. Similar to the unperturbed FSS, the amplitude of the measured transmission in the reflection bands is higher than

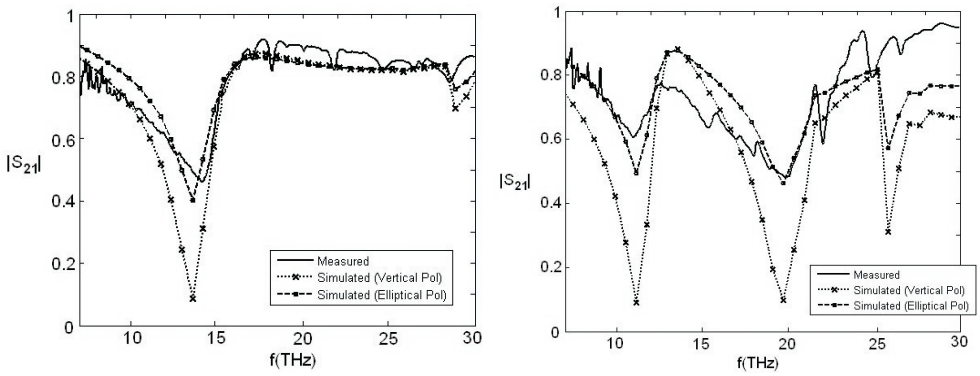

Figure 6.22: *Transmission FTIR measurements of an a) unperturbed FSS ($L = 7\mu m$, $w = 1\mu m$, $d_x = 8\mu m$, and $d_y = 11\mu m$) and a b) perturbed FSS ($L_1 = 9\mu m$, $L_2 = 5\mu m$, $w_1 = w_2 = 1\mu m$, $d_x = 8\mu m$, and $d_y = 11\mu m$) on a $1.7\mu m$ thick PI membrane. Measured responses are normalized by the PI transmission of Figure 6.21, and compared to simulated responses under vertically and elliptically polarized plane-waves.*

the simulated response under vertically polarized incident wave due to the polarization sensitivity of the elements of the FSS. Likewise, the simulation of the perturbed FSS under elliptically polarized incident wave is superimposed in Figure 6.23b in order to confirm the impact of polarization on the FSS.

Figure 6.23 plots the transmission of the dual-band dual-polarized FSS based on strip-ring configuration ($L = 9\mu m$, $D = 8\mu m$, $w = 1\mu m$, $d_x = 12\mu m$, and $d_y = 11\mu m$). In this case, the resonance at 13THz due to the ring elements, which are insensitive to polarization, shows the same value of the amplitude in the simulations with vertical polarization and measurements (with unpolarized incident wave). On the other hand, the resonance at 9.3THz due to the dipole elements indicates sensitivity to polarization, through the presence of an increase in the measured transmission (with unpolarized incident wave) compared to the simulated response with vertical polarization.

In general, good agreement is obtained for the different designs. The slight shift in the resonant frequencies between the simulated and fabricated responses is likely to be due to small variations between the simulated and fabricated values of the thickness and/or dielectric permittivity of the PI membrane, as well as accuracy in the patterning of the FSS elements.

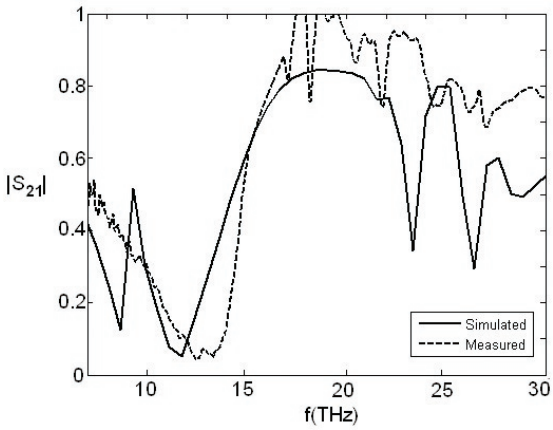

Figure 6.23: *Transmission FTIR measurements of an dual-band dual-polarized FSS based on rings and dipoles, $L = 9\mu m$, $D = 8\mu m$, $w = 1\mu m$, $d_x = 12\mu m$, and $d_y = 11\mu m$. Measured response normalized by the PI transmission of Figure 6.21.*

6.5 Conclusions

This chapter has presented the application of single-screen FSS in single- and multi- band filters as well as sensing systems. Traditional elements have been first investigated in terms of bandwidth and losses. Subsequently, perturbed FSS have been demonstrated, theoretically and experimentally, for their potential use in multiband and sensing FSS. The novelty and contributions of the work presented in this chapter is outlined in the following:

- Assessment of performance of traditional single-screen FSS in terms of induced currents and absorption at THz

The performance of various types of FSS, focusing on the amplitude and distribution of the induced currents as well as the dissipated power, has been assessed in the THz regime. It has been found that the more dissipative elements are those which induce stronger currents, similar to the results shown in the parametric analysis of chapter 4 for dipole elements. This study offers a clear view of the dissipation performance of various FSS at THz.

- Investigation of the behaviour of perturbed FSS, exhibiting even and odd modes

The type of FSS known as perturbed FSS, introduced for its application in the microwave regime by R. A. Hill and B. A. Munk back in 1996, is analyzed and

investigated in the context of THz FSS. The appearance of an odd resonance due to the length perturbation of simple dipole FSS (i.e. varying the length of every second dipole) has been investigated. The novelty of our study lies on the fact that the behaviour of perturbed FSS is investigated not only in the far-field (leading to dual-band operation), but also in the near-field, which leads to the potential application of this type of FSS in sensing systems. The new odd mode appearing from the perturbation of the FSS has been shown to lead to anti-parallel flowing currents, near-field enhancement and sharp resonances.

- *Experimental demonstration of single-screen FSS exhibiting multiband performance at THz*

To the best of our knowledge, experimental demonstration of single-screen multiband FSS operating at THz has only been done before by J. A. Bossard et al (2006) using fractal designs optimized by genetic algorithms. In this chapter, an alternative method to achieve multiband performance has been experimentally demonstrated using single-screen perturbed FSS. FTIR equipment has been used to test prototyped multiband FSS, and the measurements have shown good agreement with the simulations. The benefits of this approach lies on the easier and more intuitive design, easily related to the dissipating and storing capabilities, and the potentiality to use different type of elements simultaneously. Perturbed FSS has been designed to achieved dual-, tri-, and quad-band FSS using perturbation in the length, as well as dual-band dual-polarized FSS using dipoles and rings simultaneously.

- *Novel sensing approach based on near-field enhanced FSS*

The near-field characteristics of perturbed FSS has been used to design FSS sensitive to the materials in its vicinity. The presence of materials near the FSS array shifts the resonance of the FSS, and therefore, the presence or absence of certain material can be detected. In addition, characterization of the electromagnetic properties of materials can be carried out by measuring the amount of frequency shift with respect to a reference. FSS sensors at THz frequencies have only been started to be investigated in recent years. Some of the proposed designs also consist of asymmetric FSS exhibiting sharp resonances. However, to the best of our knowledge, detailed descriptions of the near-field enhancement explanation of these sharp resonances are given for the first

time. In addition, physical limitations of these types of resonant sensors due to thermal losses have been investigated.

Chapter 7
Multilayered and Tunable FSS at THz frequencies

7.1 Introduction

Single-screen FSS have been fully investigated in previous chapters. Single-screen arrays are mostly applied in single-band applications, as filters, polarizers or sensors. The single-band capabilities of traditional single-screen FSS can be extended to multiband performance by using sub-arrays resonating at different frequencies (e.g. concentric rings, perturbed dipoles,...), by adding other types of perturbations such as SIW waveguides, or by using optimized fractal designs. Multilayered FSS represent another approach to reach multiband performance. In contrast to perturbed FSS where two sub-arrays are placed on the same and only layer, multilayered FSS for multiband applications place the sub-arrays resonating at different frequency on different layers. This results on additional ohmic and/or dielectric losses, which may not be suitable for specific high-performance applications.

Multilayered FSS may be employed not only in multiband FSS, but also in other kinds of applications due to their characteristics in terms of higher roll-off, resonance planarity, or angular stability [1, 125, 225]. FSS consisting of more than one layer can be represented by RLC circuits representing the complex impedance of the FSS sheets, separated by transmission lines modeling the dielectric layers separating the FSS sheets. A rigorous implementation of this circuital model requires the analysis of the FSS sheet impedances for each Floquet mode, since low-order Floquet modes representing the near-field in the vicinity of the FSS layers will couple with the other closely spaced FSS layers.

For simplicity, we consider in this chapter only two cascaded FSS. When two identical FSS are placed at a distance around $\lambda/2$, a broader response is achieved, in which we can identify three so-called 'array interaction nulls' (zero reflection in capacitive FSS),

namely f_L, f_H, and f_M, corresponding to frequencies at the lower and higher ends (giving rise to characteristic 'ears' of multilayered FSS response), and the middle of the resonance, respectively [1]. The presence of the null f_M for separations others than $\lambda/2$ normally imposes strict constraints on the separation of the two-layered FSS. The presence and location of these array interaction nulls depends upon the separation between layers, and the dimensions of the two FSS arrays. Commonly, FSS with identical dimensions have been used in order to obtain broader bandwidth and/or higher roll-off performances [1, 125, 225], whereas FSS with different dimensions have been employed to obtain multiband characteristics [4]. Recently, closely coupled FSS (CCFSS) and complementary FSS (CFSS) consisting of two very closely spaced FSS layers were used for enhancing significantly the angular stability of FSS by shifting the resonance well below the grating lobe region [226, 227]. In these designs, two bands are identified, separated by an interaction null. An interesting characteristic of these closely coupled arrays lies in the effect of the separation of the layers on the location of the resonances. When closely coupled and shifted, the distance between two cascaded arrays determines the resonance frequency. This concept can be employed in (electro)mechanically tunable FSS.

In this chapter, we carried out a thorough investigation on closely coupled FSS and their potential applicability in reconfigurable plane-wave filters by mechanically varying the separation, and hence the coupling, of the two FSS arrays. For doing so, we divide the study into two main parts. First, we investigate the effects of the separation between layers with identical (equal-tuning), different (staggered-tuning), aligned and misaligned elements. The analysis is carried out for free-standing dual-layer FSS to account only for ohmic losses. Special attention is placed on the frequency-tuning capability of the different configurations. Secondly, we investigate theoretically a possible way of implementing such a reconfigurable dual-layered FSS working at THz frequencies, using Microelectromechanical Systems (MEMS). The small size of arrays resonating at THz frequencies allow for the integration of FSS and MEMS technology in a simple manner. FEM simulations of MEMS membranes which would support and move one of the FSS layer with respect to the other are carried out, and potential fabrication procedures and issues are presented.

7.2 Closely Coupled FSS

In this section, a detailed investigation of the behavior of coupled FSS is carried out in terms of resonances (including interaction nulls), losses and induced currents. For simplicity, here we consider two coupled FSS free-standing layers consisting on Al dipoles. Equal-tuning, staggered-tuning, aligned and misaligned elements with respect to the other layer are used. Commercial software Ansoft Designer, described in Chapter 3, is employed to obtained the currents and S-parameters in the following subsections. The distance between FSS layers is varied from 0.015λ to 0.3λ, and the single-layer case is also included for comparison. The variation of coupling with the distance between FSS is readily explained by the change in the capacitance between the two metallic elements of each layer of the FSS. This capacitance is inversely proportional to the distance, and therefore, the closer the FSS, the stronger coupling and resonant shift, as we will observe in the following sections.

7.2.1 Equal-tuning and aligned dipoles

The simplest and most intuitive configuration consists of two arrays of aligned identical unit cells. Such case with dimensions $L = 9\mu m$, $w = 1\mu m$, $d_x = 8\mu m$ and $d_y = 11\mu m$ is analyzed and the reflection and absorption coefficients for various separations g are plotted in Figure 7.1. We can observe two limiting cases, namely the single-layer FSS exhibiting a typical reflection band ($g = 0\mu m$), and a higher bandwidth and roll-off characteristic of a dual-layered FSS with separation tending to $\lambda/2$ ($g = 5\mu m$). Between the limiting cases, a strong interaction null is identified around 15.5THz for $g = 0.25\mu m$, shifting down to about 14.5THz for $g = 2.5\mu m$, where the interaction null lies near the lower 'ear' null f_L.

Interestingly, strong absorption is observed at the interaction-null frequency. In order to further investigate the cause of such absorption, the maximum amplitude of the currents versus frequency, and the surface current density around the interaction null are shown in Figure 7.2. As we can see, strong current flowing in opposite directions are induced at the interaction-null frequency. The phenomena occurring at this interaction null is similar to the one observed in Chapter 6 when analyzing the odd mode of perturbed FSS.

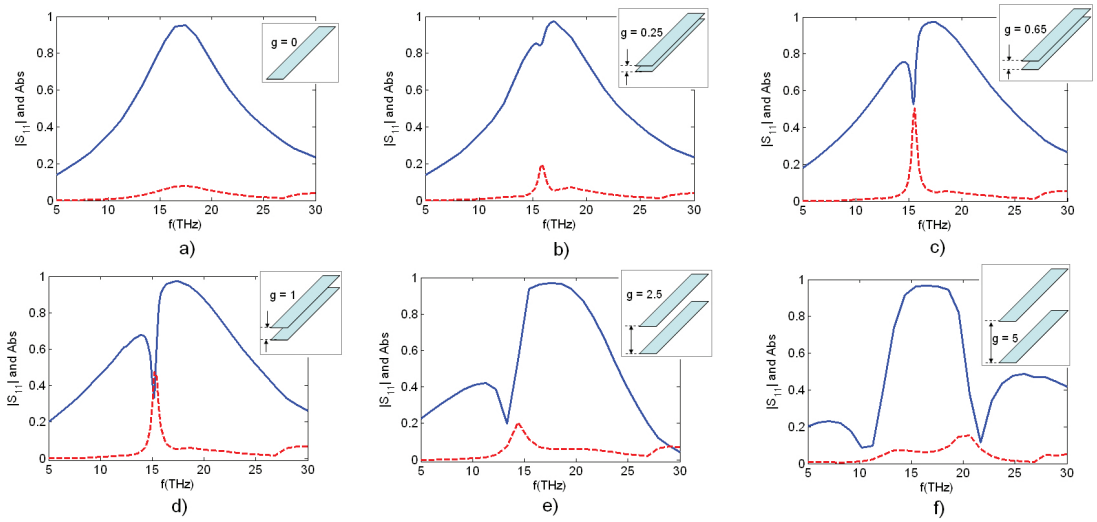

Figure 7.1: *S_{11} (blue solid line) and Abs (red dashed line) versus frequency for varying gap between the layers $g = 0, 0.25, 0.65, 1, 2.5, 5\mu m$.*

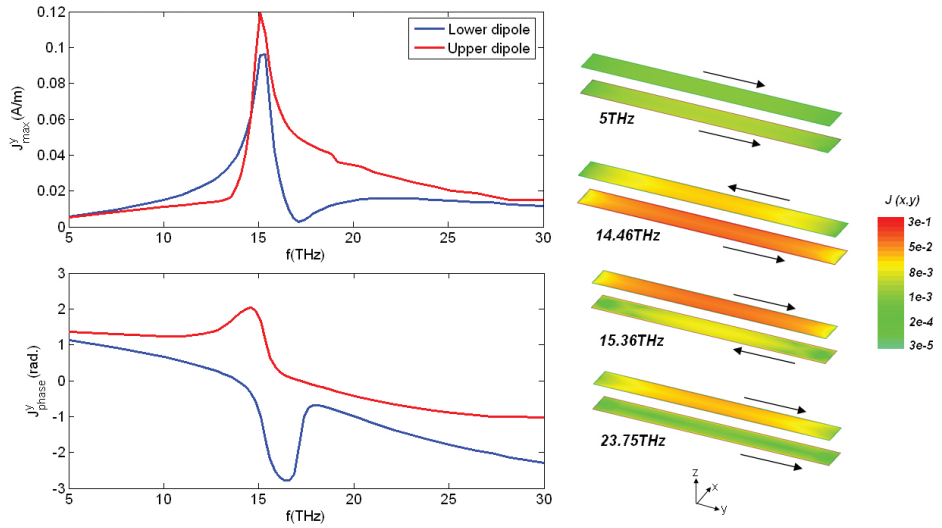

Figure 7.2: *Currents induced for $1\mu m$ gap in the FSS of Figure 7.1.*

Equal-tuning aligned elements do not lead to frequency tuning and, therefore, are not suitable for reconfigurable FSS. In order to achieve frequency-tuning, the coupling between the two layers must lead to a variation of the overall capacitance or inductance by, for instance, modifying the effective length of the dipoles. In this case, however, the effective length of the equal-tuning aligned dipoles do not change with the separation between layers.

7.2.2 Equal-tuning and misaligned dipoles

A certain misalignment between the elements of the arrays in each layer is considered now. First, a horizontal misalignment of half the horizontal periodicity d_x is applied. Second, a vertical misalignment of half the vertical periodicity d_y is introduced. As done in the previous section, we investigate the effects on the reflection and absorption coefficients, as well as the amplitude and direction of the induced currents.

7.2.2.1 Horizontal Misalignment

Figure 7.3 shows the reflection and absorption coefficients for the elements of the two arrays misaligned $d_x/2$ horizontally for various separations g. The same dimensions of the dipoles as in Figure 7.1-2 are used in this and the following sections, unless stated otherwise. In this case, the bandwidth for most of the small separations between the two layers is wider than for the equal-tuning and aligned arrays. This is because the effective horizontal periodicity for $d_x/2$ misalignments in closely coupled FSS is half of the horizontal periodicity for aligned dipoles. As it is well-known and it was also explained in Chapter 4, smaller periodicities give rise to wider bandwidths. As the separation between the two cascaded arrays increases, the coupling between their near-fields reduces significantly, and therefore, the effect of horizontal misalignments decreases. When the separation increases to $g = 5\mu m$, for instance, the reflection and absorption response of the arrays misaligned $d_x/2$ is virtually the same as the response of aligned arrays (Figure 7.3f and Figure 7.1f), due to the lack of near-field interaction.

The interaction null also appears in the reflection characteristic of horizontally misaligned arrays as a consequence of strong induced currents and high absorption or dissipated power. For brevity, the currents are not shown for this case, since their behavior is the same as in the aligned case. Interestingly, the interaction null appears at similar frequency as in the aligned case, that is around 14.5THz. This is due to the fact that the location of the interaction null is strongly determined by the length of the dipoles, which remains the same in both cases.

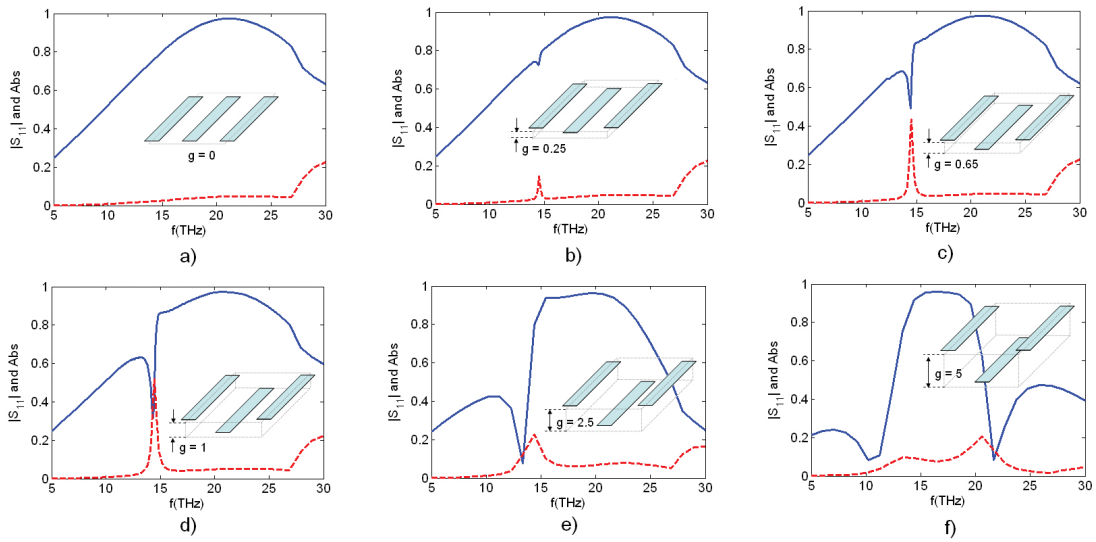

Figure 7.3: *S_{11} (blue solid line) and Abs (red dashed line) versus frequency for varying gap between the layers $g = 0, 0.25, 0.65, 1, 2.5, 5\mu m$.*

7.2.2.2 Vertical misalignment

The reflection and absorption coefficients for the elements of the two arrays vertically misaligned $d_y/2$, and for various separations g, is plotted in Figure 7.4. A vertical displacement of $d_y/2$ is chosen because it leads to a maximum area of conductor overlapping, maximum capacitance or coupling, and, therefore, maximum shift in resonance. In this case, a different behavior from that of the $d_x/2$ displacement is observed. In the lower limit, for the separation of the arrays virtually zero $g = 0$, the coupling is effectively equal to electrical contact. Therefore, the dual-layer FSS is equivalent to a single-layer FSS with effective length of the dipoles equal to d_y. The dual-layer FSS becomes a simple wire-grid polarizer, as the one shown in Figure 6.2 in the previous chapter. As the separation between the two layers is increased, the effective length decreases and, therefore, the resonance frequency increases. A frequency-tuning mechanism can be envisaged by means of moving one array with respect to the other. The maximum resonance frequency achievable corresponds to a separation of the arrays high enough to practically remove any coupling (e.g. $g = 5\mu m$). In this case, the response is the same as in the previous two cases (aligned and horizontally misaligned arrays) and the typical flat reflection band with high roll-off is observed.

Another important issue that must be addressed is the location of the interaction null. As mentioned before, the location of the interaction null is strongly determined by the length of the dipoles. In vertically misaligned arrays, the effective length of the elements changes and, therefore, the location of the interaction null does not remain at a constant frequency, but varies with the separation of the arrays. Two virtually connected arrays, exhibit infinite effective length and the interaction null vanishes. Increasing separation g gives rise to decreasing effective length, shifting the interaction null downwards in frequency. For instance, a separation of $g = 0.25\mu m$ exhibits the interaction null at nearly 25THz, whereas a higher separation of $g = 2.5$ shifts this null down to 15THz. The location of the interaction null is important insofar as such null may be located in the desired operation band of the FSS. For instance, a separation of $g = 2.5\mu m$ deteriorates the performance of the FSS by splitting the band into two.

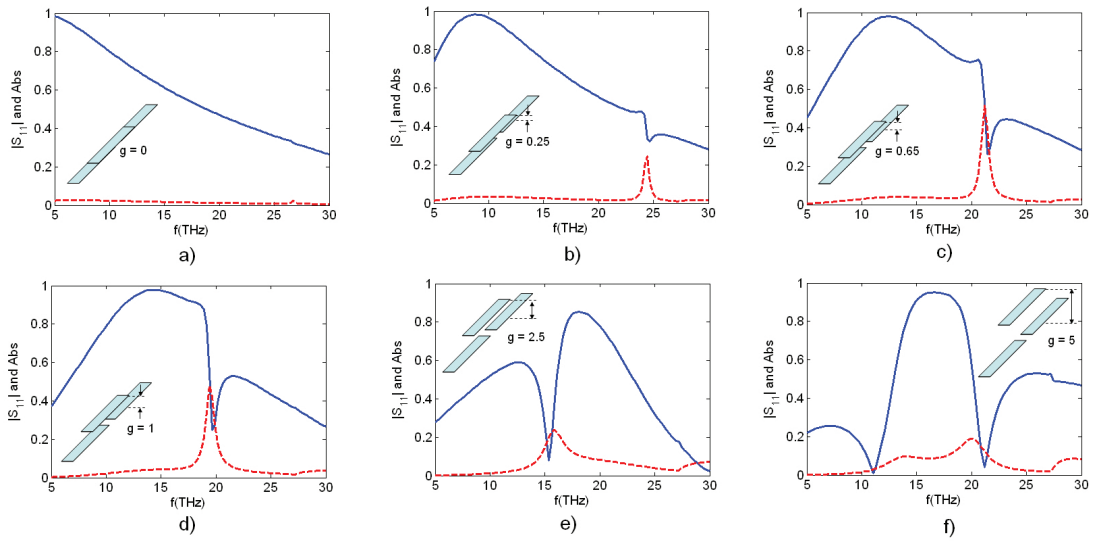

Figure 7.4: *S_{11} (blue solid line) and Abs (red dashed line) versus frequency for varying gap between the layers $g = 0, 0.25, 0.65, 1, 2.5, 5\mu m$.*

Figure 7.4 clearly shows the frequency-tuning capability of closely coupled FSS and highlights the limitations imposed by the maximum distance between layers for effective coupling between their near-fields and by the location of the interaction null. The behavior of the currents at the interaction null is the same as in previous cases, that is higher amplitudes and anti-parallel flowing, as shown in Figure 7.5.

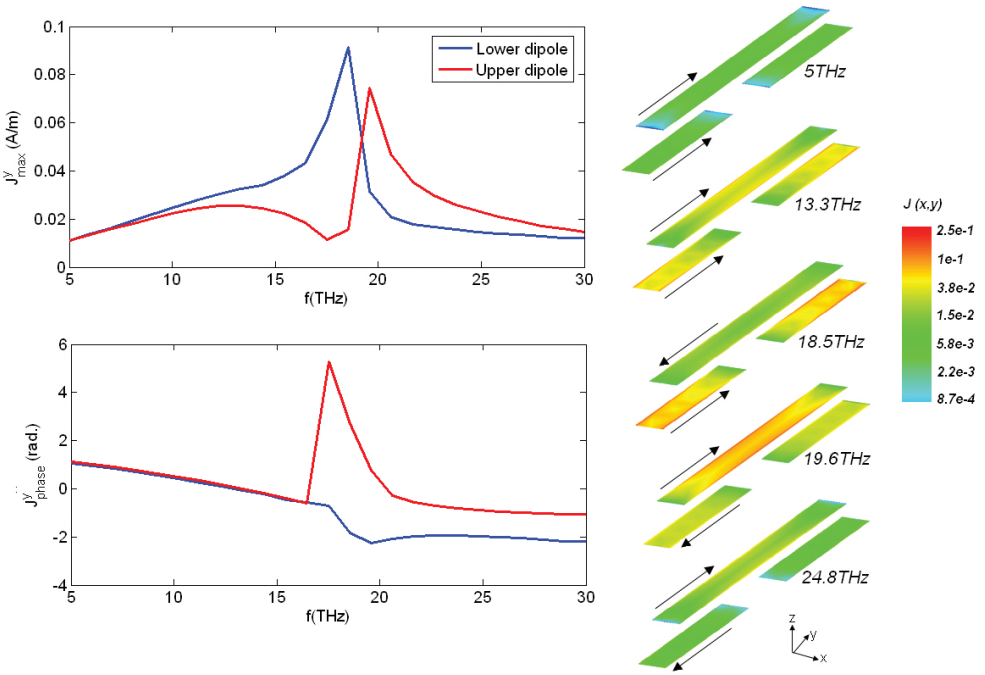

Figure 7.5: *Currents induced for* $1\mu m$ *gapin the FSS of Figure 7.4.*

7.2.3 Staggered-tuning and aligned dipoles

In this section, the effects on varying distance g between layers is examined for staggered-tuning arrays, that is each array having a different resonance frequency, for instance by varying the length of the dipoles. The reflection and absorption coefficients are shown in Figure 7.6 for aligned arrays with dipoles lengths of 6 and $9\mu m$. The solid and dashed lines represent the reflection and absorption coefficients when the shorter dipoles are in the upper array (first array that the incident wave sees), whereas the dotted lines represent these coefficients when the shorter dipoles are in the lower array (second array from the perspective of the incident wave). As we can see, the effect of using two different length for the dipoles of each array give rise to the appearance of two resonances. The location of these resonances remain constant with varying g because the lengths of the dipoles are fixed. The separation between arrays g determines the amplitude of the reflection bands and the amount of dissipated power. The currents induced in the dipoles for the case of a $1\mu m$ separation is shown in Figure 7.7. In both resonances, the currents flow anti-parallel similarly to the behavior observed in the equal-tuning arrays.

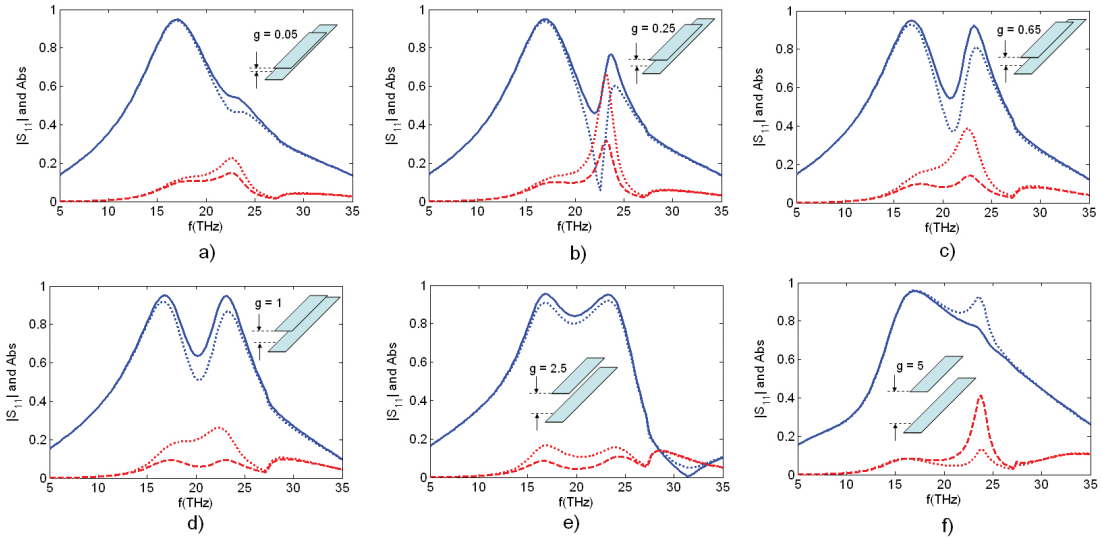

Figure 7.6: *S_{11} (blue solid line) and Abs (red dashed line) versus frequency for varying gap between the layers $g = 0, 0.25, 0.65, 1, 2.5, 5\mu m$, ($L_1 = 6\mu m$, $L_2 = 9\mu m$). Solid blue and red dashed lines represent $L_{upper} = L_2$, and $L_{lower} = L_1$. Dotted blue and red lines represent $L_{upper} = L_1$, and $L_{lower} = L_2$.*

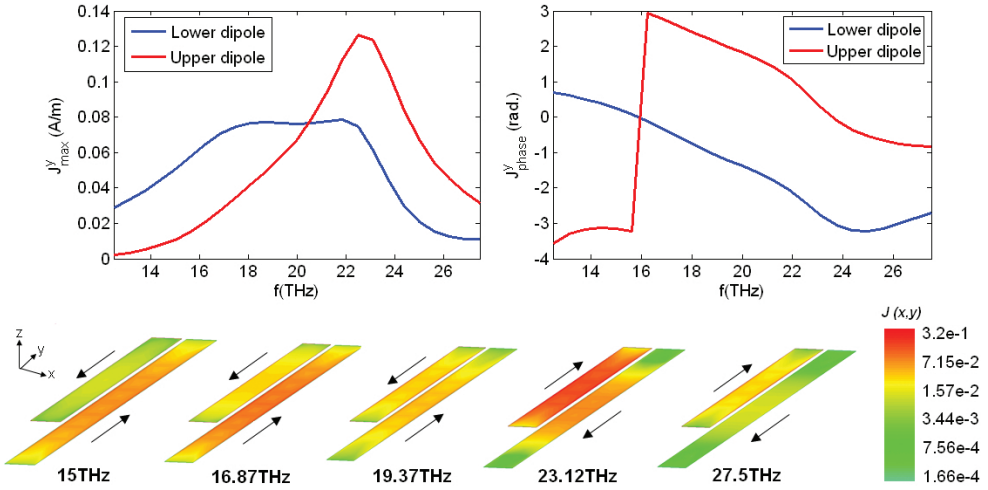

Figure 7.7: *Currents induced for $1\mu m$ gap in the FSS of Figure 7.6, and $L_{upper} = L_1$, and $L_{lower} = L_2$.*

As we could expect, using different length for the dipoles of each array does not lead to frequency-tuning capabilities, but it only gives rise to the appearance of a second resonance. This is the case not only for strongly coupled arrays (small separation), but

also for the weakly coupled arrays (higher separation).

7.2.4 Staggered-tuning and misaligned dipoles

Horizontal and vertical displacements of one array with respect to the other are investigated for staggered-tuning arrays. Figure 7.8 shows the reflection and absorption coefficients for a horizontal misalignment of $d_x/2$ and lengths of the dipoles equal to 6 and $9\mu m$.

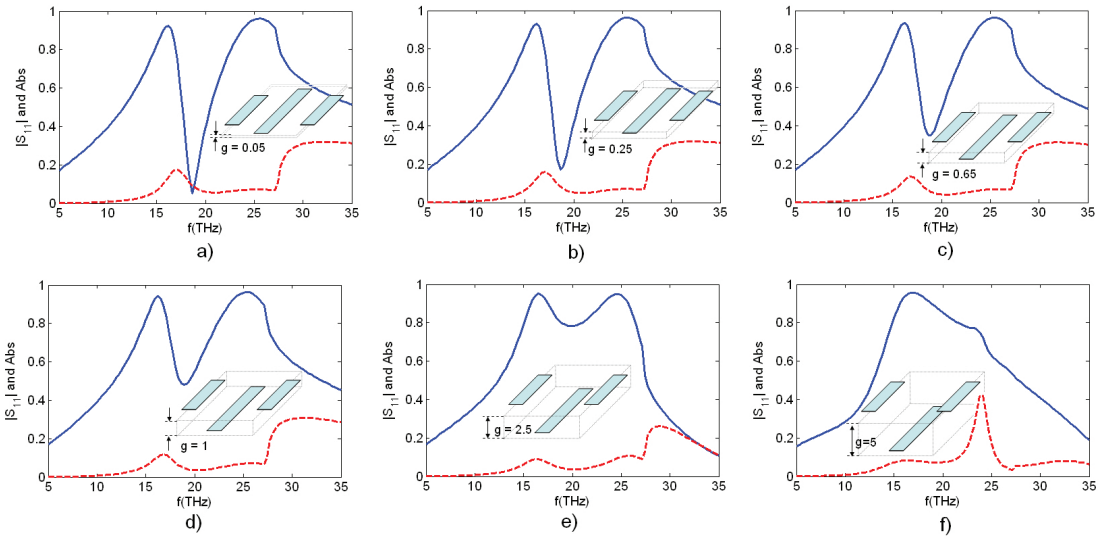

Figure 7.8: *S_{11} (blue solid line) and Abs (red dashed line) versus frequency for varying gap between the layers $g = 0, 0.25, 0.65, 1, 2.5, 5\mu m$, ($L_1 = 6\mu m$, $L_2 = 9\mu m$). Solid blue and red dashed lines represent $L_{upper} = L_2$, and $L_{lower} = L_1$. Dotted blue and red lines represent $L_{upper} = L_1$, and $L_{lower} = L_2$.*

Two different behaviors can be observed in Figure 7.8. For high distances between arrays, the performance is the same as in the aligned case of Figure 7.6f. In this case, the coupling is minimal, so that the effects of misalignments are insignificant and the dominant effect is the separation between arrays. For very small separations, the dual-layer horizontally misaligned FSS behaves the same as the single-layer FSS with perturbation in the length of every second dipole presented in Chapter 6. As the separation is increased, the reflection and absorption characteristics tends to the ones for aligned arrays. In Figure 7.9, the amplitude of the anti-parallel induced currents is

shown for a separation of $1\mu m$.

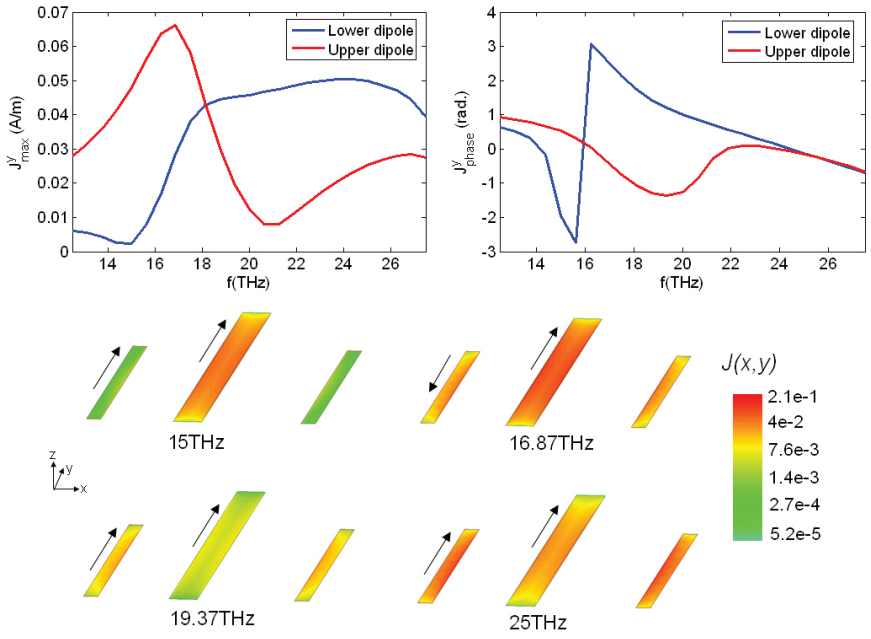

Figure 7.9: *Currents induced for $1\mu m$ gap in the FSS of Figure 7.8, and $L_{upper} = L_1$, and $L_{lower} = L_2$.*

As seen in a previous section (Figure 7.4), a vertical displacement of $d_y/2$ does lead to a frequency-tuning capability. However, the interaction null limited the range of frequency tuning. Arrays with different lengths of the dipoles, however, have been found to increase such range, as shown in Figure 7.10. The limiting factors in this case are the upper resonance frequency, defined by the length of the shorter dipole, and the onset of grating lobes, determined by the horizontal periodicity.

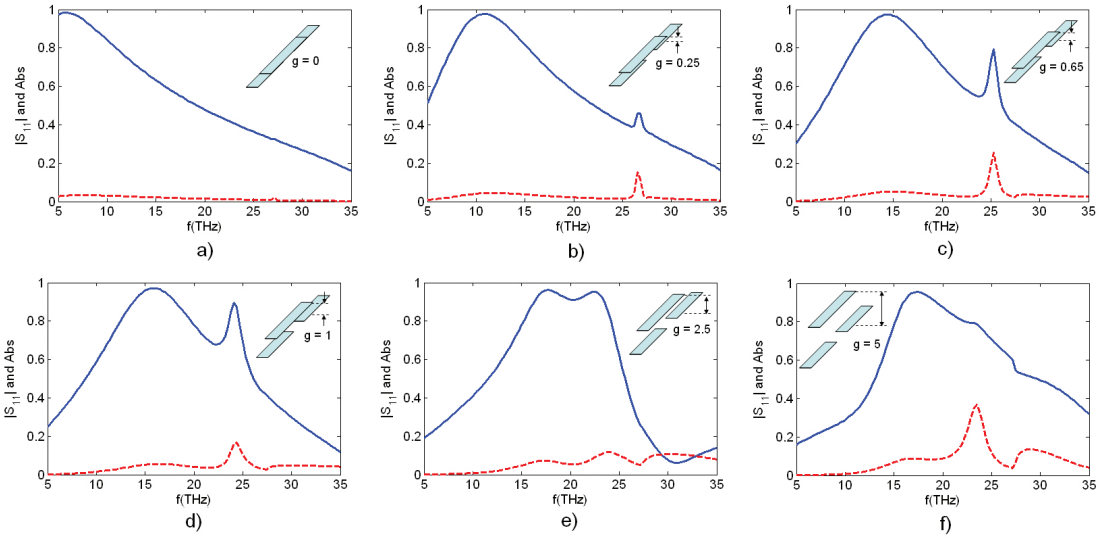

Figure 7.10: *S_{11} (blue solid line) and Abs (red dashed line) versus frequency for varying gap between the layers $g = 0, 0.25, 0.65, 1, 2.5, 5\mu m$, ($L_1 = 6\mu m$, $L_2 = 9\mu m$). Solid blue and red dashed lines represent $L_{upper} = L_2$, and $L_{lower} = L_1$. Dotted blue and red lines represent $L_{upper} = L_1$, and $L_{lower} = L_2$.*

7.3 Tunable FSS

As shown throughout this thesis, passive single-layer FSS generally exhibit static single-frequency response due to their fixed geometry and materials properties. As shown in the previous and current chapters, static multi-frequency operation devices are achievable by appropriately tailoring single-layer as well as multilayered configurations, where various resonances are obtained. However, in many applications it would be desirable to control dynamically the frequency response. Reconfigurable FSS structures, where the frequency response can be adjusted to the application's specific needs at certain moment and situation, without adding new modules, would greatly benefit communication systems (e.g. aerospace, mobile or wireless applications) in terms of flexibility and efficiency.

As seen in the first part of this chapter, varying the distance in misaligned two-layered FSS (equal-tuning or staggered-tuning) allow certain frequency tuning capability. The tuning mechanism is schemed in Figure 7.11, where the impedance of the total two-layered FSS is modified by means of varying the distance in between. The shift

in resonance frequency, as shown in previous sections, depends on the interaction of the near-fields. The further the two layers are separated, the less interaction there is between their near-fields. Therefore, the limitation of the range of frequency-tuning is mainly determined by the maximum separation at which there is still enough interaction to shift the frequency.

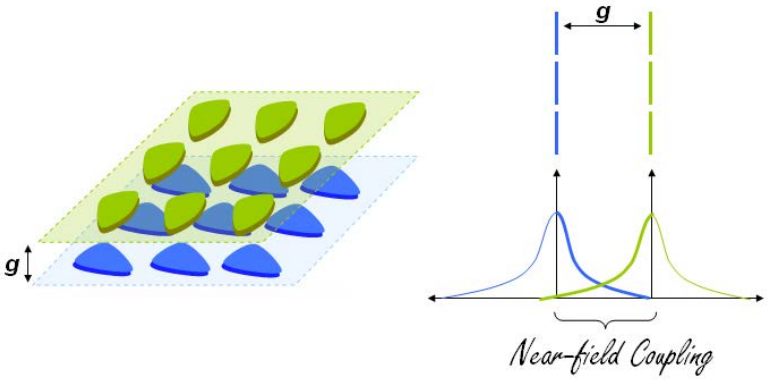

Figure 7.11: *Tunability approach by varying the coupling between two layers (near-field interaction).*

As reviewed in Chapter 2, the tunability mechanisms in periodic arrays, such as FSS, can be classified into two major groups, namely (1) geometry-tunable and (2) material-tunable devices. The former reconfigures the shape or arrangement of the elements of the array, whereas the latter exploits the tunable properties of certain materials. The first group includes PiN and varactor diodes, as well as micro-electro-mechanical systems (MEMS). In the second group, we can find plasma elements, as well as ferrite, semiconductor and liquid crystals substrates. Every tunability method exhibits unique characteristics, has advantages and drawbacks with respect to the other techniques, and therefore, its usefulness depends on the final application. MEMS structures have shown promising performance in switchable and tunable periodic arrays.

In this second part of the chapter, we report an approach to reach tunable THz FSS consisting on movable MEMS membranes, allowing rearrangement of single and multilayered periodic structures, and therefore tuning the resonance frequency. The analysis, design and fabrication of the MEMS devices, as well as its integration with periodic structures, are discussed. Various examples of its applicability in periodic

surfaces, such as FSS and AMC, are given showing the potentiality of the approach proposed.

7.3.1 Tunability approach

The proposed MEMS structure, whose schematic is shown in Figure 7.12, consists of a movable membrane with four anchored flexure arms. The actuation takes place in the arms, while the membrane follows the movement of the arms. When actuated by a voltage difference between the top and bottom electrodes, the induced electrostatic force pulls down the flexure arms of the membrane, resulting in a vertical and homogeneous displacement of the entire membrane. The displacement capability of movable membranes represents an excellent tunability approach for a wide range of EBG structures, particularly for high frequency applications (i.e. sub-millimeter waves onwards). As the working frequency increases, the size of the elements in periodic arrays decreases proportionally. Due to the small size of the elements at THz, infrared and optical frequencies, an entire array of micro/nano-sized elements can be integrated within or on top of the movable MEMS membranes with area ranging from a few hundreds of micrometers to a few millimeters.

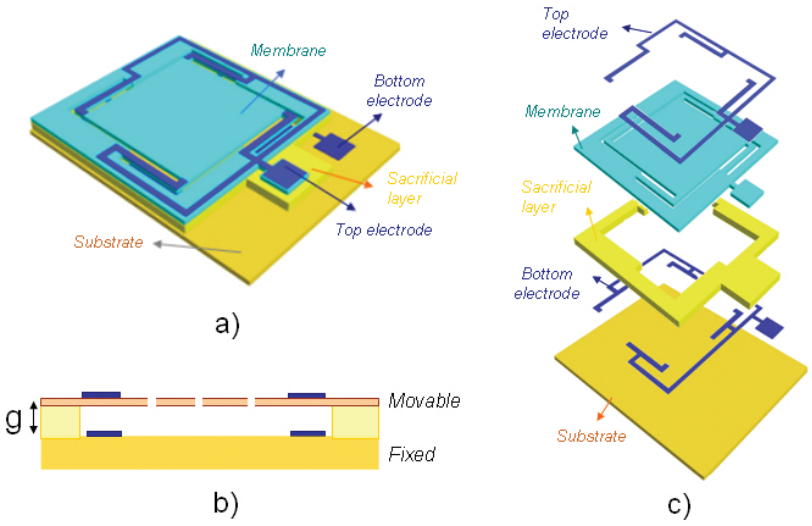

Figure 7.12: *Tunability principle based on movable membranes. The actuation takes place in the arms of the membrane, that in turns pull down the membrane itself. a) Bird's view, b) cross-sectional view, and c) description by layer.*

With external voltage actuation, we can control electronically the size of the air gap in a two-layered FSS consisting of a movable and a fixed layer. The movable layer can be a dielectric layer with metallic or dielectric elements on top; or it can be a slotted dielectric or metallic layer. The fixed layer can be any of the configurations described for the movable membrane, or simply a metallic ground plane or a dielectric slab. Such an arrangement can give rise to many possible device configurations, as shown in Figure 7.13-14, where the electromagnetic coupling between the two layers can be controlled. In other words, the equivalent impedance of the two-layered configuration is modified by changing the distance between the layers, as shown in Figure 7.11. Resonant frequency, bandwidth or reflection phase are some of the parameters which can be tuned using this approach.

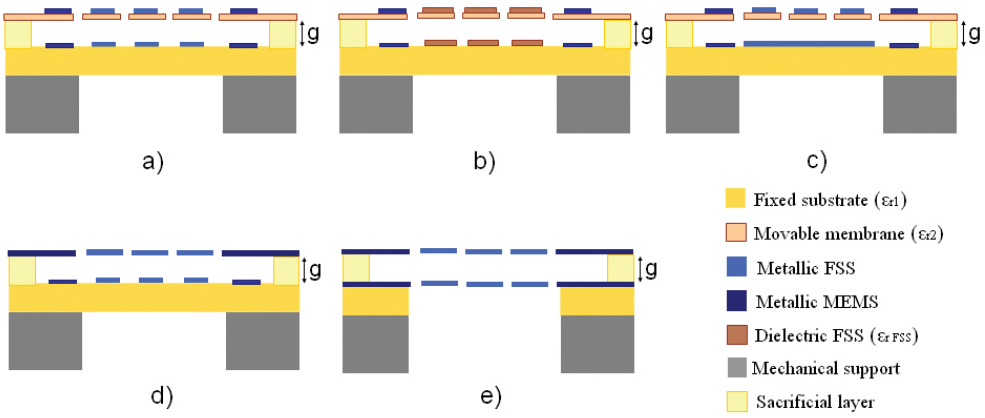

Figure 7.13: *Various possible configurations using MEMS-based dual-layer FSS.*

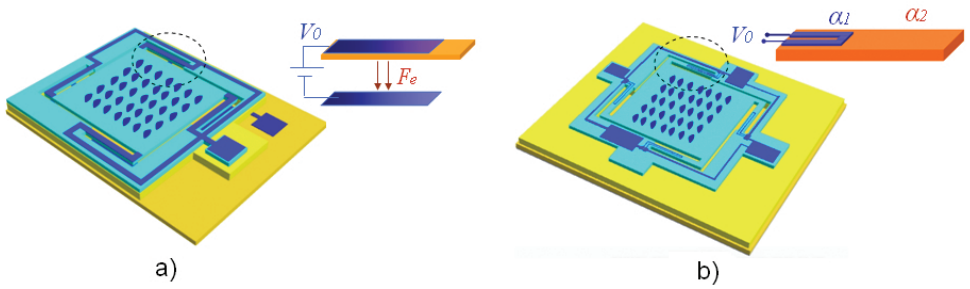

Figure 7.14: *Electro-static and electro-thermal actuation methods for actuating the movable membrane.*

An important feature of this configuration lies in the MEMS actuation area, which takes

place in the flexure arms, instead of in the membrane itself. The advantages of this approach are significant. First, the membrane is not required to be conducting (such as in other designs [228, 229]), so that it can be also dielectric. Second, the upper and lower electrodes are removed from the membrane area, so that the MEMS actuation does not affect or interact with the response of dual-layered array. Thus, we separate the MEMS actuation, which takes place outside the membrane area, and the FSS response, which is contained within the membrane area (e.g. reflection/transmission), as depicted in Figure 7.15. By doing this, the electromagnetic and mechanical parts can be analyzed and designed independently. In addition, the lower electrode can be eliminated by actuating the flexure arms electro-thermally (as shown in Figure 7.14), which has advantages over electro-static actuation, such as avoiding pull-in effect, decreasing the actuation voltage and simplifying the fabrication process.

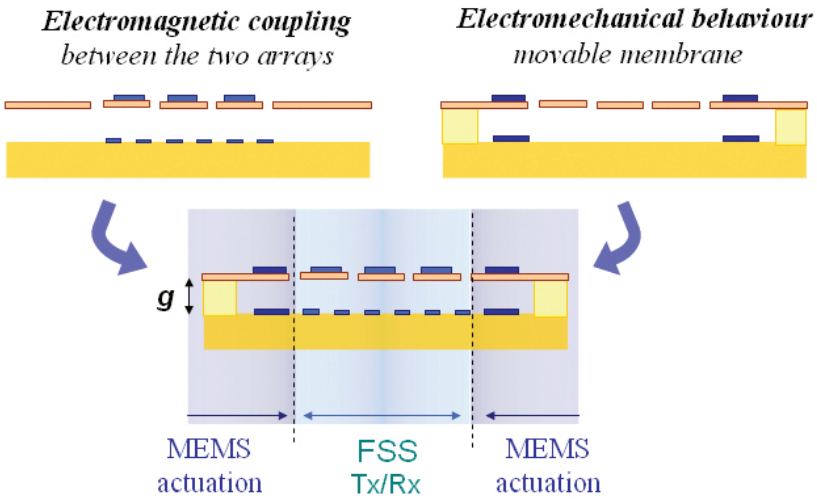

Figure 7.15: *Independent FSS and MEMS design in the proposed method. As shown, the actuation only takes place in the arms, so that the membrane area is not covered and it is free for transmission and reflection of EM waves*

In order to compare this tunability mechanism with other configurations proposed in the past, Figure 7.16 shows a table assessing the performance of the different tunability approaches in terms of manufacturing or actuation simplicity, losses introduced, and range of applications. The suggested configuration has potentially no additional losses due to the moving mechanism, it can be well adapted to a wide range of array configuration and applications, and the fabrication can be relatively simple.

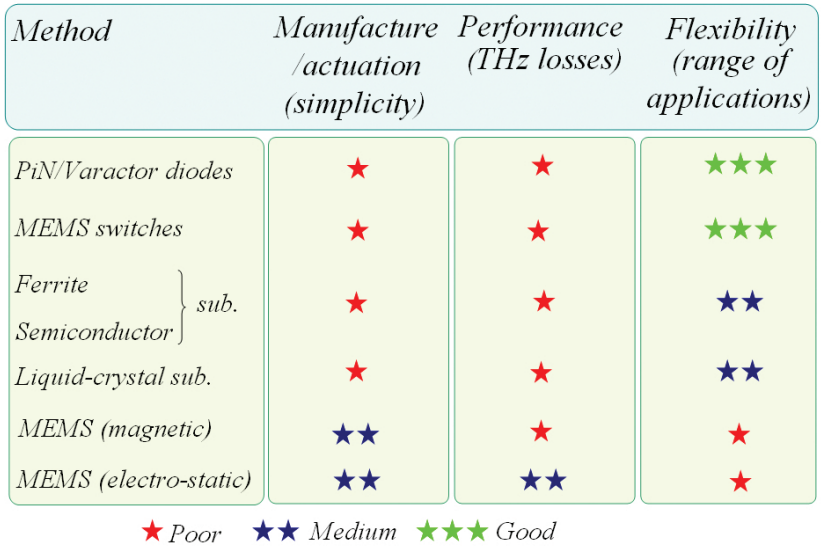

Figure 7.16: *Comparison between tunability configurations for periodic structures.*

Other issues that can be briefly addressed are the tuning speed, lifetime, reliability, tuning tolerance and cost. The tuning speed would be defined as the time that the arms of the movable membrane take to move from one position to another. Actuation time in similar moving MEMS has been shown to be in the range between milliseconds and microseconds. The cost of such an approach is inexpensive due to the fact that standard microfabrication capabilities can be employed to manufacturer the dual-layer array MEMS. However, etching of the sacrificial layer to obtain an air gap between the two array layers can be difficult. Also, for arrays resonating in the far/mid IR, where Si substrates are not transparent, the substrate would need to be removed using, for instance, DRIE etching as used in Chapter 6 for single-layer arrays. For near-IR and optical frequencies, where the availability of transparent substrate is higher, this step may not be necessary. Lifetime and reliability seem to be the most challenging issues that need thorough investigation.

7.3.2 MEMS analysis and design

Commercial simulator Coventorware based on the finite element method (FEM, similar to that explained in Chapter 2, but applied to mechanics) has been used to perform simulations of both electro-statically actuated metallic membranes and electro-thermally actuated dielectric membranes. Figure 7.17 shows the displacement

of an aluminum (Al) MEMS membrane when actuated electro-statically. The $1mm^2$ Al membrane with $500\mu m \times 50\mu m$ flexure arms is displaced up to $1.5\mu m$ when a $2V$ voltage difference is applied between the electrodes (separated $3\mu m$ when no voltage is applied).

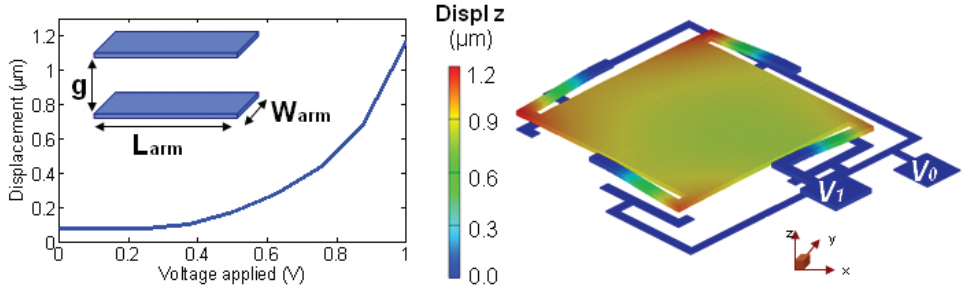

Figure 7.17: *Electro-statically actuated MEMS movable metallic membrane.*

On the other hand, Figure 7.18 shows the displacement ($1.6\mu m$) of a polyimide $1mm^2$ membrane with $300\mu m \times 50\mu m$ flexure arms actuated electro-thermally (i.e. $1V$ voltage applied in the U-shaped electrodes placed on each arm), and with $10\mu m$ and $50\mu m$ electrodes width and length.

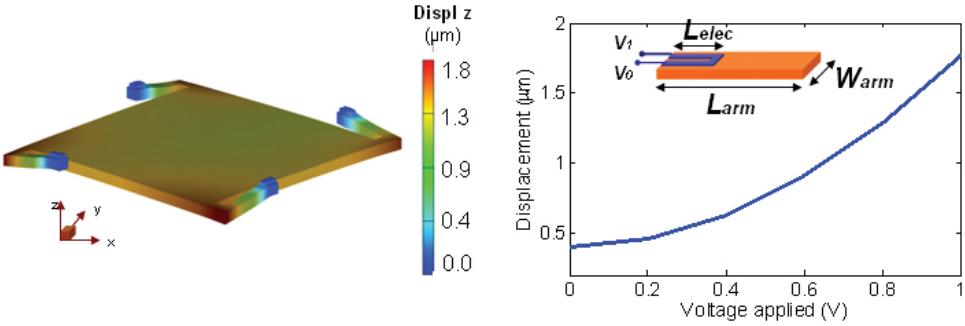

Figure 7.18: *Electro-thermally actuated MEMS movable dielectric membrane.*

7.3.3 Applicability in tunable FSS

MEMS movable membranes were shown to provide around $1.5\mu m$ displacement between two layers. As described in the first part of the Chapter, dual-layered FSS can be tuned by means of varying the distance between the two layers. This was the case when both arrays have the same or different dimensions (e.g. the length of the dipoles), that was called equal-tuning and staggered-tuning following the definitions

in [1], and a misalignment was carried out in the direction of the length of the dipoles (i.e. electric field orientation). The suggested MEMS movable membranes can deliver the displacement in such a dual-layer configuration, thus achieving tunability in the resonance frequency.

In addition, the resonant frequency can be tuned in another type of dual-layer FSS consisting of closely spaced dipoles and 90 degrees rotated slots, known as complementary FSS (CFSS) [226]. Both arrays made of dipoles and slots are designed to resonate at the same frequency ($9\mu m$ length and $1\mu m$ width), and the variable separation is responsible for varying the coupling between their near-fields, resulting in a resonance frequency shift. In the absence of losses, the resonance frequency is tuned from $4.5THz$ with $0.05\mu m$ separation to $8.2THz$ with $0.75\mu m$ separation, as shown in Figure 7.19. When losses in the dielectric ($tan\delta = 0.008$) and in the metal ($\sigma_{Al} = 38 \cdot 10^6 S/m$) are taken into account, the resonant frequencies are shifted slightly to lower values (due to reactive effects) and thermal dissipation is stronger in more closely coupled CFSS, where currents are more strongly excited. The response of the FSS in the presence of losses is also plotted in Figure 7.19 for comparison.

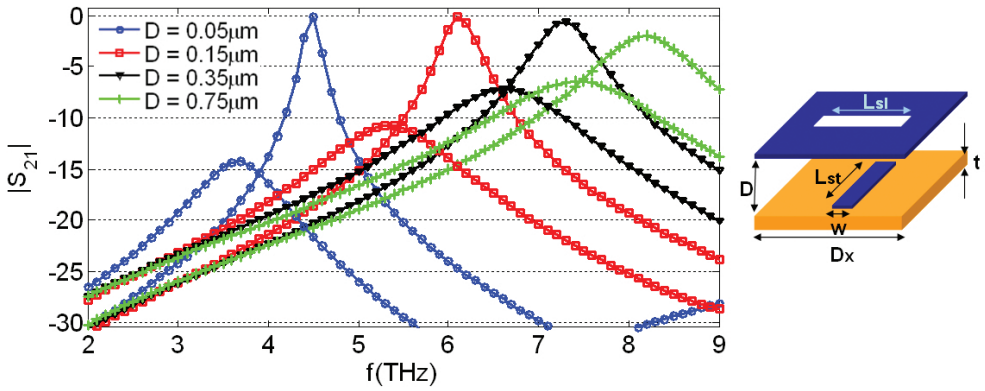

Figure 7.19: *Transmission parameter of a tunable FSS based on complementary arrays, with and without losses, for variable separation D. The curves which exhibit lower S_{21} amplitude are those in which losses are included.*

7.3.4 Other tunable applications: AMC and all-dielectric FSS

Following this tunability principle, a wide range of structures can be tuned, namely FSS, AMC, PBG, NIM, gratings, reflect-arrays, Fabry-Perot cavities, EBG/antennas, etc.

Here, we describe its use in two of those, namely an all-dielectric FSS and an artificial magnetic conductor (AMC). Commercial software HFSS based on FEM is used, and the mesh and boundary conditions are defined as explained in Chapter 3.

All-dielectric FSS (DFSS) [59] have been suggested as a candidate for overcoming the undesirable effect of thermal losses in metallic FSS. Figure 7.20 shows the tunable transmission coefficient from a low-loss single-screen DFSS ($P = 11.3\mu m$, $T = 4.3\mu m$, $\epsilon_{r1} = 4$, $\epsilon_{r2} = 7$) separated by a variable distance D from a $2\mu m$ thick polyimide layer. As D increases from $0.15\mu m$ to $2\mu m$, the reflection band is tuned from $15THz$ to $16.3THz$.

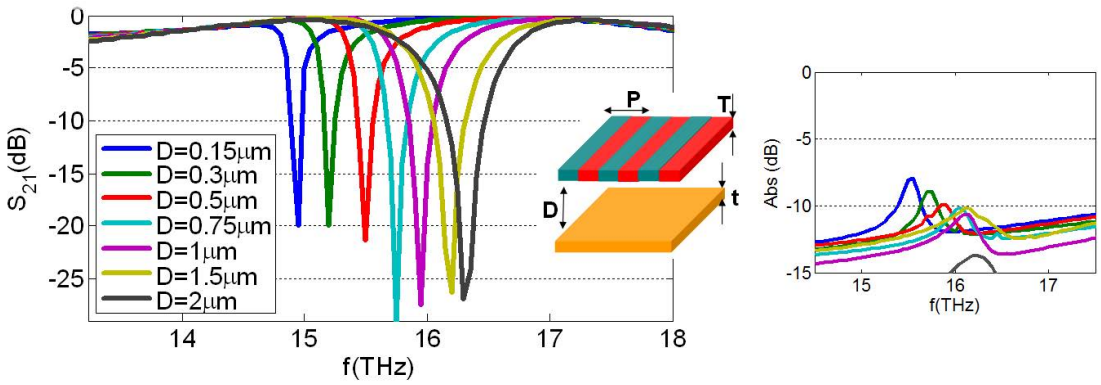

Figure 7.20: *Transmission (left) and absorption (right) parameter of a tunable all-dielectric FSS based on a dielectric grating with two different materials separated a distance D from a dielectric layer.*

Finally, the phase reflection characteristic of an AMC consisting of a periodic array of metallic patches over a ground plane [30] can be tuned using the proposed configuration. The metallic patches ($D_x = 8\mu m$ and $L = 6\mu m$) are supported by a thin polyimide layer ($t = 1.7\mu m$), which is free-standing at a distance D over the ground plane. By varying the air gap from $0.5\mu m$ to $2\mu m$, the frequency in which zero-phase reflection takes place is shifted from $6.7THz$ to $9THz$, as shown in Figure 7.21.

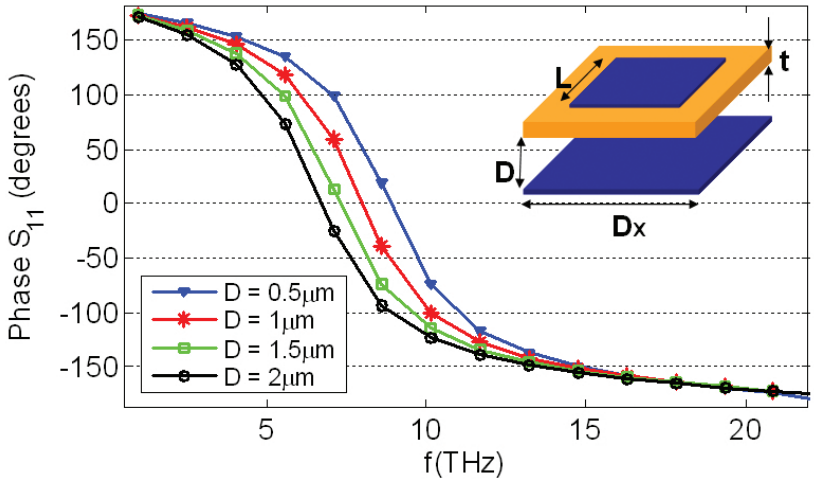

Figure 7.21: *Reflection phase of a tunable AMC consisting of an FSS separated a distance D from a ground plane*

7.4 Conclusion

In this last chapter, dual-layer and tunable FSS have been investigated at THz frequencies. The motivation of studying multilayered configurations lies in offering additional capabilities with respect to single-screen FSS, such as high roll-off, angular stability or reconfigurability. Particularly, in this chapter tuning capabilities have been demonstrated by the near-field coupling between two arrays closely spaced, and used in various types of arrays and applications. The main contributions are outlined below:

- Study of the performance of dual-layer FSS as a function of the separation between layers, with inspection of ohmic losses and induced currents for the first time

A thorough investigation of the performance of coupled dual-layer FSS have been carried out. For the first time, a detailed study of the losses and currents induced in dual-layer FSS has been presented. The performance of equal-tuning (elements with the same dimensions) and staggered-tuning (elements with different dimensions) FSS has been analyzed. Equal-tuning arrays exhibit a single resonance, while staggered-tuning elements have shown dual-band characteristics. Interestingly, interaction-nulls are evident in either case due to the coupling between the two arrays. The currents induced at these interaction nulls have been shown to be anti-parallel, similar to the behaviour obtained in perturbed FSS.

- Demonstration of tuning capability of dual-layered by near-field coupling

The near-field coupling between the two layers in a dual-layer FSS have been demonstrated to provide frequency tuning capability. Although aligned vertical dipoles or misalignments in the horizontal direction has not shown any frequency tuning effect (under vertically polarized incident-wave), misalignments in the vertical direction has been shown to offer such tuning capability. From an electrical perspective, the varying effective electrical length of y-misaligned dipoles, as the separation between the two layers increases, has been found to be responsible for the tuning effect (varying total impedance). From the near-field perspective, the interaction between the evanescent waves excited in both layers is responsible for this frequency shift. The tuning range significantly decreases as the layers are separated further apart.

- Design of a novel tunability approach based on MEMS movable membranes

In order to obtain the variation in the distance between the two layers of the dual-layer configuration, a MEMS movable membrane has been proposed. Since the size of the elements of FSS operating at THz frequencies is in the micrometer scale, an entire array can be located on the movable membrane. The suggested MEMS consist of a four-arm membrane actuated in the arms electro-statically or electro-thermally. In a tunable dual-layer configuration the lower array is kept fixed, while the upper array, located on the movable membrane, represent the movable component. The operation of the MEMS membrane has been analyzed by FEM, and it has been found that sufficient displacement is achieved (circa $2\mu m$). The advantages of this novel tunability approach are the independent design of the MEMS and the dual- layer FSS, the lack of interference or losses from the MEMS structure (outside the FSS transmission/reflection area), and its flexibility, allowing its application to a wide range of devices.

- Demonstration of tunable FSS, gratings and AMC by near-field coupling

The application of the proposed tunability approach has been demonstrated by designing three different types of tunable periodic structures, namely FSS, dielectric gratings and AMC. The tunable FSS consists of a free-standing slot array (moving part) and a 90degrees-rotated dipole array on a polyimide substrate (fixed part). In this case, the moving part (all metallic) is more readily actuated electro-statically. A frequency tuning of 1.4THz in the transmission characteristic has been obtained using

this configuration. The tunable dielectric grating, or all-dielectric FSS, consists of a one-dimensional array or grid of alternated dielectrics with a varying separation to a polyimide layer. Electro-thermal actuation seems more suitable for this configuration. A frequency tuning of 3THz for the transmission parameter has been obtained. The tunable AMC consists of an array of patches on a movable polyimide membrane, separated a varying distance to a ground plane. Electro-thermal actuation is also more suitable in this configuration. In this case, no need of deep-etching the fabrication substrate (e.g. silicon) would ease its fabrication process. A frequency tuning of 1THz in the zero-phase reflection characteristic has been achieved.

Chapter 8
Conclusions and Future Work

Frequency selective surfaces (FSS) consisting of two-dimensional periodic arrays operating at THz frequencies have been demonstrated throughout this thesis, both theoretically and experimentally. Interest in extending the applicability of the FSS technology beyond the microwave regime, towards sub-millimetre waves and THz frequencies, has led to the need of in-depth investigations of certain issues regarding the performance, manufacture and testing of FSS, which are particular to this frequency regime. This thesis has focused on three different areas within the realm of FSS technology at THz, namely, (1) addressing ohmic and dielectric losses, (2) developing a fabrication process and measurement set-up to demonstrate experimentally FSS resonating in this band of the spectrum, and (3) designing THz FSS to achieve multiband performance, tunable response and sensing capabilities. In addition, several potentially attractive research directions have been found and will be outlined in this chapter.

I. Investigation of the issues arising in FSS at THz frequencies, neglected in the past when FSS were used in the microwave, has led to a detailed description of power dissipated, energy stored and quality factors of THz FSS.

The performance of FSS at microwave frequencies is well-known due to intensive research over the past few decades. At these frequencies, metallic components are generally assumed to be perfect electric conductors and dielectric materials are the dominant source of losses in the form of dissipated power, i.e. energy neither transmitted nor reflected. At higher frequencies, however, metallic elements do not conduct electric current perfectly, and ohmic losses must be taken into account. Little research has been oriented towards determining the effects of ohmic losses on the overall FSS performance, and the relationship between power dissipated and stored (i.e. quality factor) by FSS is missing in the literature.

In the first part of this thesis, these issues have been addressed in great detail. Free-

standing as well as dielectric-supported FSS have been studied by using full-wave method of moments as well as circuital models in order to gain physical insight on the phenomena occurring in the presence of losses. A single-mode circuital model of lossless free-standing FSS consisting of the terminal impedance of the array has been extended and validated to account for ohmic losses and substrate frequency-pulling effect.

Due to the resonant nature of FSS, ohmic losses have been found to be related to the geometry of the FSS in a non-intuitive manner (represented by the parameter κ as the ratio between ohmic and radiation resistance), for instance increasing in arrays with less metallisation per unit area. The power dissipated and stored in the vicinity of the periodic arrays have been found to be strongly determined by the strength of the induced currents on the FSS elements (i.e. defined by the coupling of the FSS with the input/output ports). Arrays with higher periodicity and narrower and shorter elements have been shown to exhibit lower radiation or terminal resistance, leading to stronger currents with narrower frequency distribution. Despite greater dissipated power has been shown for higher induced currents, an overall increase in the quality factor is observed due to a simultaneous increase in the power stored in the vicinity of the FSS. Therefore, a trade-off between power dissipated and quality factor has been demonstrated. Higher Q-factor filters can be achieved at the expense of allowing more absorption. This is relevant for applications of FSS in both filtering and sensing components.

On the other hand, dielectric losses have been shown to be less important at these frequencies, resulting generally in higher absorption away from the FSS resonance due to the presence of dielectric-only resonances (e.g. odd multiples of $\lambda/2$). Interestingly, however, the inclusion of a supporting dielectric not only adds further losses to the ohmic losses, but also slightly modifies the ohmic losses. This phenomenon has been explained, again, by means of studying the induced currents, and it has been found that the modification of the induced currents when introducing a dielectric supporting layer is responsible for the slight change in ohmic losses observed in the presence of dielectric with respect to the free-standing case. However, ohmic losses variations due to the presence of a dielectric has been shown to be minimal compared to the overall value of the total losses.

These results highlight the importance of accurately accounting for ohmic losses as well as dielectric losses at THz frequencies, where assumptions of ideal materials generally are no longer valid. These findings also provide with valuable guidelines and warnings for the design of FSS at THz frequencies. The results of power dissipated in relation to the power stored are, to the best of our knowledge, presented for the first time in this thesis. Likewise, the investigations of substrate-generated power dissipation by both ohmic and dielectric losses are original contributions of this thesis.

II. Experimental demonstration of FSS operating at THz frequencies.

As part of the research undertaken in this thesis, it was aimed to develop a fabrication process in order to investigate experimentally FSS operation in the THz regime. FSS operating around 15THz, where the size of the FSS elements lies in the micrometre scale, have been experimentally demonstrated.

The fabrication of FSS operating at these frequencies has been shown to be challenging due to the lack of available high-performance transparent materials in this frequency window and materials compatible with standard microfabrication processes. Polyimide has been used due to its mechanical integrity after curing, its acceptable transparency around this frequency, and because it has been previously reported in the literature as a good candidate as supporting material for FSS and metamaterials. A fabrication process starting from a silicon wafer has been developed to ensure compatibility with polyimide and aluminum (metal used for the FSS elements). Since silicon does not show good transparency at these frequencies, deep-reactive ion etching (DRIE) has been used to etch the silicon leading to a free-standing polyimide membrane. Large membranes (more than 1cm length) showing good mechanical integrity have been achieved with thickness of only $1.7\mu m$. In order to protect the polyimide layer, an auxiliary silicon dioxide layer has been used as a silicon-etching stop layer, and removed after deep-etching was finished by means of short duration wet etching based on ammonium fluoride and acetic acid which do not damage polyimide or aluminum.

In order to measure the performance of the fabricated FSS prototypes, two different Fourier-Transform Infrared (FT-IR) spectroscopy equipments have been employed, namely a simpler and faster Perkin Elmer, and a more accurate and slower Bruker. Since the resonance of FSS is broadband compared to common sharp resonances

targeted in spectroscopy measurements, both FTIR equipments offer similar results, regardless their resolution. Unperturbed and perturbed FSS consisting of metallic dipoles have been measured showing good agreement with simulated results. Due to the polarization sensitivity of dipoles and the unpolarized nature of the FTIR source, however, the amplitude of the measured reflection band was significantly smaller than the simulated under vertical polarization. Dual-band dual-polarized FSS consisting of dipoles and square loops have been also demonstrated. In this latter case, since square loops are polarization insensitive, the reflection band amplitude agrees better with the simulations.

III. Design THz FSS with multiband performance, tunable response and sensing capabilities.

Throughout chapters 6 and 7, FSS working at THz frequencies are investigated in detail for three different applications, namely multiband operation, sensing components and tunable devices.

Multiband performance and sensing capability have been achieved using perturbed FSS consisting of arrays of dipoles with a perturbation in the length of every second dipole, or with another kind of asymmetry. Two resonances, even and odd modes with parallel and anti-parallel currents, have been found to give rise to two reflection bands separated by an interaction null. For small perturbations, the odd mode is shown to strongly enhance the currents and near-field leading to exponentially increasing quality factor, and therefore sensitivity, in the absence of losses. It has been revealed that the presence of power dissipation, however, imposes a physical limitation to the maximum quality factor achievable by this approach. Sensitivities of 4.8•m/RIU for 500nm of sensed material (n = 1.73), comparable to recently published sensors, have been achieved. Perturbed FSS have also been demonstrated to be a good candidate for single-screen multi-band filters. Up to four bands are obtained by a single-layer triply perturbed FSS. Higher perturbations than for sensing applications are preferable in order to minimize the losses arising from the strong currents flowing in the dipoles for small perturbations.

Finally, a novel tunability approach to reach electronically reconfigurable FSS has been proposed. After a detailed investigation of the effect of varying distance between the

two FSS in a dual-screen configuration, it has been shown the capability to tune the resonance frequency by varying the distance between two arrays close to each other. This effect is due to near-field coupling of the two arrays, and it has been found to decrease exponentially as the arrays are separated further apart. Since the elements in arrays resonating at THz frequencies are in the micrometre-scale, it has been proposed to integrate the dual-layer FSS in micro-electro-mechanical systems (MEMS) consisting of movable four-arm membranes. This approach allows for simple integration of both technologies by independent design of the electromagnetic and mechanical components. This approach has been compared to other tunability methods, and it has been shown to be particularly adequate for arrays with micro- scale elements, exhibiting a wide range of potential applications in various types of periodic arrays, such as FSS, gratings or artificial magnetic conductors (AMC). Design examples of metallic and dielectric FSS as well as AMC have been given offering tuning capability. Metallic FSS based on complementary arrays have been shown to offer nearly 4THz tuning capability. However, the strong absorption arising from the high currents and near-fields excited in coupled closely-spaced arrays has been shown to deteriorate its performance. As a possible alternative when low- loss is required, dielectric FSS or gratings have also been shown to acquire tuning capabilities with the proposed approach. Nearly 1.5THz tuning range has been achieved by varying the distance between the dielectric grating and a nearby dielectric layer. Finally, tunable AMC have been designed by varying the distance between a patch FSS layer and a ground plane, reaching nearly 2.5THz tuning range.

IV. Future work

Based on the research undertaken in this thesis, the following topics have been seen as potential attractive future developments:

- In order to minimize the losses incurred by using metallic elements at THz, all-dielectric FSS can be investigated for very low loss applications. Dielectric gratings usually employed in optics can be investigated for its use at lower frequencies.

- Improvement in the experimental capabilities to fabricate and measure FSS. From the fabrication point of view, improving repeatability would be desired. FTIR measurements, on the other hand, could be improved by using linear polarisers,

either from commercial manufacturer or self-made using similar fabrication process as the one employed for the FSS, in order to illuminate the FSS with a particular polarization. In addition, although oblique incidences could be obtained using the FTIR measurement scheme described in this thesis, reflection measurements are not possible. It would be interesting to develop a test bench similar to the THz-TDS explained in Chapter 2, that allows illuminating and collecting the THz radiation to and from the FSS, respectively, from various angles of incidence in transmission and reflection.

- Experimental demonstration of sensing capability of THz FSS. This can be employed to measure the dielectric properties of materials at the THz part of the spectrum, to detect the presence of a material that attaches to the array, and to differentiate two compounds in order to rapidly classify them, for instance for medical test purposes. Lab-on-chip devises where certain compound (e.g. blood) is tested could be an attractive research line.

- Experimental demonstration of MEMS movable membranes based on the design propose in this thesis. Electro-static and electro-thermal actuation methods can be investigated for this application. For the MEMS fabrication, a sacrificial layer compatible with the dielectric material supporting the FSS would be needed. Photoresist, silicon dioxide or poly-silicon deposited at low temperatures are potential candidates. Dry etching of the sacrificial layer (O_2, HF vapour, XeF_2) would be preferable to wet etching to avoid the layers of the dual-layer FSS to stick together. After MEMS membranes are experimentally demonstrated, integration with periodic arrays, to achieve tunable FSS, gratings, AMC or antennas, can be investigated. The main concerns of these tunable devices seem to be their reliability.

Appendix A
Publications

A.1 Journal Papers

[1] J. Sanz-Fernandez, C. Mateo-Segura, G. Goussetis, and R. Cheung, 'Power stored and quality factors in frequency selective surfaces at thz frequencies,' IEEE Transactions on Antennas and Propagation, Vol. 59, pp. 2205-2216, 2011.

[2] J. Sanz-Fernandez, C. Mateo-Segura, G. Goussetis, R. Cheung, and M. Demuillez, 'Near-field enhancement for IR sensor applications,' Journal of Nanophotonics, 5, 051814, 2011.

[3] J.-J. Sanz-Fernandez, G. Goussetis, and R. Cheung, 'Perturbed frequency-selective surfaces fabricated on large thin polymer membranes for multiband infrared applications,' Journal of Vacuum Science Technology B: Microelectronics and Nanometer Structures, Vol. 27, pp. 3169-3174, Nov. 2009.

[4] J. Sanz-Fernandez, C. Mateo-Segura, G. Goussetis, and R. Cheung, 'Substrate Effects on Stored and Dissipated Power in Frequency Selective Surfaces at THz frequencies,' In preparation for submission to IEEE Transactions on Antennas and Propagation.

A.2 Conference Papers

[5] (Invited) G. Goussetis, J. Sanz-Fernandez, C. Mateo-Segura, R. Cheung, and M. Demuillez, 'Near-field enhancement for IR sensor applications,' Medinano3, Belgrade, Serbia, 2010.

[6] J. Sanz-Fernandez, G. Goussetis, and R. Cheung, 'Tunable 2D electromagnetic band-gap (EBG) structures based on micro-electro-mechanical systems (MEMS) for Thz frequencies,' IEEE Antennas and Propagation Society International Symposium (APSURSI), 2010 pp. 1-4, 2010.

[7] J. Sanz-Fernandez, G. Goussetis, and R. Cheung, 'Quality factor of frequency selective surfaces at infrared,' IEEE Antennas and Propagation Society International Symposium (APSURSI), 2009, pp. 1-4, 2009.

[8] R. Dickie, J. Sanz-Fernandez, R. Cahill, R. Cheung, G. Goussetis, H. Gamble, V. Fusco, M. Henry, M. Oldfield, P. Huggard, P. Howard, N. Grant, Y. Munro, P. de Maagt, 'Frequency-selective surfaces for submillimetre and THz applications', 2nd UK/Europe-China Workshop on Millimetre Waves and Terahertz Technologies, Oxford, UK, October, 2009.

[9] C. Mateo-Segura, J. Sanz-Fernandez, G. Goussetis and R. Cheung, "Structured planar surfaces exhibiting strong near-field enhancement at FIR", presented at Photon'08, Edinburgh, 2008.

References

[1] B. A. Munk, *Frequency Selective Surfaces Theory and Design*. New York: John Wiley & Sons, Inc., 2000.

[2] C. Chen, "Scattering by a two-dimensional periodic array of conducting plates," *IEEE Transactions on Antennas and Propagation*, vol. 18, pp. 660–665, Sept. 1970.

[3] J. C. Vardaxoglou, *Frequency Selective Surfaces: Analysis and Design*. Taunton, Somerset: Research Studies Press, John Wiley & Sons, Inc., 1997.

[4] T.-K. Wu, *Frequency Selective Surface And Grid Array*. Wiley Interscience, 1995.

[5] R. Mittra, C. Chan, and T. Cwik, "Techniques for analyzing frequency selective surfaces-a review," *Proceedings of the IEEE*, vol. 76 (2), pp. 1593 – 1615, 1988.

[6] J. B. Pryor, *On Ohmic Losses in Frequency Selective Surfaces at Near-Infrared wavelengths*. PhD thesis, The Ohio State University, 2003.

[7] M. MacDonald, A. Alexanian, R. York, Z. Popovic, and E. Grossman, "Spectral transmittance of lossy printed resonant-grid terahertz bandpass filters," *IEEE Transactions on Microwave Theory and Techniques*, vol. 48, pp. 712 –718, apr 2000.

[8] J. E. Raynolds, B. A. Munk, J. B. Pryor, and R. J. Marhefka, "Ohmic loss in frequency-selective surfaces," *Journal of Applied Physics*, vol. 93, no. 9, pp. 5346–5358, 2003.

[9] C. Winnewisser, F. Lewen, and H. Helm, "Transmission characteristics of dichroic filters measured by THz time-domain spectroscopy," *Applied Physics A: Materials Science & Processing*, vol. 66, pp. 593–598, 1998.

[10] S. Govindaswamy, J. East, F. Terry, E. Topsakal, J. L. Volakis, and G. I. Haddad, "Frequency-selective surface based bandpass filters in the near-infrared region," *Microwave and Optical Technology Letters*, vol. 41, no. 4, pp. 266–269, 2004.

[11] C. Debus and P. H. Bolivar, "Frequency selective surfaces for high sensitivity terahertz sensing," *Applied Physics Letters*, vol. 91, no. 18, p. 184102, 2007.

[12] N. Liu, L. Langguth, T. Weiss, J. Kastel, M. Fleischhauer, T. Pfau, and H. Giessen, "Plasmonic analogue of electromagnetically induced transparency at the drude damping limit," *Nature Materials*, vol. 8, pp. 758–762, 2009.

[13] J. Bossard, D. Werner, T. Mayer, J. Smith, Y. Tang, R. Drupp, and L. Li, "The design and fabrication of planar multiband metallodielectric frequency selective surfaces for infrared applications," *IEEE Transactions on Antennas and Propagation*, vol. 54, no. 4, pp. 1265 – 1276, 2006.

[14] R. Hill and B. Munk, "The effect of perturbating a frequency-selective surface and its relation to the design of a dual-band surface," *IEEE Transactions on Antennas and Propagation*, vol. 44, pp. 368 –374, Mar. 1996.

[15] T. Chang, R. Langley, and E. Parker, "Active frequency-selective surfaces," *IEE Proceedings - Microwaves, Antennas and Propagation*, vol. 143, no. 1, pp. 62–66, 1996.

[16] C. Mias, "Varactor tunable frequency selective absorber," *Electronics Letters*, vol. 39, no. 14, pp. 1060 – 1062, 2003.

[17] Y. Chia and A. Alphones, "Optically controlled frequency selective surface with semiconductor substrate," in *IEEE Antennas and Propagation Society International Symposium*, vol. 1, pp. 158 –161 vol.1, June 1998.

[18] W. Hu, R. Dickie, R. Cahill, H. Gamble, Y. Ismail, V. Fusco, D. Linton, N. Grant, and S. Rea, "Liquid crystal tunable mm wave frequency selective surface," *IEEE Microwave and Wireless Components Letters*, vol. 17, no. 9, pp. 667 –669, 2007.

[19] J. Zendejas, J. Gianvittorio, Y. Rahmat-Samii, and J. Judy, "Magnetic mems reconfigurable frequency-selective surfaces," *Journal of Microelectromechanical Systems*, vol. 15, no. 3, pp. 613 – 623, 2006.

[20] L. Brillouin, *Wave Propagation in Periodic Structures*. New York: Dover Publications, Inc., 1953.

[21] C. Elachi, "Waves in active and passive periodic structures: A review," *Proceedings of the IEEE*, vol. 64, no. 12, pp. 1666 – 1698, 1976.

[22] F. Hopkinson and D. Rittenhouse, "An optical problem, proposed by mr. hopkinson, and solved by mr. rittenhouse," *Transactions of the American Philosophical Society*, vol. 2, pp. pp. 201–206, 1786.

[23] N. Amitay, V. Galindo, and C. P. Wu, *Theory and analysis of phased array antennas*. New York: Wiley-Inerscience, 1972.

[24] R. Kieburtz and A. Ishimaru, "Scattering by a periodically apertured conducting screen," *IEEE Transactions on Antennas and Propagation*, vol. 9, no. 6, pp. 506 –514, 1961.

[25] C.-C. Chen, "Transmission through a conducting screen perforated periodically with apertures," *IEEE Transactions on Microwave Theory and Techniques*, vol. 18, pp. 627 – 632, Sept. 1970.

[26] E. Yablonovitch, "Inhibited spontaneous emission in solid-state physics and electronics," *Phys. Rev. Lett.*, vol. 58, pp. 2059–2062, May 1987.

[27] E. Yablonovitch, T. J. Gmitter, and K. M. Leung, "Photonic band structure: The face-centered-cubic case employing nonspherical atoms," *Phys. Rev. Lett.*, vol. 67, pp. 2295–2298, Oct 1991.

[28] J. D. Joannopoulos, S. G. Johnson, J. N. Winn, and R. D. Meade, *Photonic Crystals: Molding the Flow of Light*. Princeton University Press, 2008.

[29] D. F. Sievenpiper, *High-Impedance Electromagnetic Surfaces*. PhD thesis, University of California Los Angeles, 1999.

[30] G. Goussetis, A. P. Feresidis, and J. C. Vardaxoglou, "Tailoring the AMC and EBG Characteristics of Periodic Metallic Arrays Printed on Grounded Dielectric Substrate," *IEEE Transactions on Antennas and Propagation*, vol. 54, pp. 82–89, Jan. 2006.

[31] D. R. Smith, W. J. Padilla, D. C. Vier, S. C. Nemat-Nasser, and S. Schultz, "Composite medium with simultaneously negative permeability and permittivity," *Phys. Rev. Lett.*, vol. 84, pp. 4184–4187, May 2000.

[32] N. Engheta and R. W. Ziolkowski, *Metamaterials: Physics and Engineering Explorations*. John Wiley & Sons, Inc., 2006.

[33] F. Yang and Y. Rahmat-Samii, *Electromagnetic Band Gap Structures in Antenna Engineering*. Cambridge University Press, 2009.

[34] B. Hooberman, "Everything you ever wanted to know about frequency-selective surface filters but were afraid to ask." 2005.

[35] H. Booker, "Slot aerials and their relation to complementary wire aerials (babinet's principle)," *Journal of the Institution of Electrical Engineers - Part IIIA: Radiolocation*, vol. 93, no. 4, pp. 620 –626, 1946.

[36] N. Marcuvitz, *Waveguide handbook*. New York: McGraw-Hill, 1951.

[37] R. Langley and E. Parker, "Equivalent circuit model for arrays of square loops," *Electronics Letters*, vol. 18, pp. 294 –296, 1 1982.

[38] R. Langley and E. Parker, "Double-square frequency-selective surfaces and their equivalent circuit," *Electronics Letters*, vol. 19, pp. 675 –677, 18 1983.

[39] R. Langley and A. Drinkwater, "Improved empirical model for the jerusalem cross," *IEE Proceedings H Microwaves, Optics and Antennas*, vol. 129, no. 1, pp. 1 –6, 1982.

[40] S. Savia and E. Parker, "Equivalent circuit model for superdense linear dipole fss," *IEE Proceedings - Microwaves, Antennas and Propagation*, vol. 150, no. 1, pp. 37 – 42, 2003.

[41] C. Lee and R. Langley, "Equivalent-circuit models for frequency-selective surfaces at oblique angles of incidence," *IEE Proceedings H Microwaves, Antennas and Propagation*, vol. 132, no. 6, pp. 395 –399, 1985.

[42] J. Meloling and R. Marhefka, "Fss equivalent circuit extraction techniques," in *IEEE Antennas and Propagation Society International Symposium*, vol. 2, pp. 793 – 796 vol.2, 2003.

[43] M. Guglielmi and A. Oliner, "Multimode network description of a planar periodic metal-strip grating at a dielectric interface. i. rigorous network formulations," *IEEE Transactions on Microwave Theory and Techniques*, vol. 37, pp. 534 –541, Mar. 1989.

[44] M. Guglielmi and A. Oliner, "Multimode network description of a planar periodic metal-strip grating at a dielectric interface-ii: small-aperture and small-obstacle solutions," *IEEE Transactions on Microwave Theory and Techniques*, vol. 37, pp. 542 –552, Mar. 1989.

[45] M. Guglielmi and H. Hochstadt, "Multimode network description of a planar periodic metal-strip grating at a dielectric interface. iii. rigorous solution," *IEEE Transactions on Microwave Theory and Techniques*, vol. 37, pp. 902 –909, May 1989.

[46] A. El-Sheikh and R. Langley, "Multiport network analysis of frequency-selective surfaces," *IEE Proceedings - Microwaves, Antennas and Propagation*, vol. 141, pp. 229 –231, June 1994.

[47] S. Monni, G. Gerini, A. Neto, and A. Tijhuis, "Multimode equivalent networks for the design and analysis of frequency selective surfaces," *IEEE Transactions on Antennas and Propagation*, vol. 55, no. 10, pp. 2824 –2835, 2007.

[48] A. Barlevy and Y. Rahmat Samii, "Bandwidth properties of odd mode resonances in frequency selective surfaces," in *Antennas and Propagation Society International Symposium, 1996. AP-S. Digest*, vol. 2, pp. 1436 –1439 vol.2, July 1996.

[49] K. Sarabandi and N. Behdad, "A frequency selective surface with miniaturized elements," *IEEE Transactions on Antennas and Propagation*, vol. 55, pp. 1239 –1245, May 2007.

[50] J. Romeu and Y. Rahmat-Samii, "Fractal fss: a novel dual-band frequency selective surface," *IEEE Transactions on Antennas and Propagation*, vol. 48, pp. 1097 –1105, July 2000.

[51] A. Chuprin, E. Parker, and J. Batchelor, "Convoluted double square: single layer fss with close band spacings," *Electronics Letters*, vol. 36, pp. 1830 –1831, Oct. 2000.

[52] D. Zhang, H. Fetterman, and Y. Rahmat-Samii, "High tc superconducting frequency selective surfaces and their theoretical computer modeling," in *Antennas and Propagation Society International Symposium, AP-S*, pp. 208 –211 vol.1, June 1991.

[53] H. A. Macleod, *Thin-Film Optical Filters*. London: Institute of Physics Publishing, 2001.

[54] S. S. Wang, R. Magnusson, J. S. Bagby, and M. G. Moharam, "Guided-mode resonances in planar dielectric-layer diffraction gratings," *J. Opt. Soc. Am. A*, vol. 7, pp. 1470–1474, Aug 1990.

[55] S. S. Wang and R. Magnusson, "Design of waveguide-grating filters with symmetrical line shapes and low sidebands," *Opt. Lett.*, vol. 19, pp. 919–921, Jun 1994.

[56] R. Magnusson and S. S. Wang, "Transmission bandpass guided-mode resonance filters," *Appl. Opt.*, vol. 34, pp. 8106–8109, Dec 1995.

[57] S. S. Wang and R. Magnusson, "Multilayer waveguide-grating filters," *Appl. Opt.*, vol. 34, pp. 2414–2420, May 1995.

[58] S. T. Thurman and G. M. Morris, "Controlling the spectral response in guided-mode resonance filter design," *Appl. Opt.*, vol. 42, pp. 3225–3233, Jun 2003.

[59] H. Bertoni, L.-h. Cheo, and T. Tamir, "Frequency-selective reflection and transmission by a periodic dielectric layer," *IEEE Transactions on Antennas and Propagation*, vol. 37, pp. 78 –83, Jan. 1989.

[60] Y. Li and X. Shanjia, "Systematical analysis of dielectric frequency selective surface for millimeter wave applications," in *2nd International Conference on Microwave and Millimeter Wave Technology*, pp. 502 –505, 2000.

[61] A. Coves, B. Gimeno, J. Gil, M. Andres, A. Blas, and V. Boria, "Full-wave analysis of dielectric frequency-selective surfaces using a vectorial modal method," *IEEE Transactions on Antennas and Propagation*, vol. 52, no. 8, pp. 2091 – 2099, 2004.

[62] L. Li and D. Werner, "Design of all-dielectric frequency selective surfaces using genetic algorithms combined with the finite element-boundary integral method," in *IEEE Antennas and Propagation Society International Symposium*, vol. 4A, pp. 376 – 379 vol. 4A, 2005.

[63] P. Callaghan, E. Parker, and R. Langley, "Influence of supporting dielectric layers on the transmission properties of frequency selective surfaces," *IEE Proceedings H Microwaves, Antennas and Propagation*, vol. 138, pp. 448 –454, Oct. 1991.

[64] C. A. Balanis, *Modern Antenna Handbook*. John Wiley & Sons, Inc., 2008.

[65] E. Topsakal and J. Volakis, "On the properties of materials for designing filters at optical frequencies," in *IEEE Antennas and Propagation Society International Symposium*, vol. 4, pp. 635 – 638 vol.4, 2003.

[66] B. Widenberg, "Dissipation in frequency selective structures." Lund Institute of Technology, 2002.

[67] R. T. Kristensen, J. F. Beausang, and D. M. DePoy, "Frequency selective surfaces as near-infrared electromagnetic filters for thermophotovoltaic spectral control," *Journal of Applied Physics*, vol. 95, no. 9, pp. 4845–4851, 2004.

[68] G. Goussetis, A. P. Feresidis, and A. R. Harvey, "Experimental realisation of electromagnetic metamaterials," *Journal of Modern Optics*, vol. 57, p. 1 • 16, 2010.

[69] J. Huang and S. Lee, "Tri-band frequency selective surface with circular ring elements," in *Antennas and Propagation Society International Symposium, AP-S. Digest*, pp. 204 –207 vol.1, June 1991.

[70] T.-K. Wu, "Four-band frequency selective surface with double-square-loop patch elements," *IEEE Transactions on Antennas and Propagation*, vol. 42, pp. 1659 –1663, Dec. 1994.

[71] T.-K. Wu and S.-W. Lee, "Multiband frequency selective surface with multiring patch elements," *IEEE Transactions on Antennas and Propagation*, vol. 42, pp. 1484 –1490, Nov. 1994.

[72] G. Q. Luo, W. Hong, H. J. Tang, J. X. Chen, and L. L. Sun, "Triband frequency selective surface with periodic cell perturbation," *IEEE Microwave and Wireless Components Letters*, vol. 17, no. 6, pp. 436 –438, 2007.

[73] M. Ohira, H. Deguchi, M. Tsuji, and H. Shigesawa, "Multiband single-layer frequency selective surface designed by combination of genetic algorithm and geometry-refinement technique," *IEEE Transactions on Antennas and Propagation*, vol. 52, no. 11, pp. 2925 – 2931, 2004.

[74] J. Bossard, D. Werner, T. Mayer, and R. Drupp, "A novel design methodology for reconfigurable frequency selective surfaces using genetic algorithms," *IEEE Transactions on Antennas and Propagation*, vol. 53, no. 4, pp. 1390 – 1400, 2005.

[75] G. Kiani, K. Esselle, A. Weily, and K. Ford, "Active frequency selective surface using pin diodes," in *IEEE Antennas and Propagation Society International Symposium*, pp. 4525 –4528, 2007.

[76] G. Kiani, K. Ford, L. Olsson, K. Esselle, and C. Panagamuwa, "Switchable frequency selective surface for reconfigurable electromagnetic architecture of buildings," *IEEE Transactions on Antennas and Propagation*, vol. 58, no. 2, pp. 581 –584, 2010.

[77] C. Mias and C. Tsakonas, "Waveguide demonstration of varactor-diode-tunable band-pass frequency-selective surface," *Microwave and Optical Technology Letters*, vol. 45, no. 1, pp. 62–66, 2005.

[78] C. Mias, "Tunable multi-band frequency selective structure," in *European Radar Conference, EURAD*, pp. 299 –302, 2005.

[79] G. Li, Y. Chan, T. Mok, and J. Vardaxoglou, "Analysis of frequency selective surfaces on biased ferrite substrate," in *Antennas and Propagation Society International Symposium, AP-S. Digest*, vol. 3, pp. 1636 –1639 vol.3, June 1995.

[80] Y. C. Chan, G. Y. Li, T. S. Mok, and J. C. Vardaxoglou, "Analysis of a tunable frequency-selective surface on an in-plane biased ferrite substrate," *Microwave and Optical Technology Letters*, vol. 13, no. 2, pp. 59–63, 1996.

[81] T. Anderson, I. Alexeff, and J. Raynolds, "Plasma frequency selective surfaces," in *The 30th International Conference on Plasma Science, 2003. ICOPS 2003.*, p. 237, 2003.

[82] T. H. Anderson, "Plasma frequency selective surface (fss) radome technology protection for space-borne phased array antennas," tech. rep., Haleakala Research and Development, Inc., www.sbirsttrmall.com.

[83] K. C. Lim, J. D. Margerum, and A. M. Lackner, "Liquid crystal millimeter wave electronic phase shifter," *Applied Physics Letters*, vol. 62, no. 10, pp. 1065–1067, 1993.

[84] D. Dolfi, M. Labeyrie, P. Joffre, and J. Huignard, "Liquid crystal microwave phase shifter," *Electronics Letters*, vol. 29, pp. 926 –928, May 1993.

[85] C. Weil, G. Luessem, and R. Jakoby, "Tunable inverted-microstrip phase shifter device using nematic liquid crystals," in *IEEE MTT-S International Microwave Symposium Digest*, vol. 1, pp. 367 –370, 2002.

[86] M. Ismail, W. Hu, R. Cahill, V. Fusco, H. Gamble, D. Linton, R. Dickie, S. Rea, and N. Grant, "Phase agile reflectarray cells based on liquid crystals," *IET Microwaves, Antennas and Propagation*, vol. 1, no. 4, pp. 809 –814, 2007.

[87] F. Yang and J. R. Sambles, "Microwave liquid crystal wavelength selector," *Applied Physics Letters*, vol. 79, no. 22, pp. 3717–3719, 2001.

[88] J. Yeh, C. Chang, C.-C. Cheng, J.-Y. Huang, and S. Hsu, "Microwave characteristics of liquid-crystal tunable capacitors," *IEEE Electron Device Letters*, vol. 26, no. 7, pp. 451 – 453, 2005.

[89] Q. Zhao, L. Kang, B. Li, J. Zhou, H. Tang, and B. Zhang, "Tunable negative refraction in nematic liquid crystals," *Applied Physics Letters*, vol. 89, pp. 221918 –221918–3, Nov. 2006.

[90] J. Bossard, X. Liang, L. Li, S. Yun, D. Werner, B. Weiner, T. Mayer, P. Cristman, A. Diaz, and I. Khoo, "Tunable frequency selective surfaces and negative-zero-positive index metamaterials based on liquid crystals," *IEEE Transactions on Antennas and Propagation*, vol. 56, pp. 1308 –1320, May 2008.

[91] A. Lima, E. Parker, and R. Langley, "Tunable frequency selective surface using liquid substrates," *Electronics Letters*, vol. 30, pp. 281 –282, Feb. 1994.

[92] B. Schoenlinner, A. Abbaspour-Tamijani, L. Kempel, and G. Rebeiz, "Switchable low-loss rf mems ka-band frequency-selective surface," *IEEE Transactions on Microwave Theory and Techniques*, vol. 52, no. 11, pp. 2474 – 2481, 2004.

[93] G. Coutts, R. Mansour, and S. Chaudhuri, "A mems-tunable frequency-selective surface monolithically integrated on a flexible substrate," in *IEEE/MTT-S International Microwave Symposium*, pp. 497 –500, 2007.

[94] A. Y. Liu, "Radome diesign for airborne radar," tech. rep., Ansoft, LLC, 2008.

[95] J. Huang and J. A. Encinar, *Reflectarray antennas*. New Jersey: John Wiley & Sons, Inc., 2008.

[96] Y. Konishi and K. Uenakada, "The design of a bandpass filter with inductive strip – planar circuit mounted in waveguide," *IEEE Transactions on Microwave Theory and Techniques*, vol. 22, pp. 869 – 873, Oct. 1974.

[97] A. Monorchio, G. Manara, U. Serra, G. Marola, and E. Pagana, "Design of waveguide filters by using genetically optimized frequency selective surfaces," *IEEE Microwave and Wireless Components Letters*, vol. 15, no. 6, pp. 407 – 409, 2005.

[98] R. Langley, "A dual-frequency band waveguide using fss," *IEEE Microwave and Guided Wave Letters*, vol. 3, pp. 9 –10, Jan. 1993.

[99] A. Robinson, R. Seager, and J. Vardaxoglou, "Waveguide with resonant array inserts," *Electronics Letters*, vol. 28, no. 23, pp. 2122 –2123, 1992.

[100] S. Amjadi and M. Soleimani, "Narrow band-pass waveguide filter using frequency selective surfaces loaded with surface mount capacitors," in *International Conference on Electromagnetics in Advanced Applications, 2007. ICEAA 2007.*, pp. 173 –176, 2007.

[101] A. Robinson, J. Vardaxoglou, and R. Seager, "Wave guidance and radiation from a hollow tube formed from frequency-selective surfaces," *Electronics Letters*, vol. 29, no. 17, pp. 1531 –1533, 1993.

[102] G. Loukos and J. Vardaxoglou, "Propagation inside strip grating fss waveguides with cylindrical cross-section," *Electronics Letters*, vol. 31, pp. 778 –779, May 1995.

[103] J. Vardaxoglou, R. Seager, and A. Robinson, "Realisation of frequency selective horn antenna incited from passive array," *Electronics Letters*, vol. 28, no. 21, pp. 1955 –1956, 1992.

[104] J. James and G. Andrasic, "Superimposed dichroic microstrip antenna arrays," *IEE Proceedings H Microwaves, Antennas and Propagation*, vol. 135, pp. 304 – 312, Oct. 1988.

[105] Y. J. Lee, J. Yeo, R. Mittra, and W. S. Park, "Design of a high-directivity electromagnetic bandgap (ebg) resonator antenna using a frequency selective surface (fss) superstrate," *Microwave and optical technology letters*, vol. 43, pp. 462–467, 2004.

[106] A. Feresidis and J. Vardaxoglou, "High gain planar antenna using optimised partially reflective surfaces," *IEE Proceedings - Microwaves, Antennas and Propagation*, vol. 148, no. 6, pp. 345–350, 2001.

[107] J. James, S. Kinany, P. Peel, and G. Andrasic, "Leaky-wave multiple dichroic beamformers," *Electronics Letters*, vol. 25, no. 18, pp. 1209 –1211, 1989.

[108] R. Seager and J. Vardaxoglou, "Characterisation of leaky wave antennas constructed from solid rectangular waveguides with a dipole frequency selective surface sidewall," in *IEE National Conference on Antennas and Propagation*, pp. 295 –298, Aug. 1999.

[109] C. Mateo-Segura, G. Goussetis, and A. P. Feresidis, "Sub-wavelength profile 2-d leaky-wave antennas with two periodic layers," *IEEE Transactions on Antennas and Propagation*, vol. 59, no. 2, pp. 416 –424, 2011.

[110] M. Gingrich and D. Werner, "Synthesis of low/zero index of refraction metamaterials from frequency selective surfaces using genetic algorithms," *Electronics Letters*, vol. 41, no. 23, pp. 1266 – 1267, 2005.

[111] O. Malyuskin, V. Fusco, and A. Schuchinsky, "Phase conjugating wire fss lens," *IEEE Transactions on Antennas and Propagation*, vol. 54, pp. 1399 –1404, May 2006.

[112] U. Ozguner, B. Baertlein, C. Cavello, D. Farkas, C. Hatipoglu, S. Lytle, J. Martin, F. Paynter, K. Redmill, S. Schneider, E. Walton, and J. Young, "The osu demo '97 vehicle," in *IEEE Conference on Intelligent Transportation System, ITSC*, pp. 502 –507, Nov. 1997.

[113] E. Parker and S. Savia, "Fields in an fss screened enclosure," *IEE Proceedings - Microwaves, Antennas and Propagation,*, vol. 151, pp. 77 – 80, Feb. 2004.

[114] G. Sung, K. Sowerby, and A. Williamson, "The impact of frequency selective surfaces applied to standard wall construction materials," in *IEEE Antennas and Propagation Society International Symposium*, vol. 2, pp. 2187 – 2190 Vol.2, 2004.

[115] B. Sanz-Izquierdo, J.-B. Robertson, E. Parker, and J. Batchelor, "Small fss arrays for indoor communications," in *International Workshop on Antenna Technology: Small Antennas and Novel Metamaterials, iWAT*, pp. 466 –469, 2008.

[116] E. Parker, J. Batchelor, R. Chiang, A. Williamson, B. Sanz-Izquierdo, M. Neve, and K. Sowerby, "Frequency selectively screened office incorporating convoluted fss window," *Electronics Letters*, vol. 46, pp. 317 –318, 4 2010.

[117] T. Timusk and P. L. Richards, "Near millimeter wave bandpass filters," *Appl. Opt.*, vol. 20, pp. 1355–1360, Apr 1981.

[118] S. Biber, M. Bozzi, O. Gunther, L. Perregrini, and L.-P. Schmidt, "Design and testing of frequency-selective surfaces on silicon substrates for submillimeter-wave applications," *IEEE Transactions on Antennas and Propagation*, vol. 54, no. 9, pp. 2638 –2645, 2006.

[119] J. Archer, "A novel quasi-optical frequency multiplier design for millimeter and submillimeter wavelengths," *IEEE Transactions on Microwave Theory and Techniques*, vol. 32, pp. 421 – 427, Apr. 1984.

[120] Y. Irimajiri and T. Takano, "Frequency selective surfaces for radio astronomy," *Experimental Astronomy*, vol. 2, pp. 123–136, 1991. 10.1007/BF00576325.

[121] R. Cahill, I. M. Sturland, J. W. Bowen, E. A. Parker, and A. C. de Lima, "Frequency selective surfaces for millimetre and submillimetre wave quasi optical demultiplexing," *International Journal of Infrared and Millimeter Waves*, vol. 14, pp. 1769–1788, 1993. 10.1007/BF02101331.

[122] R. Cahill and E. A. Parker, "Frequency selective surface design for submillimetric demultiplexing," *Microwave and Optical Technology Letters*, vol. 7, no. 13, pp. 595–597, 1994.

[123] R. Cahill and I. M. Sturland, "Frequency Selective Surfaces for Quasi-Optical Demultiplexing," in *Submillimetre and Far-Infrared Space Instrumentation* (E. J. Rolfe & G. Pilbratt, ed.), vol. 388 of *ESA Special Publication*, pp. 89–+, Dec. 1996.

[124] R. Dickie, R. Cahill, H. Gamble, V. Fusco, B. Moyna, P. Huggard, N. Grant, and C. Philpot, "Micromachined 300 ghz high q resonant slot frequency selective surface filter," *IEE Proceedings - Microwaves, Antennas and Propagation*, vol. 151, pp. 31 – 36, Feb. 2004.

[125] R. Dickie, R. Cahill, H. Gamble, V. Fusco, M. Henry, M. Oldfield, P. Huggard, P. Howard, N. Grant, Y. Munro, and P. de Maagt, "Submillimeter wave frequency selective surface with polarization independent spectral responses," *IEEE Transactions on Antennas and Propagation*, vol. 57, no. 7, pp. 1985 –1994, 2009.

[126] R. Cahill, A. Rookes, D. Bartlett, L. Porte, and I. Sturland, "Millimetric fss waveguide beamsplitter," *Electronics Letters*, vol. 31, pp. 47 –48, Jan. 1995.

[127] L. Ragan, A. Hassibi, T. Rappaport, and C. Christianson, "Novel on-chip antenna structures and frequency selective surface (fss) approaches for millimeter wave devices," in *IEEE 66th Vehicular Technology Conference*, pp. 2051 –2055, 302007-oct.3 2007.

[128] P. Vogel and L. Genzel, "Transmission and reflection of metallic mesh in the far infrared," *Infrared Physics*, vol. 4, no. 4, pp. 257 – 262, 1964.

[129] R. Ulrich, "Far-infrared properties of metallic mesh and its complementary structure," *Infrared Physics*, vol. 7, no. 1, pp. 37 – 55, 1967.

[130] R. Ulrich, "Interference filters for the far infrared," *Appl. Opt.*, vol. 7, pp. 1987–1996, Oct 1968.

[131] S. E. Whitcomb and J. Keene, "Low-pass interference filters for submillimeter astronomy," *Appl. Opt.*, vol. 19, pp. 197–198, Jan 1980.

[132] V. P. Tomaselli, D. C. Edewaard, P. Gillan, and K. D. Möller, "Far-infrared bandpass filters from cross-shaped grids," *Appl. Opt.*, vol. 20, pp. 1361–1366, Apr 1981.

[133] M. S. Durschlag and T. A. DeTemple, "Far-ir optical properties of freestanding and dielectrically backed metal meshes," *Appl. Opt.*, vol. 20, pp. 1245–1253, Apr 1981.

[134] C. M. Rhoads, E. K. Damon, and B. A. Munk, "Mid-infrared filters using conducting elements," *Appl. Opt.*, vol. 21, pp. 2814–2816, Aug 1982.

[135] S. T. Chase and R. D. Joseph, "Resonant array bandpass filters for the far infrared," *Appl. Opt.*, vol. 22, pp. 1775–1779, Jun 1983.

[136] D. M. Byrne, A. J. Brouns, F. C. Case, R. C. Tiberio, B. L. Whitehead, and E. D. Wolf, "Infrared mesh filters fabricated by electron-beam lithography," *Journal of Vacuum Science & Technology B: Microelectronics and Nanometer Structures*, vol. 3, no. 1, pp. 268–271, 1985.

[137] K. J. Kogler and R. G. Pastor, "Infrared filters fabricated from submicron loop antenna arrays," *Appl. Opt.*, vol. 27, pp. 18–19, Jan 1988.

[138] T. Schimert, M. E. Koch, and C. H. Chan, "Analysis of scattering from frequency-selective surfaces in the infrared," *J. Opt. Soc. Am. A*, vol. 7, pp. 1545–1553, Aug 1990.

[139] P. Irwin, P. Ade, S. Calcutt, F. Taylor, J. Seeley, R. Hunneman, and L. Walton, "Investigation of dielectric spaced resonant mesh filter designs for pmirr," *Infrared Physics*, vol. 34, no. 6, pp. 549 – 563, 1993.

[140] D. W. Porterfield, J. L. Hesler, R. Densing, E. R. Mueller, T. W. Crowe, and R. M. W. II, "Resonant metal-mesh bandpass filters for the far infrared," *Appl. Opt.*, vol. 33, pp. 6046–6052, Sep 1994.

[141] M. D. Morgan, W. E. Horne, V. Sundaram, J. C. Wolfe, S. V. Pendharkar, and R. Tiberio, "Application of optical filters fabricated by masked ion beam lithography," vol. 14, pp. 3903–3906, AVS, 1996.

[142] K. D. Möller, J. B. Warren, J. B. Heaney, and C. Kotecki, "Cross-shaped bandpass filters for the near- and mid-infrared wavelength regions," *Appl. Opt.*, vol. 35, pp. 6210–6215, Nov 1996.

[143] K. A. McIntosh, L. J. Mahoney, K. M. Molvar, O. B. McMahon, S. Verghese, M. Rothschild, and E. R. Brown, "Three-dimensional metallodielectric photonic crystals exhibiting resonant infrared stop bands," *Applied Physics Letters*, vol. 70, no. 22, pp. 2937–2939, 1997.

[144] S. Gupta, G. Tuttle, M. Sigalas, and K.-M. Ho, "Infrared filters using metallic photonic band gap structures on flexible substrates," *Applied Physics Letters*, vol. 71, no. 17, pp. 2412–2414, 1997.

[145] C. Winnewisser, F. Lewen, J. Weinzierl, and H. Helm, "Transmission features of frequency-selective components in the far infrared determined by terahertz time-domain spectroscopy," *Appl. Opt.*, vol. 38, pp. 3961–3967, Jun 1999.

[146] I. Puscasu, D. Spencer, and G. D. Boreman, "Refractive-index and element-spacing effects on the spectral behavior of infrared frequency-selective surfaces," *Appl. Opt.*, vol. 39, pp. 1570–1574, Apr 2000.

[147] I. Puscasu, W. L. Schaich, and G. D. Boreman, "Modeling parameters for the spectral behavior of infrared frequency-selective surfaces," *Appl. Opt.*, vol. 40, pp. 118–124, Jan 2001.

[148] K. E. Paul, C. Zhu, J. C. Love, and G. M. Whitesides, "Fabrication of mid-infrared frequency-selective surfaces by soft lithography," *Appl. Opt.*, vol. 40, pp. 4557–4561, Sep 2001.

[149] S. J. Spector, D. K. Astolfi, S. P. Doran, T. M. Lyszczarz, and J. E. Raynolds, "Infrared frequency selective surfaces fabricated using optical lithography and phase-shift masks," *Journal of Vacuum Science Technology B: Microelectronics and Nanometer Structures*, vol. 19, pp. 2757–2760, Nov. 2001.

[150] M.-H. Wu, K. E. Paul, J. Yang, and G. M. Whitesides, "Fabrication of frequency-selective surfaces using microlens projection photolithography," *Applied Physics Letters*, vol. 80, no. 19, pp. 3500–3502, 2002.

[151] H. A. Smith, M. Rebbert, and O. Sternberg, "Designer infrared filters using stacked metal lattices," *Applied Physics Letters*, vol. 82, no. 21, pp. 3605–3607, 2003.

[152] W. Wen, Z. Yang, G. Xu, Y. Chen, L. Zhou, W. Ge, C. T. Chan, and P. Sheng, "Infrared passbands from fractal slit patterns on a metal plate," *Applied Physics Letters*, vol. 83, no. 11, pp. 2106–2108, 2003.

[153] W. L. Schaich, G. Schider, J. R. Krenn, A. Leitner, F. R. Aussenegg, I. Puscasu, B. Monacelli, and G. Boreman, "Optical resonances in periodic surface arrays of metallic patches," *Appl. Opt.*, vol. 42, pp. 5714–5721, Oct 2003.

[154] F. Baumann, J. William A. Bailey, A. Naweed, W. D. Goodhue, and A. J. Gatesman, "Wet-etch optimization of free-standing terahertz frequency-selective structures," *Opt. Lett.*, vol. 28, pp. 938–940, Jun 2003.

[155] A. L'oker, O. Sternberg, H. Hein, J. Schulz, and K.-D. Mfller, "Thick capacitive meshes on polyimide substrates," *Infrared Physics & Technology*, vol. 45, no. 2, pp. 153 – 157, 2004.

[156] K. Stewart, J. Fischer, J. Baldwin, A. Miller, and K. Moller, "Microstructure optics design and fabrication," in *NASA Science Technology Conference, NSTC*, 2007.

[157] R. D. Rawcliffe and C. M. Randall, "Metal mesh interference filters for the far infrared," *Appl. Opt.*, vol. 6, pp. 1353–1358, Aug 1967.

[158] R. Ulrich, T. J. Bridges, and M. A. Pollack, "Variable metal mesh coupler for far infrared lasers," *Appl. Opt.*, vol. 9, pp. 2511–2516, Nov 1970.

[159] D. A. Weitz and W. J. Skocpol, "Capacitive-mesh output couplers for optically pumped far-infrared lasers," *Opt. Lett.*, vol. 3, pp. 13–15, Jul 1978.

[160] C. M. Horwitz, "A new solar selective surface," *Optics Communications*, vol. 11, no. 2, pp. 210 – 212, 1974.

[161] T.-K. Wu, "Infrared filters for high-efficiency thermovoltaic devices," *Microwave and Optical Technology Letters*, vol. 15, no. 1, pp. 9–12, 1997.

[162] D. J. Anderson, "Nasa radioisotope power conversion technology nra overview," tech. rep., NASA TM-2005-213981, 2005.

[163] G. Kiziltas, J. Volakis, and N. Kikuchi, "Design of a frequency selective structure with inhomogeneous substrates as a thermophotovoltaic filter," *IEEE Transactions on Antennas and Propagation*, vol. 53, no. 7, pp. 2282 – 2289, 2005.

[164] T. Walsh and S.-Y. Lin, "Power density and efficiency of thermophotovoltaic energy conversion using a photonic-crystal emitter and a -d metal-grid filter," *IEEE Transactions on Electron Devices*, vol. 55, pp. 1101 –1108, May 2008.

[165] J. Le Gall, M. Olivier, and J.-J. Greffet, "Experimental and theoretical study of reflection and coherent thermal emissionby a sic grating supporting a surface-phonon polariton," *Phys. Rev. B*, vol. 55, pp. 10105–10114, Apr 1997.

[166] S. O. C. Giraud and D. G. Hasko, "Mesoscale thermal infrared sources," *Microelectronic Engineering*, vol. 41-42, pp. 579 – 582, 1998. International Conference on Micro- and Nanofarbication.

[167] I. Puscasu, W. Schaich, and G. D. Boreman, "Resonant enhancement of emission and absorption using frequency selective surfaces in the infrared," *Infrared Physics & Technology*, vol. 43, no. 2, pp. 101 – 107, 2002.

[168] G. Schider, J. R. Krenn, A. Hohenau, H. Ditlbacher, A. Leitner, F. R. Aussenegg, W. L. Schaich, I. Puscasu, B. Monacelli, and G. Boreman, "Plasmon dispersion relation of au and ag nanowires," *Phys. Rev. B*, vol. 68, p. 155427, Oct 2003.

[169] J. Melindez, A. de Castro, F. Lspez, and J. Meneses, "Spectrally selective gas cell for electrooptical infrared compact multigas sensor," *Sensors and Actuators A: Physical*, vol. 47, no. 1-3, pp. 417 – 421, 1995.

[170] T. W. J. K. M. F. T. P. Na Liu, Lutz Langguth and H. Giessen1, "Plasmonic analogue of electromagnetically induced transparency at the drude damping limit," *Nature Materials*, vol. 8, pp. 758 – 762, 2009.

[171] N. Liu, T. Weiss, M. Mesch, L. Langguth, U. Eigenthaler, M. Hirscher, C. Sonnichsen, and H. Giessen, "Planar metamaterial analogue of electromagnetically induced transparency for plasmonic sensing," *Nano Letters*, vol. 10, no. 4, pp. 1103–1107, 2010. PMID: 20017551.

[172] M. N. O. Sadiku, *Numerical Techniques in Electromagnetics*. CRC Press LLC., 2000.

[173] Z. Chen and M. Ney, "The method of weighted residuals: A general approach to deriving time- and frequency-domain numerical methods," *IEEE Antennas and Propagation Magazine*, vol. 51, no. 1, pp. 51 –70, 2009.

[174] M. J. Madou, *Fundamentals of Microfabrication: the science of miniaturization*. CRC Press LLC., 2002.

[175] MicroChemicals, *Lithography: Theory and Application of Photoresists, Developers, Solvents and Etchants*, 2008/2009.

[176] I. Puscasu, G. Boreman, R. C. Tiberio, D. Spencer, and R. R. Krchnavek, "Comparison of infrared frequency selective surfaces fabricated by direct-write electron-beam and bilayer nanoimprint lithographies," vol. 18, pp. 3578–3581, AVS, 2000.

[177] B. Monacelli, J. Pryor, B. Munk, D. Kotter, and G. Boreman, "Infrared frequency selective surface based on circuit-analog square loop design," *IEEE Transactions on Antennas and Propagation*, vol. 53, no. 2, pp. 745 – 752, 2005.

[178] Y.-H. Ye, D.-Y. Jeong, and Q. M. Zhang, "Fabrication of strain tunable infrared frequency selective surfaces on electrostrictive poly(vinylidene fluoride-trifluoroethylene) copolymer films using a stencil mask method," *Applied Physics Letters*, pp. 654 –656, July 2004.

[179] Agilent Technologies, www.agilent.com, *Agilent Network Analyzer Basics*.

[180] C. Mias, "Frequency selective surfaces loaded with surface-mount reactive components," *Electronics Letters*, vol. 39, pp. 724 – 726, May 2003.

[181] G. Gruner, *Millimeter and Submillimeter Wave Spectroscopy of Solids*. Springer, 1998.

[182] M. van Exter and D. Grischkowsky, "Characterization of an optoelectronic terahertz beam system," *IEEE Transactions on Microwave Theory and Techniques*, vol. 38, pp. 1684 –1691, Nov. 1990.

[183] A. M. Weiner, *Ultrafast Optics*. New Jersey: John Wiley & Sons, Inc., 2009.

[184] P. R. Griffiths and J. A. de Haseth, *Fourier Transform Infrared Spectroscopy*. John Wiley & Sons, Inc., 1986.

[185] ThermoNicolet, www.thermonicolet.com, *Introduction to Fourier Transform Infrared Spectrometry*.

[186] Hamamatsu, http://www.hamamatsu.com/, *Characteristics and use of infrared detectors (technical information SD-12)*.

[187] N. L. Rowell and E. A. Wang, "Bilayer free-standing beam splitter for fourier transform infrared spectrometry," *Appl. Opt.*, vol. 35, pp. 2927–2933, Jun 1996.

[188] International Crystal Laboratories, http://www.internationalcrystal.net/, *Potassium Bromide (KBr) Optical Crystals*.

[189] Infratec, www.infratec.de, *Pyroelectric detector*.

[190] J. Kraus, *Electromagnetics*. McGraw-Hill, Inc., 1984.

[191] J. Montgomery, "Scattering by an infinite periodic array of thin conductors on a dielectric sheet," *IEEE Transactions on Antennas and Propagation*, vol. 23, pp. 70–75, 1975.

[192] K. Zhang and D. Li, *Electromagnetic Theory for microwaves and optoelectronics*. Springer, 1999.

[193] F. Wooten, *Optical Properties of Solids*. New York and London: Academic Press, 1972.

[194] R. E. Matick, *Transmission Lines for Digital and Communication Networks*. New York: McGraw-Hill, 1969.

[195] E. D. Palik, *Handbook of Optical Constants of Solids*. London: Academic Press, 1985.

[196] N. W. Ashcroft and N. D. Mermin, *Solid State Physics*. Holt-Saunders International Editions, 1976.

[197] J. Weiner and F. D. Nunes, "High-frequency response ofsubwavelength-structured metals in thepetahertz domain," *Opt. Express*, vol. 16, pp. 21256–21270, Dec 2008.

[198] R. G. Chambers, "Anomalous skin effect in metals," *Lett. Nature*, vol. 165, pp. 239–240, 1950.

[199] P. W. Gilberd, "The anomalous skin effect and the optical properties of metals," *J. Phys. F: Met. Phys.*, vol. 12 (2), 1982.

[200] *Planar EM technical notes, Ansoft Designer help*.

[201] *Assigning radiation boundaries, HFSS online help*.

[202] R. Remski, B. Gray, and L. Ma, *Frequency Selective Surfaces, Design and Analysis using the Ansoft Product suite*. Ansoft Corporation.

[203] *Getting started with HFSS: Floquet ports, HFSS online help*.

[204] H. N. Rutt, "A low-cost, ultra-wide-range infrared polarizer," *Measurement Science and Technology*, vol. 6, no. 8, p. 1124, 1995.

[205] I. O. Corporation, *http://www.ispoptics.com/PDFs/PDFCatalog/Page22a.pdf*.

[206] H. Tao, N. Landy, K. Fan, A. Strikwerda, W. Padilla, R. Averitt, and X. Zhang, "Flexible terahertz metamaterials: towards a terahertz metamaterial invisible cloak," in *IEEE International Electron Devices Meeting, IEDM*, pp. 1 –4, dec. 2008.

[207] J. Bossard, S. Yun, D. H. Werner, and T. S. Mayer, "Synthesizing low loss negative index metamaterial stacks for the mid-infrared using genetic algorithms," *Optics Express*, vol. 17(17), pp. 14771–14779, 2009.

[208] A. Byers, "Accounting for high frequency transmission line loss effects in hfss," in *Proc. Ansoft User Workshop*, (Los Angeles, CA), http://www.ansoft.com, 2003.

[209] D. Pozar, *Microwave Engineering*. John Wiley & Sons, Inc., 1998.

[210] I. Al-Naib, C. Jansen, and M. Koch, "Improved terahertz sensors based on frequency selective surfaces for thin-film sensing," *33rd International Conference on Infrared, Millimeter and Terahertz Waves, 2008. IRMMW-THz 2008.*, pp. 1–2, 2008.

[211] D. W. Peters, G. R. Hadley, A. A. Cruz-Cabrera, L. I. Basilio, J. R. Wendt, S. A. Kemme, T. R. Carter, and S. Samora, "Infrared frequency selective surfaces for sensor applications," in *Proc. SPIE 7298*, 2009.

[212] M. Lambea, M. Gonzalez, J. Encinar, and J. Zapata, "Analysis of frequency selective surfaces with arbitrarily shaped apertures by finite element method and generalized scattering matrix," in *Antennas and Propagation Society International Symposium, AP-S. Digest*, vol. 3, pp. 1644 –1647 vol.3, jun 1995.

[213] N. Farahat and R. Mittra, "Analysis of frequency selective surfaces using the finite difference time domain (fdtd) method," in *IEEE Antennas and Propagation Society International Symposium*, vol. 2, pp. 568 – 571 vol.2, 2002.

[214] S. Noge, H. Ueno, K. Hohkawa, and S. Yoshikawa, "Low resistance thin al film by simple sputtering deposition," in *IEEE Ultrasonics Symposium, Proceedings*, vol. 1, pp. 379 –382 vol.1, nov 1995.

[215] H. Nagata, A. Yamaguchi, and A. Kawai, "Characterization of thin-film interference effect due to surface roughness," *Japanese Journal of Applied Physics*, vol. 34, no. Part 1, No. 7A, pp. 3754–3758, 1995.

[216] L. W. Barron, J. Neidrich, and S. K. Kurinec, "Optical, electrical, and structural properties of sputtered aluminum alloy thin films with copper, titanium and chromium additions," *Thin Solid Films*, vol. 515, no. 7-8, pp. 3363 – 3372, 2007.

[217] G. Matthai, E. M. T. Jones, and L. Young, *Microwave Filters, Impedance-Matching Networks, and Coupling Structures*. Artech House, 1980.

[218] C. Mateo-Segura, G. Goussetis, and A. Feresidis, "Resonant effects and near-field enhancement in perturbed arrays of metal dipoles," *IEEE Transactions on Antennas and Propagation*, vol. 58, pp. 2523 –2530, aug. 2010.

[219] R. Dickie, R. Cahill, H. S. Gamble, V. F. Fusco, A. G. Schuchinsky, and N. Grant, "Spatial demultiplexing in the submillimeter wave band using multilayer free-standing frequency selective surfaces," *IEEE Transactions on Antennas and Propagation*, vol. 53(6), pp. 1904–1991, 2005.

[220] A. Fallshi, M. Mishrikey, C. Hafner, and R. Vahldieck, "Analysis of multilayer frequency selective surfaces on periodic and anisotropic substrates," *Metamaterials*, vol. 3, pp. 63–74, 2009.

[221] R.-R. Xu, Z.-Y. Zong, G. Yan, and W. Wu, "Loaded frequency selective surfaces using substrate integrated waveguide technology," *Microwave and Optical Technology Letters*, vol. 50(12), pp. 3149–3152, 2008.

[222] W. R. Folks, J. Ginn, D. Shelton, J. Tharp, and G. Boreman, "Spectroscopic ellipsometry of materials for infrared micro-device fabrication," *Physica Status Solidi. Special Issue: 4th International Conference on Spectroscopic Ellipsometry*, vol. 5, pp. 1113–1116, 2008.

[223] G. Goussetis and A. P. Feresidis, "Improved thin absorbers using perturbed artificial magnetic conductors," *IEEE Antennas and Propagation Society International Symposium*, pp. 853 – 856, 2007.

[224] T. Cwik, R. Mittra, K. C. Lang, and T. K. Wu, "Frequency selective screens," *IEEE Trans. Antennas Propag. Soc. Newsl.*, vol. 29, pp. 5–10, 1987.

[225] S. Savia and E. Parker, "Superdense fss with wide reflection band and rapid rolloff," *IEEE Transactions on Antennas and Propagation*, vol. 38(25), pp. 1688 – 1689, 2002.

[226] D. S. Lockyer, J. Vardaxoglou, and R. A. Simpkin, "Complementary frequency selective surfaces," *IEE Proceedings - Microwaves, Antennas and Propagation*, vol. 147(6), pp. 501–507, 2000.

[227] A. P. Feresidis, A. Apostolopoulos, N. Serfas, and J. Vardaxoglou, "Closely coupled metallodielectric electromagnetic band-gap structures formed by double-layer dipole and tripole arrays," *IEEE Transactions on Antennas and Propagation*, vol. 52(5), pp. 1149–1158, 2004.

[228] J. Provine, J. Skinner, and D. Horsley, "Tunable subwavelength metal gratings in the mid-ir band," *IEEE Journal of Selected Topics in Quantum Electronics*, vol. 13(2), pp. 270 – 276, 2007.

[229] J. L. Skinner, A. A. Talin, and D. A. Horsley *J. Vac. Sci. Technol. B.*, vol. 26 (6), pp. 2139–2144, 2008.